University of Southampton

Faculty of Engineering and Physical Sciences

School of Engineering

Modelling and simulation of combustion characteristics of hydrogen-enriched dual-fuel combustion

by

Faisal Saud Almutairi

ORCID: 0000-0002-1028-0355

Thesis for the degree of Doctor of Philosophy

November 2022

Abstract

Most applications are currently powered by compression ignition (CI) engines due to their reliability and superior torque, power output and fuel economy. Unfortunately, CI engines cause social and environmental harms by emitting high levels of pollutants and greenhouse gases (GHGs), thus the use of alternative, zero-carbon fuels (e.g. hydrogen and ammonia) under dual-fuel (DF) combustion in CI engines has recently drawn attention, offering the potential to burn cleaner gaseous fuel at a thermal efficiency comparable to a diesel-only engine but with substantially reduced emissions. The aim of this Thesis is to develop a comprehensive, physically based numerical modelling framework to accurately predict the combustion and emissions characteristics of hydrogen-blended DF combustion.

Dual-fuel flames comprise premixed and non-premixed combustions, hence investigating their characteristics in a laminar environment clarifies their coupled nature in DF combustion. This thesis first investigates the one-dimensional laminar hybrid DF flames of various hydrogen fuel blends relevant to DF combustion by setting the conditions so that their combination represents a DF flame. The aim is to better understand the fundamental characteristics of hydrogen-blended laminar DF flames through intensive parametric study to identify the effects of diverse parameters, such as preferential diffusion and elevated pressure, on various hydrogen fuel blends. The results reveal that preferential diffusion effects via hydrogen addition greatly enhance the reaction rate by expanding the concentrations, oxidisations and formations of highly reactive species in one-dimensional laminar flame calculations. The accurate prediction of nitric oxides (NOx) emissions requires implementing a thermal and prompt NOx formation sub-model.

The second part of the Thesis is focused on developing a novel hybrid combustion model based on flamelet generated manifold (FGM) incorporating preferential diffusion effects. The model development was achieved by coupling non-premixed and premixed flamelets databases to accurately predict the multistage combustion process in DF technology. The preferential diffusion effects were incorporated using a two-step correction to better capture the auto-ignition process, flame propagation and heat release rate. The hybrid combustion model employs three control variables—mixture fraction, reaction progress variable and enthalpy—and was thoroughly validated against the experimental data of high hydrogen content DF engine combustion. The results demonstrate that the novel hybrid

combustion model can capture the multistage processes of hydrogen-blended DF combustion.

The final part of the Thesis performs a detailed parametric study to achieve greener DF combustion in a DF combustion engine by using alternative gaseous fuels (ammonia and hydrogen) and liquid fuel, replacing diesel with hydro-treated vegetable-oil (HVO). The results reveal that the improved in-cylinder parameters and thermal efficiency of hydrogen-blended ammonia DF combustion over ammonia DF combustion. The parametric study also shows that HVO can be used as a replacement for diesel pilot fuel in hydrogen-blended DF combustion engines without compromising engine thermal efficiency, demonstrating HVO's suitability as a clean pilot fuel for hydrogen-blended DF internal combustion engine applications.

Contents

List of Figures

List of Table

Declaration of Authorship

I declare that this thesis and the work presented in it is my own and has been generated by me as the result of my own original research.

I confirm that:

i. This work was done wholly or mainly while in candidature for a research degree at this University;
ii. Where any part of this thesis has previously been submitted for a degree or any other qualification at this University or any other institution, this has been clearly stated;
iii. Where I have consulted the published work of others, this is always clearly attributed;
iv. Where I have quoted from the work of others, the source is always given. With the exception of such quotations, this thesis is entirely my own work;
v. I have acknowledged all main sources of help;
vi. Where the thesis is based on work done by myself jointly with others, I have made clear exactly what was done by others and what I have contributed myself;
vii. None of this work has been published before submission

Signature: ..... Date: 07/11/2022.

Acknowledgements

I would like to express my sincere gratitude to my supervisor Dr. Ranga Dinesh Kahanda Koralage for his invaluable supervision, support and encouragement at every stage of my PhD degree. I would not have been able to survive without his insightful comments and suggestions. I would like also to extend my thanks to my secondary supervisor Prof. Andrew Cruden for his general supervision.

I am also inconceivably indebted to my parents Saud Almutairi and Wadha Almutairi for their infinite support and love throughout this long journey. To my wife (Maram), daughters (Touq and Mesk), brothers (Fawaz, Fahad and Fares), sisters (Malak and Salma), cousins (Masoud and Majed) and friends (Meshary and Nasser) thank you for your love, encouragement and prays which have kept my confidence at the highest levels.

Last but not least, I am indebted to the Kingdom of Saudi Arabia for funding my PhD project in one of the leading universities worldwide.

Nomenclature

Upper case Latin letters

AES	Ammonia energy share	-
BTDC	Before top dead centre	
CFD	Computational fluid dynamic	
CI	Compression ignition	
CMI	Continuous intake manifold injection	
CO	Carbon monoxide	
CO_2	Carbon dioxide	
CV	Control variable	
D_a	Damköhler number	-
D_k	Diffusion coefficient of species k	$m^2\ s^{-1}$
DF	Dual fuel	
DI	Direct injection	
EVO	Exhaust valve open	
FGM	Flamelet generated manifold	
H	Hydrogen atom	
H_2	Hydrogen	
HES	Hydrogen energy share	-
HO_2	Hydroperoxy radical	
HRR	Heat released rate	J/deg
HVO	Hydro-treated vegetable oil	
IC	Internal combustion	
IVC	Intake valve closed	
K_a	Karlovitz number	-
Le	Lewis number	-
M_k	Molar mass of species k	$kg\ kmol^{-1}$
N_s	Number of species	
NH_3	Ammonia	
N_2O	Nitrous oxide	
NO_2	Nitrogen dioxide	
NO_x	Nitrogen oxides	

OH	Hydroxyl	
P	Pressure	KPa
R_u	Universal gas constant	J kmol^{-1} K^{-1}
RANS	Reynolds averaged Navier–Stokes	
RCCI	Reactivity controlled compression ignition	
Re	Reynold's number	-
SI	Spark ignition	
SOI	Start of injection	
TMI	Timing intake manifold injection	
U_k	Diffusion velocity of species k	m s^{-1}
URANS	Unsteady Reynolds averaged Navier-Stokes	
Y_c	Reaction progress variable	kmol kg^{-1}
Y_k	Mass fraction of species k	-

Lower case Latin letters

c_p	Specific heat capacity of the mixture at constant pressure	J kg^{-1}K^{-1}
$c_{p,k}$	Specific heat capacity of species k	J kg^{-1}K^{-1}
h	Specific enthalpy of the mixture	J kg^{-1}
h_k	Specific enthalpy of species k	J kg^{-1}
h_k^0	Enthalpy of formation of the species k at a reference temperature	J kg^{-1}
$\dot{m}$	Mass flow rate	Kg s^{-1}
r_c	compression ratio	-
s_L	Laminar burning velocity	m s^{-1}
u	Bulk flow velocity	m s^{-1}
x_i	Cartesian coordinates	m

Greek letters

δ_L	Laminar flame thickness	m
δ_r	Inner layer thickness	m
ζ	Mixture fraction	-
η_{dual}	dual engine thermal efficiency	-
λ	Thermal conductivity	W m^{-1} K^{-1}
ρ	Density	Kg m^{-3}

Chapter 1: Introduction

1.1 Overview

For many decades, a fossil fuel has been of paramount importance to the world as being the main, if not the only, source of energy. The high dependence on them in the transport and power generation sectors has resulted in a shortage of resources. The International Energy Agency reported in 2007 that roughly 81% of world commercial energy depends on fossil fuel, and that the transportation sector had used 98% of it [1]. The high consumption rate of fossil fuel is caused by many factors such as the growth of the economy of some countries as well as the dramatic increase in the number of vehicles around the world [1]. Thereby, the high demand for the consumption of fossil fuel has been contributing to the acceleration of their depletion.

However, the crude oil price is volatile and the fuel's price behaves proportionately. The causes may be for predictable reasons (i.e., the high demand of energy) or unpredictable reasons (i.e., political reasons); the crude oil price is significantly sensitive to the latter. In addition to the price, the protection of the environment is critical to provide a healthy life for people and to safeguard the world as the utilization of conventional fuels in vehicles releases harmful emissions such as carbon dioxide (CO_2), nitrogen oxides (NO_x) and soot, causing global warming and diseases.

Hence, this has been of concern to researchers and scientists and has triggered extensive investigations into alternative zero carbon clean fuels. Among the alternatives, hydrogen is very promising because it is a zero-carbon energy carrier and fuel, thereby using hydrogen in combustion applications can reduce carbon emissions, which helps to satisfy stringent emission norms including the greenhouse gases. In addition, hydrogen has unique combustive characteristics such as a wide flammability range, high energy content, high diffusivity rate and high flame speed [2]. The wide flammability range gives the opportunity to use lean mixtures, leading to the improvement of the fuel economy. For the energy content, hydrogen is roughly three times that of conventional fuels on a weight basis, and therefore, using lean mixtures does not affect the output power of the engine. Also, the high diffusion rate of hydrogen reduces the heterogeneity of premixed charges, whereas the high flame speed results in a roughly complete

combustion. The last two properties, consequently, improve many aspects of the engine in terms of the performance, combustion and emission characteristics when use hydrogen fuel.

In modern day transport sector, most of the light, medium and heavy duty vehicles are running by internal combustion (IC) engine based propulsion systems. Almost all IC engines are powered by fossil fuels such as gasoline and diesel. However, due to stringent emission regulations and decarbonisation issues, the utilisation of alternative clean fuels such as hydrogen is becoming critically important in the IC engine based propulsion systems. Currently, the main types of engines are the spark ignition (SI) engine and the compression ignition (CI) engine. Their operational strategies are indeed different: the former utilises a spark plug to initiate the combustion, and the latter depends on air compression until the fuel attains its auto-ignition temperature, then a spontaneous combustion takes place. Regarding the SI engine, hydrogen releases zero carbon-based emissions but reduces the volumetric efficiency, due to the replacement of the incoming air by hydrogen, and increases NO_x emissions, due to the high temperature resulted from the hydrogen combustion. Additionally, the utilisation of hydrogen in SI engines significantly reduces brake thermal efficiency due to high heat losses from the burning gases to the cylinder wall compared to that of gasoline because hydrogen has a higher burning velocity and a shorter quenching distance [3]. Thus, utilisation of hydrogen in SI engines requires appropriate engine modifications.

In terms of the CI engine, dual-fuel (DF) combustion technology is regarded as one of the most promising and cost-effective approaches of utilising substantial amount of hydrogen with some pilot diesel fuel. The DF engine consists of hybrid combustion modes, namely non-premixed combustion mode representing the pilot fuel combustion and premixed combustion mode representing the main fuel combustion. In CI DF combustion engines, both liquid and gaseous fuels are used in a way that diesel fuel is injected as a pilot fuel to start the ignition while gaseous fuel such as hydrogen (or natural gas) is injected as a main fuel.

In DF engines, hydrogen is blended with diesel, and therefore, the engine-out emissions released are mainly NO_x and a marginal amount of CO_2, carbon monoxide (CO), hydrocarbon (HC) and soot. These emissions, excepting NO_x, are caused by the contribution of diesel to the combustion. However, researchers have addressed three main practical challenges of hydrogen utilisation in DF engines, restricting its maximum addition [4] . The first one is the high NO_x emissions due to

in-cylinder temperature and oxygen availability [5]. The second one is the engine knocking, which damages the engine. The engine knocking, as shown in Figure 1, is defined as audible noise caused by premature combustion (pre-ignition) of part of the compressed air-fuel mixture in the cylinder [6]. In other words, the engine knocking takes place when a portion of the fuel mixture is ignited by the hot spots on the piston or the cylinder wall before being ignited by the flame front (defined as a thin layer that separates the fuel and oxidizer). This results in strong shock waves due to the dramatic increase in the pressure, which eventually, produces the engine knocking or the so-called pinging sounds.

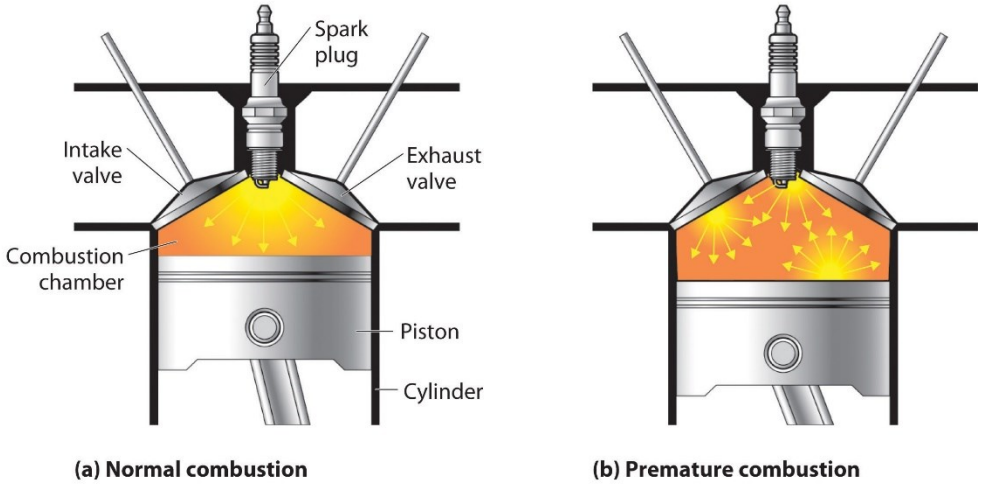

Figure 1: Schematic representations of the difference between the normal and abnormal combustions for SI engine [7].

The third one is associated with hydrogen storage due to its low density. This issue has urged researchers to find other alternatives such as the use of ammonia. Ammonia has advantages over hydrogen in terms of storage and transportation due to its high boiling temperature (-239.75 K at 1.0 atm) and high volume-based energy density (12.7 MJ/L at -239.75 K at 1.0 atm) [8]. Ammonia can power different applications such as gas turbines [9], engines [10] and fuel cells [11]. However, the utilisation of pure ammonia has concomitant practical challenges because of its combustible properties. The minimum ignition energy of ammonia (approximately 680 mJ) is much higher than that of hydrogen (approximately 0.02 mJ). Additionally, at atmospheric temperature and pressure, the ammonia laminar burning velocity is much lower compared with hydrogen as it is approximately 6–8 cm/s for the former [12] and ~300 cm/s for the latter [13]. Moreover, ammonia's substantial NO_x emissions, narrower flammability and low reactivity restrict its

utilisation in combustion applications [14] [9]. Therefore, many investigations have proposed techniques to tackle these practical challenges of ammonia-diesel DF combustion, such as blending ammonia with other fuels with higher laminar burning velocities – i.e. hydrogen – [15].

In addition to the aforementioned practical challenges related to hydrogen-diesel and ammonia-diesel DF combustion engine, the inefficient operational performance caused by the poor utilisation of gaseous fuel at low engine loads has been widely recognised and has drawn considerable attention in DF research over the years. The flames initiated from the multitude of the ignition centres of the liquid diesel pilot spray fail to propagate throughout the whole combustion chamber, leaving various amounts of the gaseous fuel-air charge unconverted. On the other hand, the utilisation of binary fuels in DF engine technology results in hybrid combustion modes, causing numerical challenges for the combustion modelling approaches in accurately capturing them.

In the past years, hydrogen-blended ammonia has been considered as one of the most promising ways to combust ammonia fuel mixtures in combustion engines. Recent investigations have proven that the addition of hydrogen to ammonia increases chemical reactivity [16] and laminar burning velocity [17] as well as expands the flammability limit [15] as opposed to combustion of pure ammonia. However, the blended fuel mixture could result in higher NO_x emissions compared with neat ammonia due to the high flame temperature and copious production of highly reactive radicals – i.e. H, O and OH – that enhance the formation of NO_x [18] [14] [19]. Thus, it is important to balance the binary fuel mixture so that acceptable levels of NO_x emissions are emitted.

Meanwhile, fossil fuels are being gradually replaced by their counterparts in an attempt to achieve transport sustainability. In this aspect, bio-diesel, particularly fatty acid methyl ester (FAME), is considered a primary alternative for diesel in CI engines because it represents 32% of the biofuel market globally [20]. However, its use is commercially limited because of its poor oxidation stability [21] and high levels of NO_x [22]. As a renewable energy source for vehicles, hydro-treated vegetable oil (HVO) has attracted attention in recent years because it enhances mixture formation, results in better combustion and mitigates emissions. In addition, HVO shortens ignition delay and leads to smoother heat release owing to its high cetane number [23]. Unlike FAME, the high similarities between HVO and diesel facilitate the use of the former in existing infrastructure; in

fact, it is currently available as a stand-alone, drop-in fuel for diesel at over 500 filling stations in Europe and North America [24].

The combustion and emissions characteristics of various fuels in canonical configurations and complex combustion engine configurations can be investigated via numerical and experimental methods. The combustion experiments are usually expensive and it can only measure limited parameters. However, numerical simulations have the ability to investigate the combustion and emissions characteristics with considerably lower cost compared to expensive experimental studies. Currently, the computational fluid dynamic (CFD) is a powerful and predictive tool in various applications. In combustion, many researchers and scientists largely rely on CFD because it helps to understand the physical and chemical aspects of the combustion processes. In CFD, the physical aspects, reaction and thermal processes of the flow are converted into non-linear partial derivative equations. Subsequently, these equations in a given domain of a system are discretized into sub-domains by using certain mathematical approaches (i.e., finite volume method), and therefore, the iterative solution takes place in the time-domain. CFD, generally speaking, contains three turbulent modelling approaches: the Reynolds averaged Navier–Stokes (RANS), large eddy simulation (LES) and direct numerical simulation (DNS). RANS is a full modelling approach that investigates the mean values of all quantities and is based on the time averaging procedure. LES is a partial modelling approach that depends on the resolution of the large eddies and the modelling of the small eddies because the former behaviour relies upon the system's geometry along with the boundary conditions and contains most of the energy, whereas the behaviour of the latter is universal and contains lower energy. DNS is a fully numerical approach that resolves the entire turbulent length scales from the integral length scale (largest length and time scale) to the Kolmogorov length scale (smallest and time length scale).

CFD modelling of combustion applications using RANS or LES approaches need turbulence and combustion models to simulate turbulent combustion problem. There are multiple combustion models available in the literature to simulate turbulent combustion problems. For example, flamelet-generated manifold (FGM), which is a tabulated chemistry approach that combines the chemistry reduction technique and the laminar flamelet modelling strategy, is one such combustion model that can be used to simulate combusting flames applicable to various combustion application [25]. The FGM combustion model has been successfully employed to simulate

turbulent premixed combustion, non-premixed combustion and partially premixed combustion applications, for example, burners, internal combustion engines and gas turbines. However, the FGM combustion model has not been employed for DF combustion applications. The focal point of this PhD study is to develop and apply an improved FGM hybrid combustion model to simulate hydrogen blended DF combustion process for a wide range of fuels such as diesel-hydrogen DF engine combustion and diesel-ammonia-hydrogen DF engine combustion and HVO-ammonia-hydrogen engine combustion. Such type of hybrid combustion model is not currently available in the literature for DF engine combustion modelling.

1.2 Aims and Objectives

The aim of this PhD study is to develop and apply an improved FGM hybrid combustion model to simulate hydrogen blended DF combustion process for a wide range of fuels such as diesel-hydrogen DF engine combustion and diesel-ammonia-hydrogen DF engine combustion and HVO-ammonia-hydrogen engine combustion. The PhD Thesis covers fluid mechanics, applied thermodynamics, combustion and emissions and numerical methods.

The objectives are described as follows:

- Fundamental study of laminar premixed and non-premixed flames relevant to hydrogen blended DF combustion under engine relevant conditions.
- Develop and optimise a physics based hybrid combustion model to predict the multi-stage process of hydrogen blended DF CI combustion.
- Validate the physics based hybrid combustion model against the experimental data for high hydrogen content DF engine combustion.
- Perform a parametric study to identify how to utilise hydrogen blended alternative fuels such as ammonia in DF engines using an improved hybrid combustion model.

1.3 Outline

This thesis is structured as follows: Chapter 2 discusses the characteristics of hydrogen fuel, the principle of the DF combustion process, the effects of adding hydrogen on performance, the

combustion and emissions characteristics of a diesel-hydrogen DF combustion engine, the challenges of hydrogen utilisation in DF combustion engine technology and the combustion modelling approaches used to predict the complex combustion of a DF combustion engine. Chapter 3 outlines the conservation equations, turbulence modelling, combustion modelling and numerical discretisation methods and details the newly improved FGM hybrid combustion model and its implementation in the CFD modelling framework. Chapter 4 provides the results of the one-dimensional laminar DF hybrid flames investigated under a wide range of conditions. Chapter 5 presents the results of the newly developed FGM combustion model in capturing the DF combustion process, auto-ignition characteristics and species concentrations of pollutant emissions of high hydrogen content diesel-hydrogen DF combustion. Chapter 6 discusses comprehensive investigations of the utilisation of alternative gaseous (hydrogen and ammonia) and liquid (HVO) fuels with the aid of the extended FGM combustion model aimed at achieving clean and green combustion. Finally, Chapter 7 summarises the thesis and offers the conclusions, recommendations for future work directions and technical challenges.

1.4 Journal publications

1. F. S. Almutairi1, K.K.J. Ranga Dinesh1, J.A. van Oijen. ‘’ Modelling of Hydrogen-Blended Dual-Fuel Engine Combustion using Flamelet-Generated Manifold and Preferential Diffusion Effects ‘’ Accepted for publication (In-press), International Journal of Hydrogen Energy, 2022.

Chapter 2: Literature Review

2.1 Introduction

This chapter provides an overview about characteristics of hydrogen fuel, the principle of DF combustion process and performance and emissions of diesel-hydrogen DF combustion engine technology. The first section provides an overview regarding the pre-utilisation processes of hydrogen, its combustive properties and the hydrogen-fuelled internal combustion engine. The second section discusses the concept of the DF engine, its operation and the design parameters, the effects of hydrogen on the performance, combustion and emissions characteristics of the engine and the challenges of using hydrogen as a fuel. The last section demonstrates the CFD combustion modelling used to simulate the DF combustion.

2.2 Hydrogen

Currently, fossil fuels are the core of the world economy as they constitute the main source of energy. However, the depletion of fossil fuels and the environmental degradation caused by their use have urged researchers to find cleaner and more efficient alternatives [26]. Hence, it is important to swift towards clean and sustainable resources to ensure the energy supply in the future. One of the most promising alternatives in the not-too-distant future is the use of hydrogen. Hydrogen is a colourless and odourless fuel and has unique combustible properties providing several advantages and a few drawbacks in comparison with the conventional fuels as discussed in Section 2.2.2. Moreover, hydrogen is environmentally benign since it is a carbon-free fuel and produces only water when two of its atoms react with one oxygen atom in the process of combustion; consequently, hydrogen satisfies the stringent emission norms [2]. Additionally, hydrogen is an energy carrier, which means it can store and deliver electrical energy via chemical reactions rather than combustion [27]. Many applications, such as vehicles and turbines, can be powered by hydrogen. However, its utilisation happens at the last stage as it needs to go through sequential pre-utilisation processes, namely, production, storage and transportation. These sequential processes pose critical issues, limiting hydrogen's practical utilisation [28].

2.2.1 Pre-utilisation processes

Hydrogen production, storage and transportation pose adverse impacts on the environment and/or are not cost-effective. For hydrogen production, the most common, economical and appropriate method is the conversion of fossil fuels, but this eventually results in pollutant emissions [29]. The safe storage and transportation of the produced hydrogen are the key stages in ensuring its future uses, and they require the consideration of different characteristics. For example, hydrogen has very low ignition energy (approximately 0.02 MJ) compared with gasoline (0.20 MJ) and natural gas (0.29 MJ), which might lead to explosions during storage. Moreover, hydrogen has a much higher diffusion coefficient than fossil-based fuel, which could yield a leakage during its transportation. Therefore, it is paramount to tackle these key issues to guarantee clean and sustainable energy in the future.

In nature, the amount of hydrogen is very minimal. In addition, it is pushed by the earth's gravitational attraction due to its low density. This makes its production from compounds rich in hydrogen indispensable. The techniques of hydrogen production can be divided into two main routes depending on the raw material used [30].

The first route is to generate hydrogen from fossil fuel-based methods, such as hydrocarbon reforming and hydrocarbon pyrolysis [31]. The hydrocarbon reforming technique is considered the cheapest, most efficient and most common hydrogen generation method in industries [32, 33]. It also represents about 95% of the hydrogen produced in the USA [34]. With this technique, the hydrocarbon fuel is reacted with steam at high temperature, resulting in a mixture of hydrogen, CO and CO_2. The implementation of hydrocarbon reforming leads to high hydrogen production. However, it also produces CO_2 and requires a high temperature input.

The second route is to generate hydrogen from renewable energy sources, such as biomass, and natural and clean resources, such as water. For the former, the gasification process can be carried out to produce hydrogen, where biomass is burned through a subsequent series of chemical reactions at a high temperature ranging from 1200 to 1500 ^{o}C, resulting in hydrogen and CO_2. The biomass gasification technique used to produce hydrogen is clean and is an almost-zero-greenhouse-emission process. However, ash deposition, sintering, fouling and clustering are the

drawbacks of biomass gasification [35]. That being said, the production of hydrogen from water splitting is achieved via electrolysis, which employs electric currents to split water into hydrogen and oxygen. This method is clean and emission-free (when the energy used for the electricity is coming from renewable sources) but consumes high amounts of energy [36].

By and large, the most economical and suitable technology for large-scale hydrogen production is currently the conversion of fossil fuels, but it poses the most adverse environmental problems [29].

Along with production issues, the safe storage of hydrogen is important for future utilities. Extremely efficient and reliable storage technologies are required to achieve a clean hydrogen economy. Various methods have been developed and suggested to store hydrogen in gas, liquid and solid phases.

A high-pressure gas steel cylinder with an operating pressure of 200 bar is a common piece of equipment used for hydrogen storage. However, to maximise the storage capacity, new lightweight composite cylinders have been designed to withstand pressures of up to 800 bar to enhance the volumetric density of hydrogen to 36 kg/m^3, which is approximately half of its liquid form at the standard boiling point of -252.87 ^oC. The compressed gaseous hydrogen storage technique is commercially available, but the low volumetric capacity, the requirement of a high operating pressure and safety problems are significant issues in its implementation.

On the other hand, the storage of hydrogen in the liquid phase promotes its energy density, as the density of liquid hydrogen at 1 bar is 70 kg/m^3 [37]. Nevertheless, the boil-off and leakage of hydrogen are major challenges during the liquefaction process. Thus, a new method called cryogenic compressed (cryo-compressed) hydrogen storage has been developed to reduce energy losses. In this method, a two-step process comprising compressing and cooling is carried out. The cooling of the compressed hydrogen gas with nitrogen up to the 77 K boiling point of nitrogen leads to an increase in energy density and enhances storage capacity. Moreover, this results in a threefold increase of the volumetric density compared with non-cooled hydrogen. However, the high compression/liquefaction energy, cryogenic temperature and cost pose considerable challenges in implementing this method to store hydrogen.

Due to safety issues and the high cost of storing hydrogen in gas and liquid forms, in the past years, hydrogen storage in solids such as metal hydride, carbon-based materials and ammonia has been

continuously improved to become more efficient. The storage of hydrogen in solid forms also entails some challenges, but ongoing efforts are intent on addressing these bottlenecks. For example, hydrogen storage with the aid of metal hydride suffers from high-temperature desorption of hydrogen. Efforts are being exerted to overcome this issue by enhancing kinetic and thermodynamic properties through ball milling [38].

Recently, the storage of hydrogen through ammonia, known as a hydrogen carrier, has become an exciting method as it ensures a high hydrogen storage capacity due to the higher density of ammonia [39]. Then, the cracking of ammonia to produce hydrogen can be carried out with the aid of a catalytic converter prior to its supply to the engine. In addition, this process ensures a reduction in NO_x emissions owing to the removal of nitrogen atoms from ammonia during its dehydrogenation process.

Besides the generation and storage of hydrogen, hydrogen transportation is an important stage toward the use of hydrogen fuel in different applications. Thus, the knowledge of hydrogen properties is critical to preventing explosion and leakage incidents.

Various hydrogen transportation options have been suggested in the literature. The most common hydrogen transportation method comprises compressed gas cylinders, cryogenic liquid tankers and pipelines. For the first two methods, the pollutant emission outputs and natural resource consumption for hydrogen transportation by trucks are crucial factors that should be taken into consideration. However, pipelines are the most cost-effective option for large power plants (~1000 metric tons/day) [40]. Besides, large-scale pipeline transportation is also considered the most environmentally friendly means of hydrogen delivery [41]. In addition, as the pipelines are mostly buried underground, the possibility of an accident occurring due to leakage and explosion can be reduced. In spite of the significant investment required to establish the pipeline network, the subsequent maintenance and operation cost is low. However, there are still many difficulties in developing an infrastructure for a hydrogen pipeline network due to its properties. For instance, the diffusivity of hydrogen is very high, which requires the establishment of pipeline network components designed to prevent leakage through valves, seals and gaskets. In addition, the embrittlement of pipeline steels and other construction materials causes the degradation of mechanical properties and cracking, resulting in pipeline failure [42].

2.2.2 Hydrogen properties

Hydrogen has notably different characteristics than the conventional fuels. A comparison of the properties hydrogen, gasoline, diesel and ammonia are set out in Table.1. These characteristics show that hydrogen has several advantages and also a few disadvantages as compared to fossil fuels. One of the advantages of hydrogen is its high energy content. This results in the production of a high amount of thermal energy, allowing hydrogen to be utilized in a lean mixture which consequently improves the fuel consumption. For example, 1 kg of hydrogen provides a vehicle with as much energy as approximately 3 kg of gasoline and diesel [4]. Also, hydrogen has a wide flammability range – defined as the concentration range or mixture strength to initiate the combustion –, allowing to use very lean fuel-air mixtures to be utilized in the engine which increases the fuel economy [43] [44]. Moreover, the high diffusivity rate and flame speed of hydrogen are very important properties which significantly affect its performance, combustion and emission characteristics. The former allows the formation of a homogenous mixture, whereas the latter increases the possibility of complete combustion by accelerating the chemical reaction rate [4]. Furthermore, the minimum ignition energy of hydrogen – known as the lowest amount of energy required to ignite a fuel-air mixture – is very low. This makes hydrogen suitable to be ignited under a lean condition. However, this increases the knocking tendency as hydrogen-air mixture can be ignited from hot spots.

However, the auto-ignition temperature of hydrogen – defined as the lowest temperature needed for the spontaneous ignition of a combustible mixture – is significantly higher than that of conventional fuels, as shown in Table 1. This creates some difficulties in igniting hydrogen-air mixture without the aid of an external ignition source. Besides, the very low density of hydrogen causes major challenges in terms of the storage space required for fuelling a vehicle for an adequate driving range. Also, this yields a reduction in the energy density of the hydrogen-air mixture inside the cylinder chambers of an engine and, therefore, may lead to low power output. The low quenching gap of hydrogen can lead to its backfiring, as hydrogen-air mixture may easily move towards the intake valve upon the fuel injection [45].

Properties	Units	Hydrogen		Gasoline	Diesel	Ammonia
Storage phase		Compressed Liquid	Compressed Gas	Liquid	Liquid	Compressed Liquid
Storage temperature	K	20	298	298	298	298
Storage pressure	kPa	102	24,821	101.3	101.3	1030
Auto-ignition temperature	K	844	844	573	503	924
Flammability limits (gas in air)	Vol. %	4-75	4-75	1.4-7.6	0.6-7.5	16-25
Minimum ignition energy	mJ	-	0.02	0.14	-	8
Fuel density	(kg/m^3)	71.1	17.5	698.3	838.8	602.8
Energy density	(MJ/m^3)	8539	2101	31,074	36,403	11,333
Energy content	(MJ/kg)	120 - 142	120 - 142	46.4	48	18.8
Quenching gas	(mm)	-	0.64	2.1	-	-

Table 1: Characteristics of Hydrogen compared to gasoline, diesel and ammonia [46] [47].

2.2.3 Hydrogen-fuelled internal combustion engines (H_2ICEs)

The unique characteristics of hydrogen gives it great advantages as a source of clean and efficient fuel for combustion engines. In terms of emissions, H_2ICEs have the potential to produce roughly zero carbon-based emissions because hydrogen conceptually emits zero carbon-based emissions, as it is a free-carbon energy carrier [48].

The engine load is defined as the output of the engine's torque and is a significantly important parameter in terms of performance, combustion and emission characteristics. H_2ICEs can operate cleanly and efficiently at low engine load, but they have some drawbacks at high engine load – the low ignition energy of hydrogen may create abnormal engine behaviour, such as pre-ignition, along with increased NO_x emission, due to the increase in temperature. These effects impose a practical limitation on H_2ICE's power densities [49].

Ignition of fuel-air mixture prior to the scheduled time of ignition is known as the pre-ignition phenomenon. It leads to the heating of the engine and the production of hot spots on the piston

and/or cylinder walls. These hot spots are classified as significant causes of engine knocking. Hydrogen is highly susceptible to the pre-ignition as its ignition energy is extremely low, as shown in Table 1. The minimum ignition energy decreases as the equivalence ratio, defined as a ratio between the actual fuel-oxidizer ratio and the stoichiometric fuel/air ratio [6], increases from the lean side towards the stoichiometric condition [49]. This means that it is difficult to run H_2ICEs under stoichiometric or near stoichiometric conditions without the occurrence of pre-ignition. Stockhausen et al. suggested that the limitation of pre-ignition in H_2ICEs is $\phi \approx 0.6$ for a four-cylinder engine, at engine speed of 5000 revolutions per minute (RPM) [50].

The volumetric efficiency, defined as the air breathing ability of the engine or the engine's capability to move the air-fuel mixture into and out of the cylinder, is an important parameter in determining the power output and is largely affected by hydrogen when it is injected in the intake manifold, because the density of hydrogen is much less than those of the conventional fuels. At a stoichiometric condition for instance, hydrogen forms 30% of the hydrogen-air mixture, whereas completely vaporized gasoline forms only 2% of the premixed mixture, even though hydrogen-air mixture provides a higher power output compared to the gasoline-air mixture, due to the high value of the energy content of hydrogen [49].

In practical applications, there are two main types of IC engines. They are SI engine and the CI engine. Hydrogen can be utilised in SI engine which would produce roughly zero emissions. On the other hand, hydrogen decreases the volumetric efficiency and increases the amount of NO_x emissions due to higher heat released by the higher energy content of hydrogen [4]. Moreover, the brake thermal energy decreases because of significant heat losses. For example, at $\phi = 0.4$ and $\phi = 1$, the percentage of the energy loss due to the wall heat transfer is 25% and 45%, respectively, when hydrogen fuels SI engine [3]. Hence, for hydrogen to be used in an SI engine, the engine requires some adjustments. Regarding the CI engine, however, the utilisation of hydrogen is challenging because the auto-ignition temperature of hydrogen is much higher than the diesel auto-ignition. This means that the CI engine needs modifications to utilise hydrogen fuel, such as the use of a glow plug to initiate the combustion [51]. On the other hand, dual-fuel engine technology is appropriate with regard to the use hydrogen, whereby both the thermal efficiency and fuel economy improve due to a high compression ratio and operatively at lean conditions respectively [4]. Also, the carbon-based emissions are considerably reduced, as hydrogen is a carbon-free fuel.

2.3 Dual fuel combustion engine

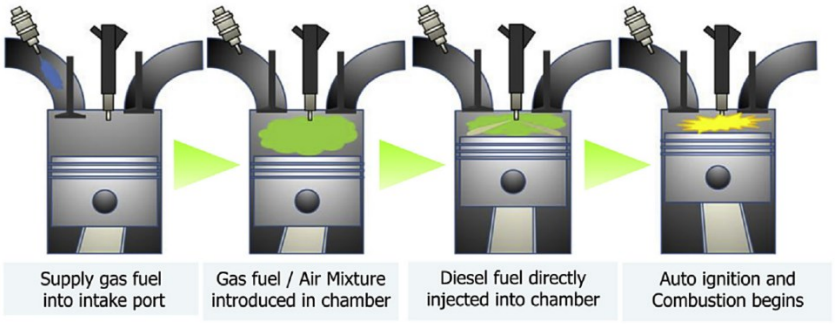

Figure 2: Schematic representation for injecting and igniting fuels in the DF combustion [52].

In internal combustion engine, the performance and emissions are significantly affected by the combustion process. The combustion process in a DF engine is a combination of both non-premixed and premixed combustion modes as shown in Figure 2. In a DF engine with gaseous intake induction, the gaseous fuel (the main fuel), which is the essential energy source, mixes with air in a gaseous phase to form a homogenous mixture in the intake manifold. It is then injected into the cylinder during the compression stroke, similar to the SI engine, whereas a small quantity of diesel fuel (the pilot fuel) is injected into the cylinder in a liquid phase at the end of the compression stroke, which is identical to the CI combustion.

When the gaseous (e.g. hydrogen-air mixture in a diesel-hydrogen DF engine) charge is compressed in the cylinder at a high pressure and temperature, as the piston reaches to the top dead centre (TDC), the appropriate environment is well-prepared to spontaneously ignite the diesel fuel, which acts here as a source of ignition. As diesel fuel is injected, spontaneous ignition occurs after the ignition delay period, which consequently creates multi-ignition sources for igniting the premixed mixture; therefore, the flame propagates from these ignition sources towards the combustible premixed mixture. However, if the engine runs out of the gaseous fuel, which is the main fuel, the engine can switch automatically from the DF mode to the CI mode, clarifying the function of diesel where the amount of the pilot fuel increases to a sufficient level to power the vehicle [53].

The quantity of the pilot fuel needs to be adjusted according to the amount of main fuel to achieve an optimum engine performance [54]. At normal load, the amount of pilot fuel required to start the

combustion of the main fuel is 10% to 20%, but it might vary according to the engine's operation and design [55].

2.3.1 Combustion processes in dual-fuel engine

As shown in Figure 3, there are five stages of the combustion process, which take place in the DF engine.

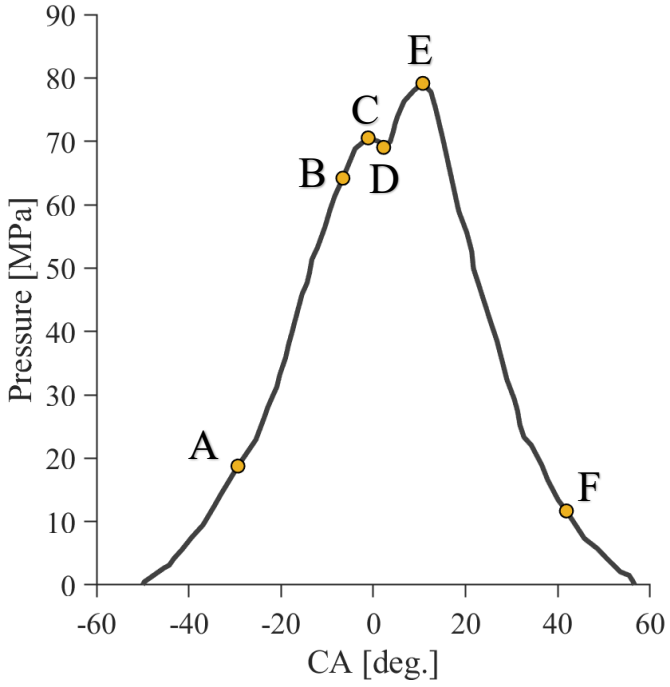

Figure 3: Pressure variation with respect to crank angle for a DF engine. For visualisation purposes.

Stage I (AB): Ignition delay of the pilot fuel, which is the time interval between the start of injection and the start of ignition.

Stage II (BC): Pilot non-premixed combustion. It occurs due to the diesel attaining the self-ignition temperature.

Stage III (CD): Ignition delay of the main fuel. This takes a very short while, because the main fuel attains the self-ignition temperature as a result of the

combustion of the pilot fuel and not from the compression that occurred in the first stage.

Stage IV (DE): Premixed combustion of the main fuel. The pressure produced in this stage is obviously higher than the pressure produced by the diesel.

Stage V (EF): Combustion of the remaining premixed charge distributed in the engine cylinder.

2.3.2 Engine operation and design parameters

Dual-fuel engine operations and design parameters play an important role in the performance, combustion and emissions characteristics of the engine. The former means the driving behaviour which largely comes down to the drive, i.e., the engine load, whereas the latter implies the engine design, i.e., the compression ratio is decided by the design engineer.

The engine load is of paramount importance to many engine aspects such as, the heat release and the combustion noise. At low load, the heat release is reduced due to injecting insufficient amount of pilot fuel which creates few ignition centres that are inadequate to ignite the premixed charge. This means, the hydrogen-air mixture does not burn completely, which causes a reduction in the thermal efficiency, temperature and pressure [4]. This also engenders negative effects, such as an excessive emission of CO, which is a product of incomplete combustion. At a medium and high load, the quantity of the pilot fuel injected is capable of roughly igniting the entire premixed charge, leading to increases in the thermal efficiency, temperature and pressure and a decrease in the CO emissions.

The injection technique plays a critical role in the performance of the engine. Hydrogen can be used in DF engine though various techniques, but the most commonly used methods are timing intake manifold injection (TMI), continuous intake manifold injection (CMI) and direct injection (DI). TMI and CMI can cause backfiring and a reduction in the volumetric efficiency as hydrogen replaces the air in the premixed charge, which limits the percentage of hydrogen utilisation [51]. As for the backfiring, it can be avoided by designing the manifold such that it is free of combustible mixtures, except in the suction stroke [4]. However, TMI has an advantage over CMI as it provides a better control on the injection timing and duration. However, DI provides a higher power output;

however, poor mixing characteristics compared to TMI and CMI. Also, the injector is exposed to a very high temperature, which damages the injector. This problem can be avoided in TMI and CMI by redesigning the manifold to keep a suitable distance between the injector and the combustion chamber and in DI by using a high-temperature resistant material [5]. According to the advantages and disadvantages, the suitable technique in the DF engine is TMI [56].

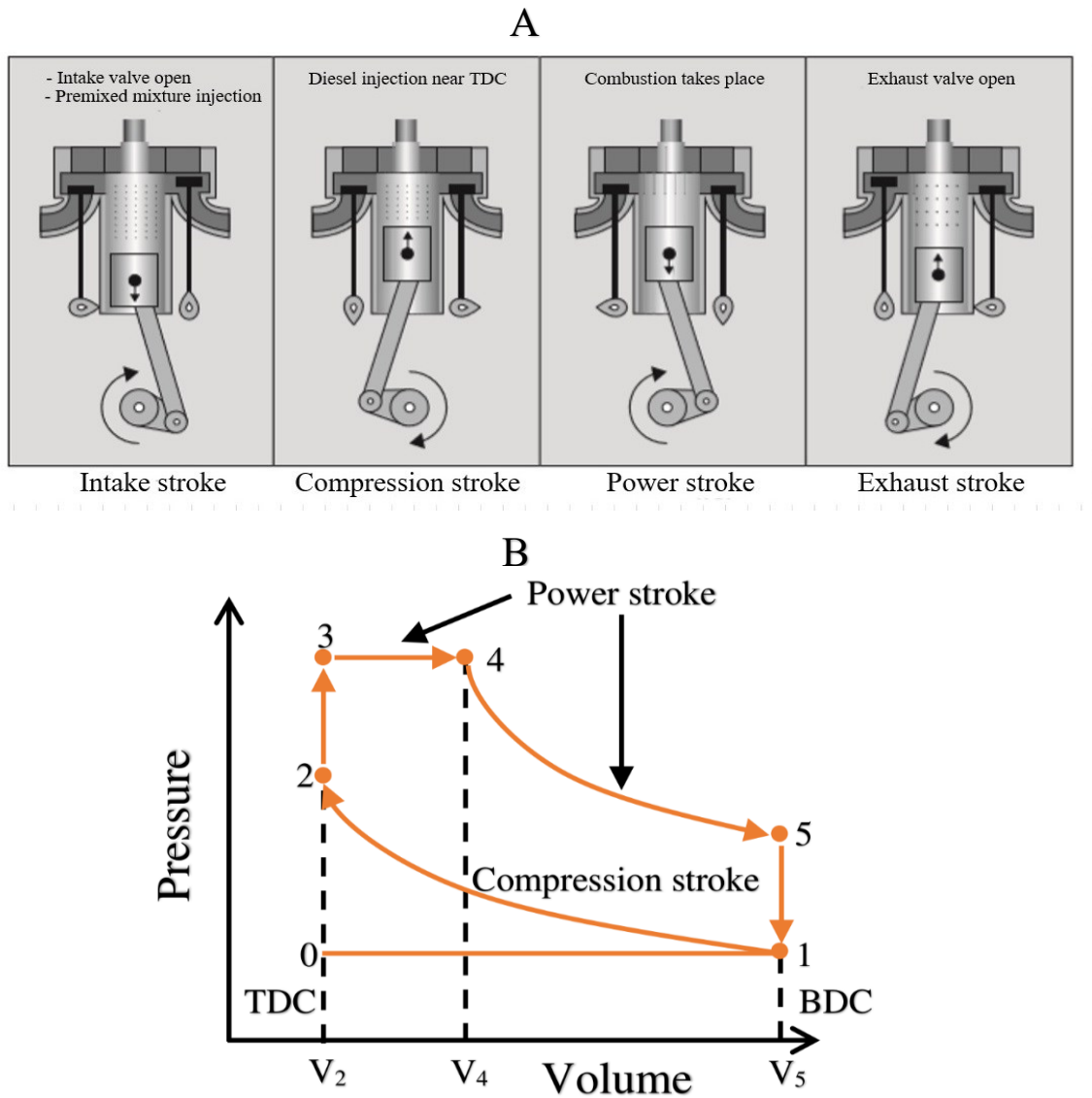

Figure 4: (A) Schematic representation of the DF strokes [57]. (B) Pressure-volume diagram of the ideal DF cycles.

The timing of injection of the pilot fuel plays a critical role in determining whether or not a complete combustion takes place [58]. At advanced injection timing, a greater amount of fuel is ignited near TDC when the cylinder volume is the smallest. This leads to complete combustion, due to the increase of in-cylinder peak pressure and temperature. At the normal injection timing, this situation is reversed because more fuel is burnt when the cylinder volume is greater.

The compression ratio is known as a ratio between the maximum and minimum cylinder volumes. It significantly affects the engine thermal efficiency, as represented in the following equation [57]:

$$\eta_{dual} = 1 - \frac{1}{r_c^{\gamma-1}}\left[\frac{r_p \alpha^{\gamma-1}}{(r_p - 1) + r_p \gamma(\alpha - 1)}\right]. \qquad 2.1,$$

where η_{dual} is the dual engine thermal efficiency, (Figure 4 is included to provide a physical visualisation for the following parameters) $r_c = \frac{V_2}{V_5}$ is the compression ratio, $r_p = \frac{P_3}{P_2}$ is the ratio of pressures, $\alpha = \frac{V_4}{V_2}$ is the ratio of volumes and $\gamma = \frac{c_p}{c_v}$ is the ratio of specific heats. The increase of the compression ratio leads to increased pressure and temperature. When these two variables exceed a critical value of the compression ratio, they cause knocking [59].

2.3.3 Effects of using hydrogen on performance, combustion and emissions in a dual-fuel engine

As mentioned in the previous section, the best way of utilising hydrogen in an internal combustion engine is to use it in a DF engine, because its use in SI and CI engines requires major modifications in the engines due to the significant heat losses and difficulties in attaining the high auto-ignition temperature of hydrogen, respectively. Having said that, as the diesel engine is highly unsatisfactory in terms of the engine exhaust emissions, as compared to gasoline and hydrogen, can significantly reduce the emissions [46], the latter was coupled in a DF engine in this study. Hydrogen is chosen as the main fuel (the main source of energy) because of its distinct combustible

characteristics. Diesel, in turn, is the pilot fuel because it is used just to ignite the hydrogen due to its high auto-ignition temperature.

By and large, this literature review focuses on three essential aspects to study their impacts on the use of hydrogen in the DF engine: the characteristics of performance, the characteristics of combustion and the engine emissions. These aspects are discussed in the following sub-sections.

As the independency of carbon-containing emissions has become increasingly critical in the past years, ammonia-enriched hydrogen gaseous premixed mixtures in conjunction with pilot fuel are investigated in this project. In addition, HVO has drawn attention over the past years as it satisfies the stringent emission norms better when compared with diesel. It is also being investigated as a renewable counterpart replacement to diesel. The effects of ammonia and HVO on combustion, performance and emission characteristics without the addition of hydrogen are discussed below due to the lack of literature on investigating them with hydrogen in DF CI engines.

2.3.3.1 Performance characteristics

Hydrogen, as mentioned, has unique combustible characteristics, which significantly influence the concomitant engine performance. This sub-section discusses how these characteristics affect the engine in terms of providing greater energy to the vehicle. The performance characteristics in are divided into brake thermal efficiency, volumetric efficiency and exhaust gas temperature, which are discussed below.

The brake thermal efficiency is defined as the ratio between the brake power and the maximum heat released. It indicates how efficient the thermodynamic processes are in terms of the conversion of the energy to mechanical work. The brake thermal efficiency has two distinct behaviours that mainly depend on the engine load. With respect to the substitution of conventional fuel with hydrogen, a low engine load causes a reduction in the brake thermal efficiency. This occurs because insufficient amount of diesel is injected, which creates a small number of ignition centres. Consequently, the premixed hydrogen-air charge cannot be ignited completely, leading to incomplete combustion [60]. Lata and Misra et al. [61] experimentally and theoretically studied the performance of a hydrogen-diesel DF engine. They reported that the reduction of brake thermal efficiency at 9% of engine load was from 19.57% to 17.37% with the addition of pure diesel and

0.04897 kg/min of hydrogen, respectively. Also, Li and Liu et al. [62] investigated the effects of hydrogen or natural gas on a DF engine. At 10% of engine load, they found a decrease in the brake thermal efficiency by 4% by using pure diesel and after the addition 6% of hydrogen by volume.

However, the brake thermal efficiency increases with the addition of hydrogen at medium and high loads. In these cases, the quantity of pilot fuel injected is enough to create an adequate number of ignition centres, enhancing the complete combustion. Furthermore, this behaviour largely arises from the high flame velocity and the diffusivity rate of hydrogen. The former results in a reduction of unburnt fuel, while the latter yields better mixing characteristics (heterogeneity reduction), which effectively reduces the combustion irreversibility [63]. Gnanamoorthi and Vimalananth [64] carried out an experimental investigation aiming to maximise the substitution of diesel with hydrogen in a common rail direct injection equipped diesel engine. The authors found that the brake thermal efficiency increased by 13.52% at 40 lpm hydrogen mixture in comparison with that of pure diesel. Moreover, Yadav et al. [65] conducted an investigation to optimise the addition of hydrogen to achieve the best performance. They found similar results where a 24.47% to 27.63% improvement of the brake thermal energy and 120 g/h hydrogen flow rate were found in neat diesel at 70%.

Saravanan et al. [2] performed an experimental study about the combustion analysis of a hydrogen-diesel DF engine. Their findings showed that the brake thermal energy increases from 16.85% in pure diesel combustion to 21.48% in 7.5 litre per minute (lpm) of hydrogen flow rate under the DF mode and at 50% load. In contrast, Karagöz and Güler et al. [51] stated a reduction of brake thermal efficiency with further hydrogen addition at a high load. The reduction was from 29.34% to 23.04% at pure diesel and with 53% of hydrogen energy fraction. This occurred because of the pilot injection timing, where the piston position during the in-cylinder pressure peak was not appropriate. They authors also recommended the optimization of the pilot injection timing to avoid this inefficiency.

On the other hand, Niki et al. [66] carried out an experimental investigation to demonstrate the effects of ammonia addition in ammonia-diesel DF combustion. They reported a slight reduction in the thermal efficiency from ~ 31% for pure diesel to ~ 30% for 13.3 lpm ammonia addition. This can be attributed to the low heat-specific ratio of the ammonia-air mixture in comparison with that of pure air. For HVO, Dimitriadis et al. [67] performed an experimental study to examine the

effects of paraffinic fuel, represented by HVO, on the combustion and emission characteristics. Their outcomes demonstrated a very slight reduction in thermal efficiency when diesel is replaced by HVO at different operating conditions. In practice, this reduction might not be noticeable and may be attributed to the difference in fuel density.

The volumetric efficiency is defined as a ratio between the volumes of air entrained into the cylinder and the swept volume. It significantly decreases in the presence of hydrogen due to the replacement of air by hydrogen in the intake manifold. Köse and Ciniviz [5] studied the effects of the addition of hydrogen with diesel on the performance and engine-out emissions. They reported that the reduction in volumetric efficiency occurred with 0.15 kg/h of hydrogen from 81.1 % in pure diesel to 78.9 % in a hydrogen based DF engine. Sharma and Dhar [60]conducted an experiment to study the combustion characteristics of hydrogen-diesel DF combustion. They reported a continuous reduction of the volumetric efficiency with the increase of hydrogen energy share at 25%, 50% and 75% engine loads. For a higher engine load, the volumetric efficiency showed further reduction, indicating that the volumetric efficiency is influenced by hydrogen addition as well as the engine loads. As the engine load increases, the in-cylinder temperature increases, which reduces the air density and then the volumetric efficiency [60]. In other words, a high in-cylinder temperature expends the gases, leading to lesser amount of air being drawn into the displacement volume.

The combustion temperature of hydrogen is much higher than that of diesel due to the significant difference in the energy content. In addition to the energy content, Varde and Frame [68] suggested that the rapid combustion due to the high flame speed of hydrogen results in an increase in the combustion temperature. Therefore, the combustion of hydrogen-blended diesel under DF mode provides a higher temperature as opposed to the neat diesel combustion. Koten [28] studied the effects of various hydrogen substitutions with diesel on the performance and emissions of a CI engine. He stated that the exhaust gas temperature, with 80% of hydrogen energy share, achieves a temperature of 534^{o}C, as opposed to 515^{o}C for pure diesel. Chintala and Subramanian [69] investigated the hydrogen-air mixture energy on combustion characteristics. They reported an increase in the exhaust gas temperature from 24.1% to 25% in pure diesel and 33.6% of hydrogen energy share blended diesel, respectively.

2.3.3.2 Combustion characteristics

In the combustion stage, there are several variables that are enhanced by the type of fuel. Hydrogen, in particular, has two unique properties, namely diffusivity rate and flame velocity. These characteristics gives hydrogen many advantages over the conventional fuels, as presented below. In this part, the combustion characteristics are categorized into heat release, in-cylinder temperature and pressure, pressure rise, ignition delay, combustion duration and combustion efficiency.

In the DF mode, the heat release is divided into three stages [70] [61]. In the first stage, the heat release occurs due to the combustion of the majority of the diesel, with a small amount of premixed mixture drawn in diesel spray region during the ignition delay period. In the second stage, the heat release takes place because of the premixed combustion due to the consumption of most of the premixed charge coupled to a small portion of the diesel. Finally, the heat is released due to the combustion of the remaining fuel distributed throughout the combustion chamber. The heat release rate of the second stage is higher than the first stage due to the combustion of most of the hydrogen, which has a higher energy content compared to the diesel. However, it was stated that the heat release rate of a DF engine has mainly two phases, which is quite similar to the mechanism of a classical conventional CI engine [71]. They represent the combustion of diesel with the premixed mixture drawn in the liquid fuel spray during the ignition delay period and the combustion of the leftover premixed charge due to the flame propagation coming from the diesel spray region.

The in-cylinder temperature represents the thermal energy. Hydrogen energy content is three times higher than the energy content of diesel; therefore, hydrogen yields a higher thermal energy, which thus generates a higher in-cylinder temperature at medium and high loads. Chintala and Subramanian [69] investigated a hydorgen-diesel DF engine using exergy analysis reporting that the in-cylinder temperature increases roughly from 1770 K to 2000 K at zero and 33.6% of hydrogen energy share, respectively. Jafarmadar [72] perfomed a study on the effects of the addition of hydrogen on DF engine using the exergy analysis. He published similar findings where the in-cylinder temperature increased from 2130.7 K to 3031.3 K with fuel-air ratios of 0.3 and 0.8, respectively.

The pressure generally is directly proportional to the temperature via the equation of state. This means that the pressure increases with the increase of addition of hydrogen, as the temperature

increases. The peak of in-cylinder pressure increases with hydrogen; this takes place earlier than in the case of pure diesel. This occurs due to the high diffusion coefficient of hydrogen, which results in a more homogenous premixed background. Yilmaz and Demir et al. [53] comprehensively investigated the combustion characteristics of the hydrogen-diesel DF mode. They stated that the increase of in-cylinder pressure was from 6.2 MPa to 7.3 MPa in pure diesel and 40% of hydrogen-blended diesel, respectively. Also, Saravanan et al. [2] reported that the in-cylinder pressure occurred 5^{o} earlier compared to diesel, due to the instantaneous combustion.

However, the peak in the pressure rise rate represents the point at which the combustion takes place [73]. Yilmaz and Demir et al. found that the peak of the rate of pressure rise increased from 0.22 MPa/ºCA to 0.23 MPa/ºCA and 0.28 MPa/ºCA with neat diesel, 20% and 40% of hydrogen addition, respectively [53]. Saravanan et al. also stated an increase in the peak of pressure rise with 7.5 lpm of hydrogen addition by 80%, compared to that of diesel [2].

The ignition delay is known as the time interval between the start of injection to the start of ignition. It behaves differently with hydrogen substitutions depending of the engine load where it increases and decreases at low load and higher loads respectively. At low load, the very reactive OH radical is reduced, where it plays a significant role in forming the intermediate compounds caused by the partial oxidation the premixed charge. Hence, the intermediate compounds are reduced resulting in a lesser amount of reactive species. These species, in turn, are not sufficient to speed up the chemical reaction rate [74]. At higher loads, however, the ignition delay decreases due to an adequate production of reactive species. The hydrogen addition increases the formation of the light radicals at medium and high engine loads and, hence, the ignition delay is decreased [75] [76]. Having said that, Reiter and Kong [77] performed an experimental study of ammonia-diesel CI DF combustion aiming at reducing the carbon-based emissions. Their findings showed an increase in the ignition delay as the ammonia substitution increases. This was caused by the high auto-ignition temperature of ammonia, which increases the resistance of the premixed charge for auto-ignition. Nevertheless, Bjørge et al. [78] carried out quantitative measurements of combustion and in-flame soot in for different fuels, including HVO and diesel. They found that the ignition delay of HVO is shorter than that of diesel due to the former higher cetane number.

The combustion duration is defined as the rotation period of crank shaft between the start of combustion, which is indicated by 3% of the accumulated heat release rate, and end of combustion,

which is indicated by 90% of the accumulated heat release. The combustion duration of hydrogen-blended diesel in DF mode increases at low load, whereas it adversely behaves at higher loads. Moreover, at higher loads, the flame speed increases as hydrogen increases, leading to an acceleration of the chemical reaction rate [46]. Chintala and Subramanian [79] studied the effects of varying the compression ratio on the maximum hydrogen energy share. They found that the combustion duration at full load decreases about 7°CA from neat diesel to 18% of hydrogen energy share. Also, Liew and Li et al. [45] investigated the combustion process of heavy-duty CI engine with the addition of hydrogen. They reported that the combustion duration decreased from 29.5°CA for only diesel to 23.8°C for 6% of hydrogen substitution by volume.

The combustion efficiency is characterised by the reaction rate, while the reaction rate, in turn, is linked to the in-cylinder temperature by the Arrhenius equation, as follows:

$$k = A \times e^{\left(\frac{-E_a}{R \times T}\right)} \qquad 2.2,$$

where k is the rate coefficient $\left(\frac{1}{s}\right)$, T is the in-cylinder temperature (K), E_a is activation energy and R_u is universal gas constant. According to the Equation (2.2), the reaction rate and in-cylinder temperature are in an exponentially direct proportion to each other. In addition, the high flame velocity of hydrogen enhances the complete combustion, whereas the high diffusivity rate of hydrogen yields better mixing characteristics. Hence, the combustion efficiency with the hydrogen addition decreases at low load and increases at medium and high loads. Chintala and Subramanian [79] reported an increase of the combustion efficiency at full load from roughly 91% for pure diesel to 99% for 18.8% of hydrogen-blended diesel. Liew and Li et al. [45] observed an improvement of the combustion efficiency from 93.4% to roughly 98% for 1% and 6% of hydrogen addition by volume, respectively.

2.3.3.3 Emission characteristics

Hydrogen is environmentally friendly as it is a free carbon energy carrier which releases zero carbon-based emissions. In DF engine, the carbon-based emissions are caused by the presence of diesel fuel, as it is blended hydrogen. Hydrogen, in turn, replaces the diesel fuel, leading to a

reduction of carbon-based emissions. However, the high in-cylinder temperature resulted from the hydrogen combustion produces higher NO_x emissions. In the following sub-sections, the effects of hydrogen on exhaust emissions are discussed.

CO emissions are a product of incomplete combustion and represent the wasted chemical energy. The formation of CO emissions relies upon a wide range of parameters, such as the equivalence ratio, the start of injection timing and the fuel properties [28]. Hydrogen, however, is an energy carrier free of carbon and capable of more complete combustion, which causes a reduction in CO emissions. Karagöz et al. [80] conducted an investigation of the performance and emission of CI engine with hydrogen enrichment. They reported a reduction in CO emissions from 5.7 g/kWh to 2.01 g/kWh with only diesel and hydrogen-blended diesel, respectively. Similar results were found by Chintala and Subramanian [79], where the CO emissions decreased from about 0.075 g/kWh to roughly zero with pure diesel and 42% hydrogen energy share. For ammonia, CO emissions were found to increase from ~ 30 g/kWh for pure diesel to ~ 90 g/kWh with the 40% of ammonia addition [77]. Its causes lie in the low flame speed of ammonia as it leads to decrease the in-cylinder temperature and consequently increase incomplete combustion products such as CO. On the other hand, Aatola et al. [81] studies the effects of HVO on the emissions using a heavy-duty engine at different speed and load operating conditions. They reported a reduction of CO emissions by 31–35 % for HVO when compared to diesel.

Regarding CO_2 emissions, they are reduced with the hydrogen addition at all loads, as hydrogen contains no carbon atoms. Sandalcı and Karagöz [82] stated that CO_2 emissions decrease from 622.5 g/kWh with neat diesel to roughly 235.4 g/kWh with 46% hydrogen energy fraction. In addition, Karagöz et al. [80] reported that the reduction in CO_2 emissions from pure diesel by 40% of hydrogen energy share was roughly 310 g/kWh. The addition of ammonia, however, results in a reduction in CO_2 from roughly 800 g/kWh to 400 g/kWh for pure diesel and 47% of ammonia substitution due to the reduction of the fuel's carbon atom contributing in the combustion [83]. For HVO. Hunicz et al. [84] investigated HVO under partially premixed compression ignition combustion mode with boost-exhaust gas recirculation (EGR) and also in conventional combustion mode. They found that the CO_2 is lower for HVO in comparison with that of diesel by 8% due to the lower C/H ratio of the former.

Hydrocarbon (HC) emissions occur when the combustion of hydrocarbon fuel is incomplete. They are decreased considerably as the hydrogen energy share increases. Chintala and Subramanian [79] found a reduction in HC emissions from 0.077 g/kWh with pure diesel to nearly zero with 45% hydrogen energy share. This reduction may be due to the increase of hydrogen addition which has no carbon atom and/or the better combustion because of the rapid combustion down to the high flame speed [82]. Koten [28] found similar results where the HC emissions decreased from 41.9 part per million (ppm) for neat diesel to 35.8 ppm for 0.8 lpm of hydrogen addition. In contrast, HC was reported to increase from ~ 0.2 g/kWh to ~ 1.1 g/kWh for pure diesel and 40% of ammonia addition, respectively, for the same reason resulting in higher CO emissions [77]. As for HVO, its use resulted in a decrease in HC by 37% as opposed to that of diesel because the higher volatility and lower viscosity of HVO leads to more complete combustion [84].

NO_x is a term which refers to both nitric oxide (NO) and nitrogen dioxide (NO_2). The formation of NO and NO_2 are based on the Zeldovich mechanism (Equation 2.3 and 2.4) and the availability of perhydroxyl HO_2 radical, respectively, as follows.

$$O + N_2 \rightarrow NO + N \quad (2.3)$$

$$N + O_2 \rightarrow NO + O \quad (2.4)$$

$$H + O_2 + M \rightarrow HO_2 + M \quad (2.5)$$

$$NO + HO_2 \rightarrow NO_2 + OH \quad (2.6)$$

NO_x emission is an incredibly harmful pollutant and considered as one of the biggest disadvantages with regard to using hydrogen. It is mainly formed due to in-cylinder temperature [5]. As earlier discussed, the unique combustible characteristics of hydrogen results in an increase in the in-cylinder temperature at medium and high engine loads and vice versa at a low engine load. As a consequence, NO_x emission increases with the addition of hydrogen at medium and high loads and decreases at low loads. Karagöz and Sandalcı et al. [80] conducted a study on the effects of the addition of hydrogen with diesel in a DF engine at different loads. They reported a decrease in

NO_x emissions at a low load from 5.9 g/kWh to 2 g/kWh and an increase of NO_x emissions at full load from 2 g/kWh with neat diesel to roughly 5 g/kWh with 46% of hydrogen energy fraction. Karagöz et al. [51] stated that NO_x emissions increased from 3.33 g/kWh with pure diesel to 11.23 g/kWh with 53% of hydrogen energy share at full load.

The formation of NO requires an oxidation of N or N_2,as shown in the Zeldovich mechanism. Hydrogen, as mentioned, releases more oxygen due to its high diffusion coefficient. However, the conversion of NO to NO_x requires HO_2, which is the main factor in this conversion. Its formation is believed to be situated in a low-temperature unburnt H_2 region before it is completely consumed via the flame propagation [85] and hydrogen is proven to significantly promotes its production [86].

For ammonia, NO_x achieved a decrease when a small amount of diesel, up to 80% diesel fuel energy contribution, is replaced by ammonia [77]. However, NO_x increased as a higher amount of diesel is substituted by ammonia due to the abundant fuel-bound nitrogen in ammonia. However, HVO is found to roughly slight engine-out NOx emissions in comparison with that of diesel [67].

2.3.4 Challenges of hydrogen utilisation under dual-fuel combustion mode

The utilisation of hydrogen in DF combustion engine provides considerable advantages, such as thermal efficiency, combustion efficiency, combustion irreversibility and curbing carbon-containing emissions. However, the utilisation of hydrogen in DF mode faced several key challenges, largely due to inherent properties of hydrogen fuel. These are discussed below.

2.3.4.1 Nitrogen oxides emissions

NO_x emission formation significantly increases in a high temperature environment, where oxygen and nitrogen can react effortlessly. This environment is well-prepared by using hydrogen as it has a high flame speed, high diffusivity rate and high energy content. Ultra-lean premixed charge $(i.e. \emptyset \leq 0.5)$ has the potential to lower the NO_x emissions, and as the temperature falls, the mixture becomes leaner [49]. Also, the exhaust gas recirculation (EGR) results in a reduction of

NO_x emissions because it redirects the exhaust air to the intake manifold, which causes a reduction in the intake air and, as a result, in the in-cylinder temperature [4]. However, EGR technology reduces the volumetric efficiency and then the power output, resulting in increased soot emission.

The strategy of water injection is another NO_x emissions reduction technique. Water has the potential to reduce the in-cylinder temperature by absorbing the combustion heat [87]. It can be injected through the intake manifold, accompanied by the premixed mixture, which also decreases the knocking tendency and opens the scope for utilizing a higher percentage of hydrogen energy share [88].

Pilot fuel injection timing is an important parameter that can control NO_x emissions. As the injection timing is more advanced, the cylinder volume in which the combustion occurs becomes smaller, which, consequently, leads to roughly complete combustion resulting in higher in-cylinder temperature and vice versa [58]. Thus, the pilot fuel injection timing should be balanced enough to produce an appropriate output of power without the penalty of releasing an excessive quantity of NO_x.

2.3.4.2 Knocking tendency

The knocking phenomenon poses restrictions on the use of high hydrogen energy share, to avoid the severe engine damages. It can be detected by several methods, such as in-cylinder pressure analysis and heat releases analysis. The former is based on using sensors to provide readings about the pressure rise rate because knocking produces high resonant frequencies caused by the quick pressure rise [89]. However, the latter is based on the detection of temperature variations, as the knocking releases much higher heat flux compared to the typical combustion [89].

Hydrogen is more susceptible to knocking, as opposed to the conventional fuel, due to its low ignition energy and small quenching distance [4]. However, there are various knocking avoidance techniques such as EGR technology, water injection technology and pilot fuel injection timing, as they cause a reduction in the in-cylinder temperature [46].

2.3.4.3 Limitation of hydrogen addition

Hydrogen is a zero-carbon fuel. It has the potential to enhance most areas of performance, combustion and emission characteristics, whereas it also results in undesirable consequences such as engine's abnormal behaviour, undesirably advanced combustion and the auto-ignition of the premixed mixture [49], as it exceeds a critical value in DF combustion applications. This critical value largely comes down to the engine load, compression ratio and pilot injection timing and other parameters. Engine load and compression ratio are inversely proportional to the hydrogen energy share, and as the pilot injection timing is advanced, the hydrogen energy share is observed to be reduced [46]. It is reported that the hydrogen energy share in different studies did not exceed 25% at a high load and could be higher in lower loads [4]. Miyamoto stated that the premixed hydrogen-air auto-ignited when the hydrogen energy fraction exceeded 8% in hydrogen-blended diesel in a DF engine [90]. Karagöz and Güler et al. stated that the hydrogen energy fraction could not go beyond 53% at full load and a comparatively low engine speed, due to the engine knocking [51]. However, the quantity of hydrogen can be increased by means of using EGR, water injection and pilot fuel timing strategies.

2.4 Combustion modelling

In the past decade, numerous efforts have been taken to simulate DF combustion process via three-dimensional CFD based engine combustion modelling. CFD modelling appears to be one of the key enabling technique in the development of engine technologies because it can provide efficient and flexible engine design guidelines before cut the metal to perform more expensive engine experiments. Many CFD modelling studies were carried out to investigate the combustion performance and emissions of DF engines with the aid of different combustion models.

Liu et al. [91], Tripathi et al. [75] and Frankl et al. [92] have carried out numerical simulations of diesel-natural gas and diesel-hydrogen DF combustion engines using the SAGE finite rate detailed chemistry solver. The SAGE combustion model is a detailed chemical kinetics model, employing finite-rate chemistry via a homogeneous reactor approach [93]. This approach models each CFD grid in the domain as a closed reactor, assuming that the species in each cell is homogeneously distributed, and uses mean scalars to solve the species and energy equations, whereas Arrhenius

type correlations compute the mean reaction rate. However, SAGE combustion modelling is computationally costly and, additionally, the absence of turbulence-chemistry interaction in its implementation results in large gradient predictions.

Kahila et al. [94] numerically studied diesel-methane DF combustion and Hosseini et al. [95] and Ramsay et al. [96] simulated diesel-hydrogen DF combustion using the species transport model with final rate chemistry. In this combustion model, in addition to solving the governing and turbulence transport equations, the predictions of convection, diffusion and reaction sources of chemical species are modelled by solving conservation equations for each species. The source terms of each species can be modelled by means of (i) laminar finite-rate model, (ii) eddy-dissipation model or (iii) eddy-dissipation-concept (EDC) model. The main drawback of implementing this approach lies in solving a high number of transport equations during the simulation run-time, which increases the computational costs.

Jafarmadar et al. [72] and Wang et al. [97] simulated the combustion characteristics of diesel-hydrogen and diesel-natural gas DF engines using the 3-Zones extended coherent flame (ECFM3Z) model. The ECFM is basically a premixed combustion model, employing a flame surface density equation to predict the wrinkling of the flame front surface by turbulent eddies [98]. This model is extended to model the diffusion combustion by incorporating the mixing state with the aid of its developed version, namely ECFM3Z. In ECFM3Z, each CFD cell is divided into three mixing zones: (i) pure fuel zone, (ii) pure air zone and (iii) mixed zone. Hence, three points of mixture fraction are used to describe the mixing rate occurring in these zones of each cell with the aid of probability density function (PDF). This allows to gradually transfer the unmixed fuel and air to the mixed zone. This model is computationally expensive because it requires to solve conservation equations of species along with the governing and turbulence transport equations and, additionally, it is necessary to incorporate an auto-ignition sub-model [99].

Although great efforts have been made in modelling, three major factors represent a challenge in accurately predicting the physical and chemical phenomena in DF combustion. The first factor lies in the accurate prediction of the multiphase process – the diffusion combustion phase, the transition phase and the premixed combustion phase – occurring during DF combustion due to the use of binary fuels – pilot (liquid) and main (gaseous) fuels. As seen in Figure 3, the diffusion combustion occurs, resulting in the consumption of most of the pilot fuel and some portion of gaseous fuel

drawn in the pilot fuel spray during the first ignition delay period. This is then followed by the main fuel ignition delay, representing the transition phase between hybrid combustion modes. Last, premixed combustion dominates throughout the combustion chamber, consuming the leftover premixed mixture due to the flame propagation from the liquid fuel ignition spots. These phases pose some difficulties for the above-noted combustion models, and capturing them has compelled researchers to make developments in some combustion models, yielding an increase in their systematic procedure's complexity and its consequential computational time – i.e. ECFM3Z combustion model.

The second one is the incorporation of transport consequences, which significantly plays an important role in determining all combustion variables. In many combustion models, the unity Lewis number – defined as a ratio of thermal to mass diffusivity – has been assumed, neglecting the effects of molecular transport properties or so-called preferential diffusion effects. In previous investigations, the incorporation of such effects was found to significantly change the behaviour of hydrogen and highly reactive radicals – such as atomic hydrogen (H) – and, consequently, affect fuel burning rate, flame propagation speed and heat release [100] [101]. Hence, it has been noted that there is still a research gap in clarifying and understanding the effects of molecular transport properties on performance, combustion and emissions characteristics of highly hydrogen blended mixtures DF combustion.

The last factor, which is in general related to the CFD field, is computational time. The CFD is established to keep up with the rapid growth and development of the research field because it is an accurate and time-efficient approach. Apart from the accuracy of the results, it is noted that the aforementioned combustion modelling approaches suffer from highly computational expenses resulting from two aspects. The first aspect is that the multiphase process in DF combustion requires greater complexity in terms of the combustion model's working procedure – i.e. incorporating additional techniques or sub-models. The second aspect results from the evaluation of unknown variables during the simulation run-time with assigning of a transport equation for each variable, leading to solve more equations.

In this project, the FGM combustion model is implemented to predict the multistage process of a hydrogen-added mixture DF combustion engine. The newly devolved FGM hybrid-flame combustion model tackles the aforementioned three factors, which represent a challenge to better

capture the combustion characteristics of DF combustion. As the implementation of the newly extended FGM combustion are discussed in Section (3.4.4), the solutions of three challenging factors are briefly presented. The first factor is overcome by coupling two flamelet datasets produced from two canonical configurations, representing the diffusion and premixed combustions, with the use of the threshold value, representing the transition phase. The second factor is solved by incorporating the preferential diffusion effects using a two-step correction process. The systematic working procedure of FGM, in turn, helps to tackle the third factor because the unknown variables during the three-dimensional simulation are (i) pre-computed, (ii) led by a few CVs and (iii) stored in the PDF table. Thus, the dependency of unknown variables on a small number of CVs implies that only the CVs transport equations with the governing and turbulence model transport equations need to be solved during the simulation run-time so that the dependent variables are retrieved from the PDF table with respect to the CVs computed values using linear interpolation. Correspondingly, this significantly results in much lower computing efforts compared to the combustion models noted above.

Chapter 3: Methodology

3.1 Introduction

In this chapter, four main aspects are covered: conservation equations, turbulence modelling, combustion modelling and numerical discretisation methods. The first section covers the conservation equations and the transport equations that govern the physical and chemical aspect of fluid flow. In the second section, the turbulence modelling is presented, covering the turbulence principle, its implementation importance and its different approaches. The third section introduces the combustion modelling, which discusses the nature and regime of premixed combustion, nature of diffusion combustion, its reduction techniques and detailed description of the newly improved FGM hybrid combustion model and its implementation on CFD modelling framework. The last section provides an overview of the boundary conditions, solver algorithm solution method and spatial & temporal discretisation schemes.

3.2 Conservation equations

In turbulent chemically reacting flow field, the temporal and spatial variations of variables such as temperature and species mass fraction are important to accurately simulate any application. The evaluation of these variations requires to consider the physical – i.e. diffusion – and chemical – i.e. chemical reactions – phenomena occurring in the systems. This can be mathematically achieved by means of solving non-linear, partial derivative equations known as conservation equations. The conservation equations, in turn, are derived with respect to the well-established concepts. In the following sections, the compressible forms of the governing equations, thermal and caloric equations and chemistry modelling of species source terms are discussed.

3.2.1 Conservation of mass

The conservation of mass equation, also the so-called continuity equation, is derived from the concept that mass gets conserved. In other words, the starting point in deriving the continuity

equation requires a consideration of the fact that the rate of mass increase in a fluid element is equal to the flow net rate of mass crossing the fluid element boundaries. The continuity equation can be written as follows:

$$\frac{\partial}{\partial t}(\rho) + \frac{\partial}{\partial x_i}(\rho u_i) = S_m, \qquad i \in \{1,2,3\}. \tag{3.1}$$

This equation states that the mass flux entering the fluid element is equal to that which leaves the fluid element. The term on the left represents the change rate of density, ρ, while the second term, also called the convection term, represents the mass flux coming in and out of the fluid element, where the mass travels via its velocity component, u_i towards the x_i direction. S_m stands for the source term representing the mass added to the continuous phase from the dispersed phase.

3.2.2 Conservation of momentum

The basis of the conservation of momentum is Newton's second law, which states that the rate of change of momentum of fluid particles is at par with the forces acting on fluid particles. The conservation of momentum is expressed as follows:

$$\frac{\partial}{\partial t}(\rho u_j) + \frac{\partial}{\partial x_i}(\rho u_i u_j) = -\frac{\partial}{\partial x_j}(P) + \frac{\partial}{\partial x_i}(\tau_{ij}) + \rho g_i + S_i, \tag{3.2}$$

where t, P, τ_{ij} and ρg_i stand for time, pressure, viscous stress and the gravitational body force, respectively. In general, the gravitational force diminishes with increasing flow momentum. Therefore, the gravitational force (buoyancy effects) is excluded in the simulations performed in this study as it is a common practice in turbulent combustion models that treats high Reynolds number flows. S_i is external body forces – i.e. that arise from interaction with the dispersed phase –. Under the assumption of Newtonian fluid, which states that the viscous stresses, τ_{ij}, are proportional to strain rate, the viscous stress can be modelled as follows:

$$\tau_{ij} = \mu \left[\left(\frac{\partial u_i}{\partial x_j} + \frac{\partial u_j}{\partial x_i} \right) - \frac{2}{3} \delta_{ij} \frac{\partial u_k}{\partial x_k} \right], \quad 3.3$$

where δ_{ij} is the Kronecker delta.

3.2.3 Conservation of energy

The conservation equation of energy needs more attention, as it has several forms. It is based on the first law of thermodynamics, which states that the rate of change of energy is equal to the rate of heat addition and the rate of work done. The equation regarding the conservation of energy can be expressed with respect to either the enthalpy, h, or the internal energy, e. As the combustion is a reacting-flow phenomena, the governing equation is expressed in terms of the enthalpy, as follows:

$$\frac{\partial}{\partial t}(\rho h) + \frac{\partial}{\partial x_i}(\rho u_i h) = \frac{\partial}{\partial x_i} \left(\frac{\lambda}{c_p} \frac{\partial h}{\partial x_i} \right) + \frac{\partial}{\partial x_i} D_h + S_h, \quad 3.4$$

where λ is the thermal conductivity, c_p is specific heat capacity and S_h is the source term accounting for any further heat losses. The second term in RHS represents the preferential diffusion effects term – discussed in details in Section (3.4.4.5) –.

3.2.4 Species transport equation

Due to the chemical reactions in the reacting flows, the species compositions significantly vary and can be described by using the governing equation of all species. The species transport equation with Fick's law reads as:

$$\frac{\partial}{\partial t}(\rho Y_k) + \frac{\partial}{\partial x_i}(\rho u_i Y_k) = \frac{\partial}{\partial x_i} \left(\left(\frac{\lambda}{c_p \, Le_i} \right) \frac{\partial Y_k}{\partial x_i} \right) + \dot{\omega}_k, \quad 3.5$$

where Y_k is the species mass fraction of species k, λ is the thermal conductivity, c_p is the specific heat capacity, Le_i is the Lewis number and $\dot{\omega}_k$ is the source term of species k. The first term in RHS represents the diffusion term and can be divided into two parts, representing the non-preferential diffusion and preferential diffusion terms, as follows:

$$\frac{\partial}{\partial t}(\rho Y_i) + \frac{\partial}{\partial x_i}(\rho u_i Y_i) = \frac{\partial}{\partial x_i}\left(\frac{\lambda}{c_p}\frac{\partial Y_i}{\partial x_i}\right) + \frac{\partial}{\partial x_i}\left(\frac{\lambda}{c_p}\left(\frac{1}{Le_k} - 1\right)\frac{\partial Y_i}{\partial x_i}\right) + \dot{\omega}_{Y_i}. \quad 3.6$$

The reaction progress variable, Y_c, is defined as a linear combination of species as:

$$Y_c = \sum_{k=1}^{N_s} \alpha_k Y_k, \quad 3.7$$

in which α_k donates the weighting factor coefficients of species k and is computed as $\alpha_k = 1/M_k$, where M_k is the molecular weight of species k. N_s is the total number of species. By substituting Equation (3.7) into Equation (3.6), this yields:

$$\frac{\partial}{\partial t}(\rho Y_c) + \frac{\partial}{\partial x_i}(\rho u_i Y_c) = \frac{\partial}{\partial x_i}\left(\frac{\lambda}{c_p}\frac{\partial Y_c}{\partial x_i}\right) + \frac{\partial}{\partial x_i}\left(\frac{\lambda}{c_p}\sum_{k}^{N_s}\alpha_k\left(\frac{1}{Le_k} - 1\right)\frac{\partial Y_k}{\partial x_i}\right) + \dot{\omega}_{Y_c}, \quad 3.8$$

where $\dot{\omega}_{Y_c}$ represents the source term of progress variable and follows its definition. For simplicity, the second term in RHS is donated by D_φ – discussed in Section (3.4.4.5) –. In addition, different variables can be computed from the species mass fraction and, hence, Y_c is replaced by φ. Thus, Equation (3.8) can be re-written as:

$$\frac{\partial}{\partial t}(\rho\varphi) + \frac{\partial}{\partial x_i}(\rho u_i \varphi) = \frac{\partial}{\partial x_i}\left(\frac{\lambda}{c_p}\frac{\partial \varphi}{\partial x_i}\right) + \frac{\partial}{\partial x_i} D_\varphi + \dot{\omega}_\varphi, \quad 3.9$$

3.2.5 Thermal and caloric equation of state

The set of equations (3.1), (3.2), (3.4) and (3.5) needs additional equations for closure purposes. The caloric equation of state relates the temperature to enthalpy and reads:

$$h = \sum_{k=1}^{N_s} Y_k \, h_k, \tag{3.10}$$

where

$$h_k = h_k^{ref} + \int_{T^{rfe}}^{T} c_{p,k}\,(T)dT, \tag{3.11}$$

$$c_p = \sum_{k=1}^{N_s} Y_k c_{p,k}, \tag{3.12}$$

Where h_k^{ref} stands for the reference enthalpy of species k at the reference temperature T^{ref}. Additionally, the thermal equation of state computes the pressure depending on density, temperature and molecular weight of the mixture as follows:

$$P = \rho T \frac{R}{M_{mix}} \qquad where \qquad \frac{1}{M_{mix}} = \sum_{k=1}^{N_s} \frac{Y_k}{M_k}, \tag{3.13}$$

where R and M_{mix} are the universal gas constant – $8.314\ Jmol^{-1}K^{-1}$ – and molecular weight of the mixture. In combusting flows density depends on thermodynamic state and the composition of the mixture. In this work, the density is computed from a pre-computed chemistry tabulation based on laminar flamelet library and link with CFD governing equations via presumed probability density function (PDF) – the approach is explained in Section (3.4.4).

3.2.6 Chemistry modelling

In the previous section, a set of conservation equations for chemically reacting flows were presented; however, the method of computing the chemical source term, $\dot{\omega}_{\varphi}$, in Equation (3.9) has not been introduced yet. Before introducing this, it is important to briefly explain combustion chemistry. In combustion, a chain of chemical reactions takes place, converting fuel into products.

It is complicated to describe these chemical reactions due to the participation of a large set of intermediate radicals. However, giving the following example may be able to explain the global reaction of combustion:

$$O_2 + H \leftrightharpoons OH + O, \tag{3.14}$$

However, a large set of elementary reactions occurs in the global reaction. A general reversible chemical reaction can be expressed as:

$$\sum_{k=1}^{N_s} \upsilon'_{kj} \mathcal{A}_k \leftrightharpoons \sum_{k=1}^{N_s} \upsilon''_{kj} \mathcal{A}_k \qquad for \qquad j \in [1, N_r], \tag{3.15}$$

where υ'_{kj} and υ''_{kj} stand for the forward and backward molar stoichiometric coefficients of species k in reaction j, whereas N_r and $\mathcal{A}_i$ are the number of elementary reactions and species k, respectively. The net chemical source term of species k largely comes down to each chemical reaction that species k participates in. This can be evaluated as

$$\dot{\omega}_k = \mathcal{M}_k \sum_{j=1}^{N_r} \left(\upsilon''_{kj} - \upsilon'_{kj}\right) r_j, \tag{3.16}$$

Where $\dot{\omega}_k$ stands for the chemical source term of species k. r_j stands for the reaction rate for elementary reaction j and can be computed as

$$r_j = \mathcal{K}_j^f \prod_{k=1}^{N_r} \left[\frac{\rho Y_k}{\mathcal{M}_k}\right]^{\upsilon'_{kj}} - \mathcal{K}_j^b \prod_{k=1}^{N_r} \left[\frac{\rho Y_k}{\mathcal{M}_k}\right]^{\upsilon''_{kj}}, \tag{3.17}$$

where $\mathcal{K}$ represents the coefficient of the reaction rate, and the subscriptions f and b are abbreviations of forward and backward, respectively. According to a modified Arrhenius expression, the reaction rate coefficient can be computed as follows [102]:

$$\mathcal{K}_j = \mathrm{A}_j T^{\mathrm{B}_j} exp\left(\frac{-\mathrm{E}_{a,j}}{R^0 T}\right), \qquad 3.18$$

where A_j, B_j and $\mathrm{E}_{a,j}$ refer to the pre-exponential constant, temperature exponent and activation energy, respectively. However, the backward reaction rate can be evaluated as follows:

$$\mathcal{K}_{eq,j} = \frac{\mathcal{K}_j^f}{\mathcal{K}_j^b} \ , \qquad 3.19$$

where $\mathcal{K}_{eq,j}$ donates the equilibrium constant. This procedure guarantees the accuracy in terms of calculating the chemical equilibrium [103]. The reaction rates A_j, B_j and $\mathrm{E}_{a,j}$ along with a large set of elementary chemical reactions are stored in the chemistry set implemented in this study.

This procedure is carried out in a one-dimensional laminar domain with the aid of CHEM1D. The chemical source term is stored in the chemistry tabulation and eventually retrieved in a three-dimensional simulation run-time after coupling the pre-computed tabulation with a CFD solver by means of the PDF – discussed in details in Section (3.4.4.4) –.

In this project, two chemistry mechanisms are incorporated. The first is used to simulate diesel–hydrogen and diesel–hydrogen–ammonia mixtures in the DF combustion engine. This mechanism is established on n-heptane [104], which is designated as a diesel-like fuel due to their similar properties, and hydrogen [105] with GRI 3.0 mechanism [106] involving ammonia and NO_x sub-mechanisms.

The second mechanism is used to predict HVO–hydrogen–ammonia combustion in DF applications. HVO is represented by hexadecane ($C_{16}H_{34}$) because of their highly similar properties, as seen in Table 2. A combination of hexadecane and natural gas reduced mechanisms was found in the literature [107], consisting of 155 species and 645 reactions. Due to the high number of species involved in these mechanisms, a further reduction is performed using the Directed Relation Graph with Error Propagation (DRGEP) technique, resulting in a newly reduced chemistry set consisting of 53 species and 300 reactions. The newly developed chemistry mechanisms are then validated against numerical and experimental findings in terms of the laminar burning velocity, demonstrating excellent agreements, as shown in Section (4.3). Since the hydrogen sub-mechanisms are incorporated by default, the developed chemistry set is completed

by adding ammonia and NO_x sub-mechanisms [106], which eventually consists of 71 species and 394 reactions – see Appendix A–.

Properties	Unit	HVO	Hexadecane
Density	kg/m^3	775 ~ 785 [81]	772 [108]
Kinematic Viscosity	mm^2/s	2.5 ~ 3.5 [81]	2.11 [109]
Lower heating value	MJ/kg	~ 44 [81]	44 [108]
Cetane number	-	80 ~ 99 [81]	100 [108]
Carbon to hydrogen ratio	-	5.6:1 [84]	~ 5.6:1[a]
Surface tension	N/m	0.028 [110]	0.027 [108]

a - calculated

Table 2: Properties of HVO and hexadecane.

3.3 Turbulence modelling

The flow in practical engineering combustion applications is mostly turbulent such as internal combustion engines or gas turbines, whereas the laminar flow presents in limited combustion applications such as lighters and candles. The combustion without turbulence is a fundamentally complicated process because the range of chemical time and length scales involved is very large. This requires to deal with a large set of species and chemical reactions, which consequently causes some numerical difficulties. However, in non-reacting flow, turbulence represents the most complicated phenomena due to the involvement of different time and length scales. As the combustion and turbulence separately have some numerical difficulties, the two-way interaction between chemistry and turbulence significantly increases the complexity and results in two mechanisms [111]. The first mechanism is the effects of combustion on turbulence – known as flame-generated turbulence –. Here, turbulence is promoted by chemistry as the heat release increases the flow accelerations through the flame front. Besides, the variation of temperature during the combustion process results in a large change in the kinematic viscosity. The second mechanism is the effects of turbulence on combustion. The mixing of fuel and oxidizer occurs at a molecular level and, thus, the flame structure can be altered due to the promotion of the mixing

rate by turbulence. Therefore, it is important to incorporate both turbulence and combustion modelling to accurately predict the practical turbulent combustion applications.

3.3.1 Turbulence principle

The fluid flow is divided into two distinct classifications, laminar and turbulence. They are completely different in terms of the physical nature, where the former is regular and the latter is not. They largely depend on a non-dimensional number – called Reynold's number –, which is defined as follows:

$$Re = \frac{UL\rho}{\mu} = \frac{UL}{v} \qquad 3.20$$

where U and L stand for mean average velocity and characteristic length scale, respectively. The Reynold's number is known as the ratio between the inertia forces and viscous forces. The critical value of Reynold's number, $Re_{critical}$, is where the flow behaves differently if it exceeds that value. Below the $Re_{critical}$, the flow is smooth, steady and regular (laminar) and otherwise, the flow significantly changes leading to an unsteady, random and chaotic flow (turbulent). Physically, the $Re_{critical}$ refers to a transition region between the laminar and turbulent flows, which can be enhanced by many parameters such as wall friction [112].

The flow properties of turbulence vary greatly in time and space, which consequently yield different length scales of eddies. The large eddies are known as integral scales and are dominated by inertia forces. The interaction between the mean flow and large eddies results in the vortex stretching process. During this process, the large eddies are influenced by the mean flow, yielding an increase in the rotation rate and decrease in the radius of eddies. This leads the large eddies to extract energy from the mean flow and to break up into smaller eddies as well. As the eddies become smaller, the inertia forces decrease and the viscous forces increase as they are reversely proportional to each other. The small eddies, in turn, which are known as Kolmogorov scales, break up into smaller eddies because they interact with large eddies and then get effectively stretched. Therefore, the smallest eddies are dissipated into heat due to the effect of viscous forces

where the inertia forces become negligible. In this way, kinetic energy is supplied by large eddies to gradually smaller and smaller eddies, referring to energy cascading process [112].

3.3.2 Turbulent modelling approaches

Computational fluid dynamics (CFD) is a powerful tool that analyses and predicts systems comprising fluid flow and heat transfer accompanied by phenomena such as chemical reactions. It is very useful in various fields in industrial as well as non-industrial aspects like weather prediction, combustion in both gas turbines and internal combustion engines [112]. In addition, it is capable of capturing and visualising scales in the fluid flow that cannot be visualised using experiments.

Most combustion systems have turbulent flows due to the real perturbations enhancing the conversion from laminar to turbulence. Researchers have been developing turbulent modelling methods to increase the scope for investigating these systems in details for the purpose of improvement. There are currently three turbulent modelling approaches, which are direct numerical simulations (DNS), large eddy simulation (LES) and Reynolds averaged Navier–Stokes (RANS). They are different in terms of accuracy, computational time and expenses.

Equations can represent physics and physics, in turn, can represent flows. This means flows can be investigated by solving equations analytically or computationally. The flow is considered as a volumetric phenomenon and the volume can be discretised into many tiny grids, ensuring accurate solutions as these grids are capable of capturing the smallest physical behaviour. Since the Navier–Stokes equations describe the Newtonian fluids, Newtonian fluids can be accurately captured by solving the Navier–Stokes equations numerically with the aid of CFD. To achieve this, the flow domain should be discretised into adequately fine grids and choosing small time steps to ensure the resolution of the Kolmogorov scale [113]. This approach is called DNS, where it does not require any model as it resolves the entire energy-carrying turbulent scales from the integral up to the Kolmogorov scales.

The different eddies' sizes behave differently depending on different parameters. Large eddies, which have higher energy as compared to that of small eddies, are anisotropic and their behaviour relies upon the system's geometry and boundary conditions [112]. However, small eddies are

roughly isotropic and behave universally. These differences led researchers to establish LES, which is grounded on computing large eddies and modelling small eddies.

RANS turbulence modelling approach, discussed in the following sub-section, is implemented in this study due to its low computational cost, when compared to DNS and LES, along with its acceptable accuracy. RANS techniques have been heavily used in internal combustion engine simulations with reasonably good accuracy.

3.3.2.1 Reynolds averaged Navier–Stokes equations

Reynolds averaged Navier–Stokes (RANS) is a fully modelled approach that is used to investigate the mean values of all quantities. This approach is mainly based on the time-averaged procedure/Reynolds decomposition that states that each scalar quantity is divided into a mean value/time-averaged value and a fluctuating component [112] as follows:

$$\varphi = \bar{\varphi} + \varphi' \tag{3.21}$$

where ϕ is a quantity, $\bar{\phi}$ is the mean value, and ϕ' is the fluctuating component. Using the time-averaged procedure on the conservation equation of mass (3.1) yields the following:

$$\frac{\partial \bar{\rho}}{\partial t} + \frac{\partial \left(\overline{\rho u_j}\right)}{\partial x_j} = S_m, \tag{3.22}$$

where

$$\overline{\rho u_j} = \overline{(\bar{\rho} + \rho')\left(\overline{u_j} + u_j'\right)} = \left(\bar{\rho}\overline{u_j} + \overline{\rho' u_j'}\right) \tag{3.23}$$

This procedure gives rise to an unclosed quantity, ($\overline{\rho' u_j'}$), correlating the density and velocity fluctuations and therefore, needs to be modelled. Consequently, applying a similar procedure to the conservation equations produces many unclosed quantities [112], which eventually causes difficulties in CFD. Favre averaging, also called density-weighted averaging, tackles this issue by reducing the unclosed quantities, which are defined as follows:

$$\tilde{\varphi} = \frac{\overline{\varphi u_j}}{\bar{\varphi}} \qquad 3.24$$

where any quantity, ϕ, is divided into the mean value, $\tilde{\phi}$, and the fluctuating components, ϕ'', as follows:

$$\varphi = \tilde{\varphi} + \varphi'' \qquad \text{where} \qquad \varphi'' = 0 \qquad 3.25$$

This implies that the mean of the density-weighted averaging is set to zero as follows:

$$\overline{\rho u_j} = \overline{\rho\left(\widetilde{u_j} + u_j''\right)} = \bar{\rho}\tilde{u}_j + \cancel{\overline{\rho u_j''}} \rightarrow \tilde{u}_j = \frac{\overline{\rho u_j}}{\bar{\rho}} \qquad 3.26$$

Applying the Favre averaging to the governing equations of mass (3.1), momentum (3.2), enthalpy (3.4) and any scalar quantity (3.5), respectively, yield the following:

$$\frac{\partial}{\partial t}(\bar{\rho}) + \frac{\partial}{\partial x_i}\left(\bar{\rho}\tilde{u}_j\right) = S_m, \qquad 3.27$$

$$\frac{\partial}{\partial t}(\bar{\rho}\tilde{u}_i) + \frac{\partial}{\partial x_j}\left(\bar{\rho}\tilde{u}_i\tilde{u}_j\right) = -\frac{\partial \bar{P}}{\partial x_i} + \frac{\partial}{\partial x_j}\left(\mu\left[\left(\frac{\partial \tilde{u}_i}{\partial x_j} + \frac{\partial \tilde{u}_j}{\partial x_i}\right) - \frac{2}{3}\delta_{ij}\frac{\partial \tilde{u}_k}{\partial x_k}\right] - \boldsymbol{\bar{\rho}\widetilde{u_i''u_j''}}\right) + \ S_i, \qquad 3.28$$

$$\frac{\partial}{\partial t}\left(\bar{\rho}\bar{h}\right) + \frac{\partial}{\partial x_i}\left(\bar{\rho}\tilde{u}_i\bar{h}\right) = \frac{\partial}{\partial x_i}\left(\frac{\lambda}{c_p}\frac{\partial \bar{h}}{\partial x_i}\right) + \frac{\partial}{\partial x_i}\ D_h + \ S_h, \qquad 3.29$$

$$\frac{\partial}{\partial t}(\bar{\rho}\bar{\varphi}) + \frac{\partial}{\partial x_i}(\bar{\rho}\tilde{u}_i\bar{\varphi}) = \frac{\partial}{\partial x_i}\left(\left(\frac{\lambda}{c_p} + \frac{\mu_t}{Sc_t}\right)\frac{\partial \bar{\varphi}}{\partial x_i}\right) + \frac{\partial}{\partial x_i}\ D_\varphi + \overline{\dot{\omega}_\varphi}. \qquad 3.30$$

These equations are in the time averaged flow properties forms. However, the averaging procedure results in the bold term in Equations (3.28), which is additional term called Reynolds stresses. It takes place in the RANS equations because of the interactions between different turbulent eddies

and account for the impact of turbulent vortices on the mean flow quantity [112]. This extra term creates some closure issues, and therefore, the use of a model is necessary. Thus, there are a wide variety of approaches proposed to model it and the most commonly used model is the eddy viscosity approach.

In the eddy viscosity model, the Boussinesq expression, which is based on the assumption that the Reynolds stress is proportional to the mean deformation rate, is used to model the Reynolds stress as follows:

$$\bar{\rho}\widetilde{u_i''u_j''} = -\mu_t\left(\frac{\partial\tilde{u}_i}{\partial x_j}+\frac{\partial\tilde{u}_j}{\partial x_i}-\frac{2}{3}\delta_{ij}\frac{\partial\tilde{u}_k}{\partial x_k}\right)+\frac{2}{3}\bar{\rho}k, \qquad 3.31$$

where μ_t stands for turbulent dynamic viscosity. The estimation of μ_t is essential in the eddy viscosity approach, and therefore, a wide variety of turbulence models in RANS are proposed. In this project, the standard k-epsilon model because it is acceptably accurate and meets the simulation conditions.

It is important to mention that the averaging procedure also yields additional terms in the enthalpy and scalar transport Equations (3.29) (3.30) and a classical gradient approach [111] is implemented to model them as follows:-

$$\bar{\rho}\widetilde{u_i''\Phi''} = -\frac{\mu_t}{Sc_t}\frac{\partial\bar{\Phi}}{\partial x_i}, \qquad 3.32$$

where Φ stands for any variable, Sc_t is the turbulent Schmidt number.

3.3.2.2 Standard k-epsilon model

The standard k-ε model is a turbulence model, which employs two additional transport equations one for the turbulent kinetic energy, k, and the other for the dissipation rate of turbulent kinetic energy,ε. The model transport equation for k is derived from the exact equation, while the model

transport equation for ε was obtained using physical reasoning and bears little resemblance to its mathematically exact counterpart. The transport equations of k and ε read as follows:

$$\frac{\partial}{\partial t}(\bar{\rho}k) + \frac{\partial}{\partial x_i}(\bar{\rho}\tilde{u}_i k) = \frac{\partial}{\partial x_i}\left[\left(\mu + \frac{\mu_t}{\sigma_k}\right)\frac{\partial k}{\partial x_i}\right] + G_k + G_b - \bar{\rho}\varepsilon + Y_M + S_k, \qquad 3.33$$

$$\frac{\partial}{\partial t}(\bar{\rho}\varepsilon) + \frac{\partial}{\partial x_i}(\bar{\rho}\tilde{u}_i \varepsilon) = \frac{\partial}{\partial x_i}\left[\left(\mu + \frac{\mu_t}{\sigma_\varepsilon}\right)\frac{\partial \varepsilon}{\partial x_i}\right] + C_{1\varepsilon}\frac{\varepsilon}{k}(G_k + C_{3\varepsilon}G_b) - C_{2\varepsilon}\bar{\rho}\frac{\varepsilon^2}{k} + S_\varepsilon, \qquad 3.34$$

where G_k and G_b stand for generation of turbulence kinetic energy due to the mean velocity gradients and buoyancy, respectively. Y_M stands for the effects of the fluctuating dilatation in compressible turbulence to the overall dissipation rate. σ_k and σ_ε are the Prandtl numbers for k and ε – defined as the ratio between momentum diffusivity and thermal diffusivity – and incorporated to link diffusivity to the turbulent eddy viscosity, μ_t. The addition of ε/k ensures that the transport equation of ε is dimensionally correct, whereas $C_{1\varepsilon}$ and $C_{2\varepsilon}$ ensure that the terms in the transport equations of ε proportionally correct. S_k and S_ε are source terms. The model constants are determined by carrying out experiments at various conditions and equal to:

$$C_{1\varepsilon} = 1.44, C_{2\varepsilon} = 1.92, \sigma_k = 1 \; and \; \sigma_\varepsilon = 1.3. \qquad 3.35$$

In the $k-\varepsilon$ model, μ_t can be computed as follows:

$$\mu_t = \bar{\rho}C_\mu \frac{k^2}{\varepsilon}, \qquad 3.36$$

where C_μ is constant and equal to 0.09.

3.4 Combustion modelling

The utilisation of turbulence modelling approaches achieves successes in solving engineering problems in terms of the non-reactive flows via LES or RANS techniques. The issue become more

complex when use LES or RAN based modelling techniques to simulate turbulent reacting flow problem (i.e. turbulent combustion modelling) because combustion takes place in a small scale which is not resolved in LES or RANS modelling. Therefore, it needs both turbulence model and combustion model to simulate turbulent reacting flows under LES or RANS modelling. Combustion needs the fuel to be mixed with the oxidizer at molecular levels. In turbulent flows, this mixing largely relies on the turbulent mixing processes. As previously mentioned, turbulence consists of a wide verity of different eddies size ranging from the integral to Kolmogorov scales. The mixing process between eddies is promoted by the strain and shear at the eddies' interface. As eddies break up producing smaller eddies, the strain and shear increase resulting in a drastic decrease in the concentration gradients at the interface between reactants. Therefore, this promotes the molecular inter-diffusion between reactants. Finally, the combustion occurs due to the molecular mixing between the fuel and oxidizer at the interface between small eddies [114]. Hence, the combustion modelling approaches are used to evaluate the chemical reaction state – such as, the concentrations of different species and their source terms – and the variables they affect such as density and temperature.

It is important to highlight some parameters associated to both combustion and turbulence, which result in increasing the complexity caused by their two-way interaction. For instance, the molecular and turbulent diffusions play a critical role in the mixing process, even though the turbulent diffusion enhances the mixing process at a higher rate than the molecular diffusion. Their essential difference lies in that the molecular diffusion is a fluid property, which does not need to apply an external force to be enhanced, whereas the turbulent diffusion is characterised by size of eddies and its promotion requires an external force. In other words, the turbulent diffusion can be enhanced by the presence of a highly diffusion specie, such as hydrogen, which represents the molecular diffusion; however, the opposite is not true. In contrast, the molecular and turbulent viscosities are independent from one another. The former is a fluid property representing the fluid's internal resistance to flow, while the latter represents no physical characteristic of the fluid, but it is a function of the local flow conditions resulting from the use of turbulence modelling to predict turbulent flow characteristics. To clarify the concept of turbulent viscosity, it is important to re-call the Boussinesq hypothesis, which assumes that the Reynolds stress is proportional to the mean deformation rate. This hypothesis introduces the turbulent viscosity, which represents a

proportionality factor between the Reynolds stress and the mean deformation rate as shown in Equation (3.31).

Prior to the discussion of combustion modelling, it is important to understand the fundamental differences between the hybrid combustion types implemented in this project, namely premixed and non-premixed, and also to identify their combustion regimes.

3.4.1 Premixed combustions

In the premixed combustion, the fuel and the oxidiser streams enter the domain from one side, represented by their mass fraction $Y_{F,u}$ and $Y_{O_2,u}$, respectively, at $x \rightarrow -\infty$, as shown in Figure 5, diffuse towards the reaction zone with burning velocity S_L. The fuel, $Y_{F,b}$, is roughly diminished, whereas the residual of oxygen, $Y_{O_2,b}$, is highly reduced. The increase of temperature is a result of the heat released due to the chemical reactions. The mass fraction of product, $Y_{P,u}$, increases from zero to $Y_{P,b}$ following the same trend of increasing the temperature from T_u to T_b.

In this phenomenon, these are some distinct length and time scales that are important to understand and required to identify the premixed combustion regime. The first length scale is known as the laminar flame thickness, δ_L, which represents the thickness of the reaction zone as illustrated in Figure 5. It can be computed from the temperature profile as follows:

$$\delta_L = \frac{T_b - T_u}{max\left(\left|\frac{\delta T}{\delta x}\right|\right)}, \tag{3.37}$$

where $max\left(\left|\frac{\delta T}{\delta x}\right|\right)$ stands for the maximum gradient of the temperature. The second length scale is the inner layer thickness, δ_r, which represents the inner structure of the reaction zone and can be calculated as

$$\delta_r = \delta_L \, \gamma, \tag{3.38}$$

where γ is a constant and equal to 0.1 for a stoichiometric laminar flame [111]. The characteristic laminar time scale, τ_L, is computed as

$$\tau_L = \frac{\delta_L}{s_L}, \qquad 3.39$$

where s_L refers to the laminar burning velocity.

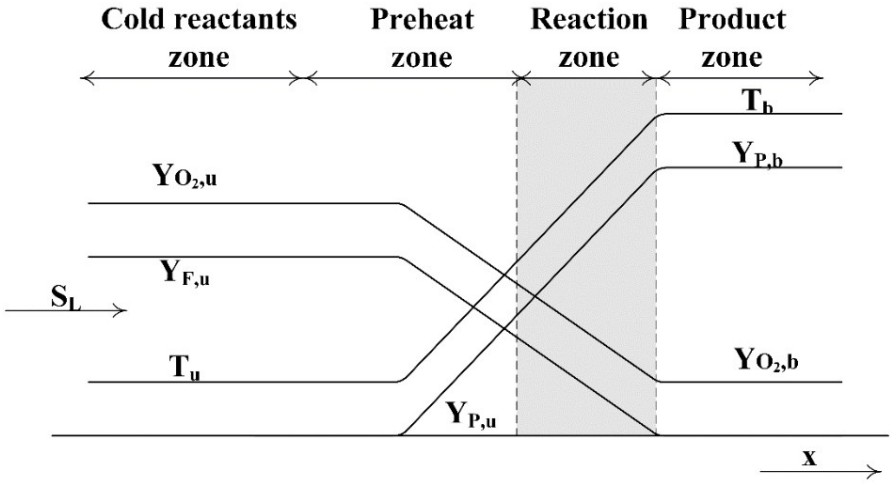

Figure 5: Schematic of the premixed flame structure.

These scales represent the fundamental physics of the premixed flame and are extremely important to identify the premixed combustion regime in a single diagram because it is based on physical analysis. This diagram is constructed on the basis of non-dimensionless characteristic numbers. The first non-dimensionless number is the Reynolds number – discussed in section (3.3.1) –. The second one is the Damköhler number, D_a, – defined as a ratio of the turbulent integral (largest eddies) time scale, τ_t, to the laminar flame time scale, τ_L, – which is computed as

$$D_a = \frac{\tau_t}{\tau_L} = \frac{s_L\, \ell_t}{u'(\ell_t)\delta_L}, \qquad 3.40$$

where ℓ_t and $u'(\ell_t)$ are the turbulent integral length scale and its velocity, respectively. Karlovitz number is the ratio between the laminar flame time scale, τ_L, to the Kolmogorov (smallest eddies) time scale, τ_k, and can be represented as:

$$K_a = \frac{\tau_L}{\tau_k} = \frac{u'(\ell_k)\delta_L}{s_L\,\ell_k}, \tag{3.41}$$

where ℓ_k and $u'(\ell_k)$ are the Kolmogorov length scale and its velocity, respectively. Another Karlovitz number is introduced to relate the thickness of the inner structure, δ_r, to the Kolmogorov length scale, ℓ_k,

$$K_{a\delta} = \frac{u'(\ell_k)\delta_L}{s_L\,\ell_k} = \frac{u'(\ell_k)\delta_r}{s_L\,\ell_k\gamma}. \tag{3.42}$$

Since these non-dimensionless numbers have been introduced, the premixed combustion diagram can be constructed as depicted in the Figure 6.

In the following discussion, five regimes have been identified:

- **Laminar flames:** The flow is laminar because the Reynolds number does not exceed the critical value. In other words, the flame is completely uninfluenced by the turbulence.
- **Wrinkled flamelet ($\mathbf{D_a > 1}$):** The laminar burning velocity is dominated; however, the flame is wrinkled by the fluctuation of the turbulent velocity.
- **Corrugated flamelet ($\mathbf{D_a < 1}$ &$\mathbf{K_a < 1}$):** The flame front is corrugated by the turbulent integral eddies, whereas, the laminar flame thickness is still larger than the turbulent Kolmogorov eddies, resulting in an unmodified flame structure.
- **Thin reaction zone ($\mathbf{K_a \geq 1}$ &$\mathbf{K_{a\delta} < 1}$):** The flame structure is penetrated by the smallest eddies as its thickness becomes smaller than that of flame thickness. However, the thickness of the inner structure is still larger than that of the turbulent Kolmogorov eddies, indicating the smallest eddies cannot penetrate the inner structure flame.
- **Broken reaction zone ($\mathbf{K_{a\delta} \geq 1}$):** The inner flame structure is penetrated by the smallest eddies and then broken since they are smaller than the structure of the inner flame, meaning the chemical reaction is locally broken-down leading to quenching the flame.

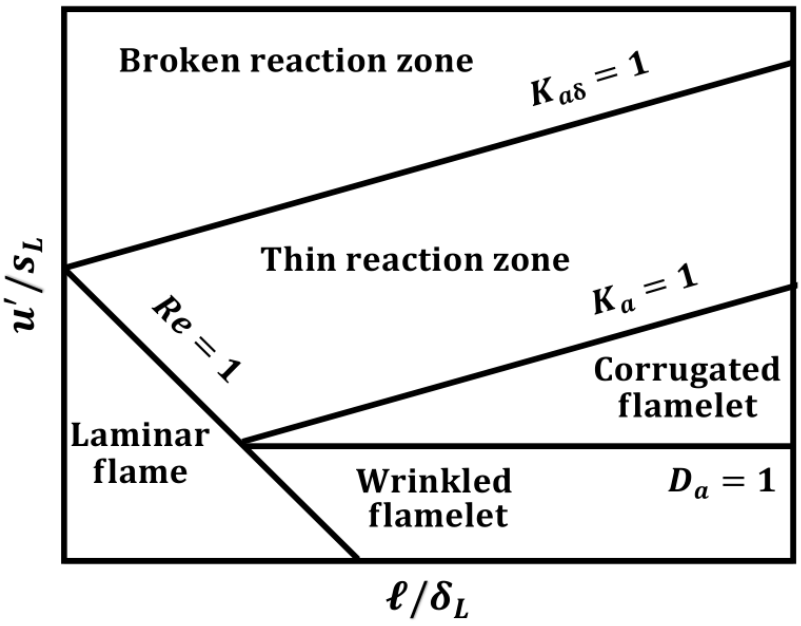

Figure 6: Premixed combustion diagram.

3.4.2 Non-premixed combustion

On the other hand, in the non-premixed flame, the structure consists of three distinct zones: the fuel-rich zone (right), the reaction zone (middle) and the oxidizer-rich zone (left) as displayed in Figure 7. The diffusion flame is not characterized by flame propagation due to the absence of oxidizer in the fuel side and vice versa, and therefore, there is no reference speed as it is controlled by the diffusion rate [111]. Thus, the fuel diffuses to the left (oxidizer-rich zone) and the oxidizer diffuses to the right (fuel-rich zone), and the combustion spontaneously occurs when they meet in the reaction zone. Hence, the heat is released, thereby the temperature increases.

In contrast to the premixed flame, the regime identification of diffusion flame is more complicated for two reasons [111]. Firstly, the chemical reaction is controlled by mixing as the reactants and oxidizer should be mixed to initiate the combustion. Secondly, the characteristic scales of the non-premixed flame are not well-defined because it does not have a propagation speed, and the local flow condition controls the local flame thickness and speed. This means, in other word, the spatial location may have significant effects on the flame structure. For instance, the laminar flame structure may be present near the injection, whereas the flame may be partially quenched in the

downstream zone. Thus, the derivation of diffusion combustion diagram existing in the literature is based on strong assumptions that require validation. Consequently, the non-premixed combustion diagram is not presented as there are various non-premixed combustion regimes in the literatures based on different assumptions, which makes it a controversial subject.

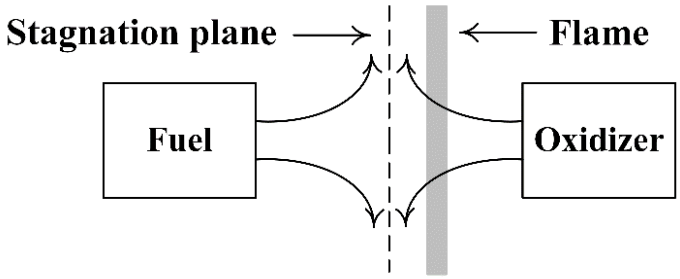

Figure 7: Schematic of a counter-flow setup.

3.4.3 Combustion modelling complexity

In a combustion system, turbulence, thermodynamics, chemical reactions and fluid flow interact with each other. This interaction is extremely difficult to numerically model due to its high degree of complexity. As a consequence, the physical aspects in real combustion systems cannot be properly captured in full details. Thus, researches are limited to model small combustion applications due to the restriction in computing power. Since this has urged researches to specially treat the flame modelling, they have come up with proper and smart techniques, relying on the fact that the most chemical time and length scales in flames are very small. Thus, in practical combustion systems, the detailed dynamics and structure of chemically reacting flows can be predicted and, besides, the use of such techniques reduces the number of transport equation needed to be solved during the simulation run-time and, accordingly, the computational cost. These techniques are the chemistry reduction technique and laminar flamelet-based model.

In the past years, the chemistry reduction technique [115] is presented and used to reduce the unknown variables, yielding a reduction of the equations required to be solved. This technique is based on the assumption stating that a few number of slow processes controls the chemical

processes and is sufficient to describe the chemistry as the fast processes can be rapidly adapted to these slow processes. To clearly demonstrate the idea behind this assumption, Figure 8 shows a schematic representation of N-dimensional manifold in the composition space with several flame trajectories.

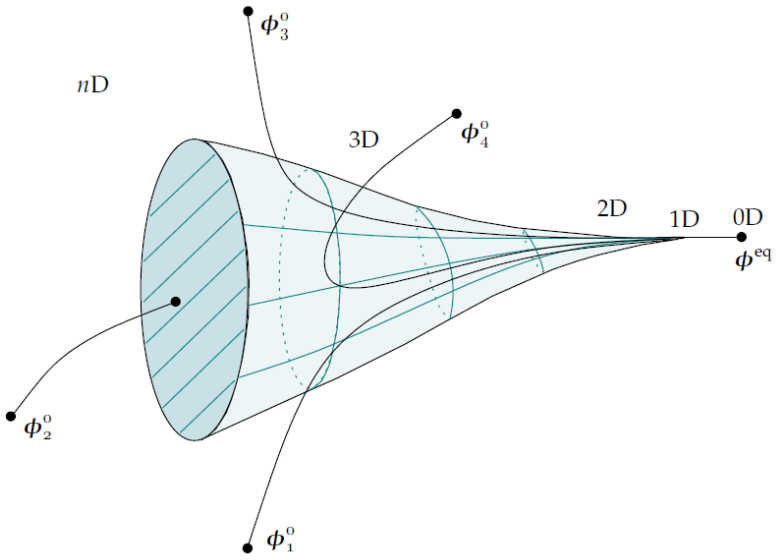

Figure 8: A schematic representation of a manifold in the composition space. The $\boldsymbol{\phi_i^o}$ stands for different initial compositions and $\boldsymbol{\phi_{eq}}$ stands for the chemical equilibrium [115].

The different initial compositions, ϕ_i^o, are the initial points where the flame trajectories start from, where they have the same initial conditions. As shown in Figure 8, all flame trajectories are collapsed as they heads towards the chemical equilibrium point, ϕ_{eq}, and finally reach it. The chemical equilibrium point can be seen as a zero-dimensional manifold. Near the equilibrium, all flame trajectories are attracted to a single line (one-dimensional manifold). On this line, an individual slow process dominates the chemical processes, whereas the steady-state assumptions are applied for the fast processes.

In a chemical reduction method, it is assumed that the chemistry can effectively be described by a low number of slow processes, by applying steady-state assumptions to the fast processes. This means that the chemical compositions are restricted to a low-dimensional manifold. Furthermore, it implies that the stiffness, which is caused by the large variation in time scales, and the dimension of the system, i.e. the number of differential equations that needs to be solved, can be reduced as well.

The laminar flamelet combustion model [116] is based on the assumption stating that the reaction zone in significantly thinner and smaller than the turbulence length scales including the Kolmogorov length scale. This assumption also means that the chemical time scale is faster than all other time scales. This can be mathematically demonstrated by re-calling the Karlovitz number, Equation (3.41), which is the ratio between the laminar flame time scale, τ_L, to the Kolmogorov (smallest eddies) time scale, τ_k, and reads as:

$$K_a = \frac{\tau_L}{\tau_k} = \frac{u'(\ell_k)\delta_L}{s_L\,\ell_k}. \qquad 3.42$$

As this model assumes that the reaction zone is thinner compared to the Kolmogorov length scale, this equation can be read as:

$$\ell_k > \delta_L, \qquad 3.43$$

which means:

$$\tau_k > \tau_L. \qquad 3.44$$

Here, the Kolmogorov time scale is greater than the laminar flame one, which also implies that the laminar burning velocity is greater than that of Kolmogorov scale:

$$s_L > u'(\ell_k). \qquad 3.45$$

In other words, all other time scales are very slow in comparison with chemistry. As the chemistry is very fast, the position of the thin flame front is highly important to be accurately determined. Thus, the successful use of such as a model requires to solve a transport equation to predict the flame front propagation and, in addition, the mixing state is highly recommended to be computed using another transport equation if necessary.

The implementation of laminar flamelet methods implies that the turbulent flame can be considered as an ensemble of discrete, steady laminar one-dimensional flames [117], referred to as flamelets. The inner structure of each flamelet can be described by solving the flamelet equations as presented below.

In this project, FGM is applied as a combustion model, forming a bridge between the chemistry reduction techniques and the laminar flamelet model. It was established in 1999 by van Oijen and de Goey [118] and has been extensively used to simulate turbulent premixed [119], non-premixed [120] and partially premixed flames [121]. Its reduction technique is similar to that of Intrinsic Low-Dimensional Manifolds (ILDM) [122] and Computational Singular Perturbation (CSP) [123]. However, the essential difference lies in the incorporation of the transport process effects. In high-temperature regions, the flame structure is significantly affected by the chemical production and consumption, implying that the chemical time scale is relatively greater than the transport time scale. However, the effects of chemical and transport processes are of the same order in low-temperature regions and, thus, the latter plays an important role in these spots. In contrast to ILDM and CSP, FGM accounts for the transport and chemical processes, resulting in accurate predictions in colder flame parts [25]. In other words, ILDM and CSP consider only the chemical aspect in their reduction techniques, whereas FGM takes into consideration both chemical and transport aspects.

3.4.4 Flamelet-generated manifold (FGM)

The use of a combustion model like FGM results in a significant reduction in computing effort and highly acceptable findings. Its source of power is premised on the procedures of decoupling and coupling the chemistry and flow. In the first process, the chemistry is decoupled from the flow as its evaluation is carried out in a one-dimensional laminar flame domain by solving the flamelet equations. Hence, a wide variety of flamelets is generated, which describes the chemical consequences (i.e. chemical reactions) along with the physical consequences (i.e. preferential diffusion and stretch effects). Then, the second stage, namely the construction of a low-dimensional manifold, takes place, which represents the most important step towards the success of the FGM implementation. The low-dimensional manifold construction is based on the representation of all variables in the flamelet database by a small number of control/leading variables. As the entire system is represented by a few variables, their choices are critical and rely on understanding the application and then identifying the most chemical and physical phenomena occurring in the system. If an important variable that describes an important phenomenon in the simulated application is ignored, the accuracy of the system will be significantly affected. For

example, the CI engine combustion is mainly controlled by diffusion, and diesel fuel ignition occurs after mixing with the oxidiser. Therefore, it is important to incorporate the mixture fraction as a CV to describe the mixing process because neglecting it would significantly impact the accuracy of the findings. However, the adaptation of an unnecessary variable as a CV to describe a relatively less important physical or chemical part is not expected to affect the accuracy of results but would yield an increase in computing effort. For instance, in SI engines, the description of mixing is relatively less important because the fuel and oxidiser are mixed in the intake manifold and then introduced to the combustion chamber. In this case, the lead of other variables by mixture fraction is not expected to provide more precise predictions.

The second process comes after the low-dimensional manifold construction, which couples the chemistry tabulations stored in manifold forms with the CFD solver via CVs by means of the PDF technique. Once the PDF table is built, the information needed to run the simulation in the three-dimensional domain is well-prepared.

It is extremely important to remember that the chemistry at this stage is computed by accounting for the chemical and physical processes and, hence, tabulated with respect to a few CVs in the decoupling process. Then, they are coupled via CVs with the CFD solver with the aid of PDF. These procedures take place in the pre-processing stage. This, in turn, represents the potential of FGM as the unknown variables during the three-dimensional simulation are already (i) pre-computed and (ii) led by a few CVs and (iii) stored in the PDF table, implying that only the transport equations of CVs with the governing and turbulence model transport equations need to be solved during the three-dimensional simulation run-time. Hence, as the unknown variables are dependent on CVs, they are retrieved from the PDF table based on the computed values of CVs by means of linear interpolation. Therefore, the computational time is significantly reduced by solving a fewer number of transport equations

In this project, the FGM combustion model is extended to predict the combustion of hydrogen blended mixtures in DF combustion processes. In the tabulated FGM, the chemistry is represented by a few CVs, namely, mixture fraction, progress variable and enthalpy. In addition, the preferential diffusion effects are taken into consideration by means of implementing a two-step correction process: laminar flamelet calculation incorporating preferential diffusion effects and

correction for the diffusion coefficients in the transport equations for the CVs incorporating preferential diffusion effects.

It has been recognised that the hydrogen blended DF combustion with gaseous hydrogen intake injection consists of non-premixed (diffusion) combustion of pilot fuel with air and with the presence of hydrogen gas in the vicinity of auto-ignition spots, and then premixed combustion of hydrogen-air mixture at later stage. Therefore, an FGM hybrid model was developed by coupling non-premixed flamelet database and premixed flamelets database. The coupling approach was used to capture the auto-ignition of the pilot fuel with air and with the presence of hydrogen gas in the vicinity of auto-ignition spots via non-premixed combustion and then the flame propagation of premixed hydrogen-air mixture via premixed combustion. Furthermore, the model incorporates preferential diffusion effects to better capture the auto-ignition process, flame propagation and heat release rate of high hydrogen content DF engine combustion.

3.4.4.1 The FGM database generation

In the FGM model, the construction of the low-dimensional manifold requires to generate the pre-computed chemistry database by means of the solution of flamelet equations [124]. The flamelet equations derived from full 3D transport equations describing the conservation of mass, species concentration, and enthalpy, are solved using the well-established in-house one-dimensional CHEM1D [125] code in a curvilinear co-ordinate as follows:

$$\frac{\partial \rho}{\partial t} + \frac{\partial}{\partial s}(\rho u) = -\rho K, \tag{3.46}$$

$$\frac{\partial}{\partial t}(\rho Y_k) + \frac{\partial}{\partial s}(\rho u Y_k) = \frac{\partial}{\partial s}(\rho U_k Y_k) + \dot{\omega}_k - \rho K Y_k, \tag{3.47}$$

$$\frac{\partial}{\partial t}(\rho h) + \frac{\partial}{\partial s}(\rho u h) = \frac{\partial}{\partial s}\left[-\lambda \nabla T + \sum_{k=1}^{N_s} h_i \rho Y_k U_k\right] - \rho K h, k = 1, \dots, N_s, \tag{3.48}$$

where s is the spatial coordinate orthogonal to the flame front, ρ is the mixture density, h is enthalpy, and K is the flame stretch rate, u is the velocity, U_k is the diffusion velocity of species K, Y_k is the mass fraction of species K, $\dot{\omega}_k$ is the chemical production rate, λ is the thermal

conductivity, c_p is the specific heat at constant pressure, and N_s is the total number of species. The flamelet equations (3.46), (3.47) and (3.48) represent the governing equations that are used for the laminar one-dimensional calculations.

From the flamelet equations presented, the momentum equation is removed due the assumption of low Mach number. This means the pressure is a function of time [25] and therefore, the density is computed with the aid of the ideal gas law, whereas the continuity equation is used to find the velocity, which makes the momentum equation superfluous. In addition, this approximation results in neglecting the pressure gradient term in the energy equation, and moreover, as the viscous heating is extremely smaller than the heat released by combustion, it is neglected [125].

The discretisation scheme used in the one-dimensional calculations is exponential finite-volume, whereas a fully implicit temporal scheme as well as a modified Newton method are used to solve the non-linear differential equation. In terms of the numerical grid, the adaptive gridding procedure is used to ensure capturing the large gradients properly because it adaptively changes from a region to another in a way of assigning more grid points in the large gradient regions compared to the lower gradient regions.

To account for the preferential diffusion effects in one-dimensional flamelet calculations, the mixture-averaged transport model, which employs the binary diffusion coefficients, D_{kj}, via the Hirschfelder-Curtiss approach [126], is used. The diffusion velocity and mass diffusion coefficients are computed, respectively, as:

$$U_k = -\frac{D_{k,m}}{X_k}\nabla X_k \ , D_{k,m} = \frac{(1-Y_k)}{\sum_{j=1,j\neq k}^{N_s}\left(X_k/D_{kj}\right)} \qquad 3.49$$

For unity Lewis number calculations, the diffusion velocity and mass diffusion coefficients are computed, respectively, as:

$$U_{k,i} = -\frac{D_{k,m}}{Y_k}\frac{\partial}{\partial x_i}(Y_k), \qquad with \qquad D_{k,m} = \frac{\lambda}{\rho\, c_p}. \qquad 3.50$$

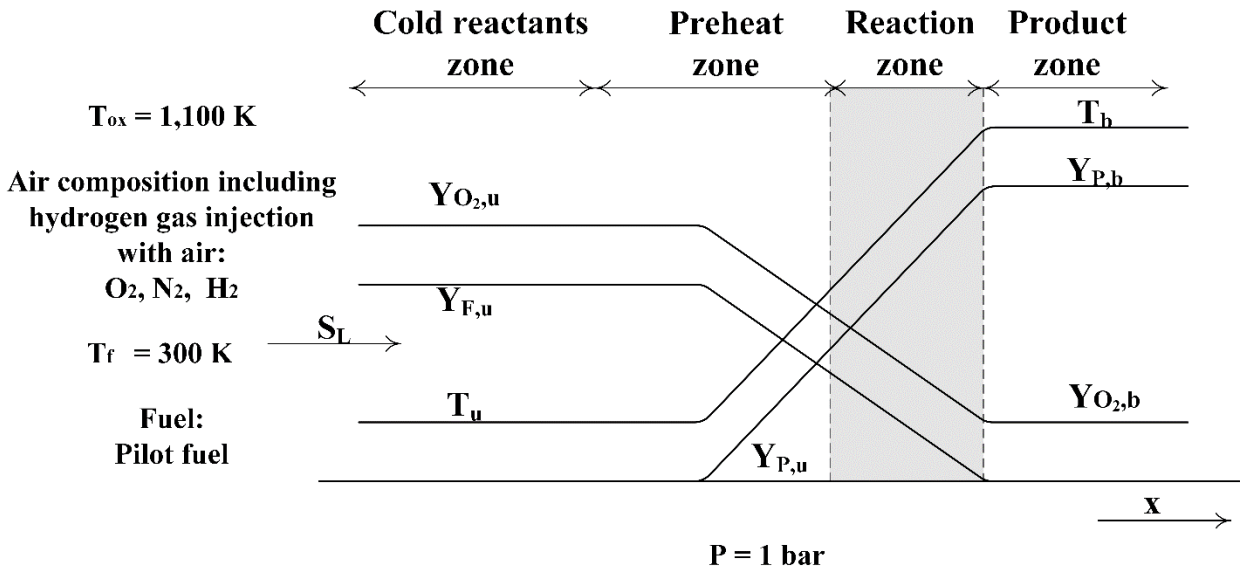

Figure 9: Freely propagating premixed flame configuration.

Figure 9 shows the freely propagating flame configuration which has been used to generate the laminar premixed flamelet database. The pilot fuel and oxidiser temperature values were set to 300K and 1,100K respectively. The oxidiser temperature of 1,100K was chosen to represent the engine relevant higher oxidiser temperature towards the end of compression stroke. The laminar premixed flamelet database is generated by solving the flamelet equations with zero stretch rate.

For the freely propagating laminar premixed flame, fuel and oxidiser enter on the same side. Hence, Dirichlet boundary conditions are imposed on the inlet side;

$$Y_i\,(s\ \rightarrow\ -\infty) = Y_{i,-\infty}, h\,(s\ \rightarrow\ -\infty) = h_{-\infty}, Z\,(s\ \rightarrow\ -\infty) = Z_m, \qquad 3.51$$

and Neumann boundary conditions are imposed on the outlet side:

$$\frac{dY_i}{ds}(s\ \rightarrow\ \infty) = 0, \frac{dh}{ds}\ (s\ \rightarrow\ \infty) = 0, \frac{dZ}{ds}\ (s\ \rightarrow\ \infty) = 0. \qquad 3.52$$

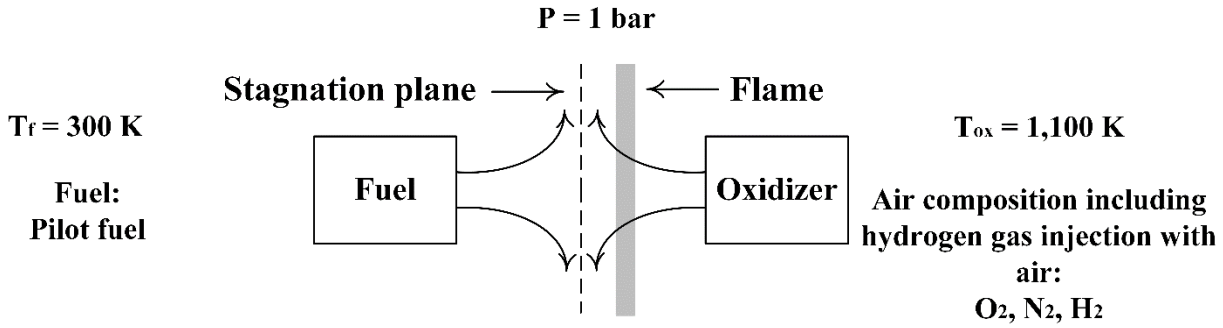

Figure 10: Counter-flow diffusion flame configuration.

Figure 10 shows the counter-flow configuration employed to produce diffusion flamelets. The pilot fuel and air temperature values were set to 300K and 1,100K respectively. In a counter-flow diffusion flamelet configuration, the fuel enters from one side, and the oxidiser enters from other side. However, in DF combustions, the main fuel (i.e. gaseous hydrogen) is injected via the intake manifold and hence mixes with the oxidiser stream, whereas a small amount of the pilot fuel is directly injected into the combustion chamber to trigger the combustion. Therefore, in the counter-flow diffusion flame configuration, hydrogen gas is introduced from the air side to represent the homogenous mixture of hydrogen-air, which presents in the combustion chamber before the pilot fuel injection.

For the counter-flow diffusion flame, the boundary conditions imposed on fuel side ($s \rightarrow \infty$) and oxidizer side ($s \rightarrow -\infty$) are as follows:

$$Y_i\,(s \rightarrow \infty) = Y_i^{fu}\,, h\,(s \rightarrow \infty) = h^{fu}\,, Z\,(s \rightarrow \infty) = 1, \qquad 3.53$$

$$Y_i\,(s \rightarrow -\infty) = Y_i^{x}\,, h\,(s \rightarrow -\infty) = h^{ox}\,, Z\,(s \rightarrow -\infty) = 0, \qquad 3.54$$

The diffusion flame is quenched at a certain strain rate. Thus, the diffusion flamelets are generated over a range of strain rates. Such an effect requires solving an additional transport equation, along with the flamelet equations, to describe the stretch field. This equation reads as:

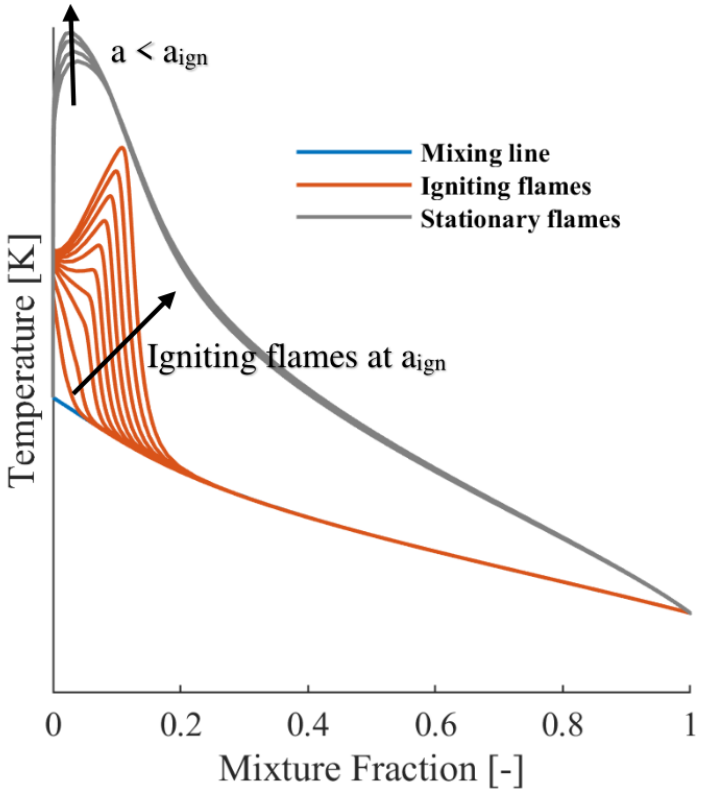

Figure 11: Illustration of diffusion flamelet generation.

$$\frac{\partial}{\partial s}(\rho u K) = \frac{\partial}{\partial s}\left[\mu \frac{\partial K}{\partial s}\right] - 2\rho K^2 + \rho a^2, \qquad 3.55$$

where a stands for the applied strain rate at the oxidiser side and μ donates the dynamic viscosity.

In this canonical configuration, many diffusion flamelets are generated in space and time, and both igniting and stationary flames are included to cover the entire regime of the DF combustion as seen in Figure 11. The igniting flames are generated at a single strain rate, which capture the ignition from the mixing line until the steady state solution. The chemistry database is completed with a set of stationary flames by varying strain rates.

3.4.4.2 Control variables

To construct the FGM look-up table, the adaptation of CVs are needed and, therefore, three variables are employed to lead the other variables. The first one is mixture fraction to represent the stratification effects, the second one is reaction progress variable to describe the chemistry evolution and the last one is enthalpy to account for heat loss.

The reaction progress variable is computed using Equation (3.7) and can take different definition based on the choices of species. In this project, it is defined as:

$$Y_c = \frac{Y_{CH_2O}}{M_{CH_2O}} + \frac{Y_{CO}}{M_{CO}} + \frac{Y_{CO_2}}{M_{CO_2}} + \frac{Y_{H_2O}}{M_{H_2O}} + \frac{Y_{HO_2}}{M_{HO_2}}. \quad 3.56$$

This definition is applied to represent the hydrocarbon combustion by the first three species and to represent the hydrogen combustion by the rest.

The mixture fraction is as a local element composition and evaluated according to the definition proposed by Bilger et al. [127]:

$$\zeta = \frac{2\left(\frac{Y_C^e - Y_{C,2}^e}{M_C^e}\right) + 0.5\left(\frac{Y_H^e - Y_{H,2}^e}{M_H^e}\right) - \left(\frac{Y_O^e - Y_{O,2}^e}{M_O^e}\right)}{2\left(\frac{Y_{C,1}^e - Y_{C,2}^e}{M_C^e}\right) + 0.5\left(\frac{Y_{H,1}^e - Y_{H,2}^e}{M_H^e}\right) - \left(\frac{Y_{O,1}^e - Y_{O,2}^e}{M_O^e}\right)}, \quad 3.57$$

in which Y_k^e stands for the elemental mass fraction of species k and subscripts 1 and 2 donate the pure fuel and oxidizer, respectively.

The FGM manifolds are constructed using a Matlab code – See Appendix B –.

It is important to mention that he enthalpy is computed using Equation (3.10) and (3.11) as discussed in Section (3.4.4.4).

3.4.4.3 FGM hybrid flames technique

To accurately predict the combustion characteristics of hydrogen-added mixture DF flames, the laminar flamelet databases generated from non-premixed table and premixed table are coupled. A threshold value is used to switch the data between the non-premixed table and premixed table. To do so, it is assumed that the flamelets with equal or greater than the mixture fraction value of 0.01 lie inside the spray of the pilot fuel (i.e. high gradient of mixture fraction indicating non-premixed combustion), whereas flamelets with the mixture fraction values lower than 0.01 lie outside the spray plume (i.e. low gradient of mixture fraction indicating premixed combustion). The threshold value is selected depending on the mixture fraction value because it represents the quantity of fuel in the mixture. Therefore, in the coupled thermo-chemical database, flamelets with equal or higher value of the mixture fraction threshold are obtained from the laminar non-premixed flame and flamelets with values less than the mixture fraction threshold of 0.01 are obtained from the laminar premixed flame. Thus, the mixing process between the pilot fuel and the oxidiser stream along with the transition from mixing to ignition of the pilot fuel are represented by the mixture fraction and progress variable, respectively, obtained from the diffusion flamelets that were produced from the counter-flow configuration – As depicted in Figure 10 –. On the other hand, the variation of the pilot fuel in the oxidiser stream along with the chemistry evolution of the premixed charge are represented by the mixture fraction and progress variable, respectively, obtained from the flamelets that were produced from the freely propagating flame configuration – As depicted in Figure 9 –.

3.4.4.4 Turbulence-chemistry interaction

At this stage, the pre-computed chemistry tabulation produced in the decoupling process is ready to be coupled with a turbulent CFD solver. Thus, the probability density function (PDF) technique is implemented to link the chemistry database generated in the laminar environment with turbulence. To do so, a presumed PDF shape takes place by integrating the chemistry tabulation via CVs, namely mixture fraction, progress variable and enthalpy $P(\zeta, c, h)$. This allows to describe the temporal fluctuation of ζ, c and h by means of integration and compute the averaged values of variables that depend on ζ, c and h. As seen in Figure 12, the Beta PDF was applied for the mixture fraction and the progress variable, assuming that the mixture fraction and the progress

variable are statistically independent. The non-adiabatic effects are important to describe the energy – i.e. heat transfer to walls – in the combustion process. Thus, the Delta function was convolved for the enthalpy – evaluated using Equation (3.10) –, assuming that the enthalpy fluctuations are negligible. With these presumed PDF shapes assumed for CVs, $P(\zeta, c, h) = \beta(\zeta; \bar{\zeta}, \overline{\zeta'})\, \beta(c; \bar{c}, \overline{c'})\, \delta(h - \bar{H})$ and the density-weighted dependent variables can be computed as:

$$\bar{\phi}\left(\bar{\zeta}, \overline{\zeta'}, \bar{c}, \overline{c'}, \bar{h}\right) = \int_0^1 \int_0^1 P(\zeta, c, h)\, \phi(\zeta, c, h)\, d\zeta dc, \qquad 3.58$$

Similarly, the mean time-averaged fluid density, $\bar{\rho}$, can be computed as

$$\bar{\rho} = \int_0^1 \int_0^1 \frac{P(\zeta, c, h)}{\rho(\zeta, c, h)} d\zeta dc, \qquad 3.59$$

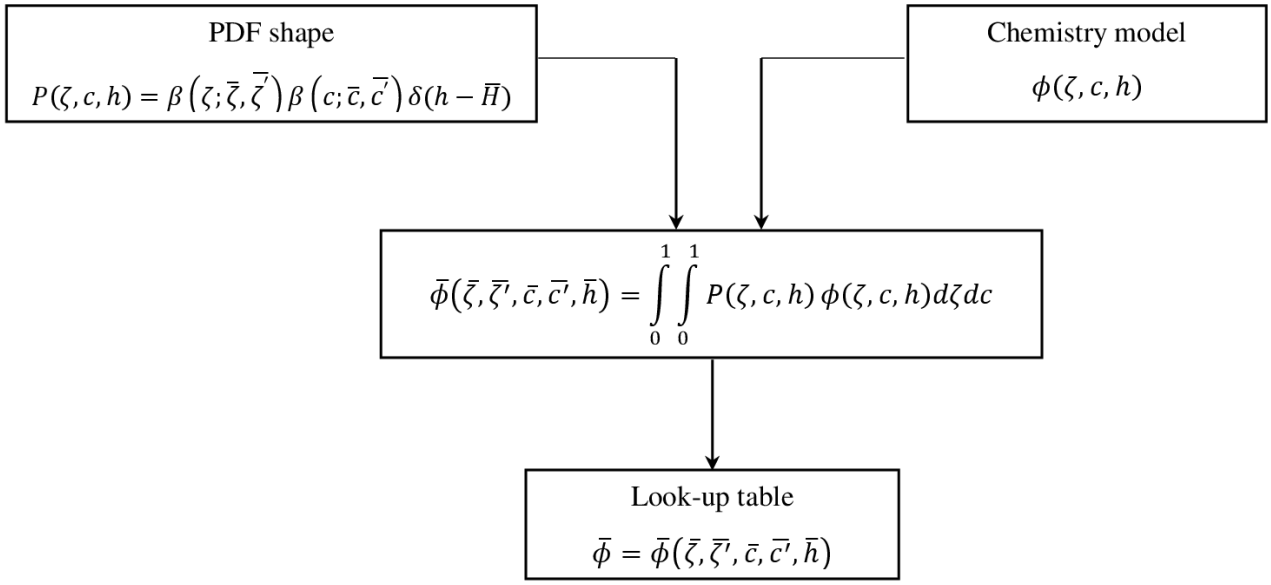

Figure 12: Schematic representation of the look-up table generation procedure. ϕ stands for the thermo-chemical variables. $\bar{\zeta}$ and $\bar{c}$ are the means of mixture fraction and progress variable, respectively, whereas $\overline{\zeta'}$ and $\overline{c'}$ are their variances, respectively.

Using Equation (3.58) and Equation (3.59) are sufficient to construct the PDF table and, then, to determine the local mean fluid state at all points in the flow field with solving only the transport equations of CVs, along with the set of equations written in Section (3.4.4.6), as the mean scalar quantities (dependent variables) are retrieved from the PDF table based on the computed values of CVs. It is important to mention that the PDF table is constructed based on one joint flamelets dataset combining both premixed and non-premixed databases together by replacing the mixture fraction values less than 0.01 part in the non-premixed flamelets with the premixed flamelets.

It is known that the Delta function is less accurate than the Beta function and, however, it is applied for enthalpy for computing effort considerations. In addition, the developed FGM hybrid-flame combustion model aims to capture DF multi-stage combustion processes and demonstrate the effects of molecular transport properties. In contrast to enthalpy, the mixture fraction and progress variable are sufficient to accurately predict the former, whereas the two-step correction process is sufficient to describe the latter.

3.4.4.5 Incorporation of preferential diffusion effects

As previously mentioned, the newly extended FGM hybrid-flame combustion model incorporates the preferential diffusion effects with the aid of two-step correction. The first step lies in incorporating such effects during the flamelet calculations as discussed in Section (3.4.4.1). The second step lies in incorporating these effects in the transport equations of CVs by means of an additional term. These additional terms are evaluated during the pre-processing stage using a C programming code – See Appendix C – and, hence, included in the CVs transport equations to compute the diffusion coefficients during the three-dimensional simulations using another C programming code with the aid of the user-defined function (UDF) – See Appendix D –.

The construction of the preferential diffusion effects term [128] for each CV can be demonstrated by re-calling the second term in RHS in Equation (3.8), which is:

$$\frac{\partial}{\partial x_i} D_{Y_c} = \frac{\partial}{\partial x_i} \left(\frac{\lambda}{c_p} \sum_{k}^{N_s} \alpha_k \left(\frac{1}{Le_k} - 1 \right) \frac{\partial Y_i}{\partial x_i} \right). \qquad 3.60$$

Using that $Y_i = Y_i(Y_c, Y_{cv2}, Y_{cv3})$ and applying the chain rule, Equation (3.60) can be re-cast as:

$$\frac{\partial}{\partial x_i} D_{Y_c} = \frac{\partial}{\partial x_i} \left(\frac{\lambda}{c_p} \sum_k^{N_s} \alpha_k \left(\frac{1}{Le_k} - 1 \right) \left(\frac{\partial Y_i}{\partial Y_c} \frac{\partial Y_c}{\partial x_i} + \frac{\partial Y_i}{\partial \zeta} \frac{\partial \zeta}{\partial x_i} + \frac{\partial Y_i}{\partial h} \frac{\partial h}{\partial x_i} \right) \right), \qquad 3.61$$

To finalise the construction of preferential diffusion effects term, the three control variables, mixture fraction, progress variable and enthalpy, (ζ, Y_c, h) are assumed to be locally a function of Y_c, $(\zeta, h) \rightarrow (\zeta^{1D}, h^{1D})$. Besides, the reaction progress variable is taken in into consideration instead of using all species, which results in:

$$\frac{\partial}{\partial x_i} D_{Y_c} = \frac{\partial}{\partial x_i} \left(\frac{\lambda}{c_p} \sum_k^{N_s} \alpha_k \left(\frac{1}{Le_k} - 1 \right) \left(\frac{\partial Y_i}{\partial Y_c} + \frac{\partial Y_i}{\partial \zeta} \frac{\partial \zeta^{1D}}{\partial Y_c} + \frac{\partial Y_i}{\partial h} \frac{dh^{1D}}{\partial Y_c} \right) \right) \frac{\partial Y_c}{\partial x_i}. \qquad 3.62$$

At this stage, the preferential diffusion effects term is constructed for the progress variable reaction. Thus, it can be generalised for the other CVs, namely mixture fraction and enthalpy, as

$$\frac{\partial}{\partial x_i} D_{\zeta} = \frac{\partial}{\partial x_i} \left(\frac{\lambda}{c_p} \sum_k^{N_s} \zeta_k \left(\frac{1}{Le_k} - 1 \right) \left(\frac{\partial Y_i}{\partial Y_c} + \frac{\partial Y_i}{\partial \zeta} \frac{\partial \zeta^{1D}}{\partial Y_c} + \frac{\partial Y_i}{\partial h} \frac{dh^{1D}}{\partial Y_c} \right) \right) \frac{\partial Y_c}{\partial x_i}, \qquad 3.63$$

$$\frac{\partial}{\partial x_i} D_h = \frac{\partial}{\partial x_i} \left(\frac{\lambda}{c_p} \sum_k^{N_s} h_k \left(\frac{1}{Le_k} - 1 \right) \left(\frac{\partial Y_i}{\partial Y_c} + \frac{\partial Y_i}{\partial \zeta} \frac{\partial \zeta^{1D}}{\partial Y_c} + \frac{\partial Y_i}{\partial h} \frac{dh^{1D}}{\partial Y_c} \right) \right) \frac{\partial Y_c}{\partial x_i}, \qquad 3.64$$

where

$$\frac{\lambda}{c_p} = 2.58 \times 10^{-5} \left(\frac{T}{298} \right)^{0.69}, \qquad 3.65$$

in which ζ_k is the mixture fraction of species k. As shown in Equation (3.62), (3.63) and (3.64), the only difference in the preferential diffusion terms among the three control variables lies in the

coefficients of α_k, ζ_k and h_k. The calculation of α_k and h_k are computed using Equation (3.7) and Equation (3.10), respectively. The coefficient ζ_k is computed by converting the form of Equation (3.57) to the form of Equation (3.7) or Equation (3.10). The use of this approach to incorporate the preferential diffusion effects is beneficial since the unity Lewis number assumption results in no incorporation of preferential diffusion effects present, as the coefficients are equal to zero $(d_\varphi = 0)$.

3.4.4.6 FGM implementation

As depicted in Figure 13, the steps of the FGM implementation contain two distinct stages, pre-processing and simulation run-time (online). The first step can also be divided into four parts: first, the pre-computed flamelet datasets are generated from CHEM1D by solving the flamelet equations in the counter-flow diffusion flame and freely propagating flame configurations. These databases are produced in space and time $f(x,t)$. Second, two two-dimensional manifolds are constructed by transforming the coordinate with respect to CVs, namely mixture fraction and progress variable.

Thus, one joint flamelets dataset is created combining both premixed and non-premixed databases together by replacing the mixture fraction values less than 0.01 part in the non-premixed flamelets with the premixed flamelets. The last step lies in linking the chemistry and turbulence by means of the construction of five-dimensional PDF table as a function of mean mixture fraction, mixture fraction variance, mean progress variable, progress variable variance and mean enthalpy.

The second stage represents the CFD solver –, where ANSYS Fluent solves the transport equations of CVs, governing equations, nitric oxide ($\bar{Y}_{NO}$) transport equation – required to model the NO_x engine-out emissions – and turbulence model transport equations as follows:

Mass conservation:

$$\frac{\partial}{\partial t}(\bar{\rho}) + \frac{\partial}{\partial x_i}\left(\rho \tilde{u}_j\right) = S_m. \qquad 3.66$$

Momentum conservation:

$$\frac{\partial}{\partial t}(\bar{\rho}\tilde{u}_i) + \frac{\partial}{\partial x_j}\left(\rho \tilde{u}_i \tilde{u}_j\right) = -\frac{\partial \bar{P}}{\partial x_i} + \frac{\partial}{\partial x_j}\left(\bar{\tau}_{ij} - \bar{\rho}\widetilde{u_i'' u_j''}\right) + \ S_i. \qquad 3.67$$

Energy conservation:

$$\frac{\partial}{\partial t}(\bar{\rho}\bar{h}) + \frac{\partial}{\partial x_i}(\bar{\rho}\tilde{u}_i\bar{h}) = \frac{\partial}{\partial x_i}\left(\frac{\lambda}{c_p}\frac{\partial \bar{h}}{\partial x_i}\right) + \frac{\partial}{\partial x_i} D_h + \overline{\dot{\omega}_\varphi} + S_h. \quad 3.68$$

Mean mixture fraction, $\bar{\zeta}$: and un-normalised progress variable, $\overline{Y_c}$:

$$\frac{\partial}{\partial t}(\bar{\rho}\bar{\varphi}) + \frac{\partial}{\partial x_i}(\bar{\rho}\tilde{u}_i\bar{\varphi}) = \frac{\partial}{\partial x_i}\left(\left(\frac{\lambda}{c_p} + \frac{\mu_t}{Sc_t}\right)\frac{\partial \bar{\varphi}}{\partial x_i}\right) + \frac{\partial}{\partial x_i} D_\varphi + \overline{\dot{\omega}_\varphi}. \quad 3.69$$

Mixture fraction variance, $\overline{\zeta'}$:

$$\frac{\partial}{\partial t}(\bar{\rho}\overline{\zeta'}) + \frac{\partial}{\partial x_i}(\bar{\rho}\tilde{u}_i\overline{\zeta'}) = \frac{\partial}{\partial x_i}\left(\left(\frac{\lambda}{c_p} + \frac{\mu_t}{Sc_t}\right)\frac{\partial \overline{\zeta'}}{\partial x_i}\right) + C_g\mu_t\left(\frac{\partial \overline{\zeta'}}{\partial x_i}\right)^2 - C_d\rho\frac{\varepsilon}{k}\overline{\zeta'}. \quad 3.70$$

Un-normalised progress variable variance, $\overline{Y_c'}$:

$$\frac{\partial}{\partial t}(\bar{\rho}\,\overline{Y_c'}) + \frac{\partial}{\partial x_i}(\bar{\rho}\tilde{u}_i\overline{Y_c'}) = \frac{\partial}{\partial x_i}\left(\left(\frac{\lambda}{c_p} + \frac{\mu_t}{Sc_t}\right)\frac{\partial \overline{Y_c'}}{\partial x_i}\right) + 2\bar{\rho}\frac{\mu_t}{Sc_t}\left(\frac{\partial \overline{Y_c'}}{\partial x_i}\right)^2 - 2\,\bar{\rho}\frac{\varepsilon}{k}\overline{Y_c'}. \quad 3.71$$

Nitric oxide, $\bar{Y}_{NO}$

$$\frac{\partial}{\partial t}(\bar{\rho}\,\bar{Y}_{NO}) + \frac{\partial}{\partial x_i}(\bar{\rho}\tilde{u}_i\bar{Y}_{NO}) = \frac{\partial}{\partial x_i}\left(\bar{\rho}D\frac{\partial \bar{Y}_{NO}}{\partial x_i}\right) + \bar{\omega}_{NO}. \quad 3.72$$

Turbulent kinetic energy, k:

$$\frac{\partial}{\partial t}(\bar{\rho}k) + \frac{\partial}{\partial x_i}(\bar{\rho}\tilde{u}_i k) = \frac{\partial}{\partial x_i}\left[\left(\mu + \frac{\mu_t}{\sigma_k}\right)\frac{\partial k}{\partial x_i}\right] + G_k + G_b - \bar{\rho}\varepsilon + Y_M + S_k. \quad 3.73$$

Dissipation rate of turbulent kinetic energy,ε:

$$\frac{\partial}{\partial t}(\bar{\rho}\varepsilon)+\frac{\partial}{\partial x_i}(\bar{\rho}\tilde{u}_i\varepsilon)=\frac{\partial}{\partial x_i}\left[\left(\mu+\frac{\mu_t}{\sigma_\varepsilon}\right)\frac{\partial \varepsilon}{\partial x_i}\right]+C_{1\varepsilon}\frac{\varepsilon}{k}(G_k+C_{3\varepsilon}G_b)-C_{2\varepsilon}\bar{\rho}\frac{\varepsilon^2}{k}+S_\varepsilon, \qquad 3.74$$

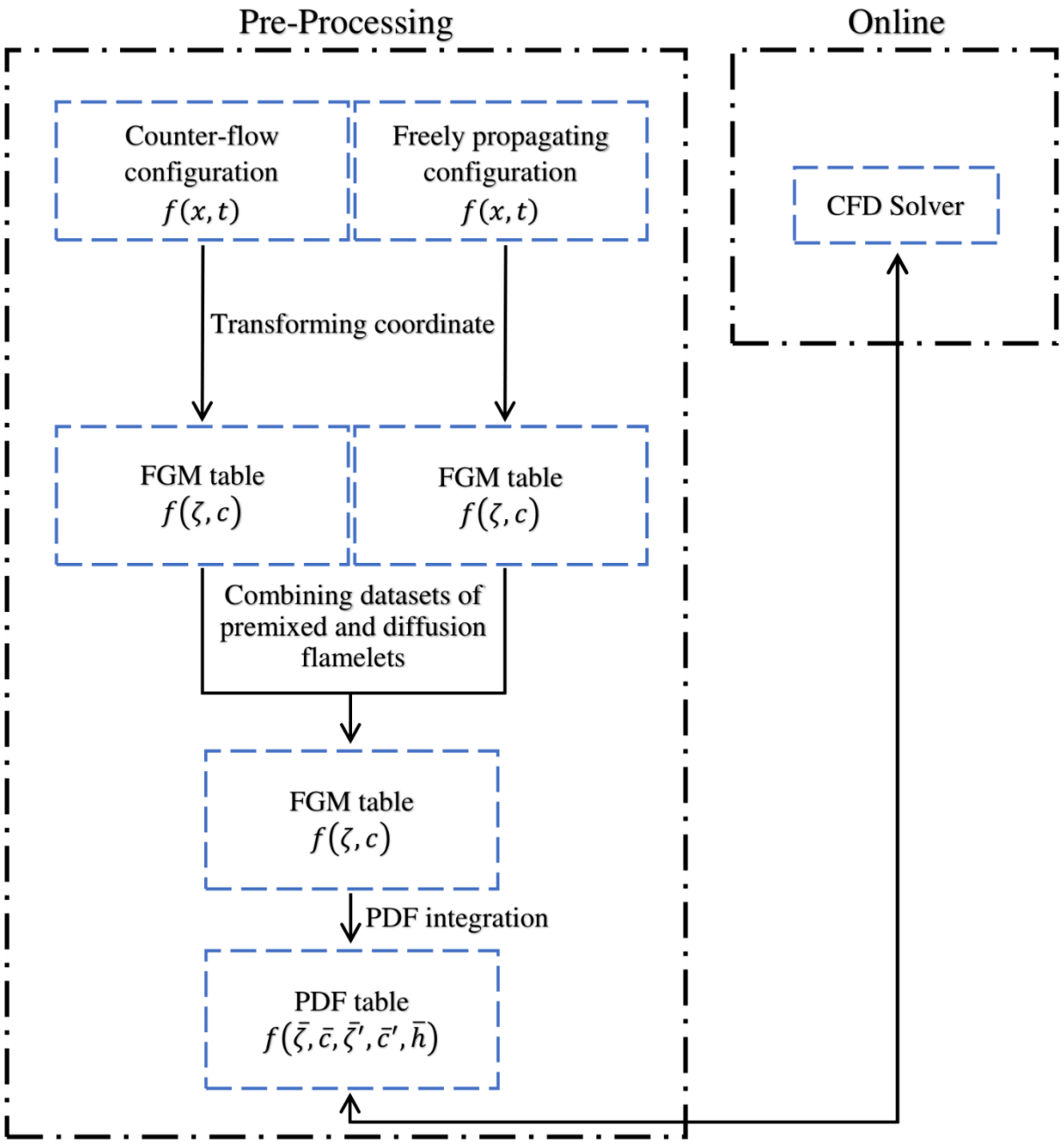

Figure 13: Schematic representation for pre-processing of FGM and coupling to CFD solver.

where C_g and C_d are constants with default values of 2.86 and 2 respectively. $\overline{\omega}_{NO}$ is the source term an additional thermal or prompt NO development.

In this research, the un-normalised progress variable transport equation is solved rather than the normalised one. This gives privilege in accurately specifying the oxidizer boundary conditions at the oxidizer inlets and, besides, predicting flame quenching because of reactant dilution. Modelling these effects with the normalised progress variable, c, requires additional terms, involving derivatives and cross-derivatives of mixture fraction, whereas they are not required for $\overline{Y_c}$ [129].

3.5 Discrete phase model

The governing equations presented in Section (3.2) are solved to treat the continuous phase, representing the premixed charge, whereas the dispersed phase, representing the pilot fuel injected in the combustion chamber in a liquid form, is treated by tracking a large number of droplets through the calculated flow field with the aid of the Lagrangian discrete phase model. The mass, momentum and energy can be exchanged between the continuous and dispersed phases via the source terms of the governing equations (3.1), (3.2) and (3.4) as presented in Section (3.5.5).

In this section, the equation of motion for particles, turbulent dispersion of particles, spray-wall interaction, breakup model and coupling between the discrete and continuous phases are discussed.

3.5.1 Equation of motion for particles

The trajectory of a discrete phase particle is predicted by integrating the force balance on the particle. This force balance is equal to the particle inertia with the forces acting on the particle, and can be mathematically expressed as:

$$\frac{d\vec{u}_p}{dt} = F_D\left(\vec{u} - \vec{u}_p\right) + \frac{\overrightarrow{g}\left(\rho_p - \rho\right)}{\rho_p} + \overrightarrow{F}, \qquad 3.75$$

where $\vec{u}$ is the fluid phase velocity, $\vec{u}_p$ is the particle velocity, ρ is the fluid density and ρ_p is the density of the particle. $\overrightarrow{F}$ is an additional acceleration (force per unit particle mass) such as the

virtual mass force, which is the force required to accelerate the fluid surrounding the particle. $F_D(\vec{u} - \vec{u}_p)$ represents the drag force per unit particle mass and F_D is computed as follows:

$$F_D = \frac{18\,\mu\,C_D Re}{\rho_p d_p^2 24}, \tag{3.76}$$

where μ is the molecular viscosity of the fluid d_p is the particle diameter. Re is the relative Reynolds number and defined as:

$$Re = \frac{\rho d_p |\vec{u}_p - \vec{u}|}{\mu}, \tag{3.77}$$

$C_D$is the drag coefficient and its prediction is based on the dynamic drag model. Due to the interaction between the droplets and the surrounding fluid along with the collision of droplets and wall, the droplet shape varies based on the local conditions. Therefore, the dynamic drag coefficient allows to dynamically compute the droplet drag coefficient with taking into considerations the droplet shape.

Many models of droplet drag coefficient assume that the droplet remains spherical throughout the domain. With this assumption, the drag of a spherical object is determined by the following:

$$C_{d,sphere} = \begin{cases} 0.424 & Re > 1000 \\ \frac{24}{Re}\left(1 + \frac{1}{6}Re^{2/3}\right) & Re < 1000 \end{cases}, \tag{3.78}$$

However, as an initially spherical droplet moves through a gas, its shape is distorted significantly when the Weber number (defined as a dimensionless quantity representing a ratio of aerodynamic forces to surface tension forces) is large. In the extreme case, the droplet shape will approach that of a disk. The drag of a disk, however, is significantly higher than that of a sphere. Since the droplet drag coefficient is highly dependent upon the droplet shape, the drag model that assumes the droplet is spherical is unsatisfactory. The dynamic drag model accounts for the effects of droplet distortion, linearly varying the drag between that of a sphere (Equation (3.78)) and a value of 1.54 corresponding to a disk. The drag coefficient is given by:

$$C_D = C_{d,sphere}(1 + 2.632y), \quad 3.79$$

where y is the droplet distortion and computed as:

$$\frac{d^2y}{dt^2} = \frac{C_F}{C_b}\frac{\rho_g}{\rho_l}\frac{u^2}{r^2} - \frac{C_k\sigma}{\rho_l r^3}y - \frac{C_d\mu_l}{\rho_l r^2}\frac{dy}{dt}, \quad 3.80$$

where r is the undisturbed droplet radius and C_F, C_b, C_k and C_d are constants and equal to 0.3, 0.5, 8 and 5, respectively. If y is equal to 0, this means the droplet is not distorted yet and the drag coefficient of a sphere will be obtained, whereas the distortion reaches the maximum if y is equal to 1 and, consequently the drag coefficient corresponding to a disk will be obtained.

3.5.2 Turbulent dispersion of particles

The presence of turbulence results in the dispersion of particles, and this is predicted using the stochastic tracking (random walk) model. The mean fluid phase velocity, $\bar{u}$, in the trajectory Equation (3.75) includes the instantaneous value of the fluctuating gas flow velocity ($u = \bar{u} + u'$). The stochastic tracking model accounts for the effects of instantaneous turbulent mean velocity fluctuations on the particle trajectories to predict the dispersion of the particles due to turbulence.

In the discrete random walk (DRW) model, the fluctuating velocity components are discrete piecewise constant functions of time. Their random values are kept constant over an interval of time given by the characteristic lifetime of the eddies. The fluid Lagrangian integral time, T_L, is computed as:

$$T_L = C_L\frac{k}{\varepsilon}, \quad 3.81$$

where C_L is constant and equal to 0.15.

The interaction of a particle with a succession of discrete stylized fluid phase turbulent eddies is simulated and each eddy is characterized by (i) a Gaussian distributed random velocity fluctuation, u_i' (where i stands for x, y and z directions), and (ii) a time scale, τ_e. The values of u_i' that prevail

during the lifetime of the turbulent eddy are sampled by assuming that it follows a Gaussian probability distribution as follows:

$$u_i' = \xi\sqrt{\overline{u_i'^2}}, \tag{3.82}$$

where ξ stands for a normally distributed random number and $\overline{u_i'^2}$ is the local root-mean square (RMS) value of the velocity fluctuations. At each point in the flow, the kinetic energy of turbulence is known; therefore, the RMS fluctuating components is defined as:

$$\sqrt{\overline{u_i'^2}} = \sqrt{\frac{2\,k}{3}}. \tag{3.83}$$

The characteristic lifetime of the eddy, τ_e, is computed as:

$$\tau_e = -T_L\ \ln(r), \tag{3.84}$$

where r is a uniform random number varying from zero to one.

The particle eddy crossing time, t_{cross}, is computed as:

$$t_{cross} = -\tau \ln\left[1 - \left(\frac{L_e}{\tau|u - u_p|}\right)\right], \tag{3.85}$$

where τ is the particle relaxation time, L_e is the eddy length scale and $|u - u_p|$ is the magnitude of the relative velocity.

The particle is assumed to interact with the fluid phase eddy over the smaller of the eddy lifetime and the eddy crossing time. When this time is reached, a new value of the instantaneous velocity is obtained by applying a new value ξ of in Equation (3.82).

3.5.3 Spray-wall interaction

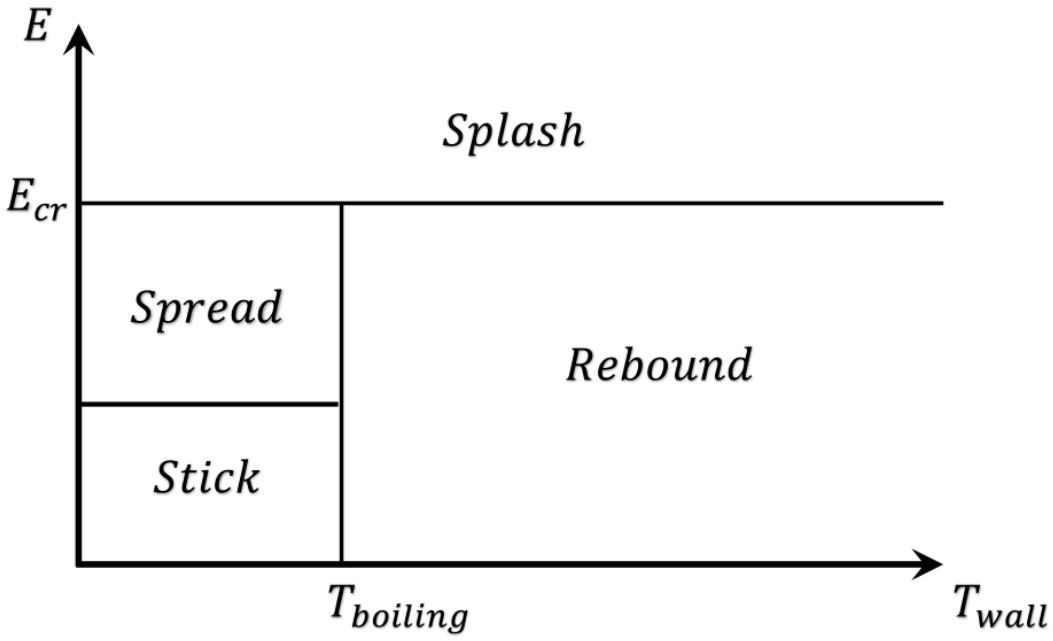

Figure 14: Illustrative chart of spray-wall Interaction Criterion.

In practical applications, the droplet of liquid fuel collides with the wall forming a thin wall. Thus, the discrete phase model is used to model the spray-wall interaction using Stanton–Rutland impingement/splashing model [130]. In this model, the impingement of liquid droplet with the boundary surface is divided into four regimes, which are stick, rebound, spread, and splash. The criteria by which the regimes are partitioned are based on the impact energy and the boiling temperature of the liquid as can be seen in Figure 14. The impact energy is defined by:

$$E^2 = \frac{\rho V_r^2 d_p}{\sigma}\left(\frac{1}{\min(h_0/d_p, 1) + \delta_{bl}/d_p}\right), \qquad 3.86$$

where ρ is the liquid density, V_r is the relative velocity of the particles in the frame of the wall, σ is the surface tension and δ_{bl} is the boundary layer thickness which is defined as:

$$\delta_{bl} = \frac{d_p}{\sqrt{Re}}, \quad 3.87$$

where Re is defined as $Re = \rho V_r d_p / \mu$.

As shown in Figure 14, Below the boiling temperature of the liquid, the impinging droplet can either stick, spread or splash. The sticking regime is applied when the impact energy is less than 16 and the particle velocity is set equal to the wall velocity. If the wall temperature is above the boiling temperature of the liquid, impingement events below (above) a critical impact energy (E_{cr}), which is equal to 57.7, results in the particles rebounding (splashing) from the wall.

3.5.4 Breakup model

In high-speed fuel injection systems, the Wave [131] and Kelvin-Helmholtz/Rayleigh-Taylor (KHRT) [130, 132] breakup models are commonly used. The former considers only Kelvin-Helmholtz (KH) instabilities driven by aerodynamic forces, whereas the latter accounts for KH instabilities along with Rayleigh-Taylor instabilities driven by droplet accelerations. Hence, the KHRT breakup model is used to accurately track and predict the liquid fuel breakup.

In KHRT breakup model, it is assumed that a liquid core exists in the near nozzle region, separating the droplet breakup into initial and secondary. The initial droplet breakup occurs within the liquid core, where the KH instabilities are dominant. Such instabilities postulate that a parent parcel with radius, r, breaks up to form new droplets with radius, r_c, such that:

$$r_c = B_0 \Lambda_{kH}, \quad 3.88$$

where Λ_{kH} is the wavelength corresponding to the KH wave with the maximum growth rate, Ω_{kH}, and B_0 is constant and equal to 0.61. The frequency of the fastest growing wave and its corresponding wavelength are given by:

$$\Omega_{kH} = \frac{0.34 + 0.38\, We_g^{1.5}}{(1+Z)(1+1.4T^{0.6})} \sqrt{\frac{\sigma}{\rho_f r^3}}, \quad 3.89$$

$$\Lambda_{kH} = \frac{9.02r\left(1 + 0.45\sqrt{Z}\right)(1 + 0.4T^{0.7})}{\left(1 + 0.865We_g^{1.67}\right)^{0.6}}, \quad 3.90$$

where the gas Weber number, We_g, and Ohnesorge number, Z, are computed as:

$$\mathrm{We}_g = \frac{\rho_g U_r^2 r}{\sigma}, \quad 3.91$$

$$Z = \frac{\sqrt{We_l}}{Re_l}, \quad 3.92$$

where U_r is the relative velocity between the liquid drop and the gas, σ is the surface tension, $\rho_g$and ρ_f are the densities of gas and fuel. The liquid Weber number, We_l, and liquid Reynolds number and Taylor number, T, are computed as:

$$\mathrm{We}_l = \frac{\rho_l U_r^2 r}{\sigma}, \quad 3.93$$

$$\mathrm{Re}_l = \frac{\rho_f U_r^2 r}{\mu_f}, \quad 3.94$$

$$T = Z\sqrt{We_g}. \quad 3.95$$

During break-up, the parent parcel reduces in diameter due to the loss of mass. The rate of change of the radius of the parent parcel is calculated using:

$$\frac{dr}{dt} = \frac{r - r_c}{\tau_{KH}}, \quad 3.96$$

where τ_{KH} is the breakup time and computed as:

$$\tau_{KH} = \frac{3.726 B_1 r}{\Omega_{kH} \Lambda_{kH}}, \quad 3.97$$

where B_1 is constant and equal to 1.73.

In the KH instabilities, mass is accumulated from the parent drop at a rate given by (τ_{KH}) until the shed mass is equal to 5% of the initial parcel mass. At this time, a new parcel is created with a radius given by r_c. The new parcel is given the same properties as the parent parcel (i.e. temperature and position) with the exception of radius and velocity. The new parcel is given a component of velocity randomly selected in the plane orthogonal to the direction vector of the parent parcel, and the momentum of the parent parcel is adjusted so that momentum is conserved.

That being said, the secondary breakup occurs outside the liquid core. both KH and RT effects are calculated and considered for breakup. Typically, the RT instability grows faster when droplet acceleration is high.

The RT model predicts instabilities on the surface of the drop that grow until a certain characteristic break-up time when the drop finally breaks-up. The RT model is a wave instability where the frequency of the fastest growing wave is given by:

$$\Omega_{RT} = \sqrt{\frac{2}{3\sqrt{3\sigma}} \frac{\left[-g_t(\rho_f - \rho_a)\right]^{3/2}}{\rho_f - \rho_a}}, \quad 3.98$$

where g_t is the acceleration. The corresponding wave number, K_{RT}, and wavelength corresponding to the fastest wave growth rate, Λ_{kH}, are:

$$\mathrm{K}_{RT} = \sqrt{\frac{-g_t(\rho_f - \rho_a)}{3\sigma}}, \quad 3.99$$

$$\Lambda_{RT} = \frac{2\pi\, C_{RT}}{\mathrm{K}_{RT}}. \quad 3.100$$

If the wavelength is smaller than the droplet diameter, RT waves are assumed to be growing on the surface of the droplet. Once waves begin to grow on the surface of the drop, the wave growth time is tracked. This time is then compared to the break-up time, defined by

$$\tau_{RT} = \frac{C_\tau}{\Omega_{RT}}, \qquad 3.101$$

where C_τ is constant and equal to 0.5. If the RT waves have been growing for a time greater than the break-up time, the drop is assumed to break-up. The radii of the new, smaller droplets are calculated using

$$r_c = \frac{\pi C_{RT}}{\mathrm{K}_{RT}}, \qquad 3.102$$

where C_{RT} is another adjustable constant set equal to 0.1.

3.5.5 Coupling between the discrete and continuous phases

As the trajectory of a particle is computed, the mass, momentum and heat gained or lost by the particles are also tracked. These quantities are incorporated in the subsequent continuous phase calculations by the source terms. This two-way coupling is accomplished by alternately solving the discrete and continuous phase equations until the solutions in one or both phases have stopped changing.

The mass, momentum and heat transfer from the discrete phase to the continuous phase is computed by examining their changes in each particle as it passes through each control volume in the computational domain. The mass, momentum and heat changes are computed as follows:

Source term of mass conservation equation

$$S_m = \frac{\Delta m_p}{m_{p,0}} \dot{m}_{p,0}. \qquad 3.103$$

Source term of momentum conservation equation

$$S_i = \sum \left(\frac{18\,\mu\, C_D Re}{\rho_p d_p^2\, 24} (u_p - u) + F_{other} \right) \dot{m}_p \Delta t. \tag{3.104}$$

Source term of energy conservation equation

$$S_h = \frac{\dot{m}_{p,0}}{m_{p,0}} \left[(m_{p,in} - m_{p,out})[-H_{lat,ref} + H_{pyrol}] - m_{p,out} \int_{T_{ref}}^{T_{p,out}} c_{p,p} dT + m_{p,in} \int_{T_{ref}}^{T_{p,in}} c_{p,p} dT \right], \tag{3.105}$$

where m_p is the mass of the particle, $m_{p,0}$ is the initial mass of the particle, $\dot{m}_{p,0}$ is initial mass flow rate of the particle injection, $\dot{m}_p$ is the mass flow rate of the particle, Δt is the time step, $m_{p,in}$ is the mass of the particle on cell entry, $m_{p,out}$ is the mass of the particle on cell exit, $c_{p,p}$ is the heat capacity of the particle, H_{pyrol} is the heat pyrolysis as volatiles are evolved, $H_{lat,ref}$ is the latent heat at reference conditions, $T_{p,in}$ is the temperature of the particle on the cell entry, $T_{p,in}$ is the temperature of the particle on the cell exit and T_{ref} is the reference temperature. $H_{lat,ref}$ is computed as:

$$H_{lat,ref} = H_{lat} - \int_{T_{ref}}^{T_{bp}} c_{p,g} dT + \int_{T_{ref}}^{T_{bp}} c_{p,p} dT \tag{3.106}$$

where $c_{p,g}$ is the heat capacity of the gas product species, T_{bp} is the boiling point temperature and H_{lat} is the latent heat at the boiling point temperature.

For the volatile part of the combusting particles, some constraints are applied to ensure that the enthalpy source terms do not depend on the particle history. The formulation should be consistent with the mixing of two streams, one consisting of the fluid and the other consisting of the volatiles. Hence, $H_{pyrol.ref}$ is derived by applying a correction to H_{pyrol}, which accounts for different heat capacities in the particle and gaseous phase:

$$H_{pyrol.ref} = H_{pyrol} - \int_{T_{ref}}^{T_{p,init}} c_{p,g} dT + \int_{T_{ref}}^{T_{p,init}} c_{p,p} dT \quad 3.107$$

where $T_{p,init}$ is the particle initial temperature.

3.6 Mechanisms of mass transportation

Each transport equation essentially consists of four terms, namely transient term, convection term, diffusion term and source term. Mathematically, the mass can be transported between two layers of fluid via convection and diffusion terms. This demonstrates the importance of both mechanisms (convection and diffusion) in exchanging the mass between fluids towards the successful predictions of any application using CFD.

In general, the main difference between the convection and diffusion mechanisms lies in their natures in transporting mass. The convection is a transportation process occurred due to the bulk motion of fluid, whereas the diffusion occurs due to the instantaneously varying, randomized motion of individual molecule. In other words, the transportation by convection takes place at a bulk of fluid scale and by diffusion at a molecular scale. This project focuses on the diffusion mechanism due to two reasons. The first one is that the potential of preferential diffusion effects is numerically not taken into considerations. This can be mathematically clarified by re-calling Equation (3.6):

$$\frac{\partial}{\partial t}(\rho Y_i) + \frac{\partial}{\partial x_i}(\rho u_i Y_i) = \frac{\partial}{\partial x_i}\left(\frac{\lambda}{c_p}\frac{\partial Y_i}{\partial x_i}\right) + \frac{\partial}{\partial x_i}\left(\frac{\lambda}{c_p}\left(\frac{1}{Le_k} - 1\right)\frac{\partial Y_i}{\partial x_i}\right) + \dot{\omega}_{Y_i}. \quad 3.108$$

As can been seen, the diffusion term (first two terms in RHS), in contrast to the convection term (second term in LHS), is split into two parts representing the non-preferential diffusion (first term in RHS) and preferential diffusion (second term in RHS) terms. The latter term is eliminated in many computational-based works carried out in the literature by applying the unity Lewis number. Therefore, the development of FGM aims to accurately predict the mass transport by diffusion using two-step correction process, as discussed in Section (3.4.4.1) and (3.4.4.5). The second reason is the high diffusion coefficient of hydrogen, which is one of its key advantages over the

conventional fuels and, therefore, the newly developed FGM hybrid combustion model intends to illustrate the effects of high hydrogen diffusivity, besides its other combustible characteristics, on the ignition process, heat released rate and flame propagation as shown in Chapter (5) and (6).

3.7 Numerical setup

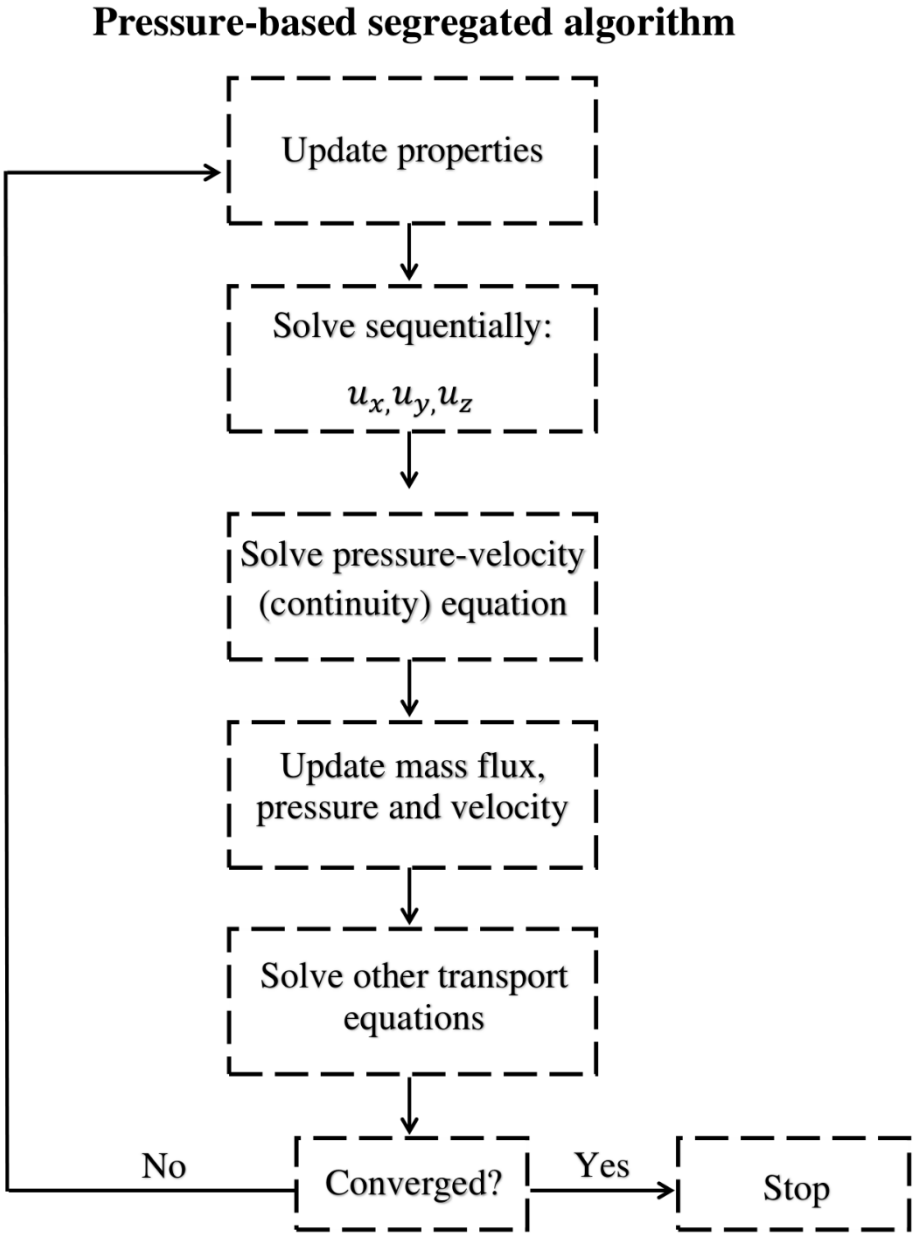

Figure 15: Schematic representation of pressure-based segregated algorithm solution method.

The CFD simulations of DF combustion were performed using ANSYS Fluent 18.1. All simulations were performed with the aid of a three-dimensional sector discretised with a fine mesh density. The sectors were created using SOLIDWORK 2017 software, whereas the meshing process was carried out using ANSYS Workbench. The utilisation of sectors significantly reduces the computational costs and is highly applicable owing to the symmetrical injector holes in the combustion chamber. The piston bowl is refined to increase the mesh quality, and inflation layers are added to enhance capturing the physical aspects. The mesh type of sectors is predominately hex to decrease the numerical diffusion and increase the computational efficiency. Comprehensive mesh sensitivity analysis was carried out in our previous study [96]. It was found that the fine mesh density well captures the in-cylinder pressure and heat release rate for the simulated test cases; therefore, it is implemented in the meshing process for Chapter 5 and Chapter 6. In IC engines, the cylinder volume changes throughout the engine cycle due to the piston movement; the mesh should change accordingly. Therefore, the rigid dynamic mesh is used to model the compression and expansion strokes, whereas the dynamic mesh is used due to its importance in determining the position of the boundaries of cell zones with respect to the other boundary of cell zones. The constant temperature boundary condition – assuming that the engine has already run for a couple of cycles – is used for the chamber main, top linear faces, piston linear face, piston bottom face and chamber top face as depicted in Table 3. The engine knocking is caused by the ignition of fuel from the hot spot on the piston or in-cylinder wall before being ignited from the ignition source; therefore, the initial boundary condition of temperatures is assumed to be 345 and 320 K for the simulations conducted in Chapter 5 and Chapter 6, respectively, to ensure that the auto-ignition temperatures of the gaseous fuels are not attained before the injection event of pilot fuel. Due to the use of sectors, periodic boundary conditions are applied over the side faces of the sector. No-slip conditions are prescribed on the solid walls, assuming that the velocity of the fluid is zero relative to the walls.

Spatial discretisation is carried out using the finite volume method. The simulations are performed using the pressure-based solver with the use of the segregated algorithm solution method, as seen in Figure 15. The spatial discretisation is carried out using the Green-Gauss Node-based scheme [133, 134] for gradients due to its second-order spatial accuracy and second-order scheme for pressure interpolation, attributed to both acceptable accuracy and computational costs. Various discretisation of transport equations is proposed in the literature and differ in terms of accuracy

and computational time. The central differencing scheme is less expensive in comparison with other schemes. However, it is not physically realistic because it does not account for the flow direction in its procedure. The exponential scheme yields highly accurate findings but is rarely used for multidimensional numerical implementations due to its extremely computational expenses. Hence, the second-order upwind scheme is applied for transport equations as its procedure takes into consideration the flow direction and maintains the numerical costs at acceptable levels [135]. The time integration is performed using the first-order implicit scheme because of its unconditional stability and robustness. The Pressure Implicit with Splitting of Operators (PISO) scheme [136] is used for the pressure-velocity coupling owing to its accuracy, which is achieved by the incorporation of two additional corrections. The convergence criteria are set with residuals of 10-6 for energy and 10-3 for other equations. A summary of the numerical methods employed in the entire modelling study is presented in Table 4.

When the engine is running, the crank shaft moves in a rotational manner and is linked to the piston, which vertical moves, by a connecting rod. Different crank angle degree represents the same in-cylinder volume. For example, the crank angle of zero (180) degree represents the minimum (maximum) in-cylinder volume. The minimum (maximum) in-cylinder volume also occurs at 360 (540), 720 (900) and 1080 (1260) crank angle degrees (CAD). Therefore, the range of CAD chosen to represent the maximum and minimum in-cylinder volumes in the project is from 540 to 900 CADs to represent the former in-cylinder volume, whereas the latter in-cylinder volume is represented by 720 CAD. It is important to mention that the numerical works in Chapter 5 and Chapter 6 are carried out with a sector from the CAD of intake valve closed (IVC) to the CAD of exhaust valve open (EVO) with respect to the aforementioned range of CAD.

SECTOR PART	**Temperature (K)**	
	Chapter 5	Chapter 6
CHAMBER MAIN LINEAR FACE	500	450
CHAMBER TOP LINEAR FACE	500	450
PISTON LINEAR FACE	500	450
PISTON BOTTOM FACE	600	550
CHAMBER TOP FACE	600	550

Table 3: Constant temperature boundary conditions.

Description	Parameters	Method/Model/Value
PRESSURE-VELOCITY COUPLING	Scheme	PISO
	Skewness correction	1
	Neighbor correction	1
SPATIAL DISCRETISATION	Gradient	Green-Gauss Node-based
	Pressure	Second order
	Density	Second order upwind
	Momentum	Second order upwind
	Turbulent Kinetic energy	Second order upwind
	Turbulent dissipation rate	Second order upwind
	Energy	Second order upwind
	Progress variable	Second order upwind
	Mean mixture fraction	Second order upwind
	Mixture fraction variance	Second order upwind
	Progress variable variance	Second order upwind
TEMPORAL DISCRETISATION	Time	First order implicit

Table 4: Summary of numerical methods employed for the entire simulation.

Chapter 4: Modelling and Simulation of Laminar Premixed and Non-Premixed Flames

4.1 Introduction

Alternative fuels such as hydrogen and ammonia have a central contribution towards compliance with future greenhouse gas and regulated pollutant emissions regulations. Dual-fuel combustion is an excellent way of utilising substantial amount of alternative fuels such as hydrogen and ammonia in compression ignition diesel engines. However, DF combustion consists of both premixed and non-premixed combustion modes which makes the DF flame complex to analyse. Modelling and simulation of laminar premixed and non-premixed flames applicable to DF flame under engine relevant conditions can improve the understanding of combustion characteristics of DF flame. This chapter investigates fundamental flame characteristics of laminar premixed and non-premixed flames under engine relevant conditions for hydrogen fuel blends including ammonia. The aim of this parametric study is to elucidate laminar flame characteristics of premixed and non-premixed diesel-hydrogen, diesel-hydrogen-ammonia and HVO-hydrogen-ammonia flames under high temperature and elevated pressure. The laminar flame calculations were performed for different hydrogen-enriched fuel blends to satisfy the similar fuel compositions employed in other two chapters for practical DF engine combustion simulations.

The evaluation of the applicability of hydrogen-enriched fuel mixtures for DF combustion requires in-depth understandings of hydrogen oxidisation at relevant engine conditions for a wide range of conditions. For example, many works have stressed the importance of accurate data on the laminar burning velocity along with some intrinsic cellular instability—such as diffusional-thermal instability [137, 138] and hydrodynamic instability [139, 140] of hydrogen premixed flames. To understand the combustion aspects of alternative fuels such as hydrogen-enriched DF flames, an accurate prediction of the laminar burning velocity, s_L, of premixed flames is important. This physicochemical property depends on the temperature, pressure, and mixture composition—such as fuel type and equivalence ratio. Thus, it is one of the most important global properties of a fuel—which could be used to characterise many premixed flame phenomena—and, as a result,

provides invaluable information on the combustion properties and the underlying oxidation chemistry of the given fuel.

Furthermore, the laminar burning velocity is enhanced by flame-front instabilities. Thermo-diffusive instability is driven by the ratio of molecular and heat diffusions, as described by Lewis number. Moreover, such instability plays an important role in the ignition and combustion of homogenous hydrogen fuel blends [103, 111]. In this instability, where the flame front is convex towards the unburnt mixture, the unburnt reactants travel towards the flame front faster than the opposite if the mass diffusivity is greater than the thermal diffusivity. These reactants are heated and thus burn faster, increasing the local laminar burning velocity in this zone. However, for the flame front to be concave to the unburnt gases, the reactants are diffused in a large zone, thus reducing the local laminar burning rate on this side. This promotes the instability of the flame due to an increase in the flame-front wrinkling along with the flame surface. Aside from the non-unity Lewis number, the preferential diffusion effects—resulting from the variation in species diffusivities leading to a local imbalance in the elemental mass fractions [141]—further enhance the thermo-diffusive instabilities more.

In addition to the importance of the laminar burning velocity, the laminar flame thickness is an important variable in determining the premixed combustion regimes as discussed in Section (3.4.1) and in measuring the hydrodynamic instability [142], which is initiated by the density jump across the flame. In this type of instability, the flame is considered to be infinitely thin, separating the upstream region of constant density, ρ_u, from the downstream region of constant density, ρ_b. In the upstream region where the flame is convex towards the burnt burnet mixtures, the flame speed—represented by the laminar burning velocity—is higher than the flow velocity; the opposite is true for the downstream region where the flame is convex towards the un- burnt mixtures. The differences between the upstream and downstream regions in terms of the flow and flame velocities are caused by thermal expansion. For the convex segment of the flame, the widening of the stream tube causes the flow to slow down. Furthermore, the local velocities of the approach flow and the flame are imbalanced, leading to further propagation of flame towards the unburnt mixture. A similar argument for the concave segment shows that it will further recede towards the burnt mixture. Hence, the flame front is unstable due to the discrepancies of flow and flame velocities between the upstream and downstream zones.

Thus, it has been noted that investigations into hydrogen-enriched (gaseous) mixtures in DF flames—premixed and non-premixed—remain scarce. Furthermore, evaluations of laminar burning velocities, flame-front instabilities, and flame structures are mostly limited to atmospheric conditions in the experimental measurements. Only a few experimental data are available at engine relevant conditions. Computationally, these parameters can be predicted by means of laminar one-dimensional calculations using chemical oxidation mechanisms. The aim of this chapter is to perform numerical simulations and analyse the laminar flame characteristics of hydrogen fuel blends in non-premixed and premixed configurations.

4.2 Numerical setup

The investigations were performed using the following two canonical configurations: (1) freely propagating for premixed flames, as shown in Figure 9, and (2) counter-flow for diffusion flames, as shown in Figure 10. For premixed flames, the results will be analysed for the flame structure, laminar burning velocity and flame thickness. Since the one-dimensional laminar investigations were carried out to assess the DF hybrid flames at engine relevant operating conditions, the initial condition of the oxidiser temperature was set to 1,100 K to represent the temperature of premixed charge at the end of compression stroke. However, it was found that there are simultaneous effects for only the premixed flames between the elevated pressure and temperature, causing the premixed flame to be unstable as discussed in Section (4.4.1.2). Therefore, the initial oxidiser temperature was varied for the premixed flame to set an instability threshold of both initial conditions of preheating temperature and pressure. Thus, for the freely propagating laminar premixed flame, the fuel temperature was set to 300 K, and the oxidiser temperature was set to 500 K; the equivalence ratio was set to 0.7. For diffusion flames, only flame structure will be discussed. Both laminar burning velocity and laminar flame thickness will only be discussed for the laminar premixed flame. The laminar burning velocity will not be analysed for diffusion flames, as this flame type is controlled by diffusion rate due to the absence of reference speed [111]. In addition, the laminar flame thickness will not be discussed for diffusion flames as it is a measure of the stretch rate effects on the hydrodynamic instabilities, and such instabilities, in turn, dominate in the premixed flame. For the counter-flow laminar diffusion flame, the temperature of the fuel and the oxidiser

were set to 300 K and 1100 K, respectively. The latter was applied given that the non-premixed fuels require a preheated oxidiser to cause the fuel to ignite.

For both configurations, the calculations were carried out at different initial pressures, ranging from 1 bar to 40 bar to assess the premixed and non-premixed flames at relevant engine conditions. The next sections investigate preferential diffusion effects by performing two simulations with unity—using constant Lewis number transport model—and non-unity Lewis number—using mixture averaged transport model—to evaluate the importance and possible effects of molecular transport properties on flame structure with the presence of such a high-diffusion-rate fuel—like hydrogen. In diffusion flames, the chemical reaction is controlled by mixing, as the reactants and oxidiser should be mixed to initiate the combustion, as discussed in Section (3.4.2). The mixing between fuel and oxidiser depend on the flow velocity gradient and preferential diffusion between heat conduction and mass diffusion, which can be quantified by the strain rate and Lewis number, respectively [143]. Therefore, the effects of the strain rate will be discussed only for the diffusion flames by carrying out one-dimensional calculations at 100, 400, and 700 1/s strain rates to demonstrate the impact of the flow velocity gradient on the diffusion flame structure. In contrast to diffusion flames, the high-preheating oxidiser at elevated pressure destabilises the premixed flame; thus, the different initial oxidiser temperatures were applied only for the premixed flames to represent an instability threshold of both initial conditions of preheating temperature and pressure.

The flame structure analysis mainly focused on hydrogen, NO, and their relevant species. H_2, H, OH, and HO_2 predominantly participate in most chemical reactions in the reduced-H_2 sub-mechanisms [105], whereas NO, N_2O, and NO_2 are the prime species in the reduced NO_x sub-mechanisms [106]. Thus, the flame structure analysis will be carried out with considering only the outlined species.

The next sections will discuss one-dimensional laminar flame results for different fuel blends with respect to energy share listed in Table 5. The contribution of fuels aimed at assessing the effects of hydrogen and ammonia by varying their energy contents and the effects of the alternative diesel counterpart fuel (HVO) by replacing diesel with it.

Test case	Fuel composition (energy share)		
	Diesel	**Hydrogen**	**Ammonia**
1	80%	20%	0%
2	27%	73%	0%
3	25%	25%	50%
4	10%	20%	70%
	HVO	**Hydrogen**	**Ammonia**
5	25%	25%	50%

Table 5: Fuel blends for simulated premixed and non-premixed flames.

All laminar flame calculations were performed using the one-dimensional chemical kinetics code, CHEM1D, by solving the flamelet equations presented in Section (3.4.4.1). The spatial and temporal discretisation schemes and numerical grid technique are discussed in Section (3.4.4.1). The domain size was chosen based on reducing the spatial coordinate and increasing the number of grids to 200 in order to get the smallest possible grid size to increase the accuracy of the solutions. The default value of the convergence criteria was implemented and equal to1.0×10^{-10}.

4.3 Validation

Experimental and kinetic modelling of the hydrogen–air mixture and ammonia–air mixture at atmospheric pressure and temperature, as well as the hexadecane–air mixture at atmospheric pressure and temperature of 443 K, over a range of equivalence ratio, $\emptyset$, are plotted in Figure 16. As can be seen in Figure 16(a), the hydrogen sub-mechanisms incorporated in this study show good agreement with the experimental and modelling laminar burning velocities at lean conditions; however, an over-prediction is noted, as the equivalence ratio increased towards rich conditions. In addition, it seems that the predicted laminar burning velocity carried out by Sun et al. [148] is expected to provide more reliable results in rich conditions compared to the hydrogen sub-mechanisms implemented in this project because it is closer to the experimental findings. For the ammonia–air mixture, the validated burning velocities are acceptable and show good agreements against the experimental data particularly with the findings obtained by Li et al. [146]. More importantly, the ammonia mechanisms used in the present work display better agreements with

measured ammonia burning velocities than the numerical data obtained by Okafor et al. [144] as shown in Figure 16(b).

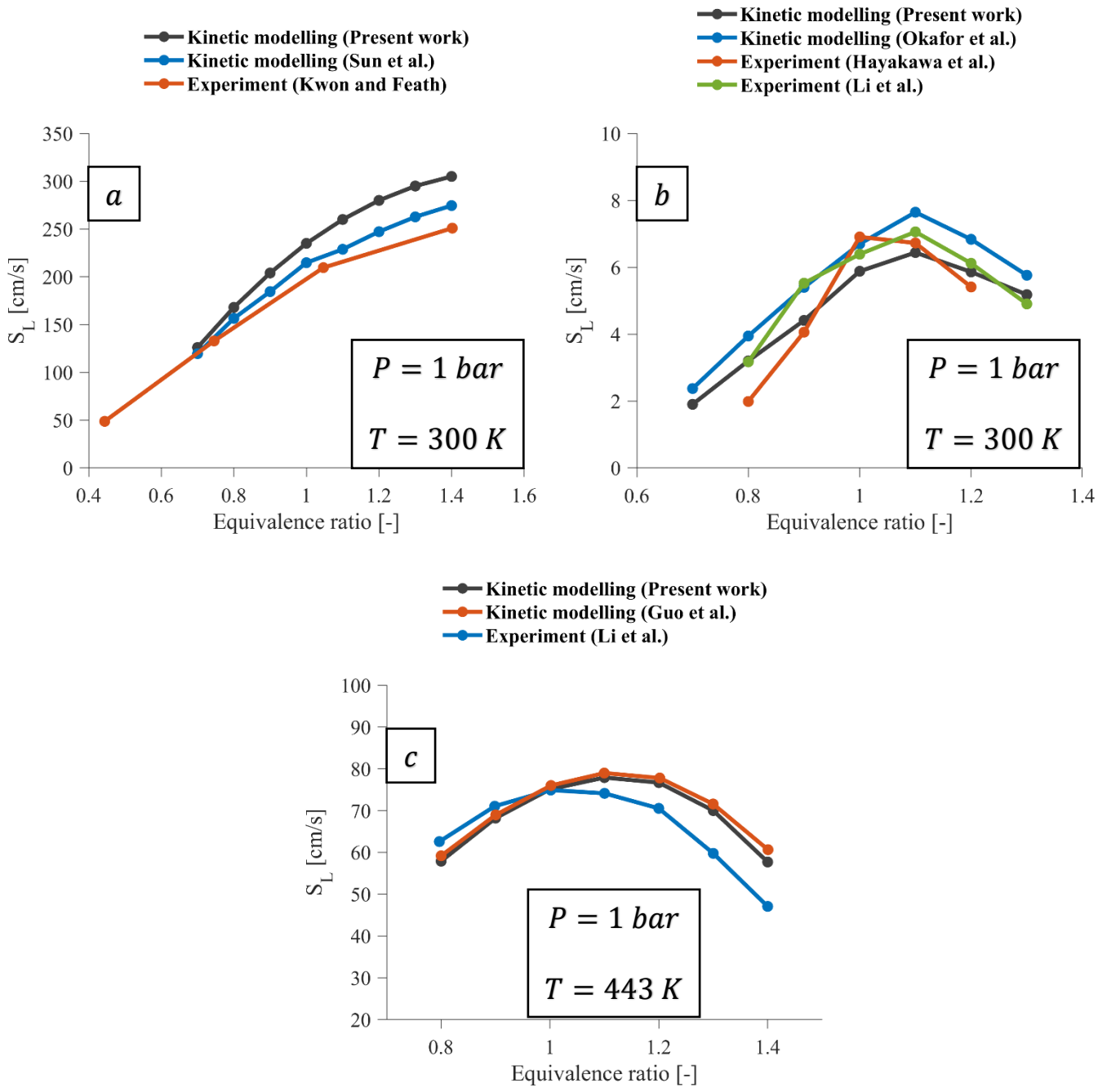

Figure 16: Comparison of measured laminar burning velocity of (a) hydrogen-air mixture, (b) ammonia-air mixture and (c) hexadecane-air mixture by Kwon and Feath [145], Hayakawa et al. [12], (b) Li et al. [146], (c) Le et al. [147] to predictions made by the kinetics models of Sun et al. [148], Okafor et al [144] and Guo et al [107].

Figure 16(c) shows the excellent agreement of the hexadecane–air mixture —HVO surrogate fuel— between the kinetic modelling data of the present work and the kinetic modelling data from the work carried out by Guo et al. [107] over the entire range of equivalence ratios as both computed data are slightly lower than the measured data for $\emptyset < 1$ and notably overestimated for $\emptyset > 1$ (rich conditions). In general, all validations are acceptable at fuel lean conditions, as the equivalence ratio of the premixed flame was set to 0.7.

4.4 Results and discussion

4.4.1 One-dimensional laminar premixed flame

The first sub-section discusses the role of preferential diffusion effects for Case 2 and Case 4—demonstrating the high and low burning rates of hydrogen and ammonia, respectively—at initial oxidiser temperature and pressure of 500 K and 1 bar. The second sub-section discusses the effects of preheating temperature at relevant engine operating elevated pressure values. The final sub-sections analyse the effects of initial pressure and the effects of alternative fuel additions. Case 2 has been used to validate the FGM hydrogen combustion model for diesel-hydrogen DF engine combustion with high hydrogen energy share while case 4 has been also simulated for diesel-hydrogen-ammonia DF engine combustion. The DF engine combustion results will be discussed in chapter 5 and chapter 6 respectively.

4.4.1.1 Effects of preferential diffusion

Figure 17 demonstrates a comparison between the unity and non-unity Lewis number of H_2, H, OH, and HO_2 mass fractions and their source terms with respect to the spatial coordinates for Cases 2 and 4 at initial oxidiser temperature and pressure of 500 K and 1 bar respectively. In general, the incorporation of preferential diffusion effects in laminar premixed flames can be split into major and minor effects. The major effects lie in affecting flame propagation, as the premixed flame in nature is mainly controlled the flame propagation as discussed in Section (3.4.1). In many investigations, the definition of flame propagation, S_s, is based on the laminar burning velocity,

S_L, where the latter depends on the unburnt-mixture density and mass flow rate as follows [17, 149]:

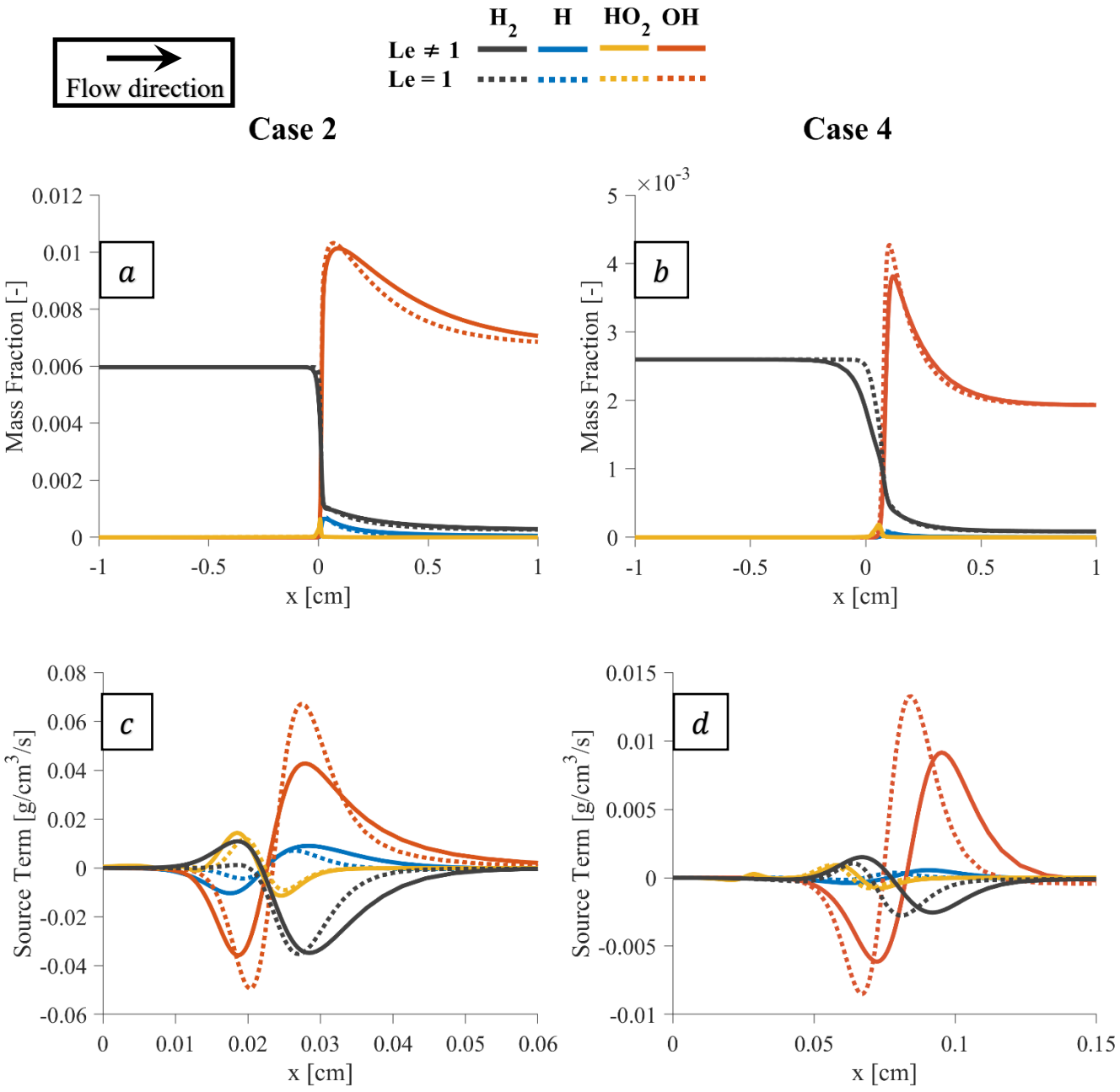

Figure 17: Distribution of mass fractions and source terms of H_2, H, OH and HO_2 with respect to the spatial coordinates with and without unity Lewis number for case 2 and case 4.

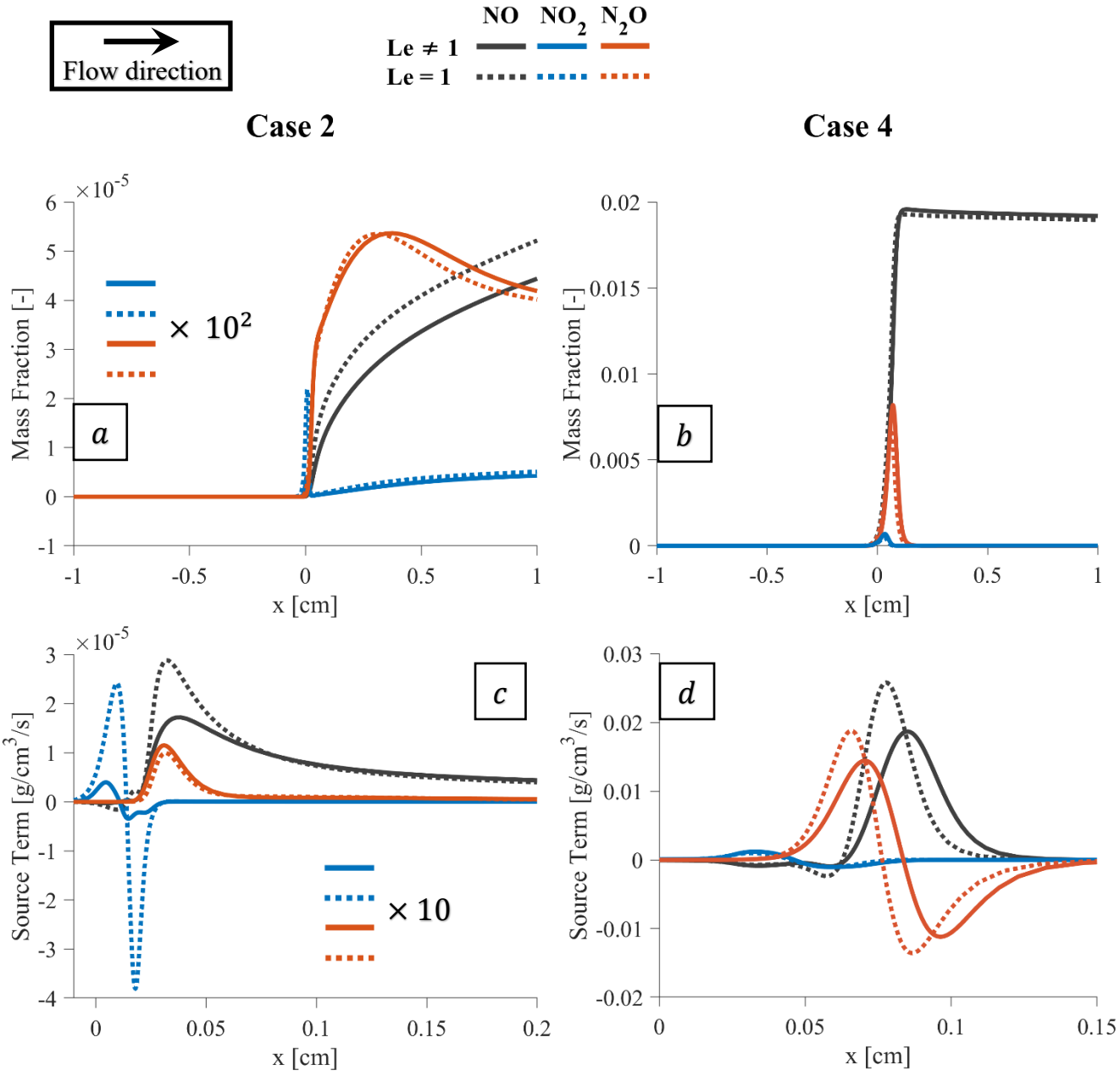

Figure 18: Distribution of mass fractions and source terms of NO, NO_2 and N_2O with respect to the spatial coordinates with and without unity Lewis number for case 2 and case 4.

$$S_L = \frac{\dot{m}_u}{\rho_u}, \qquad S_s = \frac{\rho_u}{\rho_b} S_L, \tag{4.1}$$

where $\dot{m}_u$, ρ_u, and ρ_b are unburnt mass flow rate, unburnt density, and burnt density, receptively. Using this definition to compute the flame propagation speed shows that the preferential diffusion effects—which are physical phenomena affecting flow velocity—play an important role in determining flame prorogation through the unburnt-mixture mass flow rate, as the density is a physical property of matter expressing the relationship of mass to volume.

The minor effects are caused by the variation of the binary diffusion coefficient throughout the domain because this coefficient is affected by various variables associated with flow current state—such as temperature—and physical phenomena—such as curvature.

The first aspect of the preferential diffusion effects can be clearly seen by the earlier take-off of the chain of chemical reactions in the highly hydrogen-enriched premixed mixture, due to the high hydrogen diffusivity, as seen in Figure 17(c). However, the later activation of chemistry, as seen in Figure 17(d), is due to the ammonia burning rate. The second aspect predominantly affects the range of the reaction zone, as shown in Figure 17(c–d). Apart from the peaks of species production and oxidisation, the preferential diffusion effects influence of the reactivity of the chemistry region over the domain, as this region is broader with the incorporation of preferential diffusion effects with high-reactivity fuel (hydrogen) and even low-reactivity fuel (ammonia). This demonstrates the role of the light intermediate radicals—such as OH and H—in enhancing the chemical reaction rate by expansion of their reactivity range. Surprisingly, the OH formation and consumption are greater with the unity Lewis number, indicating that the unity Lewis number assumption results in over-predicted findings.

Figure 18 shows the variations of NO, NO_2, and N_2O mass fractions and their source terms with and without the incorporation of preferential diffusion effects for both Cases 2 and 4. Interestingly, the NO mass fraction is lower (similar), with such effects for Case 2 (Case 4). However, these results cannot be considered the final findings of the NO_x engine-out emissions, as accurate NO_x predictions require the implementation of the NO_x sub-model during the three-dimensional simulations. This sub-model, in turn, employs the thermal and prompt NOx formations. The former accounts for the NO_x formations by employing highly temperature-dependent chemical reactions dependent on N_2, whereas the latter takes into consideration a set of chemical reactions of atmospheric N_2 with the combustion radicals occurring in the earlier combustion phases. That said, the preferential diffusion effects on the set of NO_x species are similar to their effects on the set of

H_2 and their relevant species. In general, the assumption of the unity Lewis number seems to over-predict the set of NOx species in the laminar environment.

Figure 19 shows the laminar burning velocities—calculated using Equation (4.1)—with and without unity Lewis number for Cases 2 and 4. As expected, the incorporation of differential diffusion effects results in a faster laminar burning velocity than when such effects are excluded such for Case 2 due to the high hydrogen addition. As seen in Equation (4.1), laminar burning velocity depends on the unburnt-mixture density and mass flow rate. The unburnt densities with and without unity Lewis number are the same, whereas the unburnt mass flow rate is faster in the non-unity Lewis number case. This could be attributed to the high-hydrogen-diffusion coefficient, which results in a greater acceleration of flow compared of that with unity. A similar argument with contrast effects for case 4 shows that the ammonia-added premixed flame with non-unity Lewis number causes the laminar burning velocity to slow down due to the low ammonia burning rate. It should be noticed that the difference between the unity and non-unity Lewis number of high hydrogen and ammonia enrichment is 16.1 cm/s and 1.7 cm/s, respectively. This is caused by the very low Lewis number of hydrogen and the slightly greater ammonia Lewis number than unity.

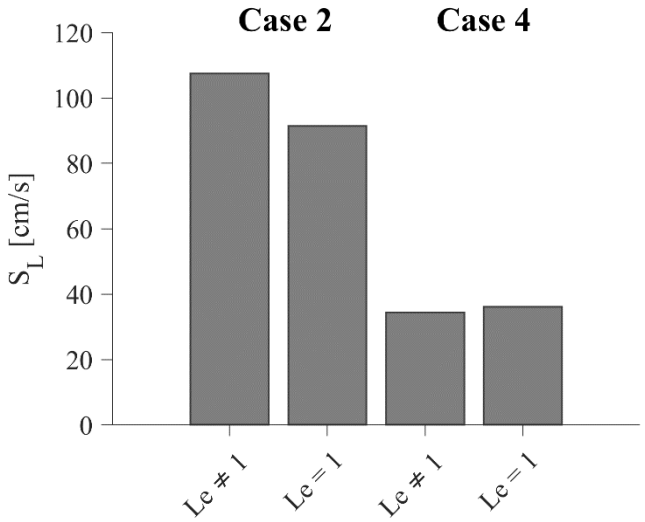

Figure 19: Comparisons of laminar burning velocities with and without unity Lewis number for case 2 and case 4.

Flame thickness, δ, is a measure of the stabilising effects of flame stretch rate on hydrodynamic instability [142]. In the literature, different flame thickness correlations have been proposed incorporating various variables. For example, the Zel'dovich correlation [150] expresses the flame thickness in terms of the laminar flame speed and the properties of the fresh gases. The Blint correlation [150] expresses flame thickness with respect to laminar flame speed, using the properties of the fresh gases and the properties of the burnt gases. It was noted that the Zel'dovich correlation underestimates calculated flame thicknesses, whereas Blint's correlation shows better agreement; however, errors increase for lean and rich mixtures at low pressures and for highly diluted mixtures at low temperatures [151, 152]. Therefore, the flame thickness in this chapter is computed using the Blint correlation as follows:

$$\delta = 2\left(\frac{\lambda}{\rho\, c_p}\right)\frac{1}{s_l}\left(\frac{T_b}{T_u}\right)^{0.7}, \qquad 4.2$$

where λ is the thermal conductivity, ρ is density, and c_p is the specific heat capacity of the fresh gases. T_b and T_u are the burnt and unburnt gas temperatures, respectively.

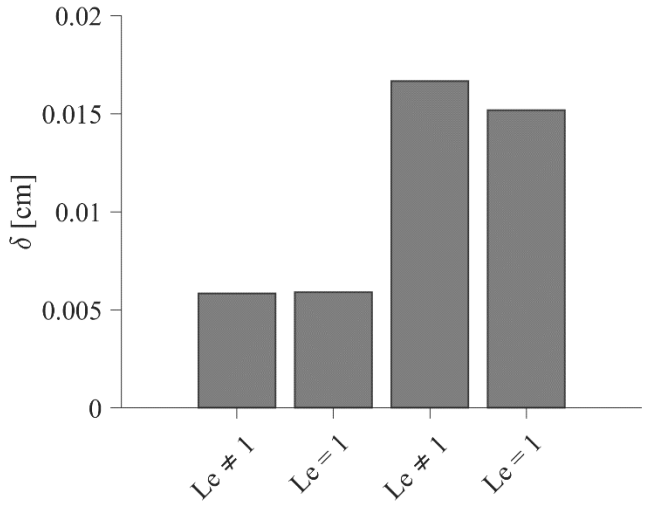

Figure 20: Comparison of the flame thicknesses with and without the incorporation of preferential diffusion effects for case 2 and case 4.

As shown in Figure 20, the incorporation of preferential diffusion effects in the highly hydrogen-enriched mixture results in roughly the same flame thickness compared to the unity Lewis number assumption. Moreover, the flame with high ammonia enrichment with a non-unity Lewis number case is thicker by 8.2×10^{-3} cm. These findings are interesting to obtain, as they indicate that the low reactivity of ammonia significantly affects the hydrodynamic instabilities by the flame stretch rate to a greater degree than the high hydrogen reactivity rate with the presence of the preferential diffusion effect.

4.4.1.2 Effects of oxidizer temperature

Figure 21 compares the hydrogen mass fractions and source terms at various initial pressures and oxidiser temperatures for Case 1. The other cases show similar behaviours. In general, the effects of elevated pressure lead to an overall increased chemistry rate, narrowing and shifting the reaction zone towards the inlet of the premixed charge, as discussed in Section (4.4.1.3). Unexpectedly, the premixed flame demonstrates instabilities at high preheating temperatures and high pressures. As shown in Figure 21(c)—where the initial oxidiser temperature was 1100 K—the 40-bar and 20-bar cases show opposite behaviours, as their reaction zones are farther from the premixed charge inlet compared to the 1-bar and 10-bar cases, in which the last two cases demonstrate expected trends. Lowering the preheating temperature to 700 K causes the 20-bar case to stabilise and the 40-bar case to show less instabilities, as seen in Figure 21(b). However, at an oxidiser temperature of 500 K, the premixed flames for the presented cases are stable because the chemical reaction rates are greater and the reaction regions are narrower and closer to the premixed mixture inlet with the increase in pressure.

The instabilities noted above can also be observed in the comparison of the laminar burning velocities of Case 1 at various initial pressure and oxidiser temperature levels, as shown in Figure 22. It is widely known that an increase in pressure results in a reduction of the laminar burning velocity due to the increase in unburnt-mixture density and mass flow rate. As the 20-bar and 40-bar cases at an oxidiser temperature of 1100 K show abnormal trends—indicating flame instabilities—their laminar burning velocities also demonstrate non-physical quantities compared to those of the 1-bar and 10-bar cases. A similar controversy is found for the 40-bar case at a preheating temperature of 700 K, where the flame is unstable in the applied initial conditions.

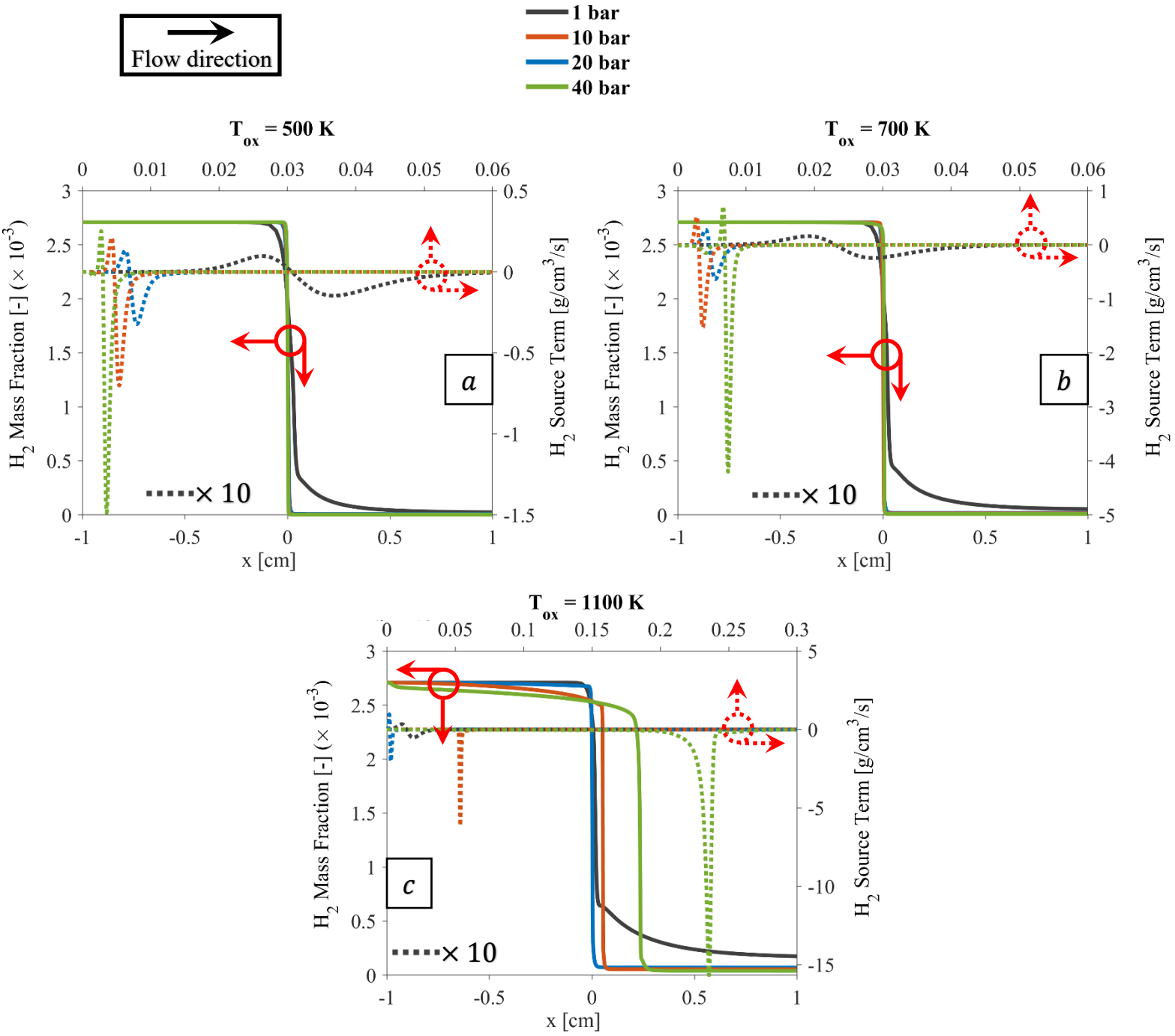

Figure 21: Comparisons of H_2 mass fraction and source term at different initial pressures and oxidiser temperatures for case 1. Simulations at 10 bar initial pressure were only performed for this section to represent an instability threshold.

Additionally, the increase in pressure decreases the laminar burning velocities at near atmospheric preheating temperatures. On the other hand, the laminar burning velocity for a given pressure is found to increase with an increase in oxidiser temperature. This could be caused by the greater unburnt-mixture enthalpy, since the unburnt-mixture temperature before the flame has a higher enthalpy compared to the lower initial temperature condition [153]. Further to this, the increase in mixture temperature increases the unburnt mass flow rate and decreases the unburnt density, causing the burning velocity to increase.

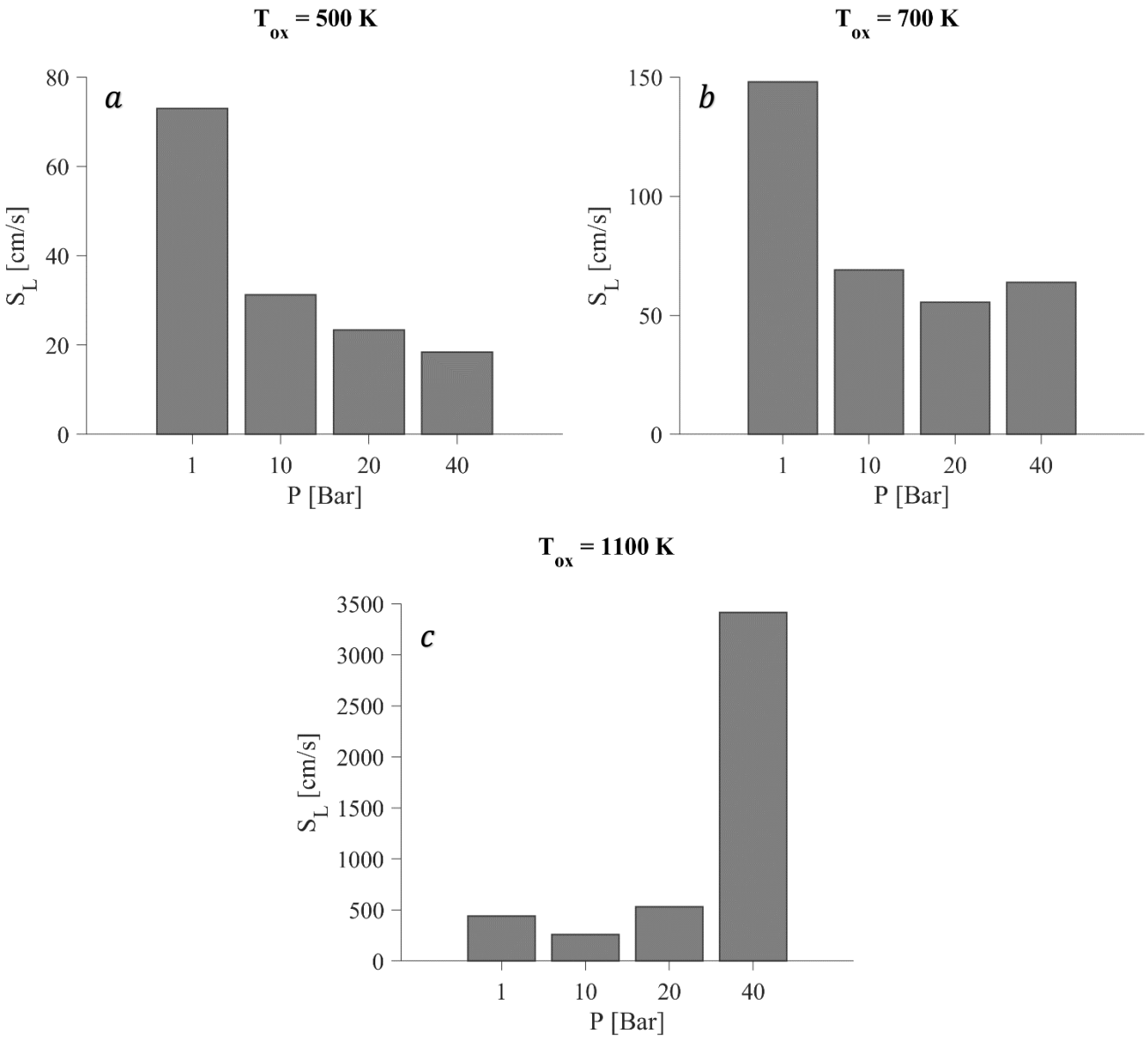

Figure 22: Comparisons of laminar burning velocities at different initial pressures and oxidiser temperatures for case 1.

These instabilities are observed for the 20-bar and 40-bar cases and 40-bar case at oxidiser temperatures of 1100 and 700 K, respectively, and can be attributed to the high preheating temperature of the oxidiser stream, where the gaseous fuels are introduced, at elevated pressure. Thus, the presence of hydrogen – which has a high laminar burning velocity – in the oxidiser stream with high preheating temperature at relevant engine operating pressure results in unstable premixed flames, indicating the possibility of knocking tendency. In addition to the preheating temperature effects, the increase in pressure enhances the flame instabilities by cracking in the flame front, which could self-turbulise the laminar flame [154, 155].

As mentioned in Section (4.1), the hydrogen premixed flame can be exposed to two intrinsic flame instabilities known as diffusional-thermal instability and hydrodynamic instability. Due to the high hydrogen diffusivity, hydrogen is highly susceptible to the former mechanism of instability as it is driven by the low Lewis number of hydrogen species. In addition, the hydrodynamic instability mechanism can destabilise the hydrogen premixed flame and it is measured by the flame thickness. In general, the thinner flame indicates the high destabilising tendency. The flame thicknesses are 4.13×10^{-2}, 2.87×10^{-2} and 1.51×10^{-2} at preheating temperature of 500, 700 and 1100 K, respectively, for initial pressure of 1 bar, 9.69×10^{-3}, 6.19×10^{-3} and 2.60×10^{-3} at preheating temperature of 500, 700 and 1100 K, respectively, for initial pressure of 10 bar, 6.49×10^{-3}, 3.86×10^{-3} and 6.44×10^{-4} at preheating temperature of 500, 700 and 1100 K, respectively, for initial pressure of 20 bar and 4.10×10^{-3}, 1.68×10^{-3} and 5.02×10^{-5} at preheating temperature of 500, 700 and 1100 K, respectively, for initial pressure of 40 bar. By and large, the increase in oxidiser temperature results in reductions in the flame thickness, demonstrating more destabilised premixed flames due to the hydrodynamic mechanisms.

As the 20-bar and 40-bar cases and 40-bar case at oxidiser temperatures of 1100 and 700 K display unexpected findings in their laminar burning velocities along with the distribution of species over the domain width, they demonstrate the thinnest flames between the test cases thicknesses, pronouncing the contribution of the hydrodynamic mechanism in destabilising the premixed flame.

4.4.1.3 Effects of elevated pressure

A comparison of the H_2, H, OH, and HO_2 mass fractions and source terms at various pressure levels for Case 1 are shown in Figure 23. Only Case 1 is presented here because the effects of the pressure increase on the other test cases are found to be similar, as demonstrated in Appendix E.

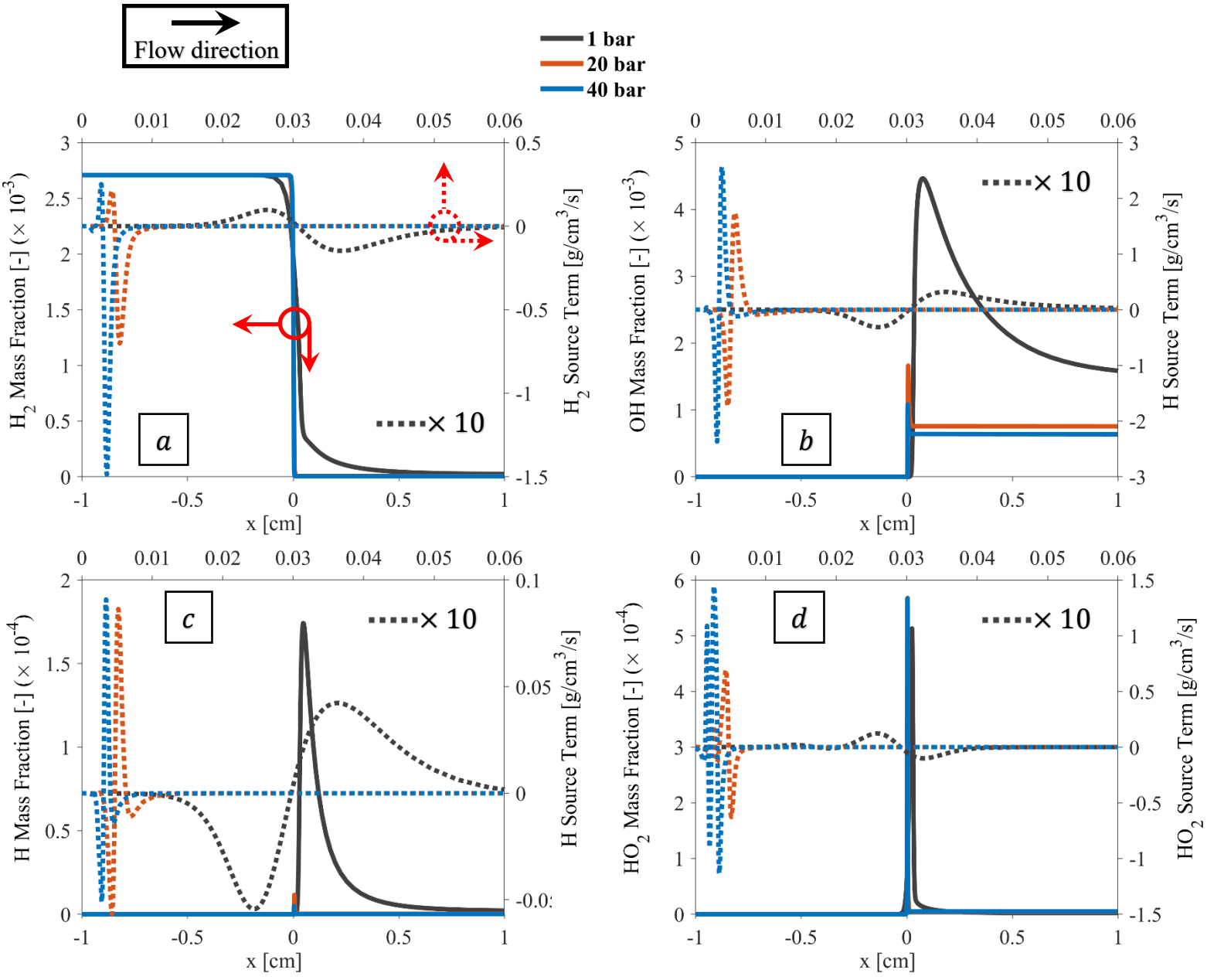

Figure 23: A comparison of H_2, H, OH and HO_2 mass fraction and source terms at various pressure levels of case 1.

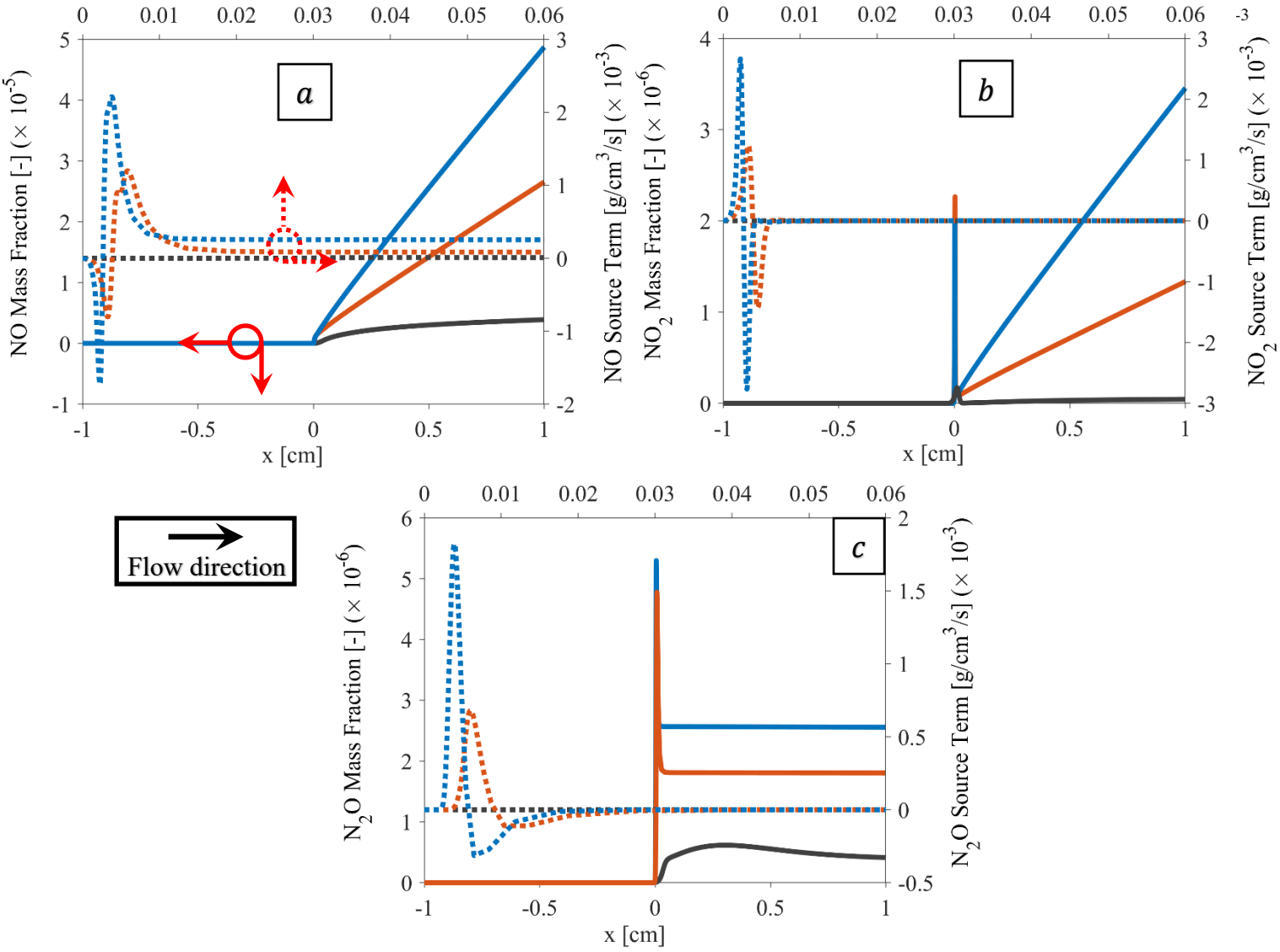

Figure 24: A comparison of NO, NO_2 and N_2O mass fraction and source terms at various pressure levels for case 1.

As seen in Figure 23, when the pressure increases, the reaction zone turns out to be quite narrower, indicated by (i) the range of spatial coordinate where the species formation and oxidisation occur and (ii) the sharp increase or decrease in the species mass fractions. In addition to this, the reaction zone shifted towards the premixed mixture inlet, as the chemistry set is initiated earlier, as shown in Figure 23 and Figure 24. Moreover, the pre-heating zone is also tighter with the increase in pressure given that the mass fraction of hydrogen in the 1-bar case is consumed prior the 20-bar and 40-bar cases, as shown in Figure 23(a). Importantly, the relative changes in the hydrogen and its relevant species between 1 bar and 20 bar are much greater than the relative changes between

20 bar and 40 bar, indicating that the effect of elevated pressure is less sensitive at higher pressure levels. Furthermore, the overall chemical reaction rates are found to be highly enhanced at elevated pressure. As shown in Figure 23(b–c), the peaks of OH and H mass fractions at 1 bar are much higher than those of 20 and 40 bar; however, their chemical reactivity are significantly greater at higher pressure levels. The reason for these variations between the OH and H mass fractions and source terms could lie in their engagements with other chemical reactions and thus, possibly result in the increased production of other species.

Although investigations into chemical reaction sensitivities are not carried out, it should be noted that the relative importance of some chemical reactions and/or species is higher at elevated pressure, resulting in the higher production and/or consumption of some species over others [103]. Hence, as shown in Figure 23(d), the chemical reactivity of HO_2 at 40 bar shows strong fluctuations compared to H_2, OH, and H at the same pressure level, referring to the possibility of its greater relative importance to the chemical reactions involving HO_2 at relevant engine-operating pressure.

Figure 24 shows the distributions of NO, NO_2, and N_2O mass fraction and source terms with respect to the spatial coordinate at various pressure levels for Case 1. Similar observations in terms of the higher promotion of chemistry rates, tighter reaction zone, and earlier initiation of chemistry are also demonstrated for NO, NO_2, and N_2O. Furthermore, their mass fractions are higher at elevated pressure. This indicates that the pressure increase enhances the chemistry rate and, accordingly, the temperature, resulting in higher concentrations of the NO_x species group.

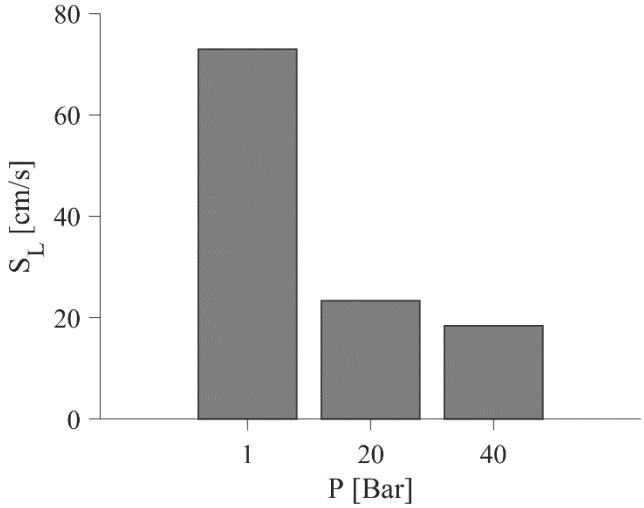

Figure 25: Laminar burning velocities at different initial pressure levels for case 1.

Figure 25 shows a comparison among the laminar burning velocities at different initial pressure levels for Case 1. As expected, the laminar burning velocity demonstrates a monotonic decrease as the pressure increases [156, 157]. The laminar burning velocity depends on the unburnt-mixture density and mass flow rate, as shown in Equation (4.1) and these parameters, in turn, are increased at elevated pressure. The increase in the density of the mixture reduces the mean free path for the molecular collisions and enhances the collision frequency. This, in turn, leads to enhanced third-body effects and higher third-body recombination reactions. On the other hand, the mass flow rate is directly proportional to the velocity; the velocity, in turn, increases when the gases in a specific domain are compressed. Thus, the laminar burning velocities are 73, 23.3, and 18.5 cm/s at 1, 20, and 40 bar, respectively. These findings support the observations noted above regarding the sensitivity effects of elevated pressure, as the difference in the laminar burning velocity between the 20-bar and 40-bar cases is minor compared to those between the 1-bar and 20-bar cases.

Figure 26 presents the effects of elevated pressure on the flame thickness for Case 1. It can clearly be seen that an increase in pressure results in a decrease in flame thickness, consistent with the significantly narrower reaction zone at higher pressure. The thinner flame front emphasises that the conditions of engine-operating pressure significantly instabilities the flame front by the stretch rate, leading to higher hydrodynamic instabilities.

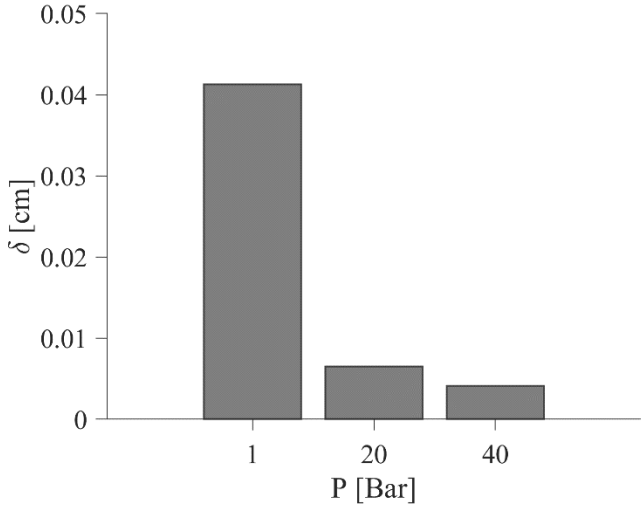

Figure 26: A comparison of flame thickness at elevated pressure for case 1.

4.4.1.4 Effects of alternative fuel additions

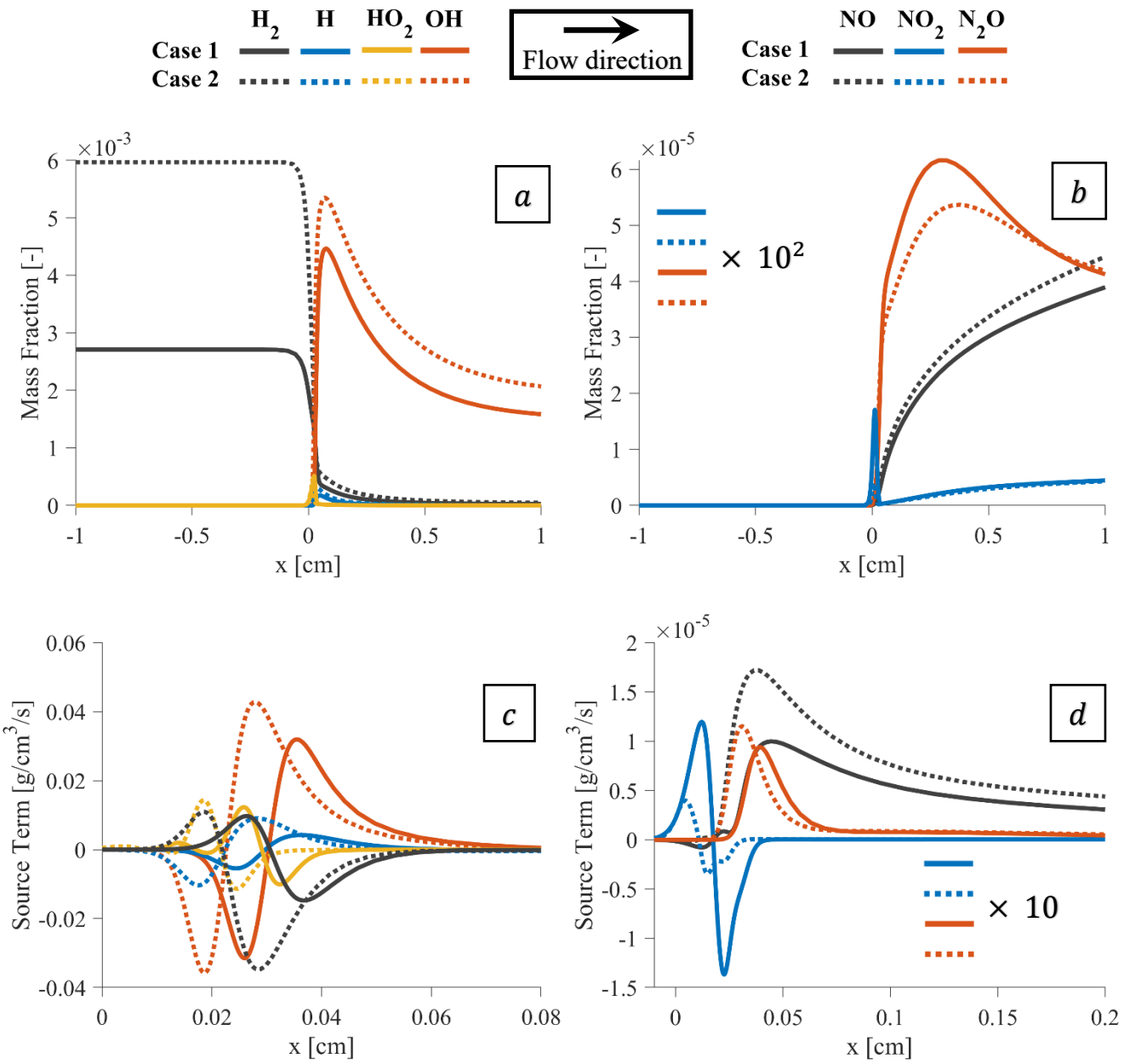

Figure 27: Distributions of H_2, NO_x and their relevant species mass fractions and source terms along the spatial coordinate between case 1 and case 2, showing the effects of increasing the hydrogen addition.

Figure 27 shows the effects of more hydrogen additions by comparing the distributions of H_2, NO_x, and their relevant species mass fractions and source terms along the spatial coordinate between Cases 1 and 2 at initial pressure and preheating temperature of 1 bar and 500 K, respectively. As

excepted, the flame structure of the more hydrogen-added premixed flame points out that the more substitution of hydrogen causes radical concentrations—i.e., the maximum mass fraction of OH—in the reaction zone to increase as opposed to the lower hydrogen-enriched flame, as seen in Figure 27(a). Further to this, Figure 27(c) demonstrates that greater hydrogen addition results in an earlier initiation of chemistry, indicting a shorter ignition delay as well as a broader reaction zone (note the start and end of species productions and consumption with respect to the spatial coordinate). The broader reaction zone along with the higher species chemical reactivity as shown in Figure 27(c) signify greater chemical reaction rates in consistent with the increase in hydrogen. It should also be noted that hydrogen in both Cases 1 and 2 is first formed and then consumed. In addition, its formation coincides with the consumption (formation) of OH and H (HO_2), while its consumption shows reversed trends.

These observations could indicate that the relevant importance of some chemical reactions change with respect to the local conditions of flame, such as the current-state temperature and concentration of O_2. On the other hand, the OH radical is found to achieve greater orders of magnitude than H and HO_2, indicating that the former seems to dominate reactive effects in hydrogen-enriched flames. This argument is supported by the greater OH oxidisation and production compared to those of H and HO_2. Higher hydrogen substitution is expected to worsen the NO_x emission performance. As seen in Figure 27(b–d), the NO maximum mass fraction and its chemical reactivity are greater with increased hydrogen-enriched flame. It is important to note that the production of N_2O and NO resulted from NO_2 oxidisation, as their source terms are found to increase with the reduction of NO_2 (see Figure 27[d]). Surprisingly, the mass fraction peaks of N_2O and NO_2 along with the NO_2 production and consumption are higher with the lower-hydrogen-content mixture, which could be an indication of the dependency of NO on other species given that its maximum mass fraction is higher with the addition of more hydrogen.

The effects of more ammonia addition on the variations of H_2, H, OH, HO_2, NO, NO_2, and N_2O mass fractions and source terms over the spatial coordinate between Cases 3 and 4 are illustrated in Figure 28. The combustible characteristics of ammonia are opposite to those of hydrogen because ammonia is a low-reactivity and low-burning-rate fuel. Therefore, Figure 28(a–c) demonstrates that the effects of more hydrogen enrichment are reversed, as in Case 4 compared to Case 3, showing that (i) the concentrations of hydrogen and its related species mass fractions are

reduced, (ii) the reaction zone is relatively narrower, (iii) the take-off of the chain of chemical reactions are later, and (iiii) lower species chemical reactivity is achieved, resulting in a reduction in the chemistry rates. Nevertheless, the higher ammonia-added premixed flame (Case 4) significantly increases NO, NO_2, and N_2O mass fractions in much higher orders of magnitude than those in Case 2 (highest hydrogen addition) as their quantities are 0.02, 6.89×10^{-4}, and 0.01 for Case 4 and 4.44×10^{-5}, 4.31×10^{-8}, and 5.37×10^{-7} for Case 2, respectively. These findings indicate that the utilisation of ammonia yields much higher NO_x engine-out emissions than the utilisation of hydrogen. The causes could lie in the considerable amount of nitrogen resulting from the ammonia cracking, which, in turn, seems to dominate the greater temperature resulting from the hydrogen combustion (high-temperature environments are favoured for NO_x formations). Interestingly, despite the 20% difference in ammonia addition between Cases 3 and 4, their NO mass fraction peaks are comparable. As previously mentioned in Section (4.4.1.1), the implementation of the NO_x sub-model is significantly important in accurately predicting NO_x emissions due to the incorporation of thermal and prompt NO_x formation. This sub-model is employed in three-dimensional simulations discussed in Chapters 5 and 6.

Figure 29 shows the effects of HVO compared to diesel in terms of the distribution of H_2, NO_x, and their relevant species mass fractions and source terms along the spatial coordinate between Cases 3 and 5. The replacement of diesel by HVO causes the maximum mass fractions of H and OH radicals to increase in the reaction spot from 9.33×10^{-5} and 4.30×10^{-3} in Case 3 to 1.01×10^{-4} and 4.90×10^{-3} in Case 5, respectively. The aforementioned species are known as highly reactive and, therefore, their increases indicates that the utilisation of HVO results in greater promotion of chemical reaction rates. This observation is supported by the relatively greater H and OH consumption and production, as shown in Figure 29(c). However, the peak mass fraction and chemical reactivity of HO_2 are found to be decreased with HVO. More importantly, the NO concentration peak is lower with HVO, indicating that HVO is more environmentally benign compared to diesel. As previously discussed, HVO is a high-cetane-number fuel and thus its use is expected to shorten the ignition delay. Figure 29(c–d) shows that the chain of chemical reactions in Case 5 takes off closer to the premixed mixture inlet compared to Case 3, indicating an earlier trigger of combustion with HVO. With respect to the reaction zone, it seems that HVO leads to relatively widening it and, consequently, the overall chemical reaction rates are expected to be higher.

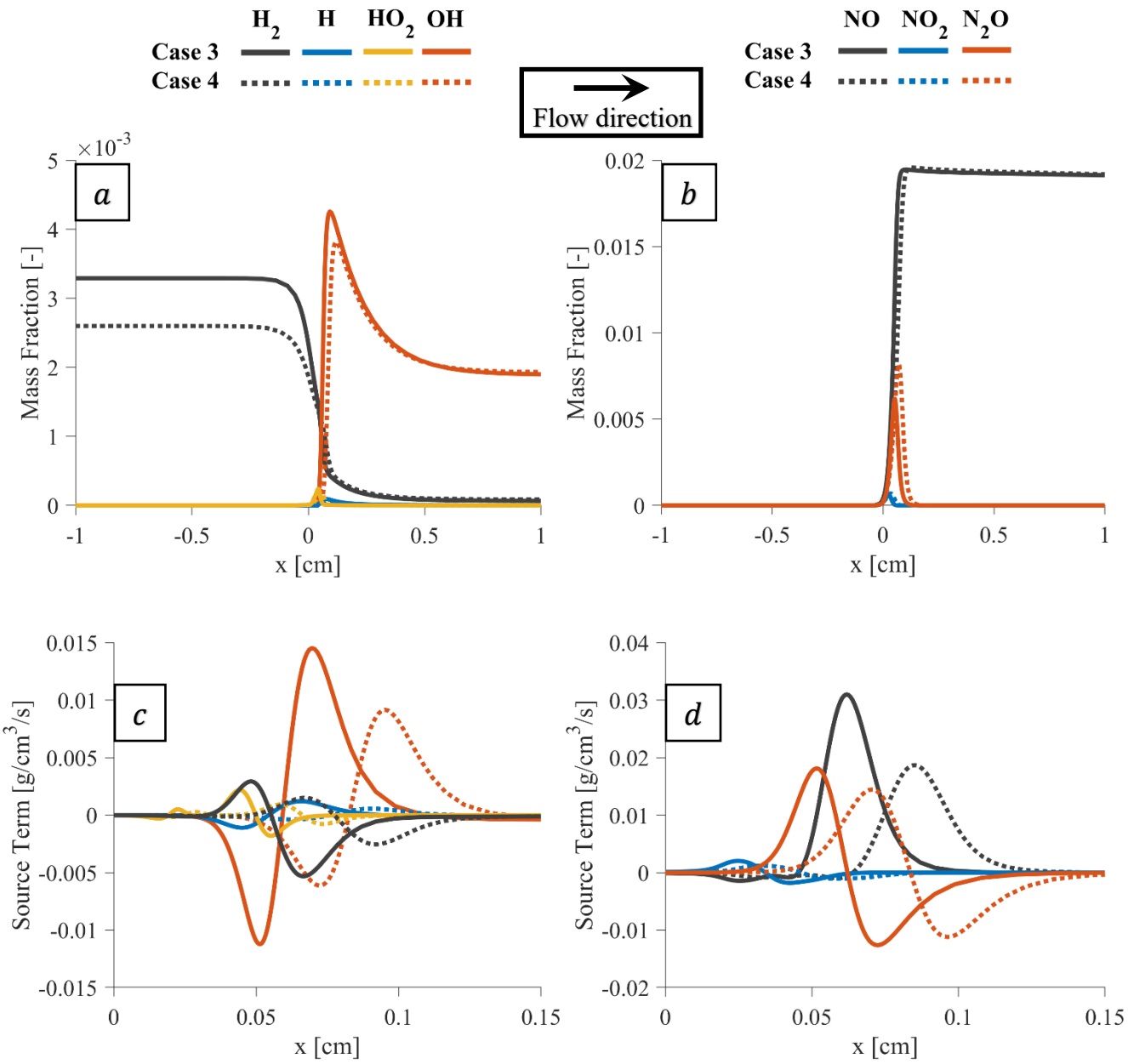

Figure 28: Distributions of H_2, NO_x and their relevant species mass fractions and source terms along the spatial coordinate between case 3 and case 4, showing the effects of increasing the ammonia addition.

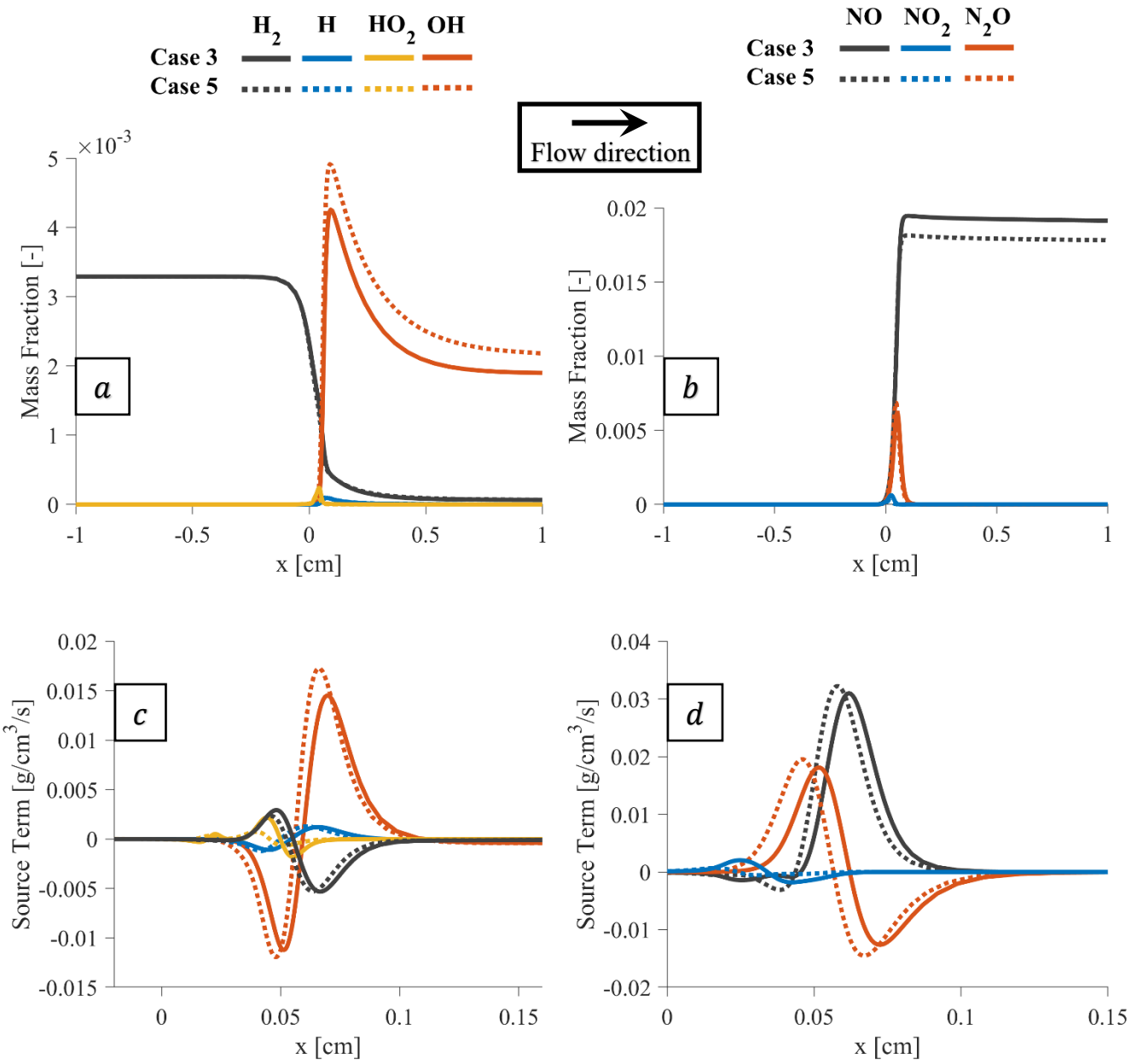

Figure 29: Distributions of H_2, NO_x and their relevant species mass fractions and source terms along the spatial coordinate between case 3 and case 5, showing the effects of potential of HVO in comparison with diesel on H_2, NO_x and their relevant species.

Figure 30 shows a comparison of the laminar burning velocity for all test cases at an initial pressure and oxidiser temperature of 1 bar and 500 K, respectively. The increase in hydrogen substitution

increased the laminar burning velocity from 73 cm/s (Case 1) to 107.5 cm/s (Case 2). This increase results from the high hydrogen-mass diffusivity, which in turn increases the diffusion velocity (calculated using Equation (3.49)) and, accordingly, the mass flow rate of the unburnt mixture. A similar argument for ammonia indicates that the low burning rate of ammonia decreases the laminar burning velocity from 45.5 cm/s (Case 3) to 34.4 cm/s (Case 4). It is encouraging that the laminar burning velocity is relatively greater with HVO compared to diesel by 2.3 cm/s. This increase with HVO is due to the higher mass flow rate, suggesting that HVO has a relatively high diffusion coefficient compared to diesel.

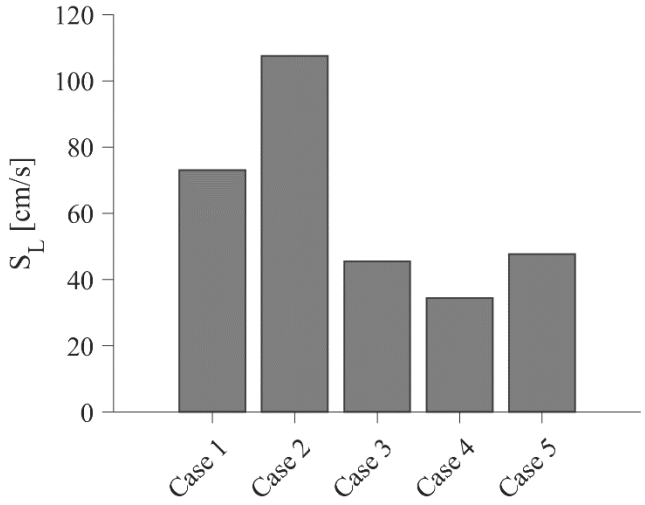

Figure 30: laminar burning velocities of all test cases at 1 bar initial pressure and 500 K initial oxidiser temperature.

Figure 31 shows the effects of different contributions of alternative fuels on flame thickness. The high-hydrogen-enriched premixed flame reduces the flame-front thickness from 0.04 cm to 0.32 cm, resulting in greater hydrodynamic instabilities. On the other hand, the increased addition of ammonia resulted in more stabilised premixed flame, whereas the hydrodynamic instability is slightly higher with HVO compared to diesel. It is important to recall that the difference in the energy share of hydrogen between Cases 1 and 2 is 53%, and the ammonia energy share between Cases 3 and 4 is 20%. Despite the large variations between hydrogen and ammonia in the

aforementioned test cases, the effects of ammonia on the hydrodynamic instabilities are greater than those of hydrogen, as the difference in the flame thickness between Cases 1 and 2 is 8.6×10^{-3} cm and between Cases 3 and 4 is 2.2×10^{-2} cm.

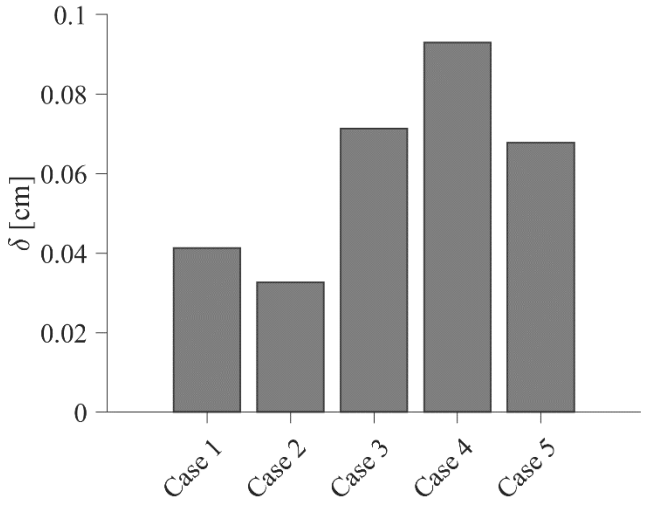

Figure 31: A comparison of flame thicknesses of all test cases at 1 bar initial pressure and 500 K initial oxidiser temperature.

4.4.2 One-dimensional laminar non-premixed flame

The following sub-sections investigate the role of preferential diffusion effects for Cases 2 and 4, the effects of initial pressure, as well as the effects of alternative fuel addition in the spatial distributions of the H_2, H, OH, HO_2, NO, NO_2, and N_2O mass fractions and source terms.

It should be noted that the generation of laminar diffusion flames is different than laminar premixed flames, as the former requires the production of many diffusion flamelets, describing the chemistry evolution from mixing state to the steady state which are represented by igniting and stationary flamelets, respectively, as aforementioned in Section (3.4.4.1). Both set of flamelets should be considered during the construction of FGM tabulations to cover all combustion phases of the mixing, ignition, and combustion process. Their effects are shown in Chapters 5 and 6 in the FGM manifold representations, as the variations of the species mass fraction and source terms are significantly affected by the initial boundary conditions, particularly in the igniting flamelets. However, only the stationary flamelets are discussed here for consistent representation between

premixed and non-premixed flames, as the incorporation of igniting flamelets requires a different illustrative style; moreover, the latter is illustrated in the following chapters.

4.4.2.1 Effects of preferential diffusion

The spatial distributions of the H_2, H, OH, HO_2, NO, NO_2, and N_2O mass fractions and source terms with and without the unity Lewis number for Cases 2 and 4 demonstrate the preferential diffusion effects on high-hydrogen and ammonia-enriched laminar diffusion flames at initial pressure of 1 bar and preheating temperature of 1,100 K, as shown in Figure 32. As mentioned in Section (4.4.1.1), the effects of flame propagation are prevalent over the preferential diffusion effects in the premixed flames, while the latter effects are predominant in diffusion flames due to the absence of the flame speed reference. As shown in Figure 32(a–b), the H_2 and H concentrations achieve higher peaks in the mixing zone with the unity Lewis number, whereas the OH maximum mass fractions are comparable between instances with and without the incorporation of preferential diffusion effects. However, by incorporating such effects, their distributions cover a broader spatial coordinate range, indicating higher chemistry rates. This observation can be clearly shown in Figure 32(c–d) because the highly diffusive species—namely H_2, H, and OH—dominate the chemically reactive effects with the non-unity Lewis number resulting in much higher chemical reaction rates caused by their greater diffusion motilities.

In contrast, the HO_2 source term shows a higher formation without incorporating the preferential diffusion effects due to its lower diffusion coefficients. On the other hand, the H_2, H, and OH mass fractions and chemistries are increased and initiated earlier, respectively, with the incorporation of preferential diffusion effects in both Cases 2 and 4. This indicates that the ignition delay is shortened with such effects. A shorter ignition delay is expected with high hydrogen enrichment due to the highly diffusive mobility of hydrogen, whereas the low reactivity of ammonia seems not to play a significant role in the ignition delay with the presence of hydrogen in the gaseous mixture. This could confirm that the ammonia dehydrogenation in ammonia-containing premixed mixtures produces hydrogen—aside from the already introduced hydrogen in the mixture. The overall hydrogen concentration, in turn, forms more light radicals compared to the pure ammonia. Thus, hydrogen along with the greater availabilities of light radicals enhance the mixing rate—leading to a more homogenous mixture—and, accordingly, the chemical reaction rate. This

argument is evident in Figure 32(d), as the OH consumption and HO_2 formation are higher with the non-unity Lewis number and, more importantly, begin prior to the hydrogen consumption. those of hydrogen near the oxidiser inlet and, then, the latter dominates throughout the domain.

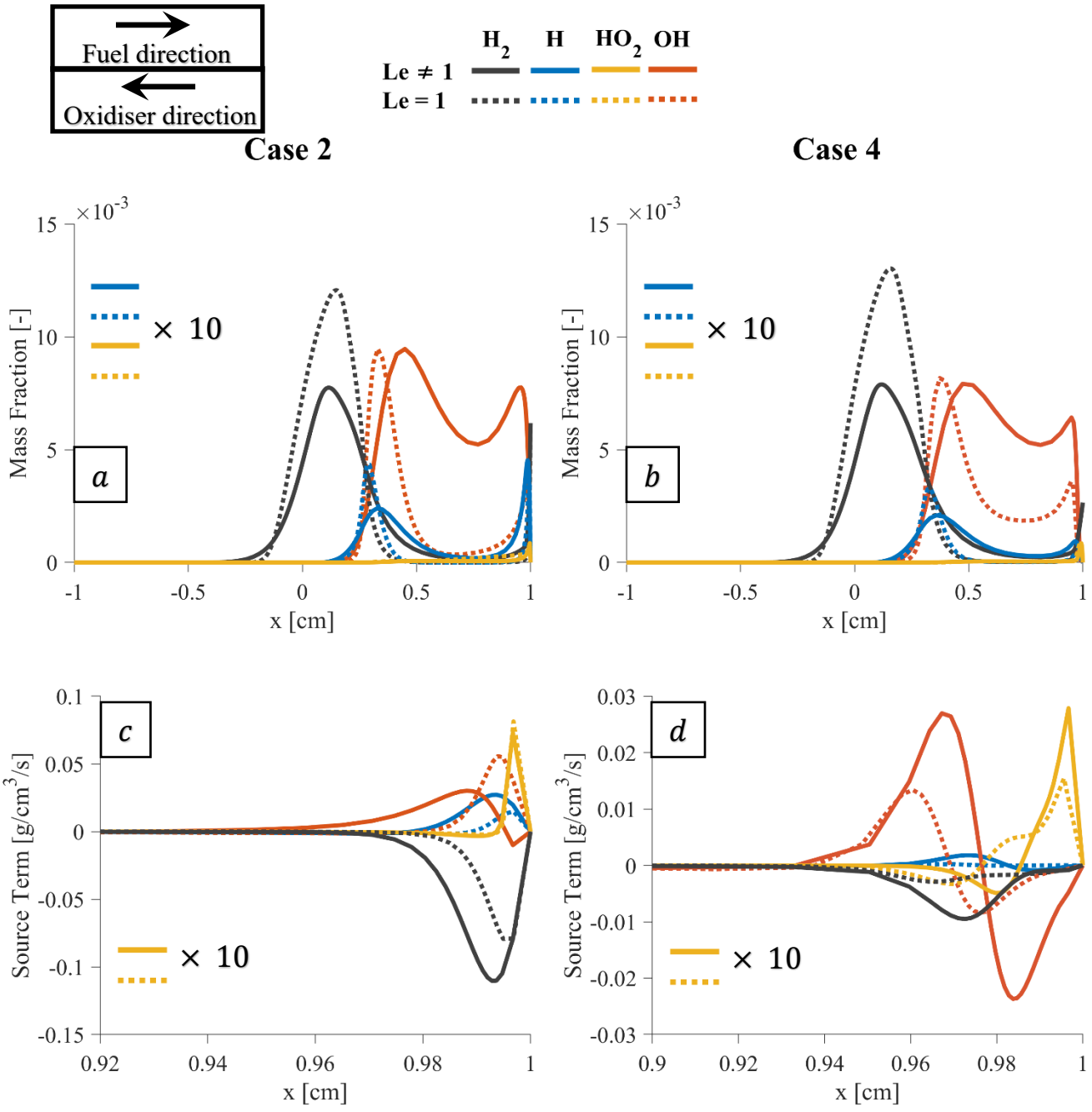

Figure 32: the spatial distributions of H_2, H, OH, HO_2, NO, NO_2 and N_2O mass fractions and source terms with and without unity Lewis number for case 2 and case 4.

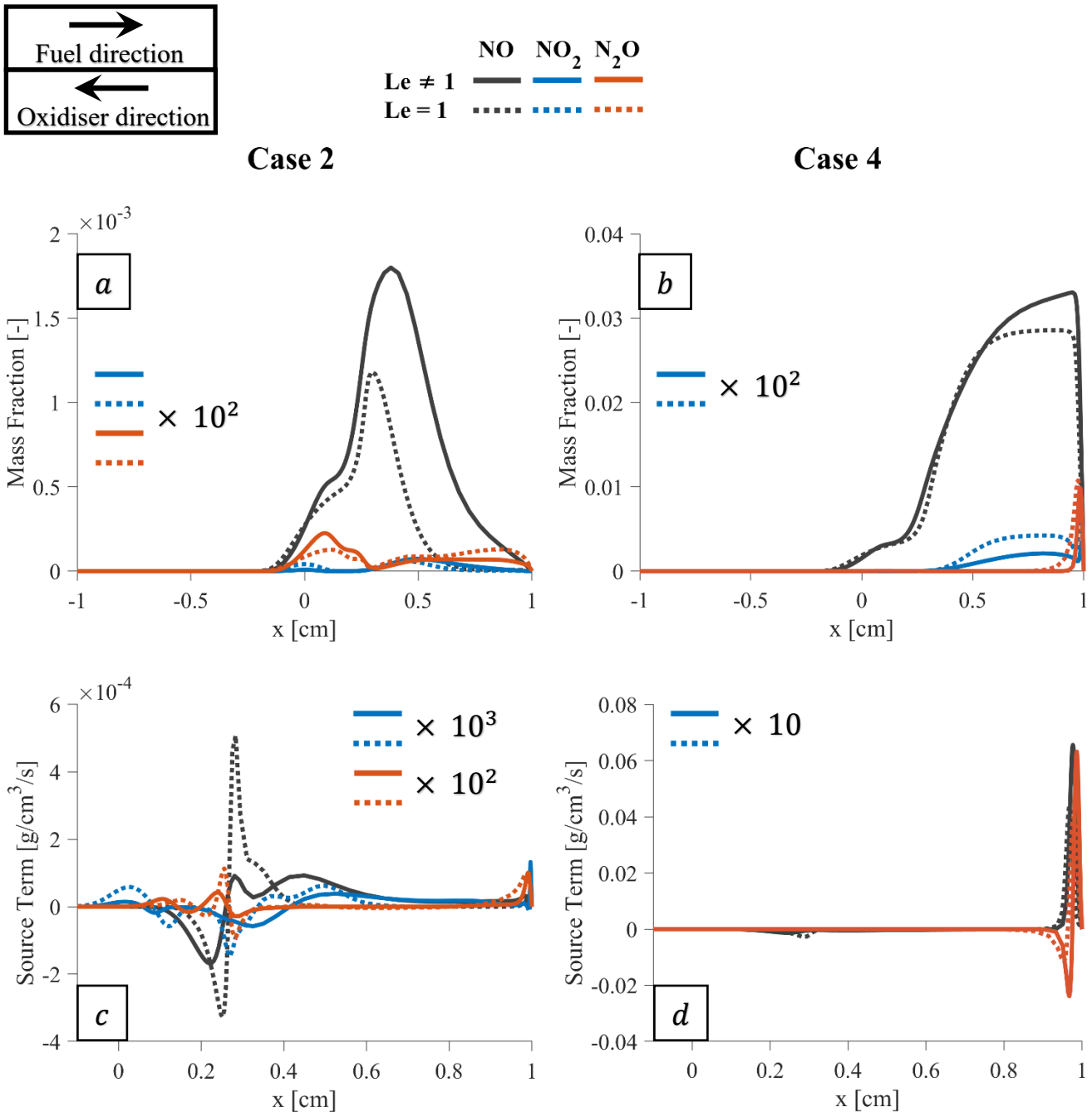

Figure 33: Distribution of mass fractions and source terms of NO, NO_2 and N_2O with respect to the spatial coordinates with and without unity Lewis number for case 2 and case 4.

This indicates that the hydrogen production rates dominate over its consumption rates due to the ammonia cracking. Furthermore, the hydrogen oxidisation and H production coincide with the OH

production and HO_2 consumption, pointing to the possible domination of the hydrogen chemistry set over that of ammonia from this region towards the fuel inlet (left side). As these trends are not similar to those obtained in Case 2, this could indicate that the relevant importance of ammonia's chemical reactions is greater than

Figure 33 shows the variations of mass fractions and source terms of NO, NO_2, and N_2O with respect to the spatial coordinates with and without the unity Lewis number for Cases 2 and 4. The role of the incorporation of preferential diffusion effects in diffusion flames is clearly demonstrated in the NO maximum mass fractions and their wider distribution in both presented cases. However, the relevant difference between the unity and non-unity Lewis numbers in terms of NO concentration peaks in the high-hydrogen-enriched non-premixed flame (Case 2) is greater than the high-ammonia-enriched non-premixed flame (Case 4), confirming the potential of the high-hydrogen-diffusion coefficient. That said, the group of NO_x species shows significantly different distributions, as their concentrations and source terms are found to be localised in the mixing and reaction spots for Case 2 and near the oxidiser inlet region for Case 4. These observations could emphasise that the NO_x formations mainly result from the high-temperature regions caused by the hydrogen combustion in highly hydrogen-added diffusion flames (see Figure 33[a–c]) and by ammonia cracking in highly ammonia-added diffusion flames (see Figure 33[b–d]).

As noted above regarding premixed flames, the highly ammonia-added diffusion flame caused the NO_x species group to achieve much greater orders of magnitude than those with high hydrogen enrichment. This confirms that the utilisation of ammonia results in worse NOx emission performance in both premixed and diffusion flames.

4.4.2.2 Effects of elevated pressure

Figure 34 shows variations of the H_2, H, OH, and HO_2 mass fraction and source terms at different initial pressure conditions in Case 1. As the effects of elevated pressure are the same for all cases, only Case 1 is discussed here; the other test cases can be found in Appendix E. As the pressure increases, the mixing and reaction zones—indicated by the increase and decrease of species mass fraction—are considerably narrower. In addition, it can be clearly seen that the trend of species mass fraction is much steeper, meaning that the mixing rate between the gaseous premixed charge

and pilot fuel along with the chemical reaction rate are highly enhanced at elevated pressure. These observations can be confirmed by the much greater fluctuations of H_2, H, and OH source terms in roughly the middle of the spatial coordinate at high initial pressure conditions. Although the increase of the hydrogen mass fraction at 1 bas prior the high-pressure conditions, it is difficult to determine whether the mixing process occurs earlier in the lower initial pressure conditions, as the data presented describes the steady-state flamelet. In counter-flow configurations, the pilot fuel and premixed mixture enter the domain from the left and right sides, respectively. Then, the pilot fuel is mixed with the gaseous mixture at the intermediate preheating temperature; this is followed by an ignition and flame diffusion towards the oxidiser inlet (right side). As shown in Figure 34(a), by considering the left side (fuel inlet) as a reference, the hydrogen mass fraction in the 1-bar case is reduced after the 20- and 40-bar cases. This means that the engine operating-pressure conditions promote the thermo-diffusive instabilities in non-premixed flames and, hence, increase the species diffusion coefficients, resulting in farther hydrogen consumption from the oxidiser inlet. That said, the H_2, H, and OH source terms fluctuate greatly in the and mixing and reaction zones in the 20- and 40-bar cases, whereas their consumption and production are greater near the oxidiser inlet. This can be attributed to the considerably narrower mixing and reaction zones at high initial pressure conditions. Notably, the aforementioned zones are tighter, and the H_2, H, and OH chemical reactivity is greater as pressure increases. However, the HO_2 mass fraction and source term are higher near the oxidiser inlet as HO_2 is considered as a product not intermediate radicals such as OH and H.

An argument similar to that for premixed flames can also be made for diffusion flames, in which the sensitivity of pressure increase is lower at higher initial pressure conditions because the relative changes between the 1- and 20-bar cases in the flame structure are much higher than those between the 20- and 40-bar cases. For the ignition delay, the peaks of species concentration in the reaction zone are earlier at higher pressure conditions and, therefore, the ignition delay seems to be shortened.

Figure 35 shows the variations of NO, NO_2, and N_2O mass fraction and source terms at different initial pressure conditions in Case 1. Similar effects of elevated pressure on hydrogen and its relevant species in terms of tighter mixing and reaction zones, higher overall chemical reaction rates, and earlier initiation of the chemistry set can be clearly seen in the NO_x-relevant species, as

demonstrated in Figure 35. As the increase of pressure enhances the chemical reaction rates, the temperature is also elevated, resulting in more NO_x pollutant emissions, as shown in Figure 35(a).

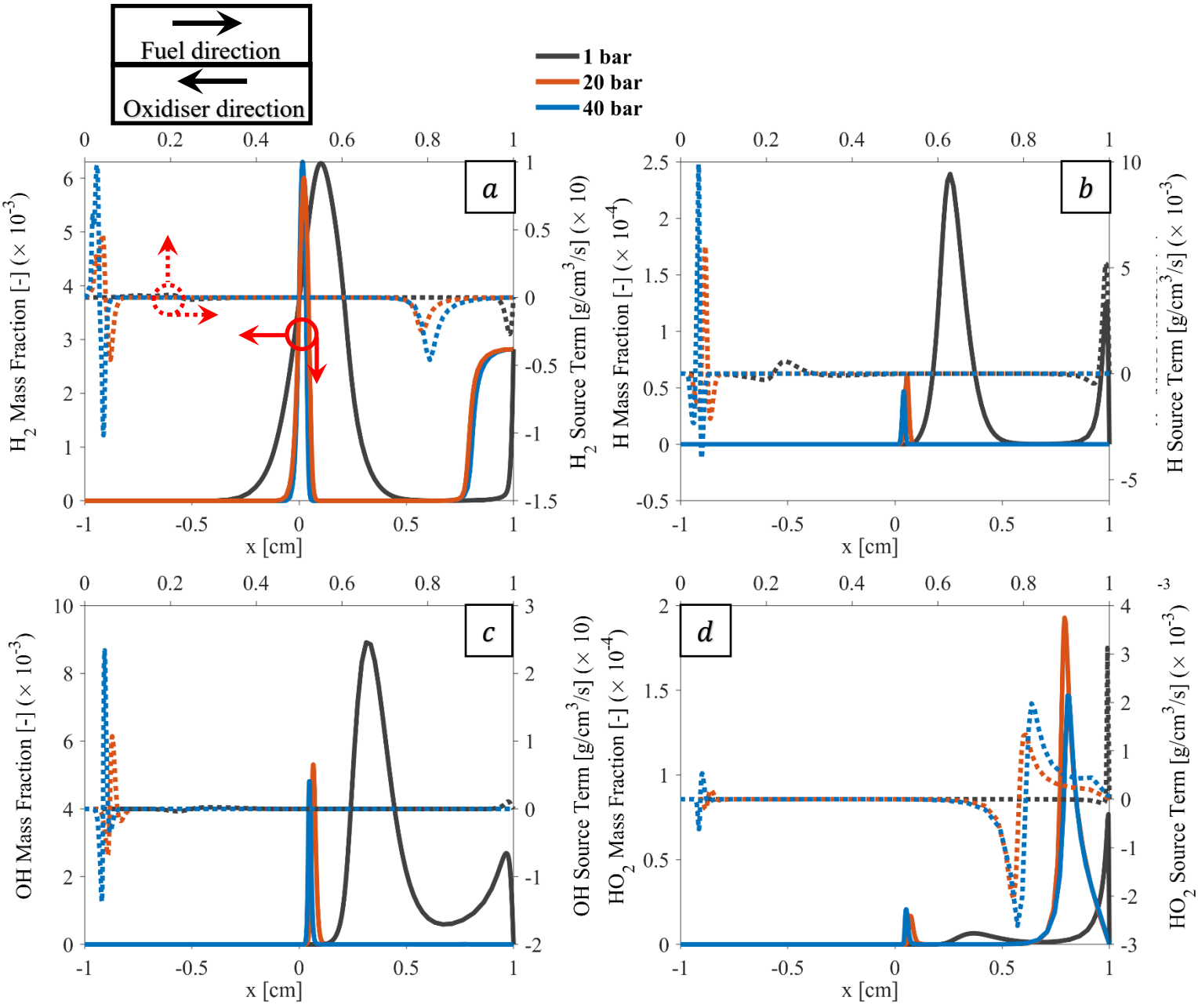

Figure 34: A comparison of H_2, H, OH and HO_2 mass fraction and source terms at various pressure levels of case 1.

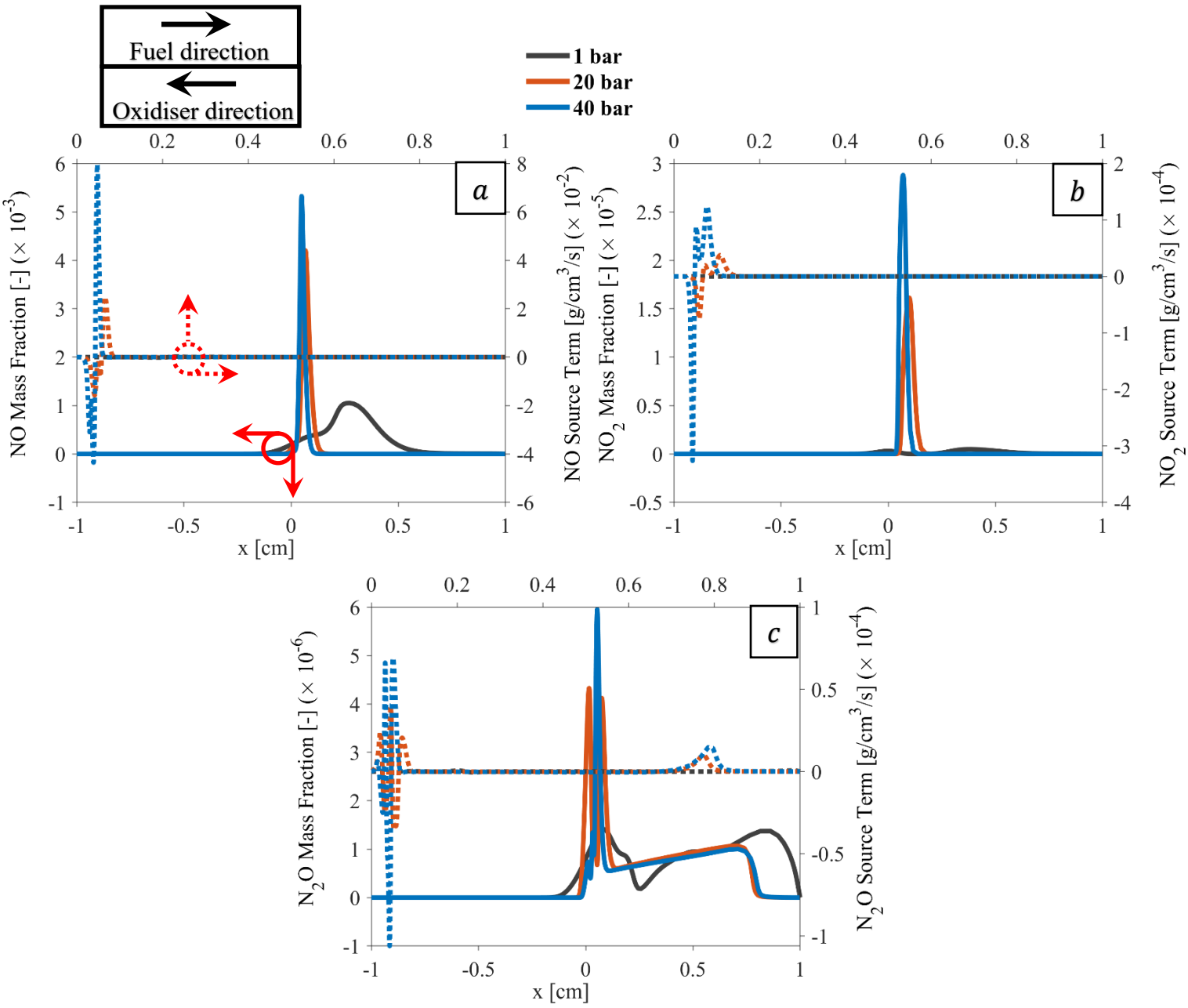

Figure 35: A comparison of NO, NO_2 and N_2O mass fraction and source terms at various pressure levels for case 1.

4.4.2.3 Effects of alternative fuel additions

Figure 36 demonstrates the variations of H_2, NO_x and their relevant species mass fractions and source terms along the spatial coordinate between Cases 1 and 2, showing the effects of increasing

the hydrogen addition. In general, the effects of pressure increase are roughly similar to those of increased hydrogen enrichment. However, both effects are different in shape and magnitude.

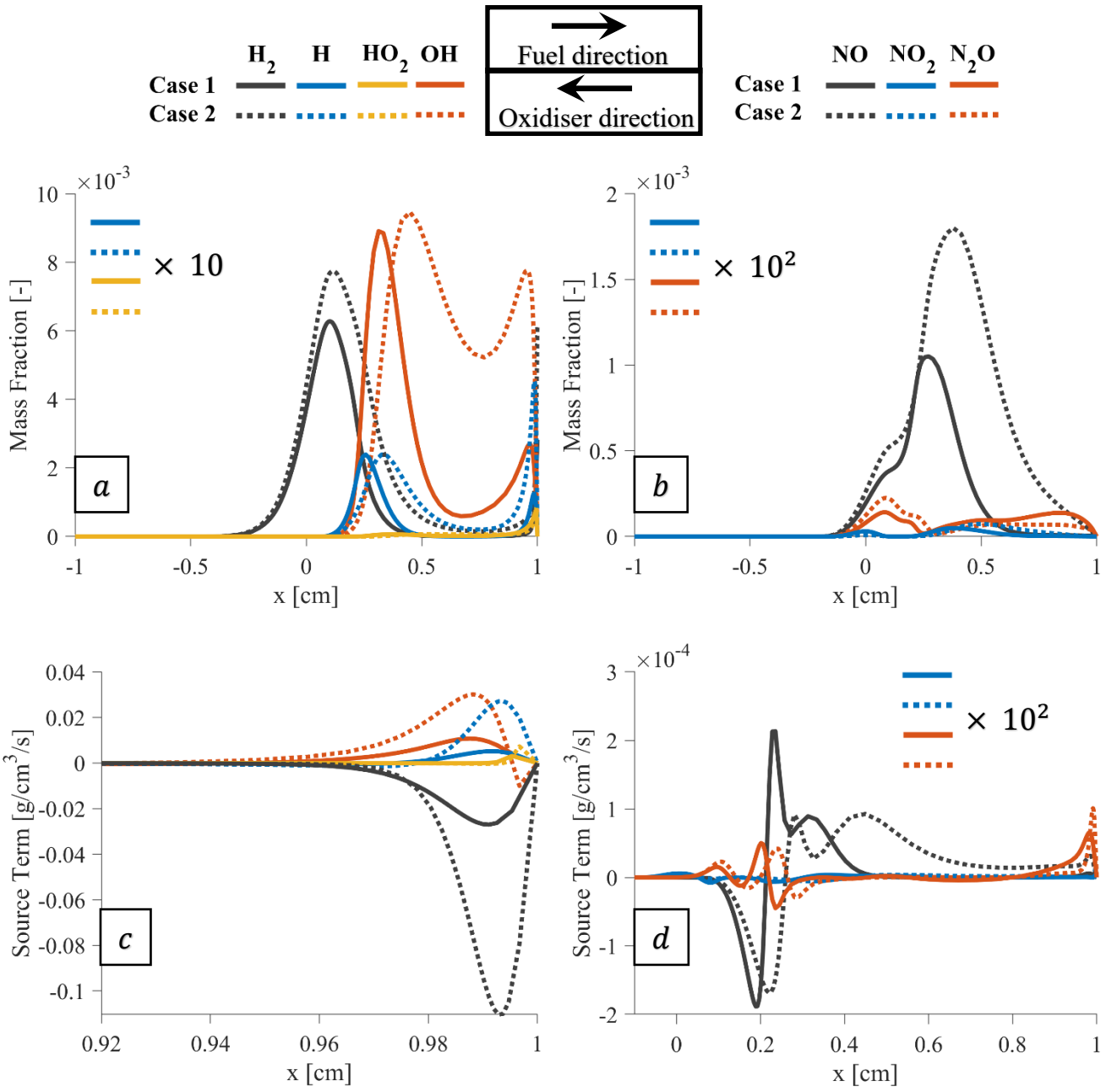

Figure 36: variations of H_2, NO_x and their relevant species mass fractions and source terms along the spatial coordinate between case 1 and case 2, showing the effects of increasing the hydrogen addition.

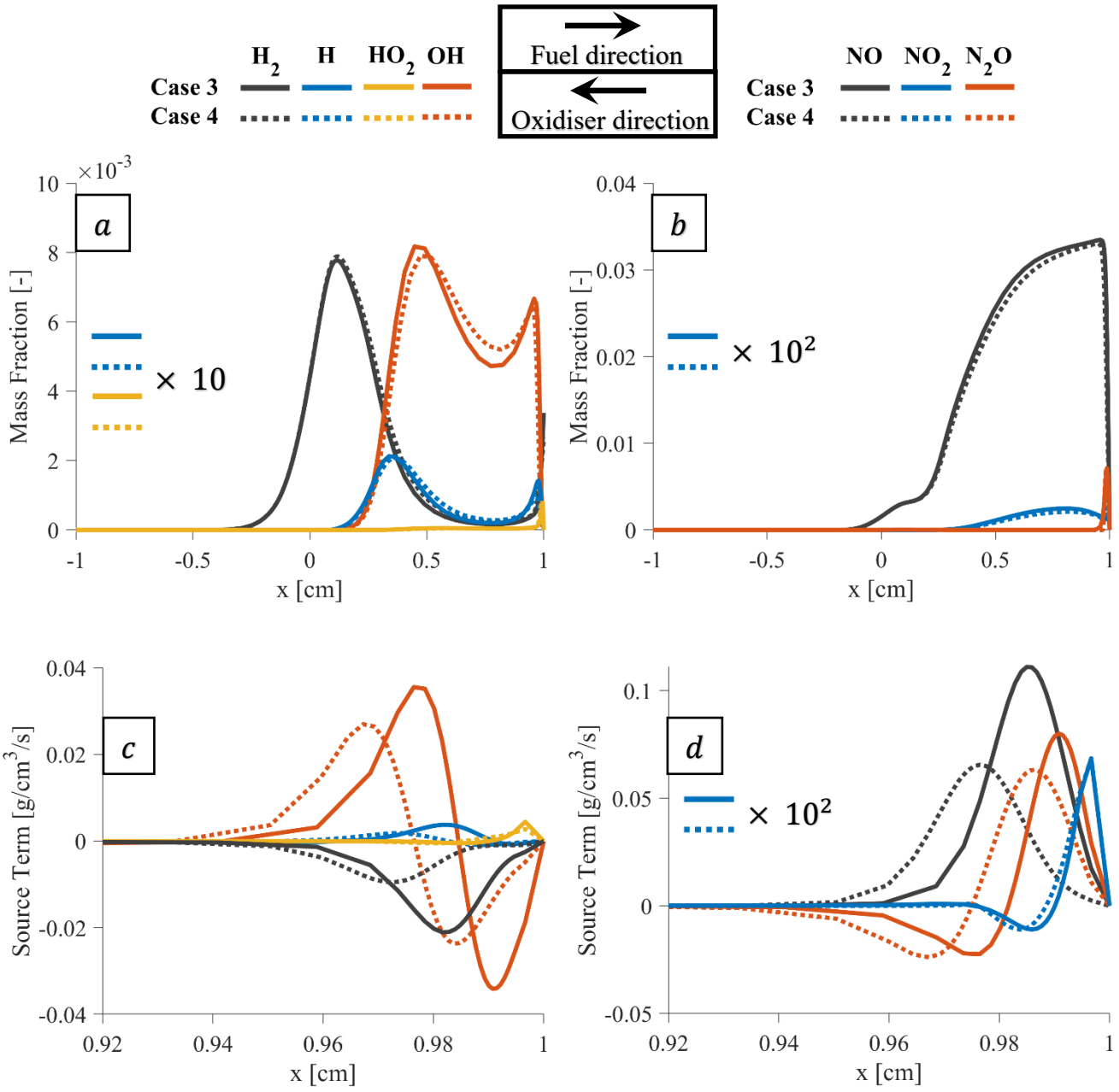

Figure 37: Distributions of H_2, NO_x and their relevant species mass fractions and source terms along the spatial coordinate between case 3 and case 4, showing the effects of increasing the ammonia addition.

For instance, the higher initial conditions of pressure promote the chemistry rate within a narrower range, whereas adding more hydrogen does the same within a wider range. As shown in Figure

36(a), the higher-hydrogen-containing diffusion flame (Case 2) expands the mixing and reaction zones, as H2, H, and OH are found to be broadly distributed with respect to the spatial coordinate in comparison to the decreased addition of hydrogen (Case 1). This indicates that the utilisation of more hydrogen results in higher chemistry rates and, in addition, that chemical reactivity covers a broader range. Figure 36(b) confirms these observations, as hydrogen and intermediate radicals achieve greater production and oxidisation values. Furthermore, the concentration of H and OH radicals are spread out to a larger degree in Case 2, pointing to higher levels of chemically reactive effects of hydrogen sub-mechanisms owing to the more hydrogen-enriched gaseous mixture.

As the overall chemical reaction rates are more significantly enhanced with the addition of high levels of hydrogen, the temperature is expected to greater, resulting in worse NO_x emission performance (as seen in Figure 36[b]). It is true that the NO sources achieve greater peaks in Case 1, as demonstrated in Figure 36(d), but its formation and consumption are high with respect to the spatial coordinate in Case 2. It is important to note that the effects of elevated pressure promote the chemistry in much higher orders of magnitude than the effects of higher hydrogen additions, as the fluctuation rates of species mass fractions and source terms are much steeper with the former effects.

Figure 37 shows the effects of ammonia-enriched diffusion flames by comparing the variations of H_2, NO_x, and their relevant species mass fractions and source terms along the spatial coordinate between Cases 3 and 4. From the steady-state flamelet data, it can be noted that the effects of ammonia addition are split into two distinct parts—before and after ignition. As seen in Figure 37(a), the species distribution in the mixing and reaction zones agree in shape and magnitude between the high- and low-ammonia-added gaseous mixtures, representing ‘before ignition.’ This can be attributed to the 5% difference in the hydrogen contribution between Cases 3 and 4, indicating the potential of hydrogen in reducing the heterogeneity of the premixed mixture and enhancing its overall reactivity in spite to the 20% difference in ammonia additions between the presented cases. In addition to this, the ammonia dehydrogenation process produces more hydrogen, which could be clearly observed in the slightly higher peak of hydrogen concentration shown in Figure 18(a) – note that ammonia has higher hydrogen atom more than hydrogen itself.

However, the low burning rate of ammonia seems to influence the flame diffusion towards the unburnt mixture. This can be confirmed, as shown in Figure 18(c–d), as the species source terms

in the higher-ammonia-enriched mixture (Case 4) fluctuates farther from the oxidiser stream inlet than those with lower ammonia additions (Case 3).

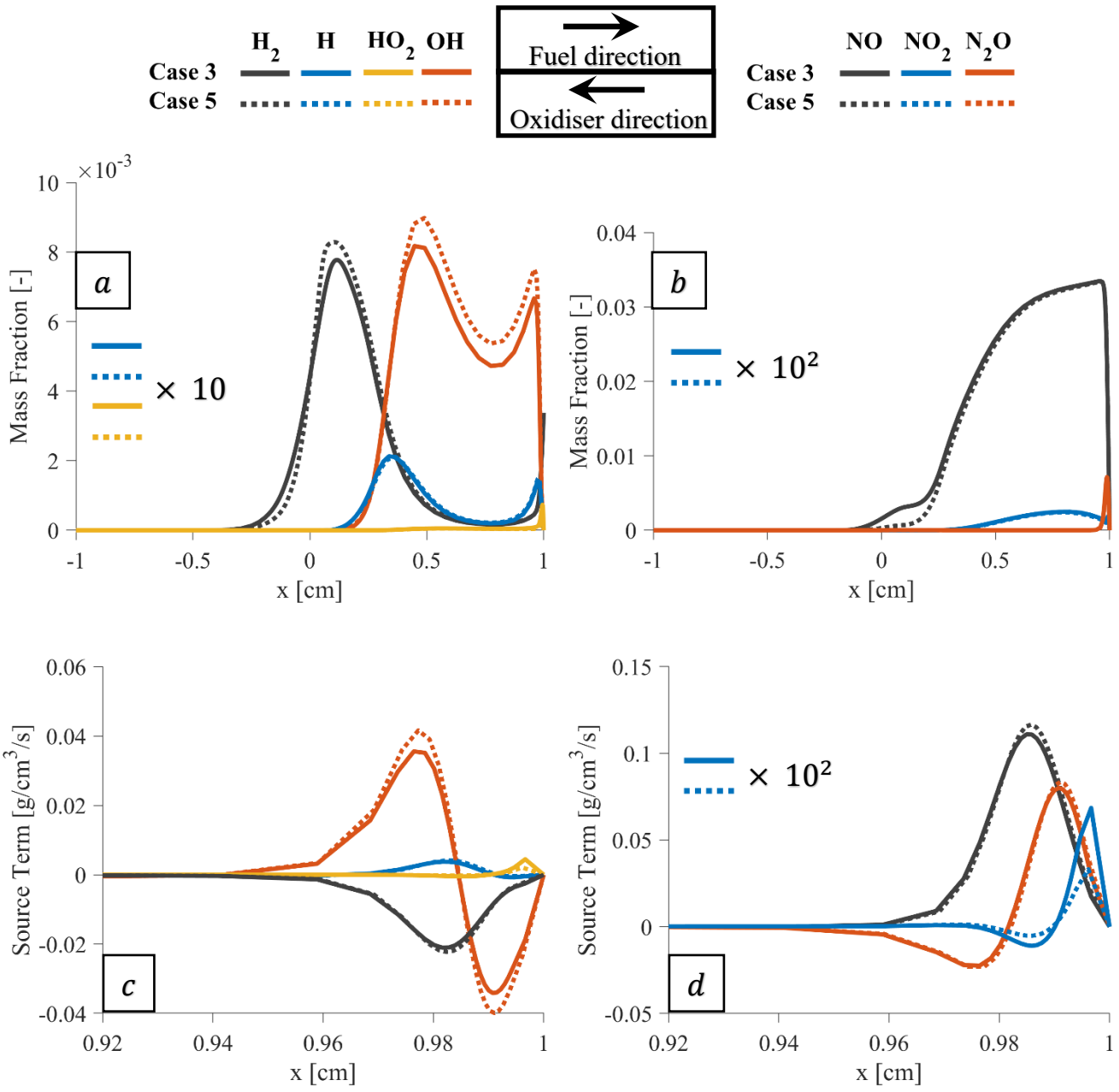

Figure 38: Distributions of H_2, NO_x and their relevant species mass fractions and source terms along the spatial coordinate between case 3 and case 4, showing the effects of HVO compared to diesel.

An elevated initial condition of pressure leads to farther hydrogen consumption from the premixed charge inlet, as mentioned in Section (4.4.1.3), indicating the increased enhancement of thermo-diffusive instabilities, which in turn increase the species diffusion coefficients. However, the relevant engine operating pressure yields steeper production and consumption of species, pointing to faster burning rates. Therefore, as the fluctuation rates of species source terms in Case 3 are closer to the oxidiser inlet and relatively more acute, it could be concluded that the burning rate is greater than in Case 4. As seen in Figure 37(b), the NO concentrations between the high and low ammonia substitutions are comparable. However, it is difficult to confirm this using only the steady-state dataset, as it is widely known that increased ammonia addition results in increased NO_x engine-out emissions. Along with this, the incorporation of the NO_x sub-model is needed for accurate NO_x predictions, which is not used in the flamelet generation.

Figure 38 shows the effects of HVO compared to diesel on the variation of H_2, NO_x, and their relevant species mass fractions and source terms along the spatial coordinate between Cases 3 and 5. In general, the effects of diesel replacement by HVO on the stationary flamelets are found to be minor. Although Figure 38 clarifies that the peak of hydrogen concentration with HVO is higher—suggesting that the utilisation of HVO enhances the mixture formation—and, in addition, its increase in the mixing zone is sharper, pointing to the possibly greater chemical reaction rate.

Furthermore, the OH mass fraction achieves higher peak and greatly spread out from the developed flame region until the gaseous mixture inlet. This can be an indication of slightly increased promotion of net chemical reaction rates with HVO due to its better mixing properties. This can be confirmed by Figure 38(c), as HVO increases the rates of OH consumption and production. In contrast to the premixed flame, the potential of HVO high cetane number along with its role in mitigating the NO_x emissions are not demonstrated in Figure 38(a–b), which are probably caused by neglecting the igniting flamelet databases.

4.4.2.4 Effects of strain rate

Figure 39 and Figure 40 illustrate the variation of H_2, NO_x, and their relevant species mass fractions and source terms over the spatial coordinate at initial strain rates of 100, 400, and 700 1/s for Case

1. For the range of mixing and reaction zones, the effects of elevated initial strain rates agree with the increase of initial pressure levels, as both effects yield narrow aforementioned zones.

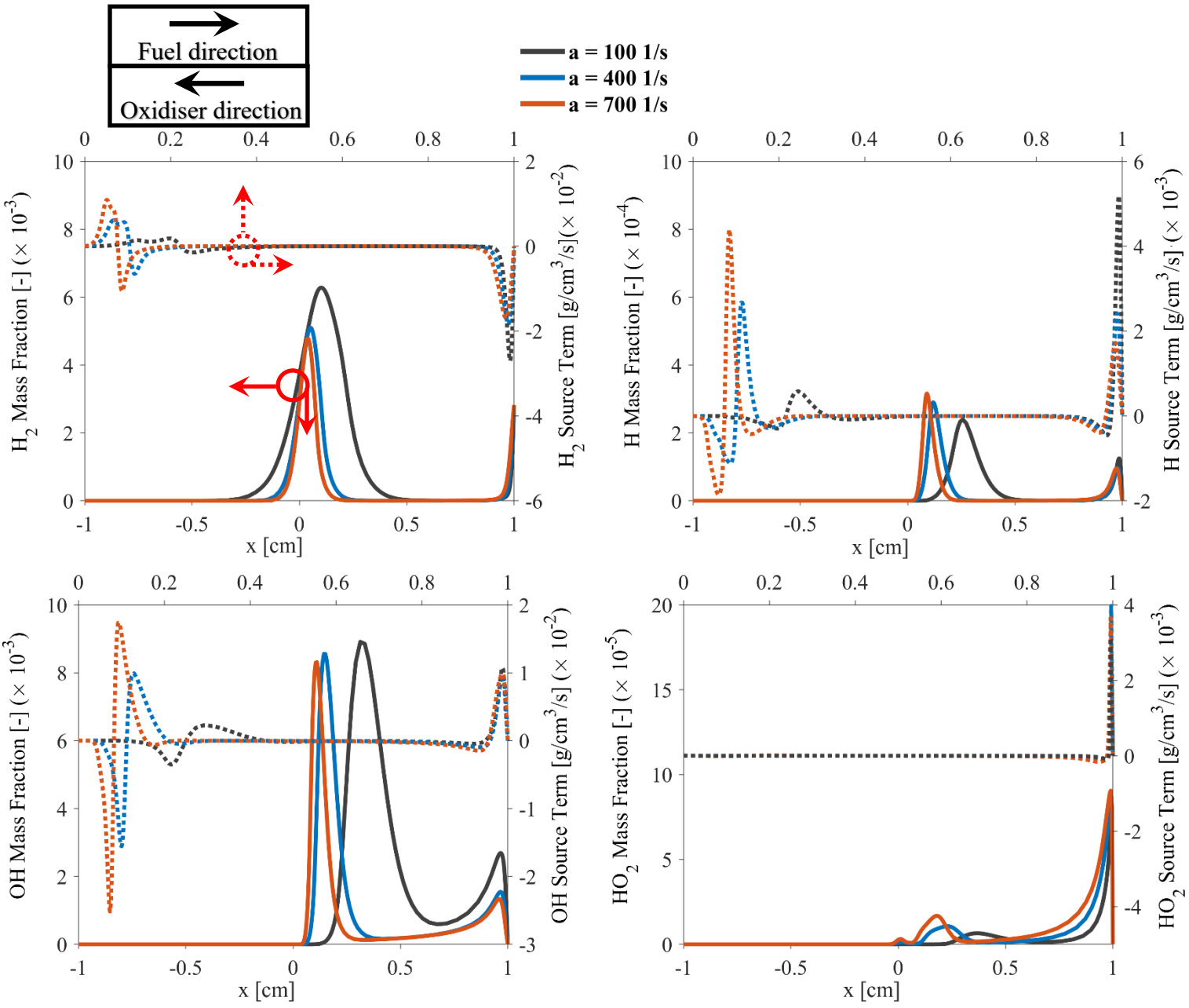

Figure 39: Effects of elevated initial strain rate on the variation of H_2 and its relevant species mass fractions and source terms over the spatial coordinate for case 2.

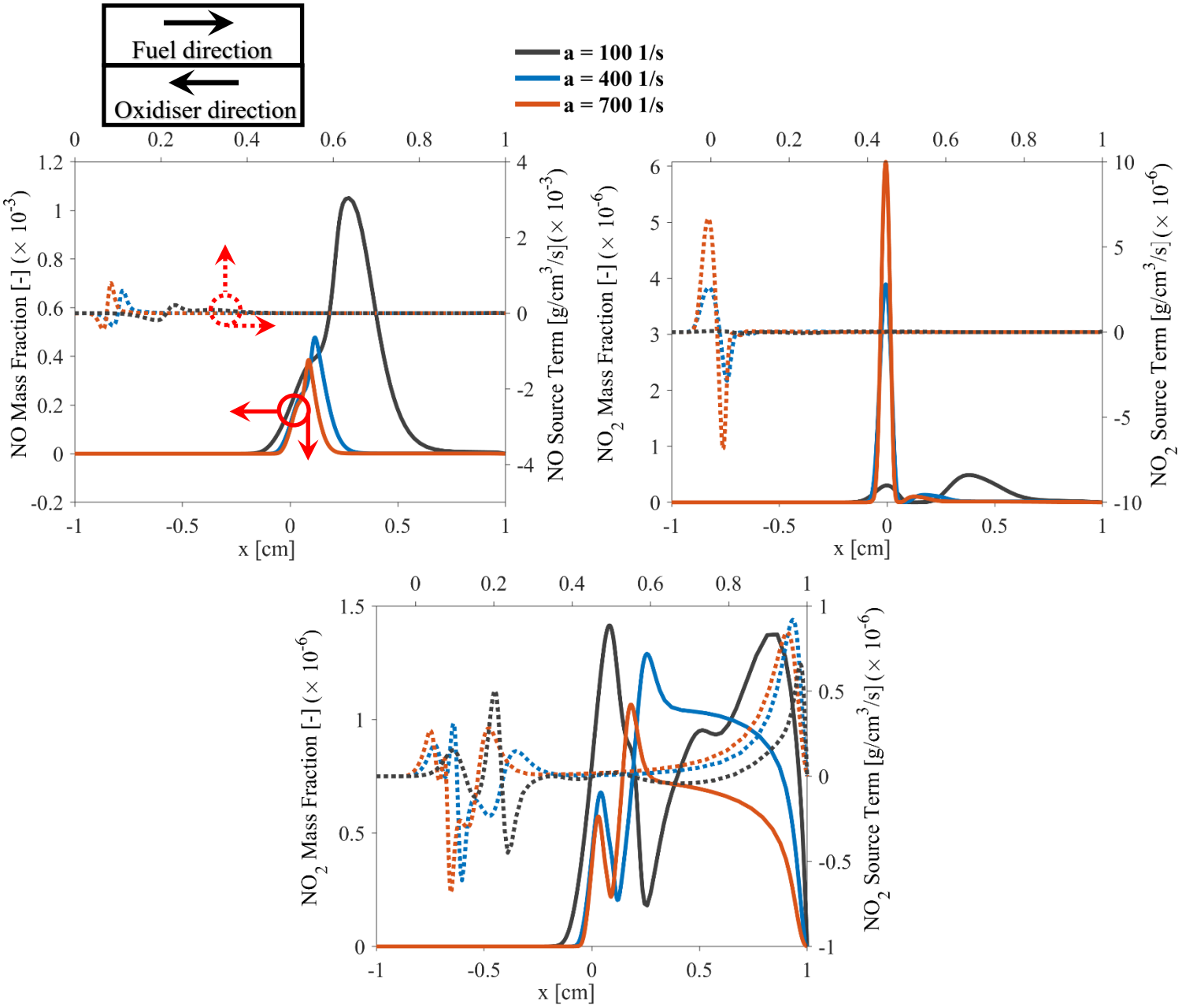

Figure 40: Effects of elevated initial strain rate on the variation of NO, NO_2 and N_2O mass fractions and source terms over the spatial coordinate for case 2.

In addition, both effects promote the net chemical rates given that the species oxidisation and production are in larger degree as seen in Figure 34 and Figure 35 for higher pressure levels and in Figure 39 and Figure 40 for elevated strain rates. However, the difference between these effects lies in the temperature, where the temperature is increased with higher pressures and decreased

with higher strain rates. The temperature trends are not covered in the investigations, but they can be easily concluded from the peaks of NO concentration, as it is higher with an increase in pressure (see Figure 35) and lower at higher strain rates (see Figure 40). This conclusion relies on the fact that the NO formations in hydrogen-content mixtures are mainly caused by high-temperature regions, as discussed in Section (4.4.2.1). The reduced temperature in the reaction zone even with higher fluctuations of species source terms at elevated strain rates are caused by the difficulty of chemical reactions in keeping up with the rate at which fuel and oxidiser enter the reaction zone [111]. Therefore, the chemistry becomes unable to burn the incoming reactants in the reaction zones, resulting in a leakage of more fuel and oxidiser across the reaction zone. This leakage is caused by the shorter residence time of radical species resulting from a higher strain-rate environment [143].

4.5 Conclusions

In this chapter, intensive one-dimensional laminar investigations were carried out to deeply assess combustion and emission characteristics of hydrogen blended one-dimensional laminar premixed and diffusion flames under engine relevant conditions relevant to DF engine combustion. The parametric study was performed using the one-dimensional chemical kinetics code, CHEM1D. For both the premixed and non-premixed flames, the flame structure by means of demonstrating the variations of H_2, H, OH, HO_2, NO, NO_2, and N_2O with respect to the spatial coordinate to cover the hydrogen and NO_x sub-mechanisms was analysed. Furthermore, in the premixed-flame analysis, the laminar burning velocity and thermal diffusion coefficients were discussed due to their major roles in characterising many premixed flame phenomena and indicating hydrodynamic instabilities, respectively. These analyses were computed at elevated pressures, ranging from 1 to 40 bar, to investigate the premixed flame and non-premixed flame flames at relevant engine-operating conditions. The preferential diffusion effects were examined by carrying out two simulations with and without the unity Lewis number assessing such effects with the presence of a high-diffusion-coefficient fuel like hydrogen. The effects of more hydrogen- and ammonia-enriched gaseous premixed mixtures along with the potential of utilising a renewable diesel-counterpart alternative fuel (HVO) were discussed. For the premixed flames, the initial conditions of the unburnt-mixture temperature were varied to set an instability threshold for both initial

pressure and oxidiser temperature due to the instabilities observed at high conditions of these variables. For the non-premixed flame, the analysis was carried out at different initial strain rates ranging from 100 to 700 1/s to demonstrate the effects of strain rate on the mixing and reaction zones due to its importance in enhancing these zones by the flow-velocity gradient in a mixing-controlled type of flame.

The main findings of the study are outlined below.

Laminar premixed flames.

1. The incorporation of preferential diffusion effects in the premixed flame results in an earlier take-off of the chain of chemical reactions in the greater-hydrogen-enriched gaseous mixtures owing to the high hydrogen burning rate. The low laminar burning velocity of ammonia yields a farther chemical activation from the premixed mixture inlet with such effects. Furthermore, the preferential diffusion effects demonstrate that the chemically reactive effects are found to be in a broader spatial coordinate range regardless of the concentration of hydrogen and ammonia in both premixed and diffusion flames, confirming the roles of light-intermediate radicals in enhancing chemistry in the reaction zone. The unity Lewis number assumption in premixed flames produces non-physical oxidisations and productions of OH, along with NO mass fraction trends, leading to an over-prediction of their quantities.
2. The elevated oxidiser temperatures cause the premixed flame to be unstable at relevant engine operating pressure, as the 20- and 40-bar cases are unstable at an initial oxidiser temperature of 1100 K. Only the 40 bar show instabilities at an initial oxidiser temperature of 700 K. The conclusion to draw from these observations is that there are correlated effects between the initial conditions of pressure and oxidiser temperature in enhancing the instability of the premixed flames. Aside from the flame-front cracking induced by the flame instabilities at higher pressure levels, the high pre-heating oxidiser temperature applied to the high fuel burning rate (hydrogen) significantly promotes the premixed flame instabilities. The increase in temperature for a given pressure causes the laminar burning rate to increase due to the greater unburnt-mixture enthalpy and mass flow rate and lower unburnt density.

3. For premixed flames, the effects of increase in pressure turn out the preheating and reaction zones to be quite narrower, shift them towards the premixed mixture inlet and significantly enhance the net chemical reaction rates. Correspondingly, the temperature is increased, which could be indicated by the higher NO_x emission levels at elevated pressure. The initial increase in pressure decreases the laminar burning velocity due to the greater unburnt-mixture density and mass flow rate. The sensitivity of an increase in pressure becomes less at higher levels, as the relative changes in the flame structures and laminar burning velocities between the 1- and 20-bar cases are considerably greater than those between the 20- and 40-bar cases.
4. The increased hydrogen-enriched premixed flame causes the concentration of highly reactive radicals to increase and also shortens the ignition delay. For chemistry, the increased hydrogen addition expands the reaction zone and enhances the species oxidisation and production, indicating an enhancement of the overall chemistry rates. The NO_x mass fraction peak is higher with more hydrogen enrichment due to the higher temperature resulting from the hydrogen combustion. OH dominate the reactive effects compared to H and HO_2 because of its greater order of magnitude in both mass fraction and source term distribution.
5. The effects of more ammonia additions are found to be opposite to those of more hydrogen additions due to the former's low burning rate. However, the group of NO_x species achieves much higher mass fraction peaks in with increased ammonia-added premixed flame owing to the greater nitrogen availability from the ammonia dehydrogenation process and indicating that the NO_x performance emissions are worse with ammonia than hydrogen. However, the NO_x emission levels are comparable between the high- and low-ammonia-containing premixed flames in the laminar calculation due to the absence of incorporating thermal and prompt NO_x formations.
6. The replacement of diesel by HVO increases the concentration and chemistry reactivity of the light radicals, pointing to the increased promotion of chemical reaction rates. In addition, the initiation of chemistry is earlier with HVO, indicating a shorter ignition delay owing to the high cetane number of the HVO. The NO_x pollutant emissions are lower with HVO, suggesting that the HVO is more environmentally benign compared to diesel.

Laminar diffusion flames.

7. Apart from the species concentration peaks, the incorporation of preferential diffusion effects in both higher ammonia and hydrogen enrichment clearly results in broader distributions in terms of species mass fractions and source terms, indicating much higher chemical reaction rates. In both test cases, the NO maximum mass fraction and its distribution are greater when accounting for such effects. In the high-hydrogen-content gaseous mixture, the NO_x species group are produced in in the reaction zone due to the hydrogen combustion. In contrast to this, the chemistry of the NO_x species group are highly reactive near the oxidiser inlet, indicating that NO_x emissions are predominantly caused by ammonia cracking in ammonia-enriched diffusion flames. Similar to the premixed flames, the NO_x species group achieve much higher concentrations, emphasising that the NO_x emissions is worse with the utilisation of ammonia compared to hydrogen in both flames.
8. The increase in pressure results in tighter mixing and reaction zones; furthermore, the mixing and chemistry rates are much greater, resulting in sharper trends of species concentrations. The species diffusion coefficients are found to be increased due to the increased promotion of the thermo-diffusive instabilities at higher pressure levels, resulting in farther hydrogen consumption from the oxidiser inlet. The NO_x pollutant emissions are greater with the increase in pressure due to the higher temperature resulting from the higher rate of chemistry.
9. The greater hydrogen-containing mixture results in wider mixing and reaction zones. In addition, the increase in hydrogen energy share causes the concentrations of light radicals to spread out to a larger degree and promotes chemistry rates, leading to more NO_x engine-out emissions.
10. In the mixing and reaction zones, the high- and low-ammonia-added mixtures agree in shape and magnitude, indicating that the presence of hydrogen in the gaseous charge enhances the mixing rate due to its high diffusivity regardless of the ammonia concentrations. However, the low burning rate of ammonia seems to influence the flame diffusion towards the gaseous mixture due to the farther chemical reactivity of species from the oxidiser inlet along with its relatively less steep trends with higher ammonia enrichment.

11. The effects of HVO utilisation in the steady-state flamelet are minor compared to diesel. However, the OH mass fraction achieves a higher peak and greatly spread out from the developed flame region until the gaseous mixture inlet, pointing to a possibly higher chemical-reaction rate.
12. The increase in initial strain rates results in higher fluctuations of species oxidisation and production, resulting from the increased enhancement of mixing layer by the greater flow velocity gradient. However, the low concentrations of NO_x species group at elevated strain rates are an indication of lower temperature. This is caused by the low capability of chemistry to burn the incoming reactant to the reaction zone due to the shorter residence time.

Chapter 5: Modelling and Simulation of Diesel-Hydrogen Dual-Fuel Combustion: FGM hybrid combustion model validation and the role of preferential diffusion on hydrogen blended dual-fuel combustion

5.1 Introduction

The combustion and emissions modelling of DF combustion systems have been studied using various different combustion models. For example, the literature indicates DF combustion modelling and simulation studies using different combustion models such as the SAGE finite rate detailed chemistry solver [91] [75] [92], species transport model with final rate chemistry [94] [95] [96], partially stirred reactor (PaSR) combustion model [158], 3-Zones extended coherent flame model [72] [97] and multi-zone combustion model [159].

Though great efforts have been made in modelling, comprehensive simulations of hydrogen blended diesel DF combustion are highly desirable to explain the complex multistage process of dual fuel combustion. For example, in the diesel-hydrogen DF flame, the heat release process can be classified into three modes; (1) the ignition of the pilot diesel fuel, (2) the combustion of the pilot diesel fuel with some hydrogen available within the diesel spray plume, (3) the combustion of hydrogen-air premixed mixture [160]. Therefore, the interplay between non-premixed combustion mode of the pilot liquid fuel and premixed combustion mode of the gaseous-air mixture presents a challenge for above noted combustion models to better capture the combustion characteristics of diesel-hydrogen DF combustion. For example, the recent investigation carried out by Tuchler et. al. [161] have highlighted that the multi-zone combustion model struggles to accurately predict hydrogen entrainment resulting in under-prediction of peak values of in-cylinder pressure and heat release rate in diesel-hydrogen DF combustion process. This finding highlights

the importance of considering a comprehensive combustion model to simulate high hydrogen content diesel-hydrogen DF engine combustion.

Another crucial factor to be considered is preferential diffusion effects which is an important physical phenomenon for combustion and heat release of hydrogen-blended fuels in both premixed [100] and non-premixed combustion modes [162]. Preferential diffusion is usually described by the Lewis number, Le, defined as the ratio of thermal to mass diffusivity. Non-unity Lewis number leads to preferential diffusion between chemical species as well as between species and heat. Our previous investigations found that the high diffusivity of light chemical species such as atomic hydrogen (H) and H_2 affects high hydrogen content fuel burning, flame propagation speed and heat release through preferential diffusion in engine relevant conditions, for example high turbulence and elevated pressures [100] [101]. Although, most of the aforementioned modelling studies focused on diesel-hydrogen DF combustion modelling with unity Lewis number assumption, there is still lack of fundamental understanding of preferential diffusion effects on combustion characteristics of hydrogen blended diesel-hydrogen DF combustion. There is a research gap in a detailed explanation of preferential diffusion effects on in-cylinder pressure, temperature, auto-ignition and chemical species formation such as unburned hydrogen and NOx emissions of hydrogen blended diesel-hydrogen DF combustion engines.

The objective of this chapter is to apply the novel hybrid combustion model based on Flamelet Generated Manifold (FGM) incorporating preferential diffusion effects discussed in the methodology chapter to predict a multistage process of high hydrogen content diesel-hydrogen DF combustion. The FGM technique enables reliable CFD predictions of combustion process incorporating detailed chemical reaction mechanisms with significantly low computational cost. The FGM combustion model has been extensively used to simulate turbulent premixed [119], non-premixed [120] and partially premixed flames [121]. However, the FGM combustion modelling approach coupling with preferential diffusion effects has not been applied to simulate hydrogen blended DF combustion process.

As discussed in the methodology chapter, the innovative interest of this study is the further improvement of the FGM combustion model to simulate high hydrogen content diesel-hydrogen DF engine combustion by means of three-dimensional FGM in which the pre-computed chemistry databases is a function of mixture fraction (representing the stratification effects), progress variable

(representing the chemistry evolution) and enthalpy (representing the heat loss) with the incorporation of preferential diffusion effects (representing the high diffusivity of hydrogen). The emphasis is put on assessing and interpreting applicability of the modified FGM hybrid combustion model coupling non-premixed flamelet generated manifold and premixed flamelet generated manifold with preferential diffusion effects to capture the multistage process of high hydrogen content diesel-hydrogen DF engine combustion. The modelling framework is validated against the experimental data of high hydrogen content diesel-hydrogen DF engine combustion carried out by Tsujimura et al. [52]. The incorporation of preferential diffusion effects is demonstrated by performing simulations with the unity Lewis number approach and the non-unity Lewis number approach. The work quantifies preferential diffusion effects on in-cylinder pressure, heat release rate, temperature, auto-ignition and radical chemical species formation such as unburned hydrogen and NOx emissions of high-hydrogen content diesel-hydrogen DF combustion. The results also contribute to improving modified FGM hybrid combustion model capability to predict dual-fuel combustion process, auto-ignition characteristics and species concentrations of pollutant emissions of dual-fuel combustion engines. The proposed modelling framework can be effectively used to accurately predict the combustion characteristics of hydrogen fuel blends with green alternative fuels such as ammonia and bio-fuels as well as conventional fuels such as natural gas operating under dual-fuel engine combustion mode.

5.2 Numerical setup

In the present study, we employed the single cylinder diesel-hydrogen DF compression ignition engine configuration experimentally conducted by Tsujimura et al. [52]. The newly extended FGM hybrid combustion model was applied to simulate two cases: pure diesel case with no hydrogen energy share (0% HES) and diesel-hydrogen DF case with 73% hydrogen energy share (73% HES) at high load condition (i.e. Case 2 in Table 5, Chapter 4). This engine configuration has been employed in our previous numerical study of diesel-hydrogen DF engine performance and emissions under a novel constant volume combustion phase [96]. Table 6 provide the engine specification and experimental conditions of pure diesel (0% HES) case and diesel-hydrogen DF case (73% HES) at high engine load [52].

Engine type		**Single cylinder**	
Displacement volume (L)		1.3	
Bore × stroke (mm)		115 × 125	
Compression ratio		17.5:1	
Fuel		Diesel fuel (direct injection)	
		Hydrogen (Port injection)	
Engine speed (RPM)			1500
Indicated mean effective pressure (MPa)			0.9
Maximum hydrogen fraction (input energy base) (%)			73
Intake gas pressure (kPa)			160
Intake Oxygen (O_2) concentration by volume (%)			18.6
Diesel fuel injection	Pattern	Double (pre/main)	
	Timing (deg. CA) ATDC	Pre	-9.9
		Main	6.1
	Quantity (mm^3/cycle)	Pre	1.2
		Main	76-21
	Pressure (MPa)		116

Table 6: Diesel-Hydrogen dual fuel compression ignition engine specification and experimental conditions [52].

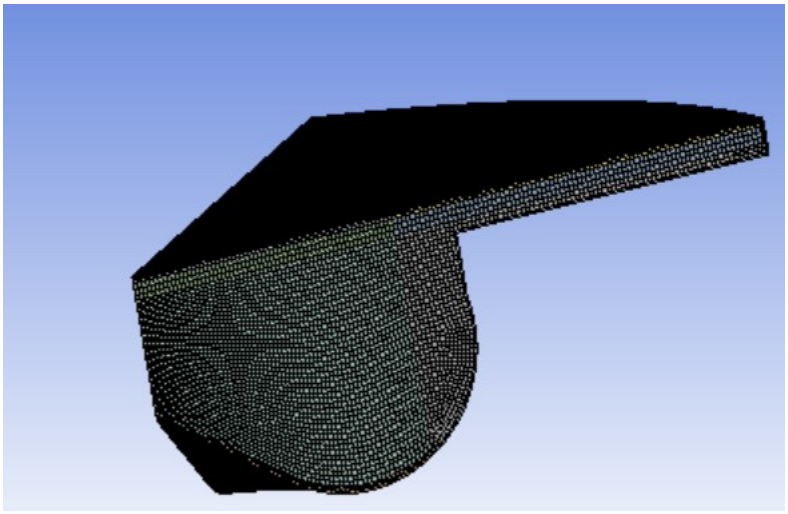

Figure 41: The section of the numerical grid at Top-dead centre (TDC).

The FGM implementation follows the procedure explained in Section (3.4.4). As seen in Figure 41, a sector of 51.43 degree consisting of one injector is used as it represents a portion of a full engine with 7 injectors. The geometry consists of 1,190,215 elements. The mesh density, meshing process, models related to the diesel-like fuel injection, discretisation schemes and solver algorithm solution method are presented in Section (3.7).

5.3 Results and discussion

In this study, novel modifications to the flamelet generated manifold combustion model coupling non-premixed combustion mode and premixed combustion mode were carried out to simulate the hybrid combustion process of diesel-hydrogen dual-fuel combustion. The model also incorporated preferential diffusion effects to identify its influence on predicting the combustion characteristics of high hydrogen content dual-fuel combustion process. The importance of considering preferential diffusion effects in the FGM hybrid combustion model to predict the combustion characteristics of high hydrogen content dual-fuel combustion process is demonstrated by comparing numerical simulations with and without Lewis number effects.

The following sections discuss the premixed and diffusion FGM manifolds, validation of the FGM hybrid model with the experiential data and the role of preferential diffusion on combustion characteristics of high hydrogen content diesel-hydrogen dual-fuel combustion process.

5.3.1 Premixed and diffusion FGM manifolds

Figure 42 and Figure 43 show non-premixed and premixed manifolds for temperature and species concentrations of OH (hydroxyl), H_2 and H radicals as a function of the mixture fraction and progress variable obtained from the one-dimensional flamelet calculations for the diesel-hydrogen DF test case with 73% HES. The FGM premixed and non-premixed manifolds were obtained using unity and non-unity Lewis number approaches. The FGM non-premixed manifolds were generated using 133 flamelets while FGM premixed manifolds were created using 8 flamelets for a limited mixture fraction range.

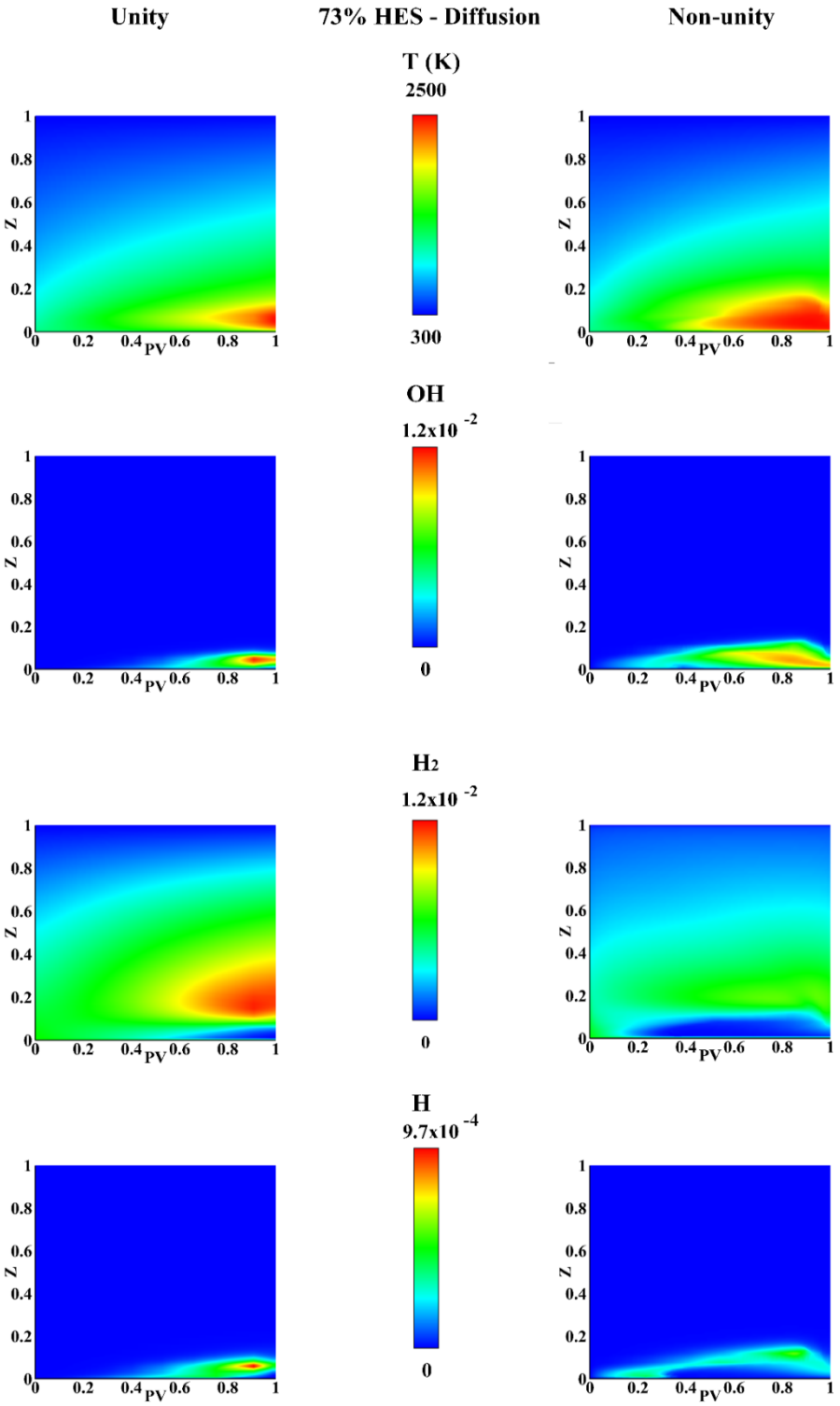

Figure 42: Non-premixed manifolds for temperature, OH, H_2 and H with unity Lewis number (left) and non-unity Lewis number (right) as a function of the mixture fraction and progress variable for the diesel-hydrogen case with 73% HES.

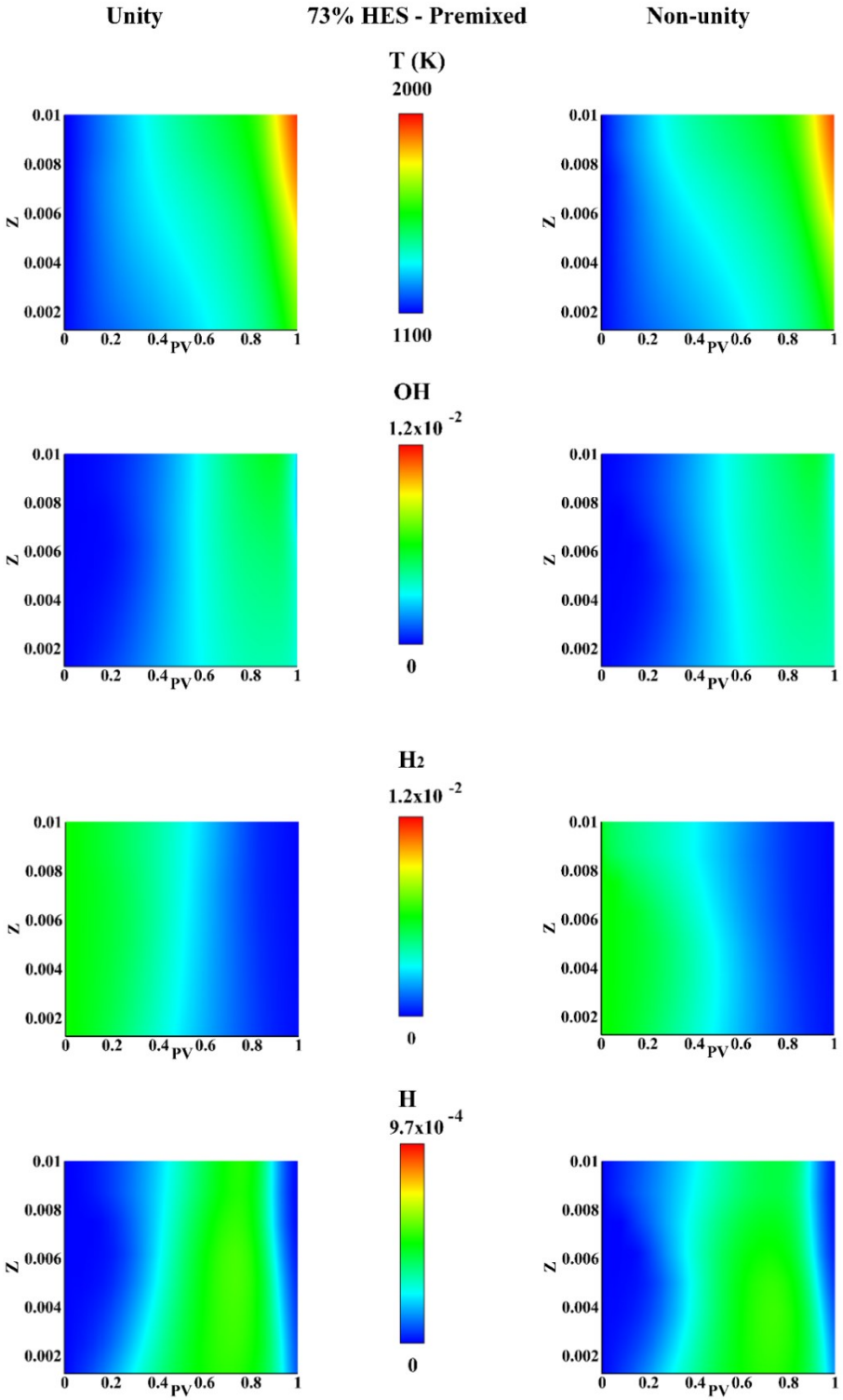

Figure 43: Premixed manifolds for temperature, OH, H_2 and H with unity Lewis number (left) and non-unity Lewis number (right) as a function of the mixture fraction and progress variable for the diesel-hydrogen case with 73% HES.

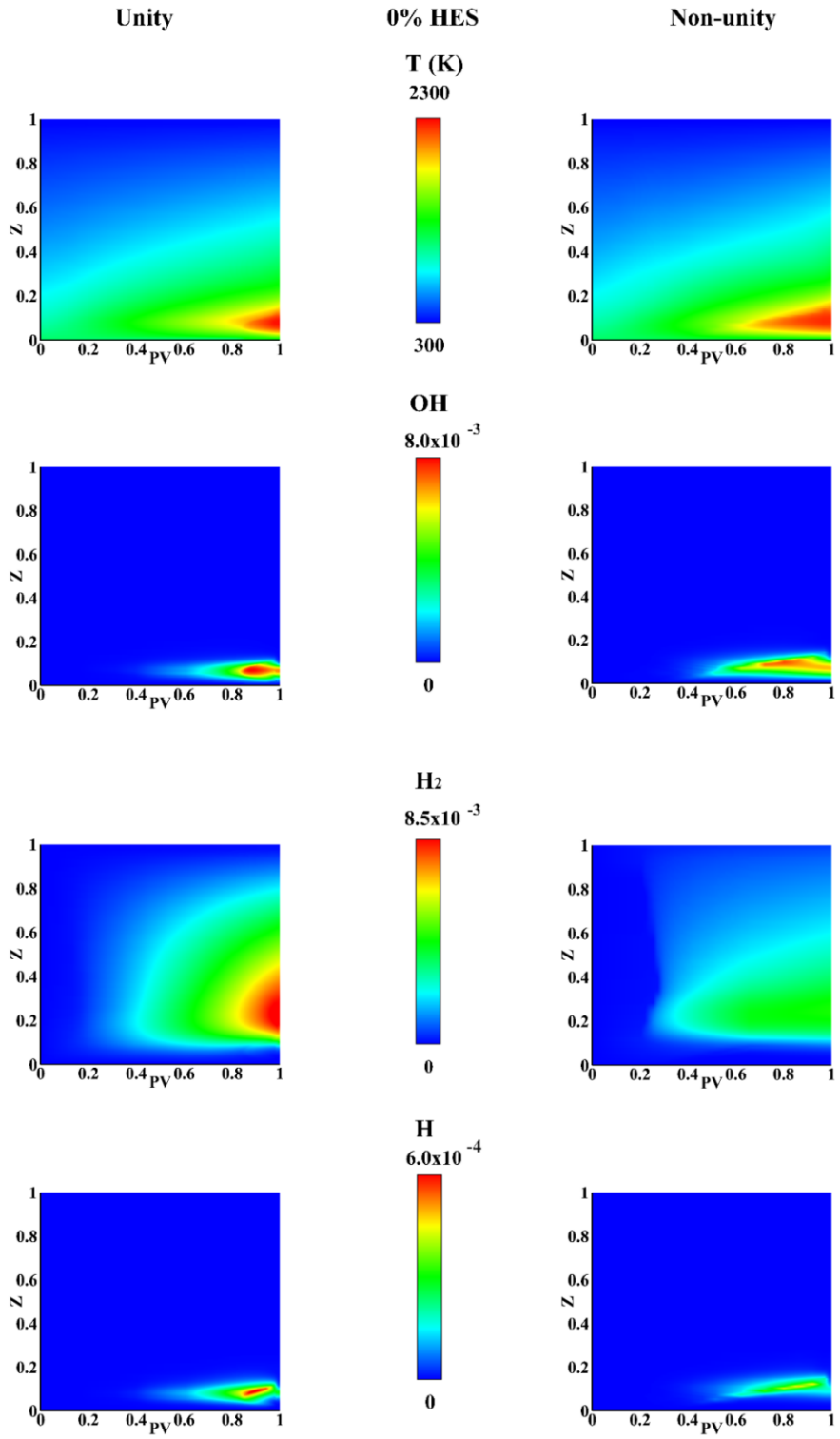

Figure 44: Non-premixed manifolds for temperature, OH, H_2 and H with unity Lewis number (left) and non-unity Lewis number (right) as a function of the mixture fraction and progress variable for the pure diesel case.

As shown in Figure 42, for the laminar diffusion flame, the intermediate and high-temperature zones cover most of the region below the mixture fraction value of 0.2 for the non-unity Lewis number case, indicating a greater rise and wider distribution of the temperature over the domain compared to the unity Lewis number case. This behaviour can be attributed to the high consumption rates of the highly reactive species, which consequently increase the overall chemical reaction rate. For example, for the laminar diffusion flame, the mass fraction of H_2 distribution indicates that the preferential diffusion effects result in a smaller region over the domain, as well as earlier and greater consumption of H_2 below the mixture fraction of 0.15, causing the increase of the flame temperature. It is also observed that the equal-diffusive behaviour of species yields a high production of H_2 due to the restriction of H_2 reactivity for the unity Lewis number case, as opposed to the non-unity Lewis number case. For the H atom, its distributions with and without preferential diffusion effects are relatively similar; however, its production in the unity Lewis number case is greater as a result of the larger production of H_2 along with the restriction of its reactivity. By contrast, the OH radical is located in the high-temperature and high H_2 consumption regions in the diffusion flame and is widely distributed as a results of preferential diffusion effects, indicating the occurrence of higher reaction rates in these regions.

While the laminar diffusion flame shows more clear differences between unity and non-unity Lewis number approaches, the laminar premixed flame shows minor differences between the two approaches. Since we use a threshold value based on the mixture fraction to switch the data between the non-premixed manifold and the premixed manifold, the premixed manifold was created for a region of mixture fraction values equal or lower than 0.01. More details about selection of the threshold value and switching the data between the non-premixed manifold and the premixed manifold will discussion in the next section. In Figure 43 preferential diffusion effects yield a slightly earlier increase of temperature and a greater consumption rate of H_2 in the region of mixture fraction value greater than 0.004. Consequently, this results in earlier productions of OH and H radicals in the same regions in the non-unity Lewis number case. This is due to earlier activation of the chemistry as well as the strong chemical reaction rates throughout the domain owing to the highly diffusive mobility of H_2.

Figure 44 shows flamelet generated non-premixed manifolds for temperature and species concentrations of OH, H_2 and H radicals as a function of the mixture fraction and progress variable

obtained from the one-dimensional flamelet calculations with and without Lewis number effects for the pure diesel (0% HES) case. The non-premixed manifolds were created using 84 flamelets. It can be seen that the distributions of species concentrations of H_2, H and OH for the pure diesel case behave similar to the diesel-hydrogen DF case, but with significantly lower values. Even with the low diffusivity of the diesel-like n-heptane fuel, the temperature manifold of the laminar diffusion flame indicates that the highly diffusive species such as H and H_2 enhance the chemical reactions rates involved with these species, which result in wider high temperature spots and earlier increase of temperature due to preferential diffusion effects.

5.3.2 Model Validation

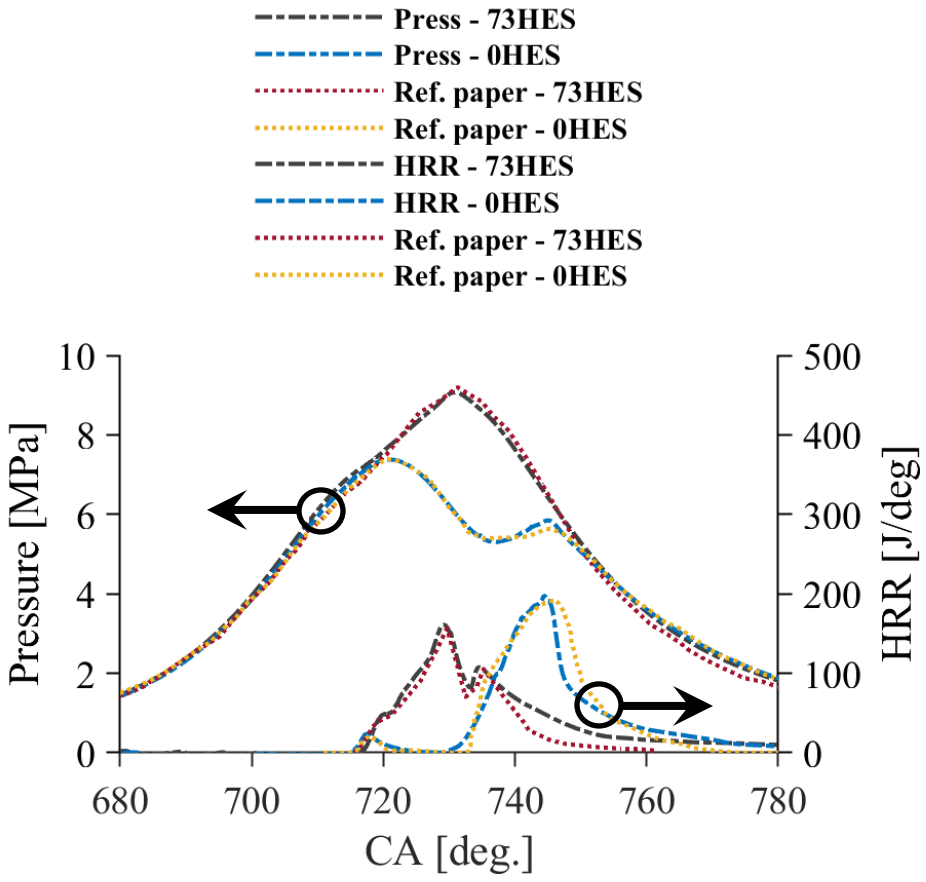

Figure 45: Validation of the FGM hybrid combustion model incorporating preferential diffusion effects. Comparison between experimental [52] and numerically predicted in-cylinder pressure and heat release rate for the diesel-hydrogen DF case with 73% HES and the pure diesel case with 0% HES.

Figure 45 shows a comparison of in-cylinder pressure and HRR between numerical results obtained from the modified FGM combustion model incorporating preferential diffusion effects and experimental results [52] for the pure diesel case (0% HES) and diesel-hydrogen dual-fuel case (73% HES). The computational and experimental findings during the compression, combustion and expansion strokes are in good agreements. For both cases, the numerically predicted in-cylinder pressure profiles compared well with the experimental data during compression, combustion and expansion. The in-cylinder pressure distribution indicates only minor differences for the peak pressure values and their crank angles (CA) between numerical predictions and the experimental data. For example, for the pure diesel case (0% HES) case, the first peak value is well predicted, whereas the second peak value is over-predicted by 0.11 MPa. For the diesel-hydrogen DF case (73% HES), the peak pressure value is under-predicted by 0.13 MPa and occurs slightly early by 0.5 CA. Furthermore, the in-cylinder pressure curves indicate that the peak pressure increases from 7 MPa for diesel only combustion to 9 MPa for diesel-hydrogen DF combustion which is about 28% increase in peak pressure when operate the engine with substantial hydrogen addition compared to diesel only operation.

From Figure 45, it is seen that the peak HRR is over-predicted by 5.52 J and 4.31 J and also advanced by 1.63 CA and 1 CA for the pure diesel case and diesel-hydrogen case respectively. The HRR curve shows two major peaks for the DF flame with hydrogen addition while it shows only one major peak for the diesel only case. For the second peak for the DF flame, the calculated maximum pressure value is over-predicted by 3.1 J and occurs slightly later (0.76 CA) than the experimental value. In addition, the rate of HRR increase displays minor discrepancy between predicted and measured values in both cases. For example, numerically predicted rate of HRR increase is lower for the pure diesel case and higher for the diesel-hydrogen DF case compared to experimentally measured curves. These discrepancies may occur due to the auto-ignition characteristics of diesel only and diesel-hydrogen DF flames. Particularly, the addition of hydrogen results in fast reaction rate in the vicinity of the diesel pilot auto-ignition spots, hence influences the auto-ignition characteristics [163]. Also, the rate of HRR fall off is lower in predictions, which may be attributed to wall heat transfer. In general, the minor differences between numerical results and the experimental data may be attributed to several reasons, for example, the reduced chemistry mechanisms employed in CFD calculations, uncertainty of the theoretically calculated compression ratio etc. For example, the theoretically calculated

compression ratio may slightly differ from the real compression rate. Therefore, it results in the over and/or under-predictions of in-cylinder pressure and HRR [164].

Generally, Figure 45 clearly shows that the FGM hybrid combustion model incorporating preferential diffusion effects well captures the in-cylinder pressure and HRR profiles of diesel-hydrogen DF combustion with high accuracy.

5.3.3 The role of preferential diffusion on combustion characteristics of hydrogen blended dual fuel combustion

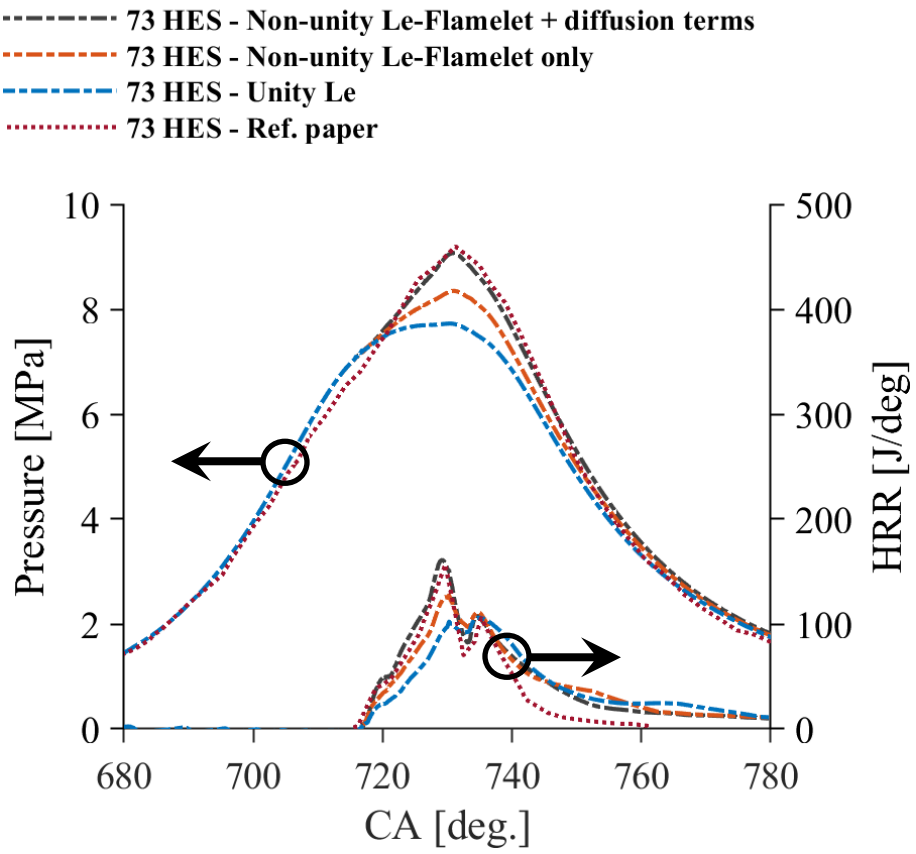

Figure 46: Comparison of in-cylinder pressure and heat release rate between non-unity Lewis number approach in the flamelet calculation and diffusion coefficients in the transport equations of the control variable, non-unity Lewis number approach in the flamelet calculation only, Unity-Lewis number approach, and the experimental data for the diesel-hydrogen DF case with 73% HES.

The intention of this section is to clarify the role of preferential diffusion during auto-ignition, combustion and flame propagation stages in a high hydrogen content diesel-hydrogen DF combustion engine. In this section, we compare the numerically predicted combustion characteristics between unity- and non-unity Lewis number approaches to demonstrate the role of preferential diffusion during ignition and combustion in a high hydrogen content diesel-hydrogen DF engine. The effects of preferential diffusion on in-cylinder pressure, temperature, heat release rate, radical species concentrations, NOx emissions and auto-ignition delay response are analysed by comparing numerical results between unity- and non-unity Lewis number approaches.

It is important to note that preferential diffusion effects are implemented using a two-step correction: non-unity Lewis number effects in the flamelet calculation using the mixture averaged transport model and additional diffusion coefficients in the transport equations for the control variables. We found that only considering non-unity Lewis number effects in the flamelet calculation under-predict the peak values of the in-cylinder pressure and HRR. For example, Figure 46 clearly shows that the FGM hybrid combustion model incorporating preferential diffusion effects in the flamelet calculation and the transport equations of the control variables (i.e. two-step correction) better captures the experimentally measured in-cylinder pressure and HRR profiles of diesel-hydrogen DF combustion with high accuracy compared to numerical results obtained from FGM hybrid combustion model incorporating preferential diffusion effects in the flamelet calculation only. This finding suggests that a two- step correction is needed for the proposed FGM hybrid combustion model to better capture preferential diffusion effects for hydrogen blended DF combustion modelling.

5.3.3.1 In-cylinder pressure and heat release rate

Figure 47 represents the in-cylinder pressure, and HRR between unity and non-unity Lewis number approaches for pure diesel and diesel-hydrogen DF cases. It is evident from Figure 47 that the potential of preferential diffusion effects is significantly demonstrated in the DF case compared to the pure diesel case. For the pure diesel case, preferential diffusion does not play a major role in predicting in-cylinder pressure and HRR profiles due to nature of non-premixed combustion and slow diffusivity of diesel like N-heptane fuel. For example, we observed very minor

differences for the peak pressure and peak HRR between unity and non-unity Lewis number approaches for the pure diesel case.

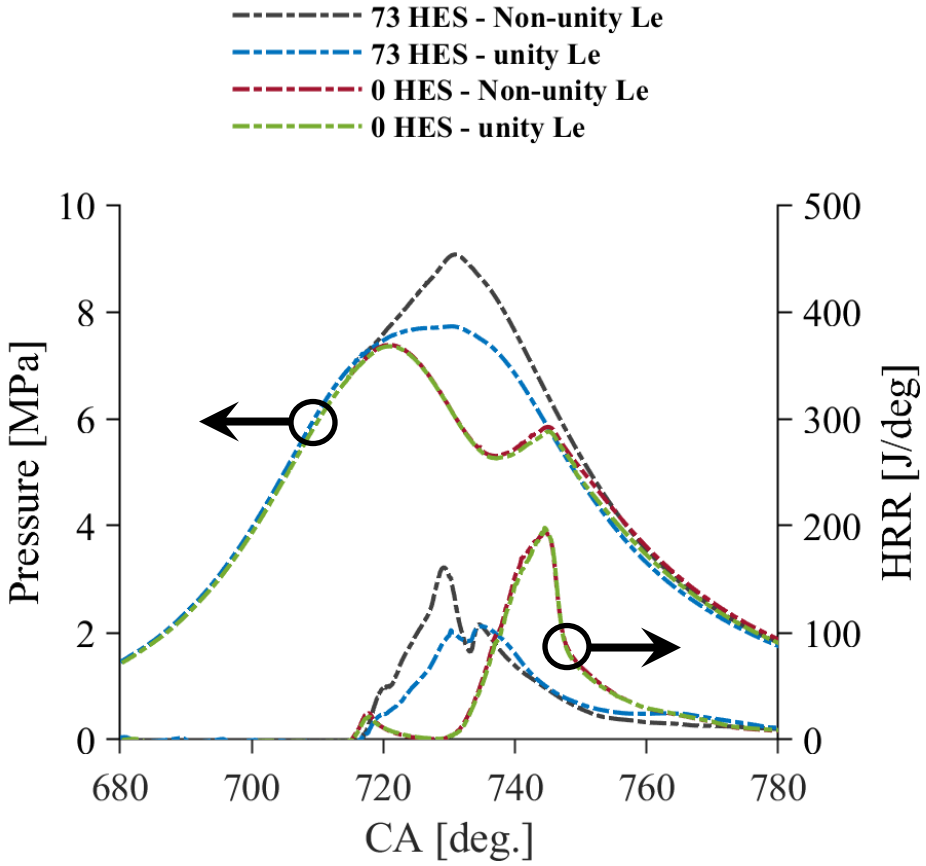

Figure 47: Comparison of in-cylinder pressure and heat release rate between non-unity Lewis number approach and Unity-Lewis number approach for the diesel-hydrogen DF case with 73% HES and the pure diesel case with 0% HES.

On the other hand, it is obvious that in Figure 47 preferential diffusion plays a major role in predicting in-cylinder pressure and HRR profiles for diesel-hydrogen DF combustion. Both pressure and HRR profiles indicate that addition of hydrogen has an apparent effect on diesel combustion. This trend has been demonstrated by a sharp increase in peak in-cylinder pressure and peak HRR which is well captured by the FGM hybrid combustion model with preferential effects compared to the one without preferential diffusion effects. For example, there is a clear gap in peak in-cylinder pressure and peak HRR values between unity and non-unity Lewis number approaches which is about 1.34 MPa and 55.15 J for pressure and HRR respectively. Figure 47

also revealed that the introduction of hydrogen leads to an early start of combustion compared to the pure diesel case which is well captured by the FGM hybrid model with preferential diffusion effects. The early start of combustion leads to high in-cylinder pressure for the diesel-hydrogen DF case compared to the pure diesel case. Also the rate of increase of HRR is greater for the non-unity Lewis number approach compared to the unity Lewis number approach for the diesel-hydrogen DF case.

Furthermore, the presence of hydrogen has a more pronounced effect on the peak values of HRR which are better captured by the FGM hybrid model with preferential diffusion effects. For example, the HRR profile obtained from the non-unity Lewis number approach exhibits two major peaks in HRR throughout for the DF flame. For the simulated DF flame with preferential diffusion effects, a first peak in HRR is located around 727 CA followed by a period of drop in HRR, beyond which there is an increase in HRR resulting in a second peak at around 735 CA. The first major peak in HRR at around 727 CA is characterised by the activation of high temperature chemistry with the influence of ambient hydrogen in the vicinity of the diesel fuel spray tip [165]. During this stage, the high temperature combustion chemistry of light radicals such as H and OH due to ignition of hydrogen along with preferential diffusion effects play an important role. The addition of hydrogen increases the productions of light radicals, and the incorporation of preferential diffusion effects result in considerable impacts of their distributions throughout the combustion chamber. The radicals such as H and OH are highly reactive species, enhancing the in-cylinder pressure, HRR, flame temperature and ignition delay. Furthermore, at this stage, the high diffusivity of hydrogen leads to increase the intrinsic flame instabilities such as thermo-diffusive instability which occurs due to due to an imbalance between chemical and sensible enthalpy fluxes from the reaction zone as a result of preferential diffusion (non-unity Lewis number) effects [100]. The impact of thermo-diffusive instability plays an important role in the ignition and combustion of diesel-hydrogen DF combustion process when lean hydrogen start to ignite and burn [166].

Beside the thermo-diffusive instability, the gas expansion known as hydrodynamic instability also plays a role and enhances the flame acceleration. The FGM hybrid model incorporating preferential diffusion effects in flame chemistry and transport equations of control variables was able to adequately predict the first major peak in HRR profile of diesel-hydrogen DF combustion with high hydrogen energy share as compared to the FGM hybrid model without preferential

diffusion effects. The second major peak in HRR is represented by the oxidation of available hydrogen and premixed flame initiation [165]. This peak in HRR has been captured by the FGM hybrid model with and without preferential diffusion effects.

5.3.3.2 In-cylinder temperature

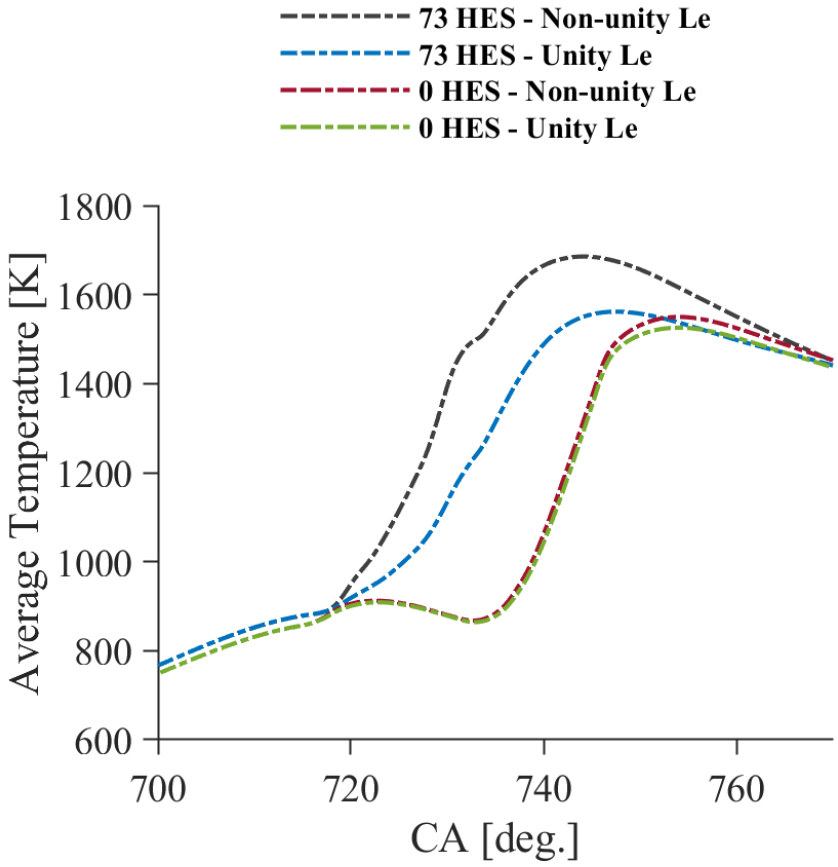

Figure 48: Comparison of the average in-cylinder temperature between non-unity Lewis number approach and Unity Lewis number approach for the diesel-hydrogen DF case with 73% HES and the pure diesel case with 0% HES.

Figure 48 shows the average in-cylinder temperature for the diesel-hydrogen DF case and the pure diesel case with unity and non-unity Lewis number approaches. As seen from the in-cylinder pressure and HRR profiles, preferential diffusion effects the average temperature for the diesel-hydrogen DF case compared to the pure diesel case. The predicted results obtained from the FGM hybrid model with preferential diffusion effects show gradual increase of the average in-cylinder temperature during ignition, combustion and expansion compared to predictions obtained from the

FGM hybrid model without preferential diffusion effects. As preferential diffusion effects the flame acceleration and radical species diffusive flux such as H and OH [100], the predicted average temperature curve shows higher temperature values and steep gradient for the non-unity Lewis number approach compared to the unity Lewis number approach. There is a clear difference for the peak temperature between the two approaches. The non-unity Lewis number approach shows higher peak temperature compared to the unity Lewis number approach due to the influence of preferential diffusion. This is linked with the high temperature combustion chemistry of light radical species such as H and OH. The radicals of H and OH will be discussed in the next section. Furthermore, the heat loss to walls seems to be slightly greater with the presence of preferential diffusion effects since the rate of temperature drop during the expansion stoke is steadily higher than that of the unity Lewis number case. For the pure diesel case, the average temperature is slightly greater with the incorporation of preferential diffusion effects, indicating that the effects of the highly reactive species are likely to dominate over the effects of low diffusivity of the diesel like N-heptane fuel.

5.3.3.3 Contour plots of temperature and species concentrations

The spatial distributions of in-cylinder temperature and unburned H_2, radicals such as OH and H and NO_x emissions at 730 CA and 750 CA for the diesel-hydrogen DF case with unity- and non-unity Lewis number approaches are shown in Figure 49 The contour plots of the diesel-hydrogen DF case indicate obvious differences between unity- and non-unity Lewis number approaches, demonstrating the role of preferential diffusion effects on in-cylinder flame temperature and key emissions associated with hydrogen combustion. For example, at 730 CA, which is about 12 CA after start of combustion (SOC), the flame propagates faster for the non-unity Lewis case as it distributes in a wider range and, also, its maximum temperature is greater in comparison with the unity Lewis number case. The same observations are also displayed at the end of combustion (EOC) - at 750 CA– for example, wider flame distribution with higher temperature for the simulated DF case with preferential diffusion effects compared to the one without preferential diffusion effects. This can be attributed to the faster flame front propagation of the hydrogen-air mixture during combustion owing to preferential diffusion effects, which greatly enhances the reaction rates and, hence, yields broader distributions of high and intermediate temperature spots.

In contrast, the high flame temperature of the unity Lewis number case is narrower near the pilot fuel zone and becomes wider until roughly the middle of the geometry at 750 CA.

The effect of preferential diffusion is clearly demonstrated in the contour plot of unburned hydrogen gas. For example, at 730 CA, the rate of hydrogen consumption is higher for the non-unity Lewis number case, indicating greater reactivity rates. Furthermore, at 750 CA, the high hydrogen concentration is localised in a narrow region close to the cylinder wall for the non-unity Lewis number case, indicating faster turbulent flame propagation of the hydrogen premixed change compared to the unity Lewis number case. However, due to the slower flame propagation speed, the high hydrogen spots for the unity Lewis number case are centralised near the cylinder wall and the piston bowl.

For H and OH radicals, their maximum values and distributions appear to be wider with the presence of preferential diffusion effects, indicating that such effects promote the chemical reaction rates thus forming these highly reactive radicals in a wider area of the combustion chamber. These radicals significantly affect the SOC and EOC which will be discussed in the following section. Regarding NOx emission, its medium and high zones are more prevalent with preferential diffusion effects due to the higher consumption rate of hydrogen, which results in faster flame propagation throughout the combustion chamber and higher combustion temperatures.

These observations demonstrate that the effects of preferential diffusion result in (i) higher hydrogen consumption rate, (ii) higher and wider flame temperature distributions and faster flame propagation, (iii) wider formations of the light radicals such as OH and H, indicating higher chemical reaction rates and faster combustion process, respectively, for the diesel-hydrogen DF case.

Figure 50 shows the spatial distribution of temperature, OH and NO_x emissions for the pure diesel case with unity and non-unity Lewis number approaches. Generally, there are some minor differences between the two approaches. For example, at 750 CA, the distribution of highest OH and NO_x emission slightly wider for the non-unity Lewis number approach compared to the unity Lewis number approach. Their causes may lie in the domination of highly reactive radicals at the end of combustion due to the diesel-like fuel, which results in slightly higher in-cylinder temperature.

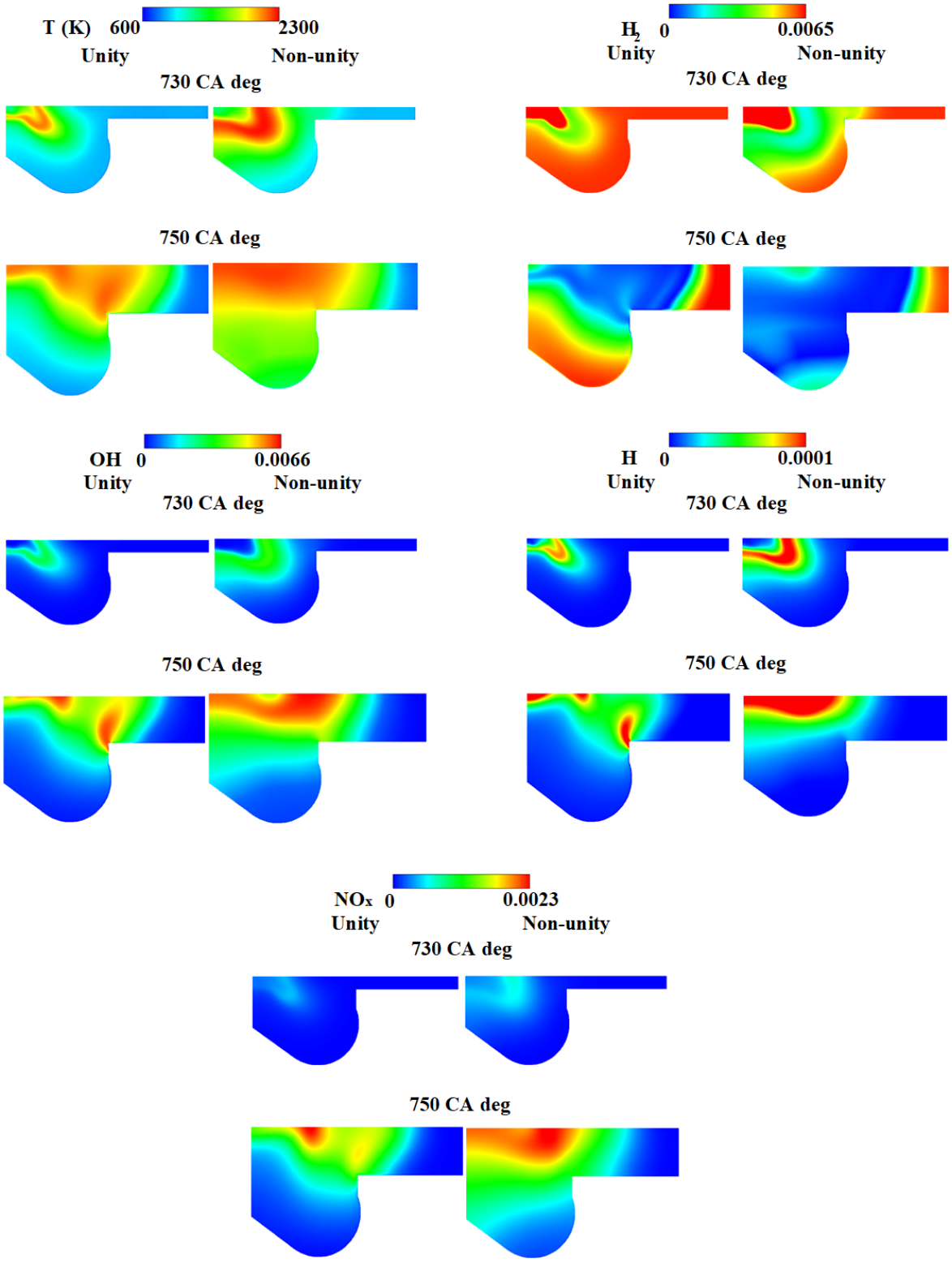

Figure 49: Contour plots of temperature, H_2, OH, H and NOx distributions at 730 CA and 750 CA between non-unity Lewis number approach and Unity Lewis number approach for the diesel-hydrogen DF case with 73% HES.

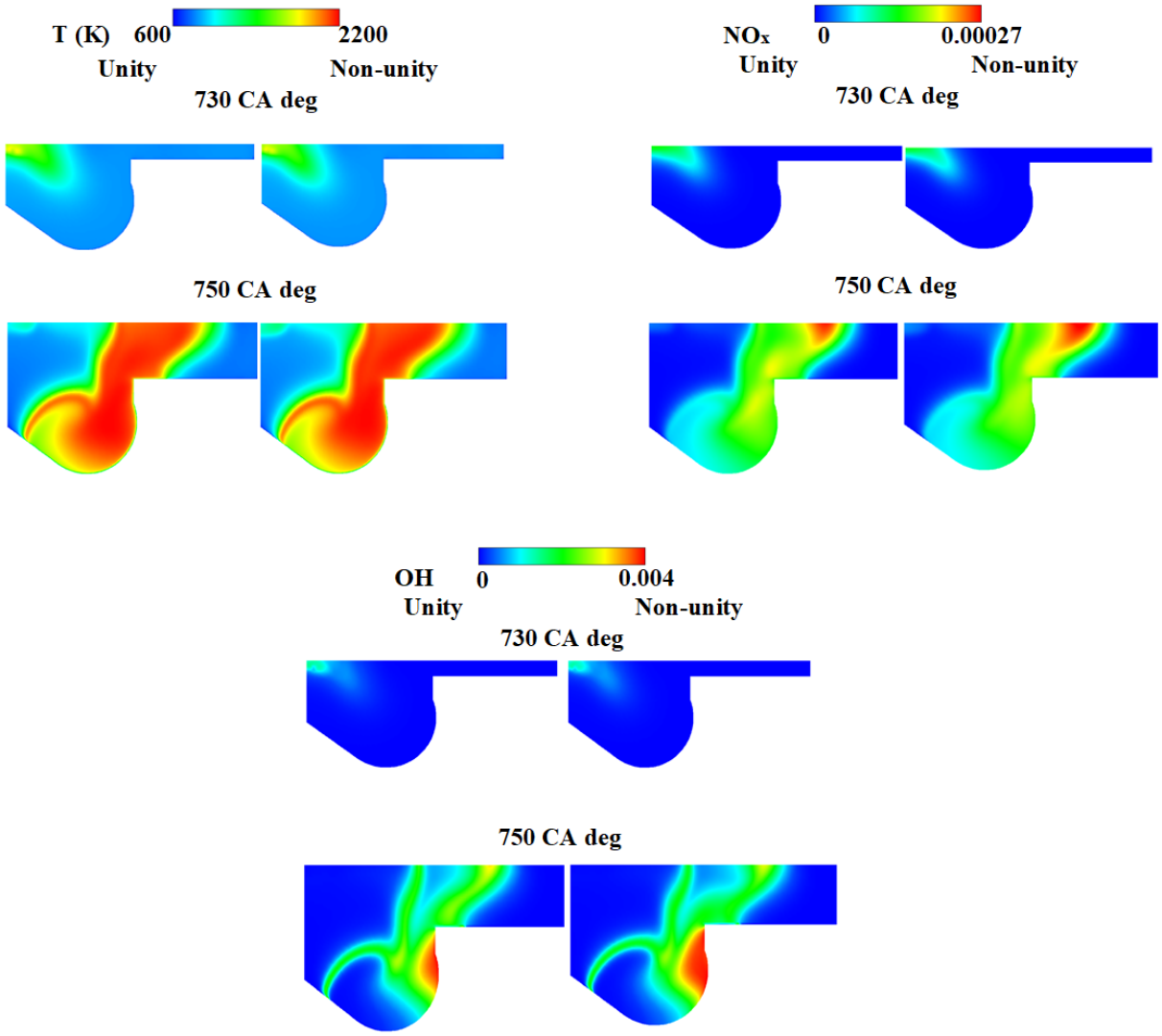

Figure 50: Contour plots of temperature, OH and NOx distributions at 730 CA and 750 CA between non-unity Lewis number approach and Unity Lewis number approach for the pure diesel case with 0% HES.

5.3.3.4 Ignition delay and combustion duration

Figure 51 shows the effects of preferential diffusion on ignition delay and combustion duration for the diesel-hydrogen DF case and the pure diesel case. Here, the ignition delay is defined as the period from the start of injection (SOI) to SOC. The SOC can be evaluated from the total heat release rate (THRR) [167]or the rate of pressure rise variation [168]. In this work, SOC is computed as 3% of the THRR [167]. The combustion duration is the period from the SOC to EOC, which is 90% of THRR [167].

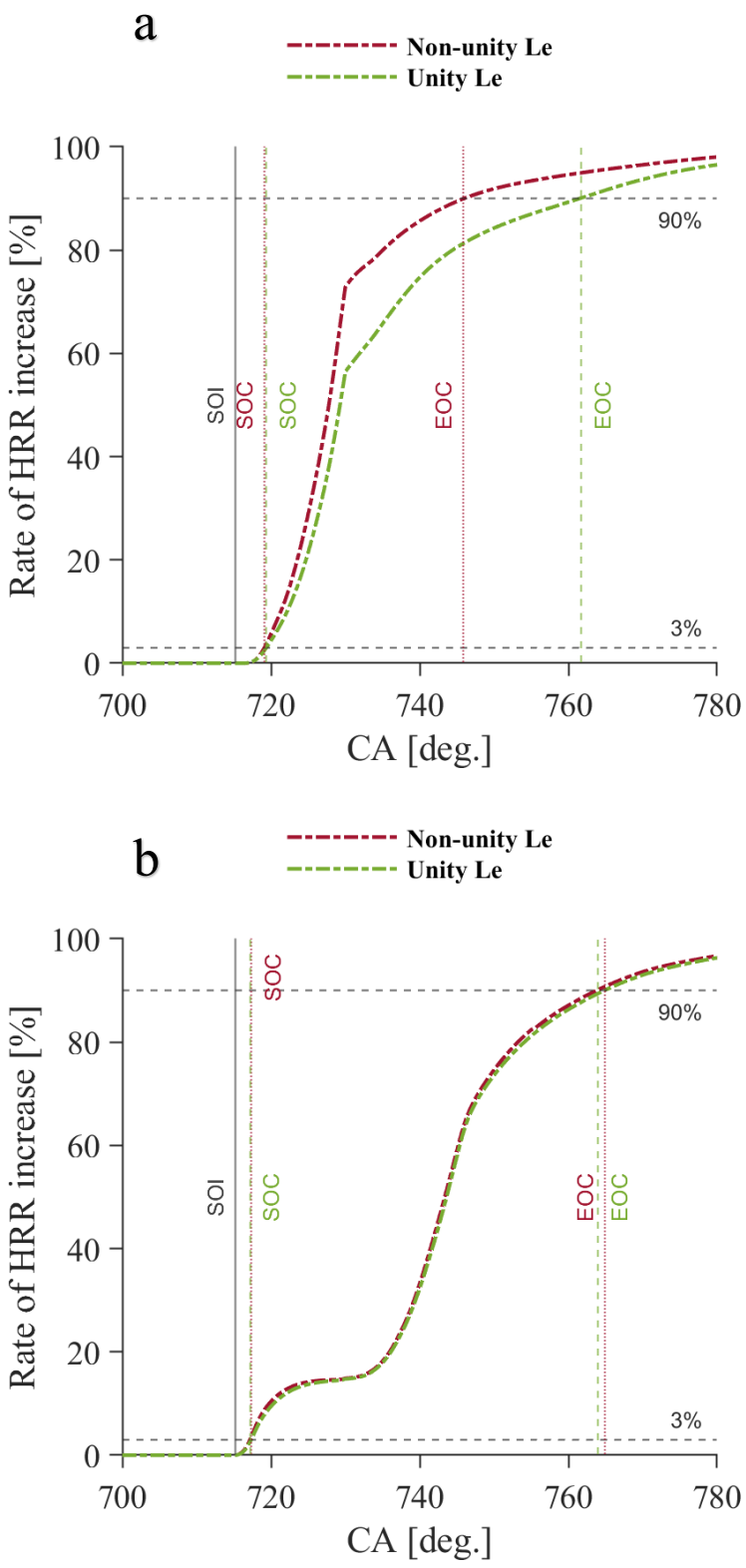

Figure 51: Ignition delay and combustion duration for the simulated cases with and without preferential diffusion effects, a) diesel-hydrogen DF case with 73% HES. b) pure diesel case with 0% HES.

Figure 51 (a) exhibits that the incorporation of preferential diffusion effects slightly advances the SOC for the diesel-hydrogen DF case compared to the one without preferential diffusion effects. This has resulted in the shorter ignition delay for the DF case with non-unity Lewis number approach compared to the unity Lewis number approach. This advancement in the SOC is caused by the higher temperature chemistry and faster flame propagation of the hydrogen-air mixture in the immediate vicinity of the diesel pilot spray due to preferential diffusion effects, which increase the overall combustion rate and the flame temperature. In addition, the highly reactive radicals such as OH and H are evident to increase due to preferential diffusion effects (see Figure 49) and enhance the combustion and flame propagation in the high hydrogen content DF case. These radical species have significant effects on fuel ignition and combustion chemistry due to their high diffusivities. Thus, with preferential diffusion effects, their broader distributions as shown in Figure 51 primarily enhance combustion by promoting the chain of chemical reactions and increasing the overall combustion rates. For the same reason, the diesel-hydrogen DF case with non-unity Lewis number approach has a shorter combustion duration as opposed to that of the unity Lewis number case by 15.7 CA. As shown in Figure 51 (b), the incorporation of preferential diffusion effects does not play a major role for the pure diesel case as the ignition delay and the combustion duration are almost the same between unity- and non-unity Lewis number approaches. Furthermore, Figure 51 (a) and (b) demonstrate that the ignition delay time is longer for the diesel-hydrogen DF case compared to the pure diesel case.

5.4 Conclusions

In this chapter, a novel flamelet generated manifold hybrid combustion model incorporating preferential diffusion effects discussed in the methodology chapter was applied to better capture the complex multiple combustion process of a high hydrogen content diesel-hydrogen dual-fuel combustion engine. The FGM hybrid combustion model was developed by coupling flamelet databases obtained from diffusion flamelets and premixed flamelets. The model employed three control variables, namely, mixture fraction, reaction progress variable and enthalpy. The diffusion flamelet database was employed to capture the auto-ignition of the diesel pilot fuel with air and with the presence of hydrogen gas in the vicinity of the auto-ignition spots while the premixed flamelet database was used to predict the flame propagation of the premixed hydrogen-air mixture.

A threshold value based on the mixture fraction was used to switch the data between diffusion flamelets and premixed flamelets. The preferential diffusion effects were accounted in the laminar flamelet solution and the diffusion coefficients in the transport equations of control variables. The numerical simulations were performed using the Reynolds-averaged Navier-Stokes approach. The simulations are based on the diesel-hydrogen dual-fuel engine configuration of Tsujimura et al. [52], enabling validation of the proposed FGM hybrid combustion model against experimental data on the in-cylinder parameters. We compared results for the diesel-hydrogen dual-fuel test case with 73% hydrogen energy share and pure diesel case at high engine load conditions. In order to demonstrate preferential diffusion effects, the simulations were carried out with unity- and non-unity Lewis number approaches.

The main findings of the study are listed in the following:

1. The comparison between numerical results and the experimental data demonstrates that the FGM hybrid combustion model incorporating preferential diffusion effects well captures the combustion characteristics of the high hydrogen content diesel-hydrogen dual-fuel combustion process with high accuracy. The inclusion of preferential diffusion effects in the laminar flamelet calculation and the diffusion coefficients in the transport equations of control variables was shown to have significant effects on capturing all phases of the high hydrogen content dual-fuel combustion process.
2. The analysis of in-cylinder pressure and heat release rate profiles indicates that addition of hydrogen has an apparent effect on diesel combustion. The sharp increase in in-cylinder pressure and early start of combustion are well predicted by the FGM hybrid combustion model with preferential diffusion effects. The occurrence of major peak heat release rate values due to activation of the high temperature chemistry with the influence of ambient hydrogen in the vicinity of the diesel fuel spray tip and the oxidation of available hydrogen under partially premixed combustion, as well as subsequent premixed combustion of the hydrogen-air mixture are better captured by the FGM hybrid model with preferential diffusion effects.
3. The FGM hybrid combustion model with preferential diffusion effects predicts higher peak in-cylinder combustion temperature due to faster flame propagation of the premixed charge and high temperature combustion chemistry of light radical species such as H and OH. The

consumption rate of hydrogen is much greater for the non-unity Lewis number approach owing to higher diffusivity rate which is better captured by the FGM hybrid model with preferential diffusion effects. The numerical results obtained with non-unity Lewis number approach show wider distribution of H and OH radicals, indicating high reactivity of light radicals. The NO_x emission is widely distributed in the non-unity Lewis number approach in comparison with that of unity Lewis number approach as a result of broader high and intermediate temperature values, which are caused by the faster hydrogen consumption rate.

4. The preferential diffusion effects slightly advance the start of combustion for the dual-fuel case. This has resulted in the shorter ignition delay for the dual-fuel case with the non-unity Lewis number approach compared to the unity Lewis number approach. The advancement in the start of combustion is caused by the higher temperature chemistry and faster flame propagation of hydrogen-air mixture in the immediate vicinity of the diesel pilot spray due to preferential diffusion effects, which increase the overall combustion rate and the flame temperature. For the same reason, the diesel-hydrogen dual-fuel case with non-unity Lewis number approach has a shorter combustion duration compared to that of the unity Lewis number approach. The numerical results also demonstrate that the ignition delay time is longer for the diesel-hydrogen dual-fuel case compared to the pure diesel case.

Chapter 6: Modelling and Simulation of Hydrogen Blended Dual-fuel Combustion with Ammonia

6.1 Introduction

The world is facing serious difficulty attaining a clean environment both now and in the foreseeable future. In 2018, fossil fuel consumption was reported at a peak rate of 81.5% and approaching depletion at an even faster pace [169]. At a forum held in Paris in 2015, the utilisation of various alternative energy sources—such as solar, wind, and biomass—were proposed as means of reducing greenhouse gas emissions [170]. Energy from these sources is stored in batteries and can be utilized in intermittent form, whereas chemical energy provides a continuous form of energy. Therefore, hydrogen and ammonia have been proposed as alternative energy sources available in chemical form. Over the years, researchers have proposed hydrogen as the best carbon-free fuel option. However, hydrogen as an energy carrier and clean fuel has several disadvantages - such as production, storage, and transport - present concerns, as highlighted in Section (2.2.1). Compared to hydrogen, ammonia is considered a potential energy carrier. It contains 17.6% hydrogen by weight and acts as a green fuel due to the absence of carbon content, resulting in zero greenhouse gas emissions. The boiling point of ammonia (-33.8 ºC) is significantly higher than hydrogen (-252.9 ºC), making fuel storage and transportation of the former much easier than the latter.

Ammonia can power both SI and CI engines. The literature on ammonia-fuelled spark ignition engines is vast and shows that ammonia is a viable solution for spark-ignition (SI) engines. Ammonia benefits from a high octane number (~130) that can improve the combustion properties and reduce engine knocking or any other undesirable combustion effects seen in gasoline SI engines [171]. On the other hand, the combustion of ammonia in CI engines is a challenging task due to the high resistance of the fuel to auto-ignition and poor combustion quality with low reactivity. One way to run ammonia in CI engines is to utilise it with extremely high compression

ratios which needs engine to be re-built to suit higher compression ratio, hence this method not economically viable [172]. Another solution is to use ammonia in DF operation mode with the aid of a secondary fuel with a lower auto-ignition temperature to trigger the combustion of the ammonia–air gaseous mixture. This solution was used in 1966 by Gray et al. [173], with the authors highlighting the successful ammonia–diesel DF combustion that was achieved with a compression ratio as low as 15.2:1 compared to the 35:1 used for the ammonia-only operation. Nevertheless, the findings of the ammonia–diesel DF combustion engine were not encouraging due to the low combustion efficiency, longer ignition delay, and high unburnt ammonia, NO_x, and N_2O—Note that N_2O is about 300 times more potent than CO_2 and depletes the ozone layer [174]. This has been highlighted in several investigations [66, 175-177]—for example, Niki et al. [177] concluded that increasing the combustion temperature could itself prevent the N_2O formation and enhance the ammonia combustion rate.

Therefore, with the urge to use ammonia in DF CI operation mode, there is a need to overcome the disadvantages outlined above. One solution to overcome such a disadvantage is to blend ammonia with a fuel with high reactivity and flame speed, such as hydrogen. In 2010, Lee et al. [178] studied the effect of hydrogen addition on ammonia–air flames in order to enhance the burning velocity. The authors concluded that an increase in the laminar burning velocities of ammonia–air flames is achieved when 3–5% hydrogen is added. The increase was observed due to higher hydrogen content, as hydrogen has higher mass diffusivity than both ammonia and air. The hydrogen–ammonia blended mixture was investigated in SI engines, as discussed in [179-182]. On the other hand, to the best of the author's knowledge, the premixed hydrogen–ammonia mixture in CI DF engine combustion has not been studied, except the recent investigation carried out by Pochet et al. [183] in homogeneous charge compression ignition (HCCI) engines. In their study, hydrogen was inducted to promote and stabilise the operation of the engine, and the combustion of the mixture was achieved at an intake gas pressure of 1.5 bar and temperature in the range of 428–473 K. The authors operated the engine with an ammonia content rate of up to 70%, but as highlighted, this required the combustion temperatures to remain above 1300 K to maintain hydrogen-like combustion efficiencies.

This chapter aims to apply the newly developed FGM hybrid combustion model and perform a series of engine simulations to investigate combustion and emission characteristics of hydrogen

blended compression ignition ammonia DF combustion. This chapter has three key objectives: (i) apply the newly developed FGM hybrid combustion model to simulate diesel-ammonia DF combustion and validate the model for ammonia DF combustion. The validation of the numerical results will be carried out against the experimental data of Niki et al. [83], (ii) perform a parametric study to investigate the impact of hydrogen addition on diesel-ammonia DF engine combustion demonstrating how low reactivity and low burning rate of ammonia can be tackled with hydrogen addition and pilot diesel fuel injection optimisation, (iii) perform a parametric study to replace pilot diesel fuel with HVO in ammonia DF engine aiming to find a truly renewable ammonia DF engine combustion.

6.2 Numerical setup

In this chapter, the newly developed FGM hybrid combustion model presented in Chapter 3 and implemented in Chapter 5 is applied to simulate the ammonia–diesel CI DF combustion engine and then validate the computational results against the experimental data of a single-cylinder diesel–ammonia CI DF engine carried out by Niki et al. [83]. The numerical modelling framework was applied simulate the diesel–ammonia case with 47% ammonia energy share (AES) at high engine load. The engine specifications and experimental conditions of the aforementioned test case are illustrated in Table 7. Parametric studies were then performed by making hydrogen additions to the ammonia-enriched gaseous mixture, as well as by replacing diesel with its alternative counterpart fuel (HVO); this is presented in Table 8. The purpose of fuel variations includes the following: first, to demonstrate the effects of hydrogen on enhancing the performance and combustion characteristics in blended fuels with high ammonia content up to 80%; second, to achieve possible clean, green combustion by reducing the diesel contribution in fuel blends to 5% of the energy share; and third, to mitigate the carbon-containing and NO_x pollutant emissions by replacing diesel with its alternative green diesel fuel (HVO). It should be noted that the fourth objective of the investigations was carried out with the highest energy share of pilot fuel (Case 3) to demonstrate the maximum potential of HVO in suppressing the engine-out emissions, as the effects of HVO in the cases with lower pilot fuel contributions was expected to be minor (as shown in Section 6.3.5). Lastly, the injection timing of the pilot fuel was altered to identify further ways to optimise the performance, combustion, and emission characteristics.

Base engine	AVL type 520	
Engine type	4-stroke, single cylinder	
Displacement volume (L)	1.08	
Bore × stroke (mm)	112 × 110	
Compression ratio	18.5:1	
Fuel	Diesel fuel (direct injection)	
	Ammonia (Port injection)	
Included spray angle (degree)	149	
Number of holes	6	
Hole diameter (mm)	0.13	
Engine speed (RPM)		1500
Engine torque (Nm)		51
Maximum ammonia fraction (input energy base) (%)		47
Intake gas pressure (MPa)		1.5
Ammonia mass flow rate (kg/s)		2.20
Intake air mass flow rate (kg/s)		50.7
Diesel fuel injection	Timing (deg. CA) ATDC	-10
	Quantity (mg/cycle)	23.6
	Pressure (MPa)	100

Table 7:Diesel-ammonia DF CI engine specification and experimental conditions [83].

Test case	**Fuel mixture (energy share)**		
	Diesel	**Hydrogen**	**Ammonia**
1	53%	0%	47%
2	25%	25%	50%
3	10%	20%	70%
4	5%	15%	80%
	HVO	**Hydrogen**	**Ammonia**
5	25%	25%	50%

Table 8: Fuels contributions in the test cases.

The FGM implementation and technique followed the procedure used in Chapter 5. Figure 52 shows a sector of 60 degrees, consisting of one injector used in this study and representing a portion of a full engine with six injectors. The geometry consisted of 1,315,312 elements. The mesh density, meshing process, models related to the pilot fuel injection, discretisation schemes, and solver algorithm solution method are presented in Section (3.7). In this chapter, two different chemistry sets were incorporated to predict the diesel-ammonia-hydrogen DF engine combustion, using n-heptane sub-mechanisms [104], hydrogen sub-mechanisms [105] and GRI 3.0 sub-mechanism [106] involving ammonia and NO_x sub-mechanisms, and HVO-ammonia-hydrogen DF engine combustion, using the reduced chemistry mechanisms presented in A.

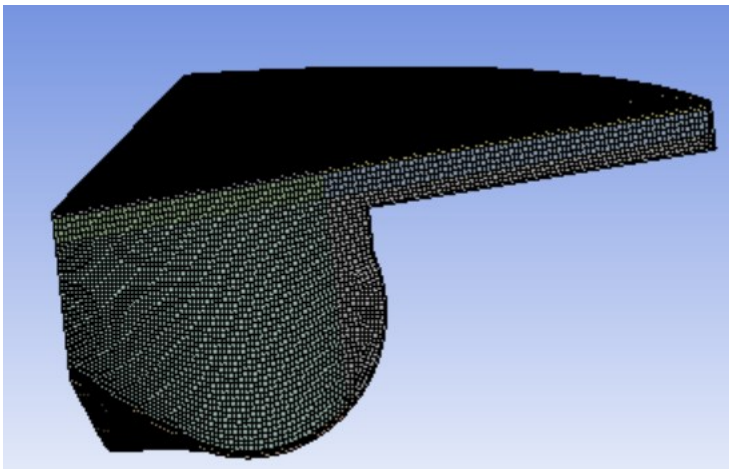

Figure 52: The sector of the numerical grid at top-dead centre (TDC).

6.3 Results and discussion

In these investigations, the extended FGM hybrid combustion model simulated the multiphase combustion process of the ammonia–air and ammonia–hydrogen gaseous mixtures with diesel and HVO as secondary fuels in the CI DF combustion engine. The combustion modelling approach incorporates the preferential diffusion effects by means of two-step correction and couples the non-premixed and premixed flamelet datasets with the mixture fraction threshold of 0.01, designing to capture the non-premixed combustion mode, the premixed combustion mode and the transition between the hybrid combustion modes. The procedure can be found in Section (3.4.4).

In the following sub-sections, the diffusion and premixed FGM manifolds for all test cases are presented, including the validation of the numerical results of the ammonia–diesel CI DF combustion engine against the experimental data conducted by Niki et al. [83], the potential of hydrogen addition in highly ammonia-enriched premixed mixtures, the effects of earlier injection timing of pilot fuel on performance, combustion, and emissions characteristics, the effects of alternative green diesel fuel (HVO), and the shortage and proposed solution of the FGM model implemented in this study in predicting the low-temperature combustion strategies—reactivity controlled compression ignition (RCCI).

6.3.1 Premixed and diffusion FGM manifolds

Figure 53 presents the variations in hydrogen, ammonia, and temperature in the diffusion manifolds with respect to mixture fraction and progress variable with non-unity Lewis number effects for Cases 1, 2, 3, and 4. In general, hydrogen is produced through chemical reactions, even if hydrogen is not introduced in the premixed mixture as a fuel. As seen in Figure 53, the distribution of hydrogen in Case 1 (no hydrogen addition) indicates that the ammonia induction results in the significant formation of hydrogen in the mixing and reaction regions in terms of its variation throughout the domain and its peak being relatively closer to the cases with hydrogen enrichment (Cases 2, 3, and 4). This can be attributed to the content of hydrogen in ammonia, as the latter contains more hydrogen atoms than the former. As expected, the increase in hydrogen substitution increases the hydrogen formation in the mixing and reaction zones as well as expands the outlined zones as hydrogen is found to be formed closer to the highly diesel-enriched areas (regions with higher mixture fraction values). More importantly, the hydrogen addition considerably enhances the reactivity rates even with high ammonia induction (low-reactivity fuel), as the hydrogen distributions in the 70-AES and 80-AES cases (Cases 3 and 4, respectively) are obviously broader and achieves higher peaks than in the 47-AES case (no hydrogen induction). These observations confirm the potential of the high hydrogen diffusivity and reactivity in promoting the mixing and chemical rates, respectively. It should be noted that the contribution of ammonia in Case 2 is greater than Case 1 by 3%. However, the ammonia consumption in Case 2 occurs earlier than in Case 1 with respect to the progress variable, which represents the chemical evolution, due to the hydrogen addition indicating a wider reaction zone and higher chemistry rate.

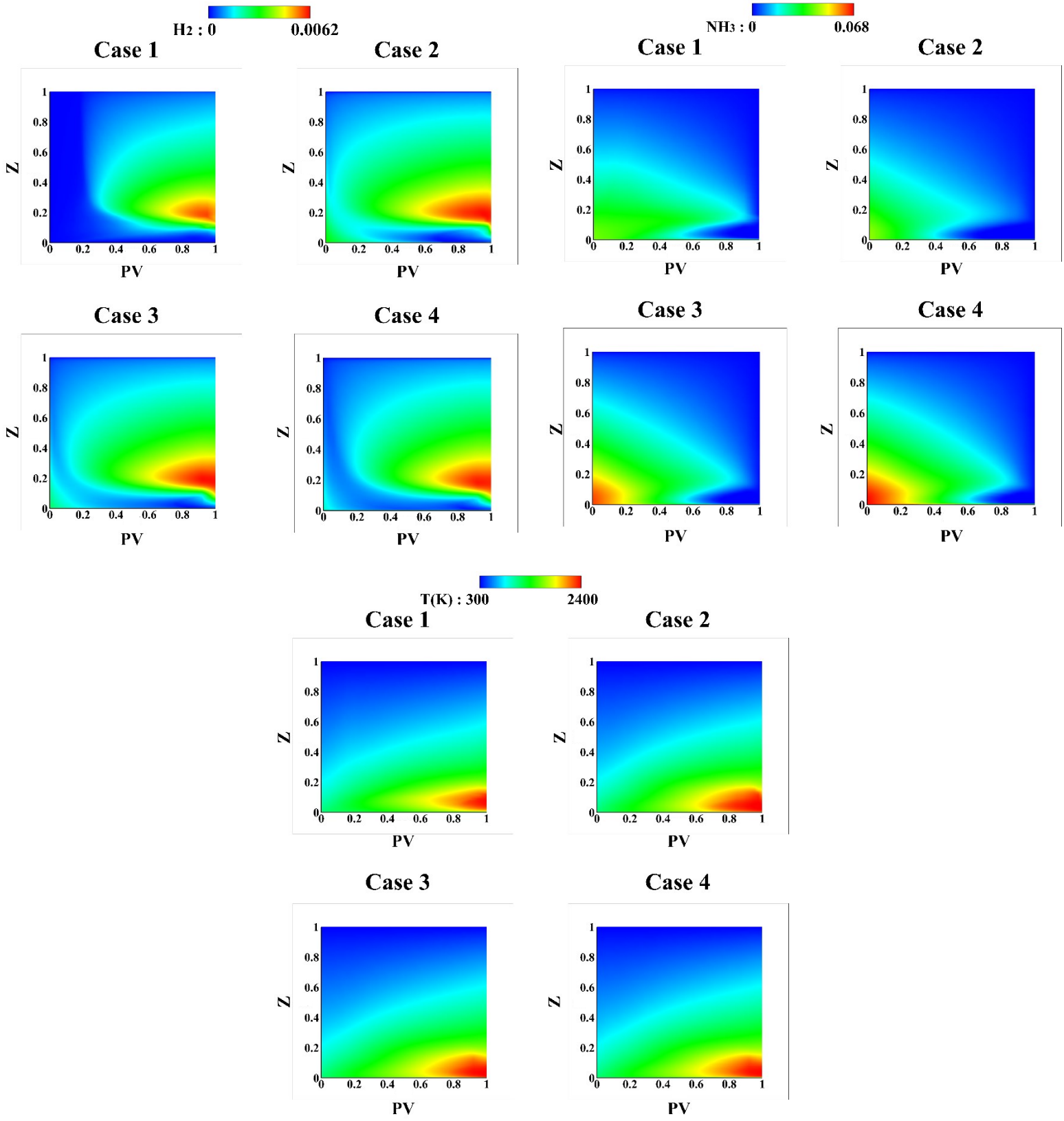

Figure 53: Non-premixed manifolds for H_2, NH_3 and temperature with the incorporation of preferential diffusion effects as a function of the mixture fraction and progress variable for case 1, 2, 3 and 4.

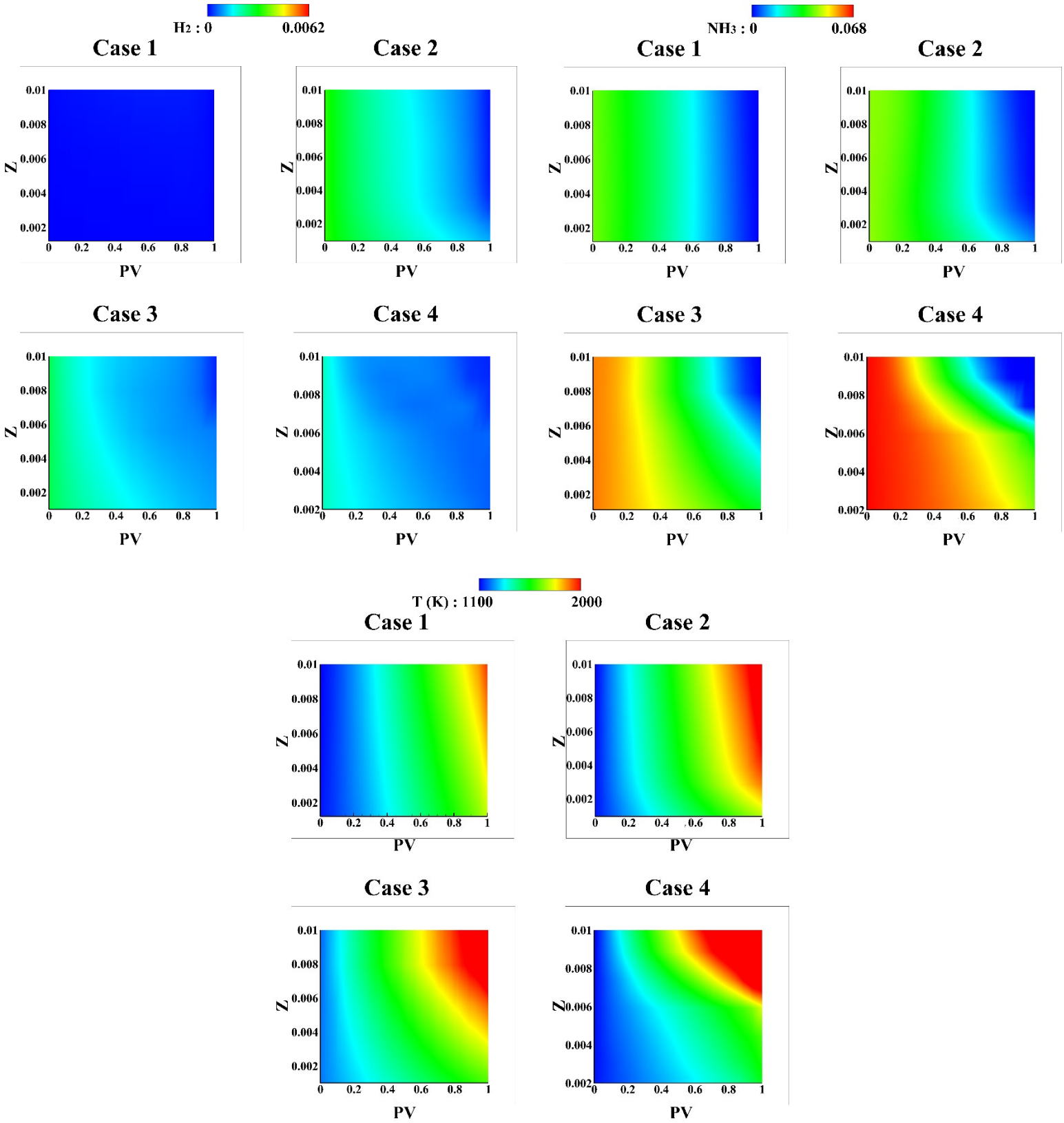

Figure 54: Premixed manifolds for H_2, NH_3 and temperature with the incorporation of preferential diffusion effects as a function of the mixture fraction and progress variable for case 1, 2, 3 and 4.

Therefore, the region with the highest temperature is wider for Case 2, as shown in Figure 53. In general, the temperature of hydrogen addition cases are relatively changes, in terms of its variation over the domain and peak values, depending on the hydrogen energy share. Thus, the increase in hydrogen addition results in a broader region with high temperature, as well as a relatively higher temperature peak value.

Figure 54 shows the variations in hydrogen, ammonia, and temperature in the premixed manifolds with respect to mixture fraction and progress variables with the non-unity Lewis number for Cases 1, 2, 3, and 4. Similar observations in the diffusion manifolds for hydrogen and ammonia can be also seen in the premixed manifolds. However, the premixed manifold of temperature demonstrates the effects of ammonia narrower flammability range as the temperature indicates that the premixed flames of cases with high ammonia inductions (70-AES and 80-AES cases) in the extremely lean conditions have no combustion from mixture fraction of 0.004 and 0.006, respectively, and below.

6.3.2 Model validation

Simulated in-cylinder pressure and heat-released rate results obtained from the CFD analysis with the aid of the newly modified FGM combustion model incorporating the preferential diffusion effects are compared with the experimental results [83] for the same engine operating conditions, as plotted in Figure 55. The in-cylinder pressure predicted by the numerical simulation means during the compression, combustion, and expansion strokes matches very well with the experimental findings. These findings indicate that the FGM combustion model accurately captures the pilot fuel-ignition delay, diffusion combustion of diesel with some portion of ammonia–air gaseous mixture drawn in the diesel-spray region during the diesel ignition-delay period, transition phase between the hybrid combustion mode in DF combustion representing the ignition delay of the main fuel (ammonia), and premixed combustion of the leftover gaseous mixture throughout the combustion chamber.

From Figure 55, it can be seen that the heat loss to the walls in the numerical results is under-predicted, as the rate of heat released rate fall off is lower than that of the experimental results. It is important to remember that the enthalpy is incorporated as an additional control variable to

describe the energy (i.e., heat loss to walls) during PDF construction with the aid of the Delta function, which is less accurate than the Beta function, as earlier mentioned in Section (3.4.4.4). Therefore, the under-prediction of heat released rate drop rate could be a result of convolving Delta function for enthalpy, which correspondingly assumes that the enthalpy fluctuations are negligible. In general, the comparison of in-cylinder pressure and the rate of heat released between the computed and measured data shows acceptable agreements in terms of shape and magnitude.

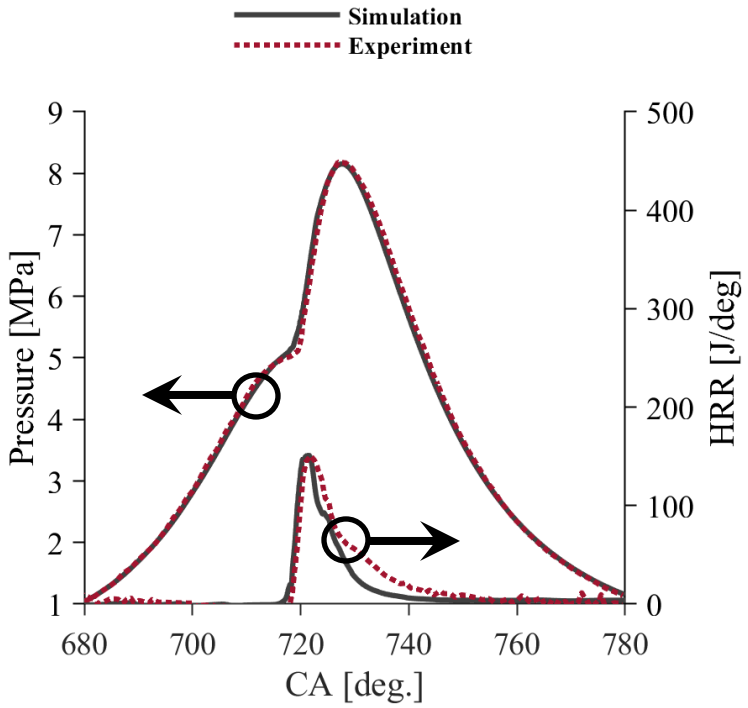

Figure 55: Validation of the numerically predicted in-cylinder pressure and heat released rate (HRR) obtained from the FGM hybrid combustion model incorporating preferential diffusion effects for ammonia-diesel DF case with 47 AES against measured data [83].

6.3.3 Effects of hydrogen addition

6.3.3.1 In-cylinder pressure and heat released rate

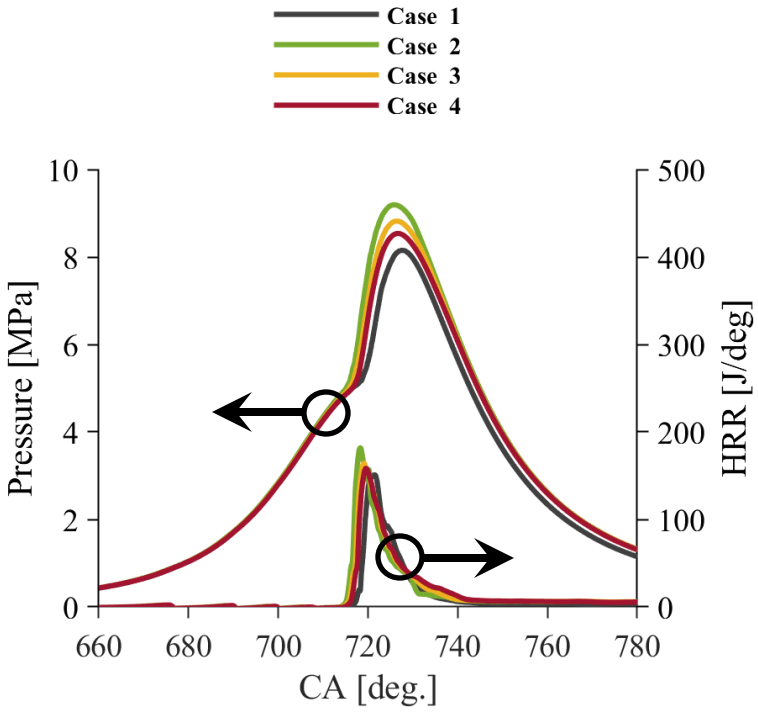

Figure 56: Comparison of in-cylinder pressure and HRR between case1, 2, 3 and 4.

The variations of in-cylinder pressure and HRR for the 47-AES (Case 1), 50-AES (Case 2), 70-AES (Case 3), and 80-AES (Case 4) cases are plotted in Figure 56. The hydrogen addition in highly ammonia-enriched gaseous mixtures cause the in-cylinder pressure to increase consistently with the increase of hydrogen substitution. The maximum in-cylinder pressure are 9.19, 8.82, 8.54, and 8.15 MPa for the cases with ammonia (hydrogen) induction of 50% AES (25% HES), 70% AES (20% HES), 80% AES (15% HES), and 47% AES (0% HES), respectively. This is mainly because the high diffusion coefficient of hydrogen enhances the gaseous mixture to become more homogenous, which enables more complete combustion and promotes the mixing process. Additionally, the high burning rate and reactivity of hydrogen increase the overall combustion rate and peak heat-release rate (as discussed below), resulting in an increase in the pressure rise rate and maximum in-cylinder pressure. As outlined in Section (6.3.1), the addition of hydrogen enhances the reactivity and mixing rates in mixtures containing high amounts of ammonia (the 70-AES and 80-AES cases) more than in mixtures with the lowest ammonia additions (the 47-AES

case). This results in broader distributions and higher peaks in high-temperature regions, as shown in Figure 53. Therefore, the percentage increases in the peak in-cylinder pressure are 8.21% and 4.74% between the 70-AES and 47-AES cases and 80-AES and 47-AES cases, respectively.

The heat releases rate for 47%, 50%, 70%, and 80% AES is plotted in Figure 56. The increase in hydrogen enrichments affects the five stages in the DF combustion engine. First, it shortens the pilot (diesel) fuel-ignition delay (1st stage), owing to the role of its high diffusivity in enhancing the mixing rate. Second, it roughly enhances the diffusion combustion stage due its availability within the diesel spray plume (note that hydrogen burns quickly because it is a highly reactive fuel). Third, it shortens the main (gaseous) fuel-ignition delay (3rd stage). Fourth, it speeds up the flame propagation of the first and late premixed combustion phases (4th and 5th stages). Thus, the increase in hydrogen energy content increases the peak heat-release rate, regardless of the ammonia contributions, which are 182, 164.22, 158.44, and 151.08 J/deg for the cases with ammonia (hydrogen) energy content of 50% (25%), 70% (20%), 80% (15%), and 47% (0%), respectively.

As earlier noted, the use of the Delta function for enthalpy under-estimates the heat loss, resulting in lower rates of the decrease in heat-release rate. Therefore, as hydrogen increases the peaks of the in-cylinder pressure and heat-release rate, their fall off of rates in hydrogen addition cases—Case 2, 3, and 4—are found to lower—due to the higher amounts of fuel combusted during the first phase of premixed combustion—than the case with no hydrogen addition (Case 1). This fact, combined with the low quenching gap of hydrogen causes the flame front to propagate near the walls, leading higher under-predictions of the heat loss.

6.3.3.2 In-cylinder temperature

The average in-cylinder temperature variations of the 47-AES (Case 1), 50-AES (Case 2), 70-AES (Case 3), and 80-AES (Case 4) cases are shown in Figure 57. As noted in the previous sub-section, the highly diffusive mobility and high burning rate of hydrogen increases the heat-release rate and, correspondingly, the rate of pressure rise and in-cylinder pressure peak. Thus, it is clear that the predicted in-cylinder temperature obtained using the FGM hybrid model with the greatest hydrogen enrichment (Case 2) shows an earlier and sharper increase than the other cases. This

indicates a shorter ignition delay and faster flame propagation throughout the combustion chamber. It should be noted that the ignition delay is shorter with the hydrogen induction regardless of the ammonia (low reactivity and high auto-ignition temperature fuel) energy contents.

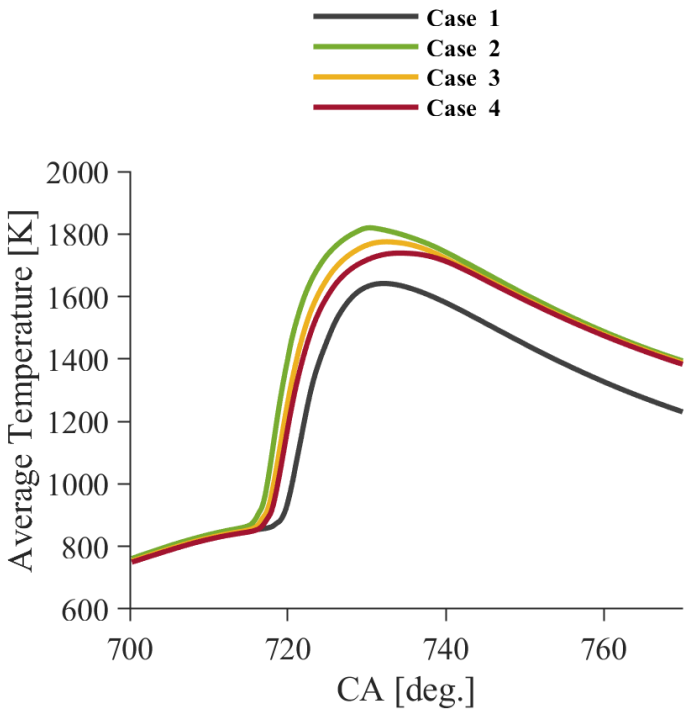

Figure 57: Comparison of the average in-cylinder temperature between the 47-AES (case 1), 50-AES AES (case 2), 70-AES AES (case 3) and 80-AES (case 4) cases.

However, the low burning rate of ammonia is found to affect the flame propagation of the premixed charge during the first and second premixed combustion phases, which is indicated by the increase and decrease of average in-cylinder temperature, respectively. Figure 57 shows that the average in-cylinder temperatures for the cases with hydrogen induction are roughly similar to each other in the second premixed combustion phase. This indicates that the flame propagation is low in the first premixed combustion phase, consistent with the ammonia induction, and thus results in higher amounts of fuel combusted, announcing a short combustion duration. . Consequently, the mixture with more ammonia-added increases the consumption rate in the late premixed combustion phase due to the greater availability of energy throughout the combustion chamber, leading to similar in-cylinder temperature from 740 CA deg onwards. On the other hand, the large gap between the cases with and without hydrogen states could be attributed to the under-prediction of heat losses.

6.3.3.3 Contour plots of temperature and species concentrations

Figure 58 shows the distribution of temperature and hydrogen at 730 CA deg and 750 CA deg between the 47-AES (Case 1), 50-AES (Case 2), 70-AES (Case 3), and 80-AES (Case 4) cases. The 730 CA deg corresponds to the crank angle of roughly the end (beginning) of the first (second) premixed combustion phase, which is indicated by the peak of in-cylinder pressure, as discussed in Section (2.3.1).The second crank angle (750 CA deg) corresponds to the crank angle of roughly the middle of the late premixed combustion. The temperature distributions throughout the combustion chamber at the end of the first combustion phase show significant differences between the cases with and without hydrogen induction. For instance, the combustion progresses slowly in the 47-AES case (Case 1), as the flame propagates close to the pilot fuel plume due to the low burning rate of the ammonia–air premixed mixture, whereas the progress of first premixed combustion stage is at a faster rate and higher intensity for the cases with hydrogen energy contents, owing to the high hydrogen flame speed. These observations indicate higher consumption rates of the liquid and gaseous fuels with the addition of hydrogen, resulting from further enhancement of the overall chemical rates caused by the high reactivity and burning rate of hydrogen. Therefore, the greater consumption of hydrogen is consistent with the hydrogen energy contents, as shown in Figure 58. For ammonia, the increase in the addition of hydrogen increases its consumption rate, as its distribution over the combustion chamber in Case 2 is lower than Case 1. In addition, its distribution in Cases 3 and 4 indicates the oxidisation of more ammonia compared to Case 1 (consider the differences in the ammonia energy content between the outlined cases). In addition to this, the higher consumption rate of ammonia in Cases 3 and 4 compared to Case 1 can be confirmed by comparing its distribution between the middle and beginning of the late premixed combustion phase.

Figure 59 compares the predicted variations of N_2O and NO_x engine-out emissions throughout the combustion chamber between the 47-AES (Case 1), 50-AES AES (Case 2), 70-AES AES (Case 3), and 80-AES (Case 4) cases. The shape of the NO_x concentration contours at both 730 and 750 CA deg show that the higher formation of NO_x occurs in the regions with higher gaseous fuel oxidisations. For example, the predicted NO_x production at the end of the premixed combustion phase is higher in the middle of geometry, matching the region of higher hydrogen consumption.

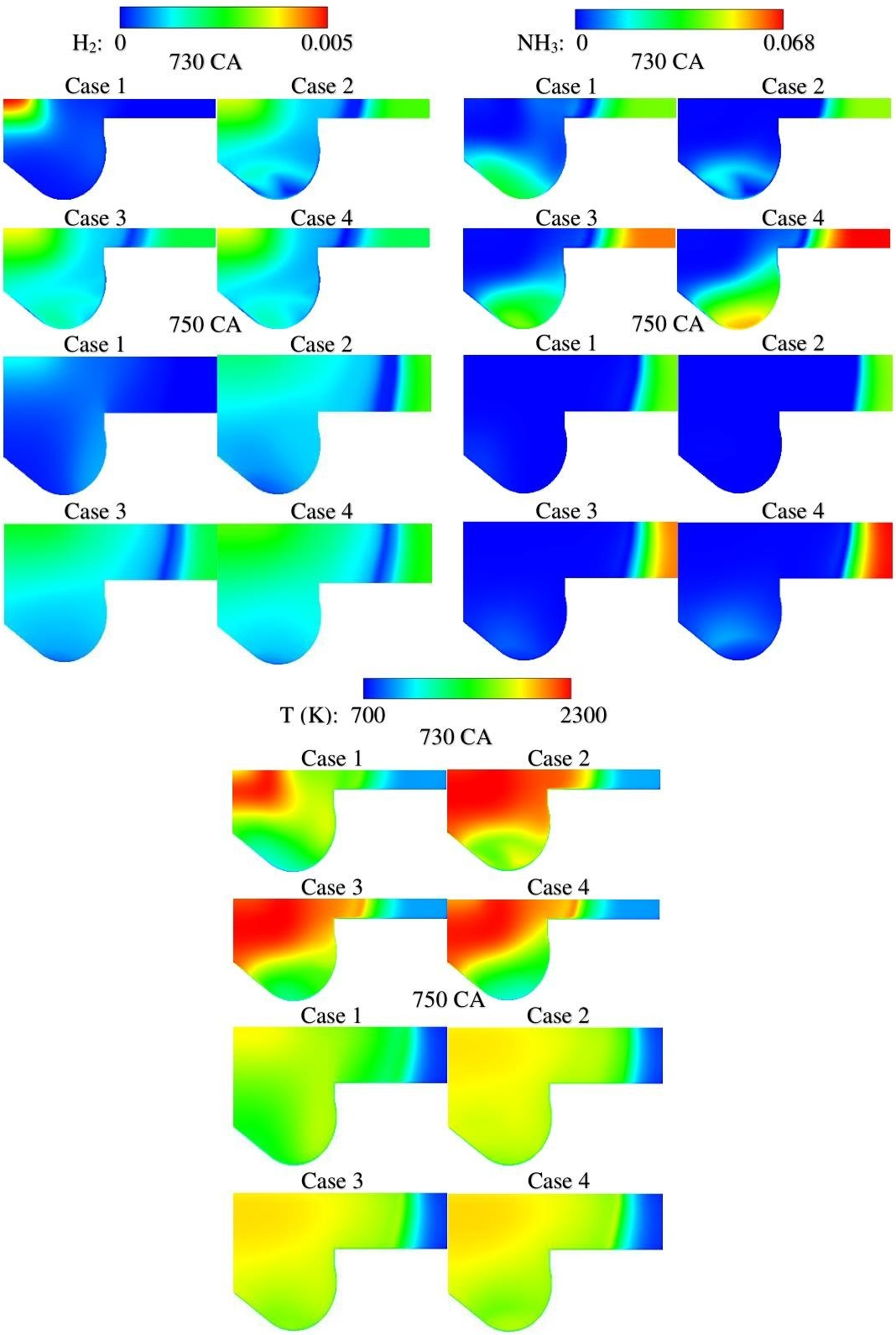

Figure 58: Contour plots of temperature and H_2 distributions at 730 CA deg and 750 CA deg between the 47-AES (case 1), 50-AES AES (case 2), 70-AES AES (case 3) and 80-AES (case 4) cases.

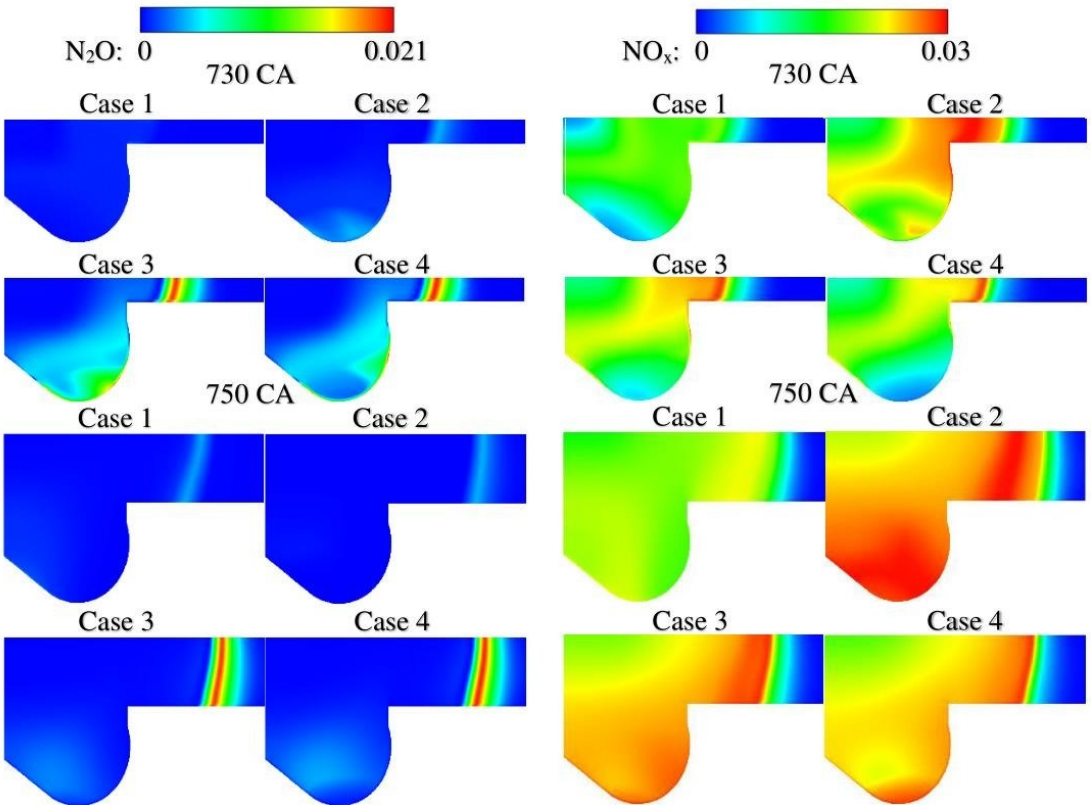

Figure 59: Variations of N_2O and NO_x engine-out emissions throughout the combustion chamber for the 47-AES (case 1), 50-AES AES (case 2), 70-AES AES (case 3) and 80-AES (case 4) cases.

Furthermore, NO_x is formed in a narrower range in the piston bowl, matching the region of higher ammonia oxidization. As previously discussed in Chapter 4, the effects of ammonia in NO_x formations are greater than those of hydrogen due to the abundant fuel-bound nitrogen in ammonia. However, due to the incorporation of thermal and prompt NO_x formations, the high temperature caused by the hydrogen combustion increases the NO_x production more than the ammonia cracking via chemical reactions. Consequently, the increase in the predicted NO_x mass fractions is proportionate with the increase in hydrogen gas injection.

In general, N_2O greenhouse emissions are produced in the low temperature areas of the main combustion flame and ammonia combustion in the expansion stroke (late premixed combustion phase). From Figure 59, it is seen that N_2O at roughly the end of the first premixed combustion phase is formed in the low-temperature flame regions (clearly seen in Cases 3 and 4 due to the high ammonia enrichment), whereas it is significantly formed during the late premixed combustion

phase in the regions with high ammonia oxidisation. The increase in ammonia increases the N_2O formations; however, the computed N_2O mass fractions in the 70-AES and 80-AES cases are quite similar due to the possible similar propagation rates of the flame front at 750 CA deg.

6.3.3.4 Indicated thermal efficiency and emissions

The performance characteristics are calculated based the gross indicated values due to the utilisation of the numerical work with a sector from IVC to EVO. The calculations were done to identify the work by integrating the area between pressure–volume curves with the aid of the trapezoidal rule. Then, the power and thermal efficiency were calculated. As all performance characteristics are proportional to one another, only the brake thermal efficiency is presented.

Figure 60 compares indicated thermal efficiency, NH_3, N_2O, CO, CO_2 emissions, and the unburnt ratio of NH_3 between the 47-AES (Case 1), 50-AES AES (Case 2), 70-AES AES (Case 3), and 80-AES (Case 4) cases. The comparison between the numerical (Case 1) and experimental (Exp.) is good agreement for thermal efficiency, NH_3 emission, N_2O emission, and the unburnt ratio of NH_3; however, the predicted CO and CO_2 emissions are over- and under-estimated compared to those obtained by experiment, respectively. This may have been caused by using reduced chemistry mechanisms.

The calculated thermal efficiency is 38.55% at 47% (0%), 44.54% at 50% (25%), 42.85% at 70% (20%), and 40.67% at 80% (15%) ammonia (hydrogen) energy content, respectively. The increase in thermal efficiency is caused by the addition of hydrogen to the ammonia–air mixture, which is credited to improved combustion due to the superior combustion rate caused by the high burning rate of hydrogen. The induction of hydrogen with 25% energy share (Case 2) results in a reduction in the indicated specific ammonia emission compared to the ammonia–air case (Case 1), indicating the role of hydrogen in enhancing the mixing rate and the overall chemistry rate owing to its high diffusivity and flame speed, respectively. The increases in the indicated specific ammonia emission in Cases 3 and 4 compared to Case 1 were mainly caused by the high ammonia induction in the former two cases. This does not indicate lower consumption of fuel, as (i) the thermal efficiency for Cases 3 and 4 are higher than for Case 1; (ii) the difference in the unburnt ratio of

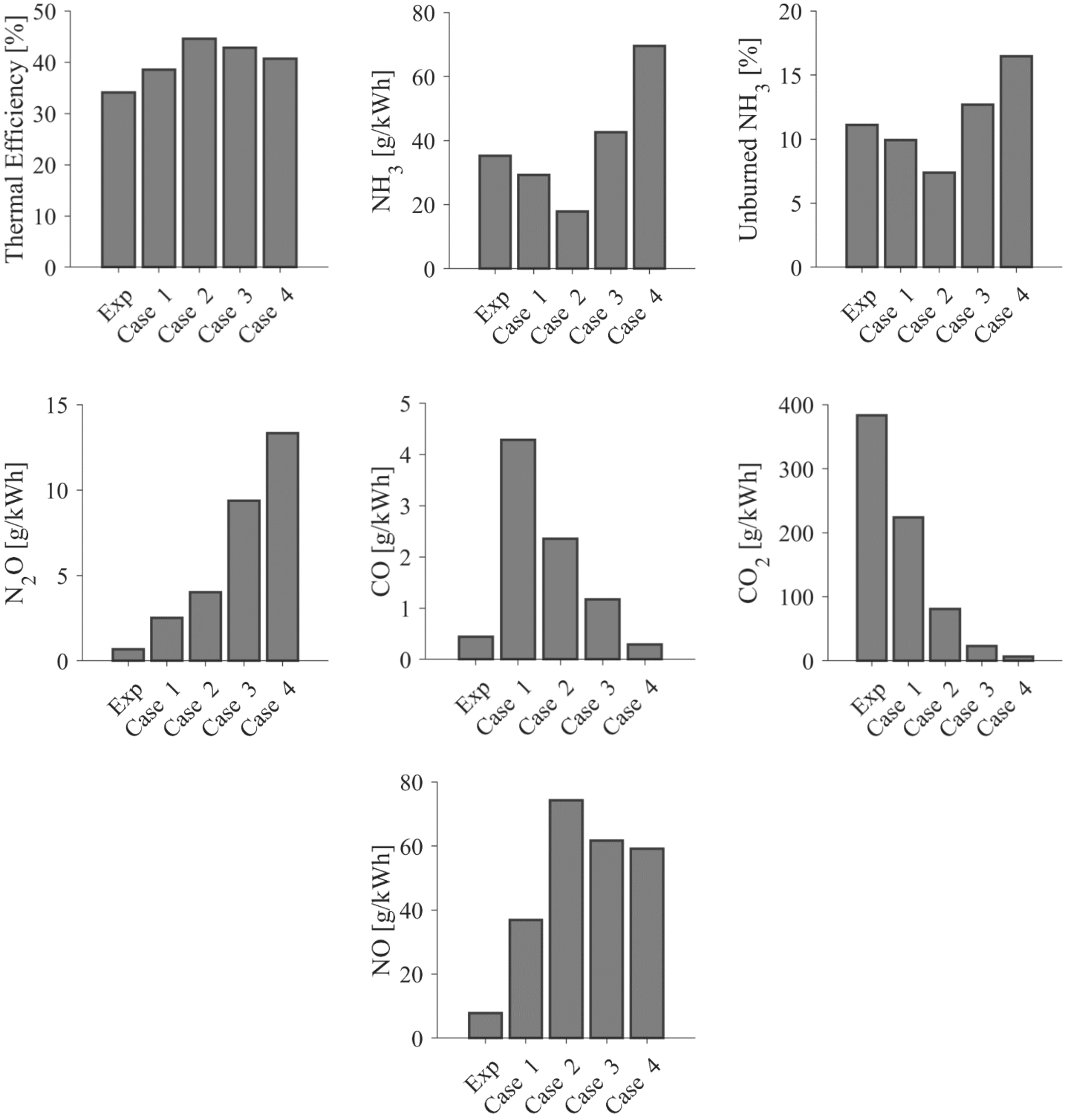

Figure 60: Comparison of brake thermal efficiency, NH_2, N_2O, CO, CO_2 emissions and unburned ratio of NH_2 between the experimental data, 47-AES, 50-AES AES, 70-AES AES and 80-AES cases.

ammonia is 2.9% between Cases 1 and 3 and 6% between Cases 1 and 4, indicating much greater ammonia oxidisation for the cases with high ammonia enrichment, resulting from the presence of hydrogen in the gaseous mixture.

Figure 60 reveals significant reductions in carbon-containing engine-out emissions consistent with the reduction of diesel in the fuel blends, resulting from the utilisation of environmentally benign alternative fuels such as hydrogen and ammonia. These alternative fuels are devoid of any carbonaceous compounds, so when they are used as surrogates for diesel fuel, the fuel blends condense the indicated specific CO and CO_2 to smaller values. The NO_x emissions are higher in agreements with the increase in hydrogen inductions due the higher temperature caused by the hydrogen combustion. Furthermore, the higher H/C ratio of the blended fuel (caused by the induction of ammonia and hydrogen to diesel), the better the homogeneity of the combustible mixture (due to the high hydrogen diffusivity) and the increase in in-cylinder pressure and therefore thermal efficiency (owing to the faster flame propagation of hydrogen) enable the diminution of CO and CO_2 emissions. As outlined in Section 6.3.3.3, the N_2O formation occurs in (i) low-temperature flame regions of the main combustion and (ii) ammonia combustion during the second phase of premixed combustion. Figure 60 shows that the enhancement of hydrogen by 25% energy content (Case 2) roughly doubles the indicated specific N_2O emissions compared to the case with no addition of hydrogen (Case 1). This indicates more ammonia consumption during the expansion stroke. In addition, the high N_2O formation at 750 CA deg, as seen in Figure 59, is formed in regions with high ammonia oxidisation. Therefore, it could be concluded that the effects of ammonia combustion in producing N_2O seem to dominate over its production in low-temperature flame regions in the first phase of premixed combustion. Hence, the indicated specific N_2O emissions can be considered a measure of the energy released by ammonia, and thus its formation is proportional to the ammonia energy content.

6.3.4 Effects of pilot fuel injection timing

As seen in Figure 60, the different hydrogen inductions to the ammonia–air gaseous mixture (Cases 2, 3, and 4) show disparities regarding the predicted thermal efficiency and emissions. Case 2 achieves the highest thermal efficiency and lowest indicated specific N_2O emissions; however, the 25% energy share of diesel (hydrogen) yields the formation of more carbon-based (NO_x) emissions

compared to Cases 3 and 4. On the other hand, in spite of the lowest CO and CO_2 emissions, the high contribution of ammonia in the blended fuel increases the N_2O emissions, which are about 300 times more potent than CO_2, and decrease the thermal efficiency compared to Cases 2 and 3. Therefore, Case 3 can be considered as the best test case. In this section, the pilot fuel-injection timing was altered at three different crank angles, 9 deg (the one presented in Section 6.3.3), 14 deg, and 19 deg before top dead centre (BTDC), for Case 3 only aiming to optimise the performance, combustion, and emission characteristics.

6.3.4.1 In-cylinder pressure and heat release rate

Figure 61 shows the predicted in-cylinder pressure and heat released rate with different start-of-injection (SOI) timing at 9 deg, 14 deg, and 19 deg BTDC. The advancement of SOI increases the peaks of in-cylinder pressure, which are 10.09 MPa at 19 deg BTDC, 9.63 MPa at 14 deg BTDC and 8.82 MPa. In general, the primary idea of retarding the injection timing is to elongate the ignition delay, allowing for increased mixing and evaporating time for the liquid fuel with the gaseous fuels. Therefore, this enhances the homogeneity between diesel and the gaseous mixture, shifting the combustion regime from mixing-controlled to premixed combustion.

The effects of diesel injection timing can be split into three parts; the ignition process of diesel, the first premixed combustion phase, and the late premixed combustion phase. From Figure 61 , it is shown that the retarding SOI results in the earlier onset of pressure increase, indicating the earlier initiation of combustion (first effect). As a result, the first phase of premixed combustion occurs at higher rates, causing the predicted peaks of in-cylinder pressure to increase in proportion with the retarding of the SOI. The enhancement of the maximum in-cylinder pressure with earlier SOI is caused by the increase in the amount of fuel combusted during the compression stroke. In contrast, the late phase of premixed combustion, representing the combustion of the remaining premixed charge after the peak of in-cylinder pressure, is found to be at a lower intensity for the cases with advancing SOI, resulting in lower rates of in-cylinder pressure fall-off. This can be attributed to the high consumption of fuels in the first phase of premixed combustion with retarding SOI, leading to a relative reduction in the propagation speed of the flame front during the expansion stroke. Apart from the start of ignition, it is surprising to note that the heat released rates

agree in shape and magnitude for the presented test cases, which could be caused by the small differences in the pilot fuel injection timing.

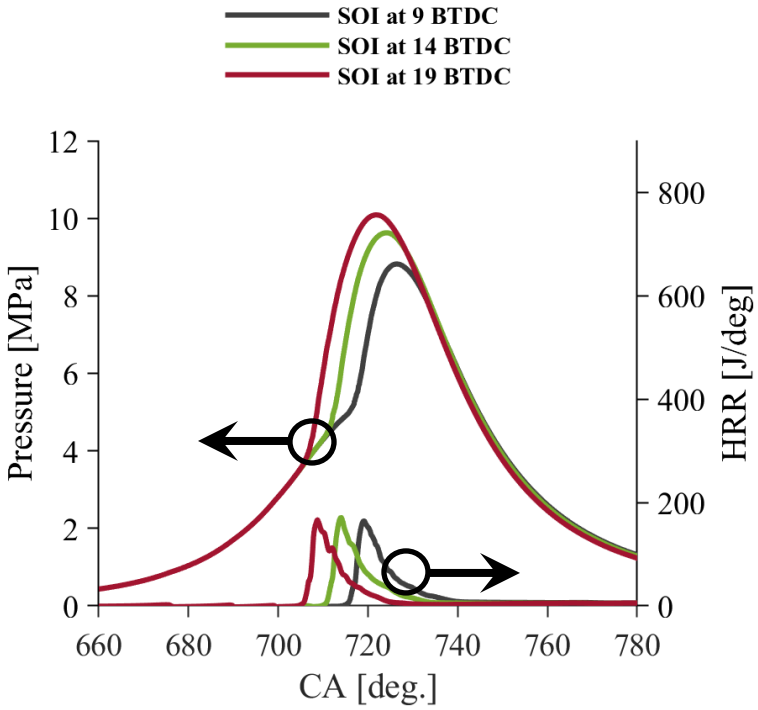

Figure 61: Predicted in-cylinder pressure and heat released rate at different start of injection (SOI) timing at 9 deg, 14 deg and 19 deg BTDC.

6.3.4.2 In-cylinder temperature

Figure 62 presents the average in-cylinder temperature at 9 deg, 14 deg, and 19 deg SOI. The average in-cylinder temperature for the case with SOI at 19 deg is greater than that of SOI at 9 deg and SOI at 14 deg by 5.44% and 2.41%, respectively. Therefore, The flame's average temperature confirms the observations above stating that the retarding SOI promotes the burning rate of the flame front due to the greater amount of fuel consumed during the compression stroke. As the peak of the in-cylinder temperature roughly matches the peak of the in-cylinder pressure, the greater higher rate of the former drop is consistent with the earlier SOI. This supports the idea that the rate of the flame propagating towards the leftover gaseous mixture in the late premixed combustion phase is lower with retarding SOI due to the higher consumption of the gaseous mixture during the compression stroke. It is important to remember that the piston in the compression stroke

moves towards TDC, which in turn increases the pressure in the combustion chamber and could cause the flame propagation to increase, leading to higher intensity rates in the first stage of premixed combustion.

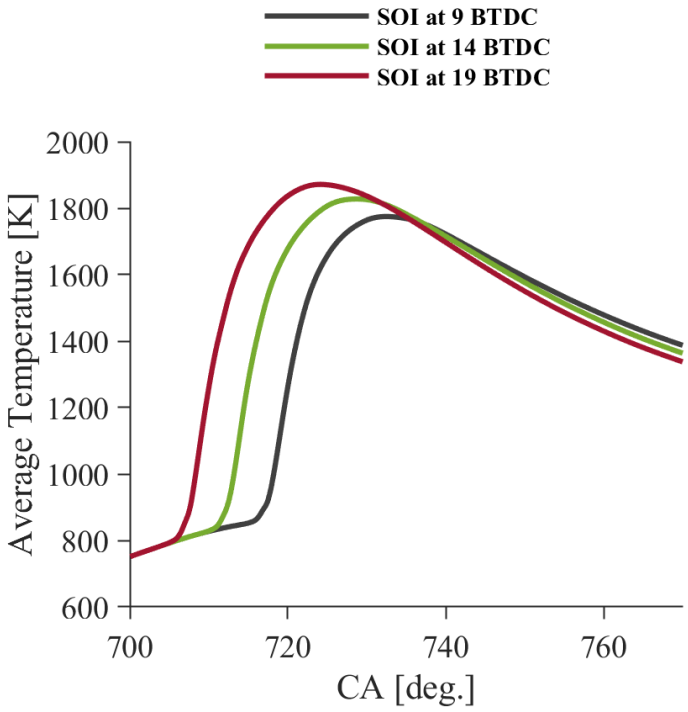

Figure 62: Comparison of average in-cylinder temperature between different SOIs at 9 deg, 14 deg and 19 deg.

6.3.4.3 Contour plots of temperature and species concentrations

Figure 63 shows the spatial distributions of temperature and hydrogen at 730 CA deg and 750 CA deg for different SOIs at 9 deg, 14 deg, and 19 deg BTDC. The contour plots of temperature, hydrogen, and ammonia can explain the effects of retarding the injection timings of diesel on the combustion characteristics noted above. From Figure 63, it is seen that the flame prorogation at 730 CA deg is spread out to a larger degree in proportion with the retarding SOIs; however, its distribution is found to be similar for all cases at 750 CA deg. Thus, it can be concluded that the rate propagation of the flame front towards the remaining unburnt gaseous mixture is greater in the late phase of premixed combustion during the expansion stroke as the SOI advanced.

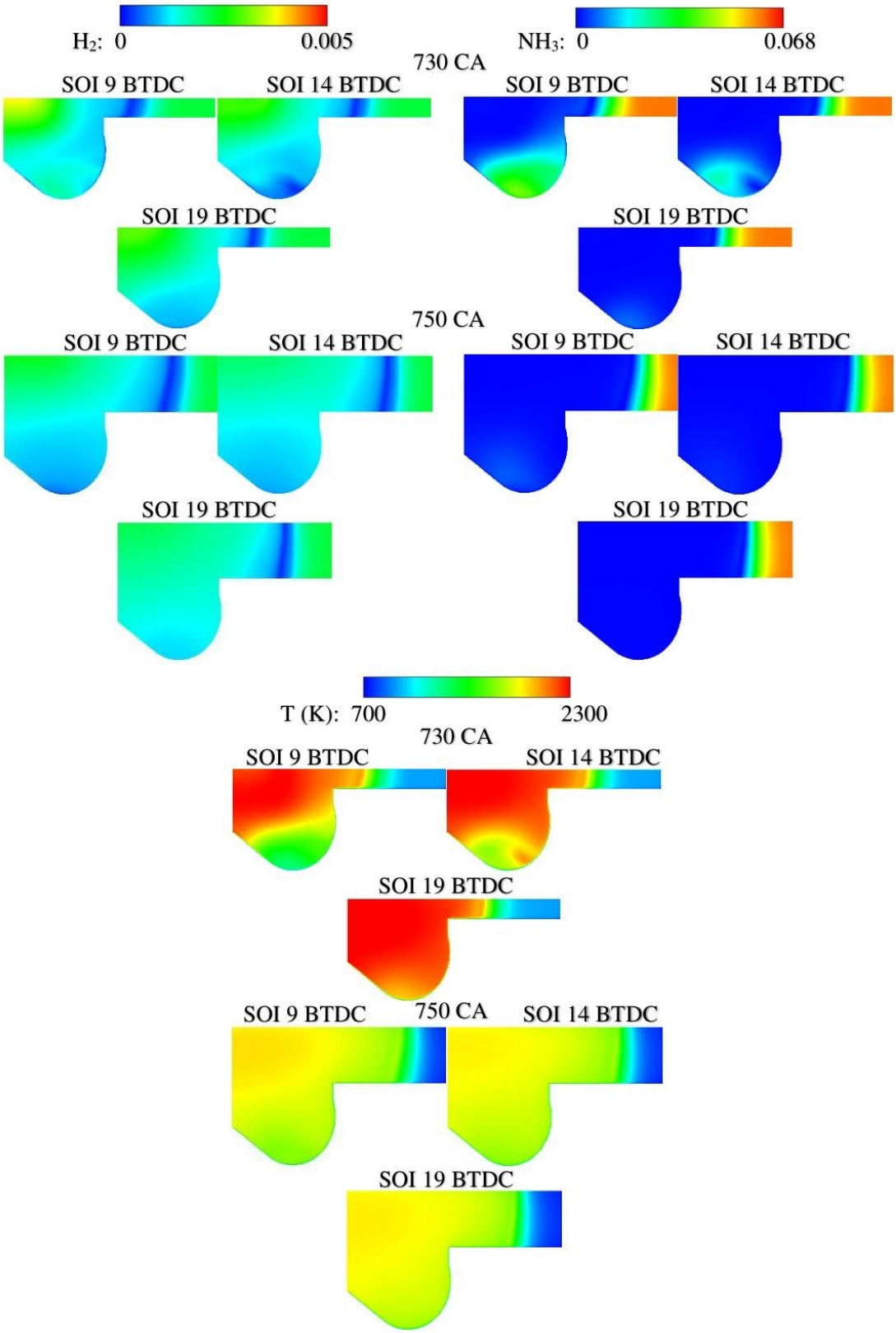

Figure 63: Contour plots of temperature and H2 distributions at 730 CA deg and 750 CA deg for different SOIs at 9 deg, 14 deg and 19 deg BTDC.

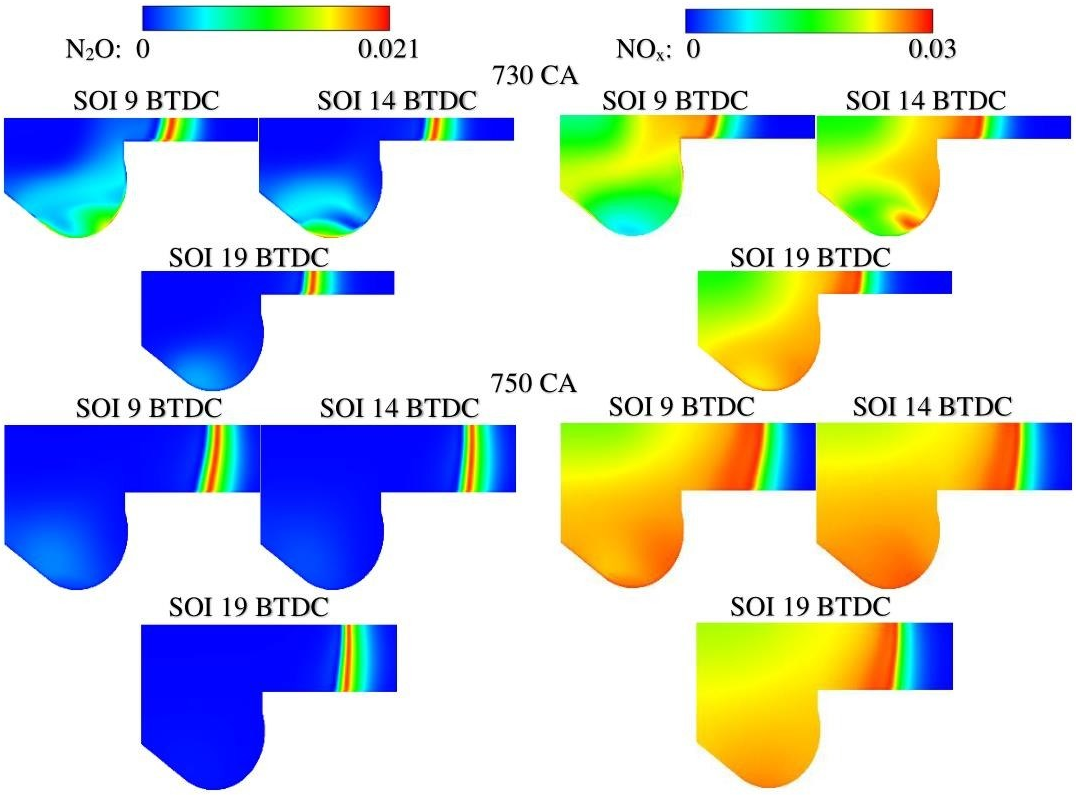

Figure 64: Contour plots of N2O and NOx distributions at 730 CA deg and 750 CA deg for different SOIs at 9 deg, 14 deg and 19 deg BTDC.

This observation can be confirmed via the ratio of hydrogen and ammonia consumption rates at 730 CA deg and 750 CA deg. For example, the greater ratio of ammonia oxidisation rates between the presented crank angles is consistent with advancing SOI. As well, a similar observation of ammonia is found for hydrogen, as seen in Figure 63. Furthermore, a similar argument for the distributions of NO_x and N_2O emissions show that the advancement of SOI enhances their formations during the late phase of premixed combustion, as shown in

Figure 64. The conclusion to draw from these observations is that the continuously higher rate of temperature fall-off during the expansion stroke with retarding SOI results in a lower exhaust temperature and, accordingly, the key emissions of hydrogen and ammonia.

6.3.4.4 Indicated thermal efficiency and emissions

Figure 65 compares of indicated thermal efficiency, NH_3, N_2O, CO, CO_2, NO_x emissions and unburned ratio of NH_3 between different SOIs at 9 deg, 14 deg and 19 deg BTDC. In general, the

thermal efficiency is comparable between the investigated cases; however, its lower computed value is in agreement with advancing SOI. This consistency between the higher thermal efficiency and advancing SOI lies in the lower rate propagation of the flame front in the last phase of premixed combustion. It is true that the retarding SOI increases the ignition delay period of diesel, providing more mixing time between the liquid and gaseous fuel and therefore reducing the heterogeneity. As a result, more fuel is consumed in the first premixed combustion stage during the compression stroke, increasing the peak of in-cylinder pressure. However, the first premixed combustion phase lasts for only a very short time compared to the second premixed combustion phase, as the latter lasts from peak in-cylinder pressure until EVO. In addition to this, the increase in in-cylinder pressure and temperature do not always increase the thermal efficiency as there are some important parameters to consider. For example, Tao et al. [184] reported that the thermal efficiency decreases and then increases with advancing SOI. As highlighted by authors, the thermal efficiency is significantly affected by CA50, defined as the crank angle at which 50 % of the heat from combustion has been released. When the combustion center is close to the optimal CA50 moment, the thermal efficiency increases, and when the combustion center deviates from the optimal CA50 moment, the thermal efficiency decreases. As seen in Figure 61, CA50 significantly differs in the presented cases and, as a result, it can be concluded the that SOIs at 14 deg and 19 deg BTDC seem not to be the best injection timing for further optimisations of the performance and emissions characteristics. The trends of thermal efficiency can be confirmed by the slightly greater indicated specific NH_3 emissions, where it agrees with the advancing SOI. As mentioned above, the continuously lower rate of flame propagation with retarding SOI during the expansion stroke yields a lower exhaust temperature. For this, the indicated specific CO, CO_2, NO_x, and N_2O pollutant emissions are lower with earlier SOIs, as seen in Figure 65.

In general, the disparities are not significant due to the small difference between the crank angles of injection timing. However, these parametric studies were conducted to provide an initial overview of the investigation of the addition of hydrogen to an ammonia–diesel CI DF combustion engine using low-temperature combustion strategies such as RCCI, where the liquid fuel is injected roughly 65 BTDC. The newly developed FGM combustion model is capable of simulating the RCCI combustion; however, the pressure should be incorporated as an additional control variable, as discussed later.

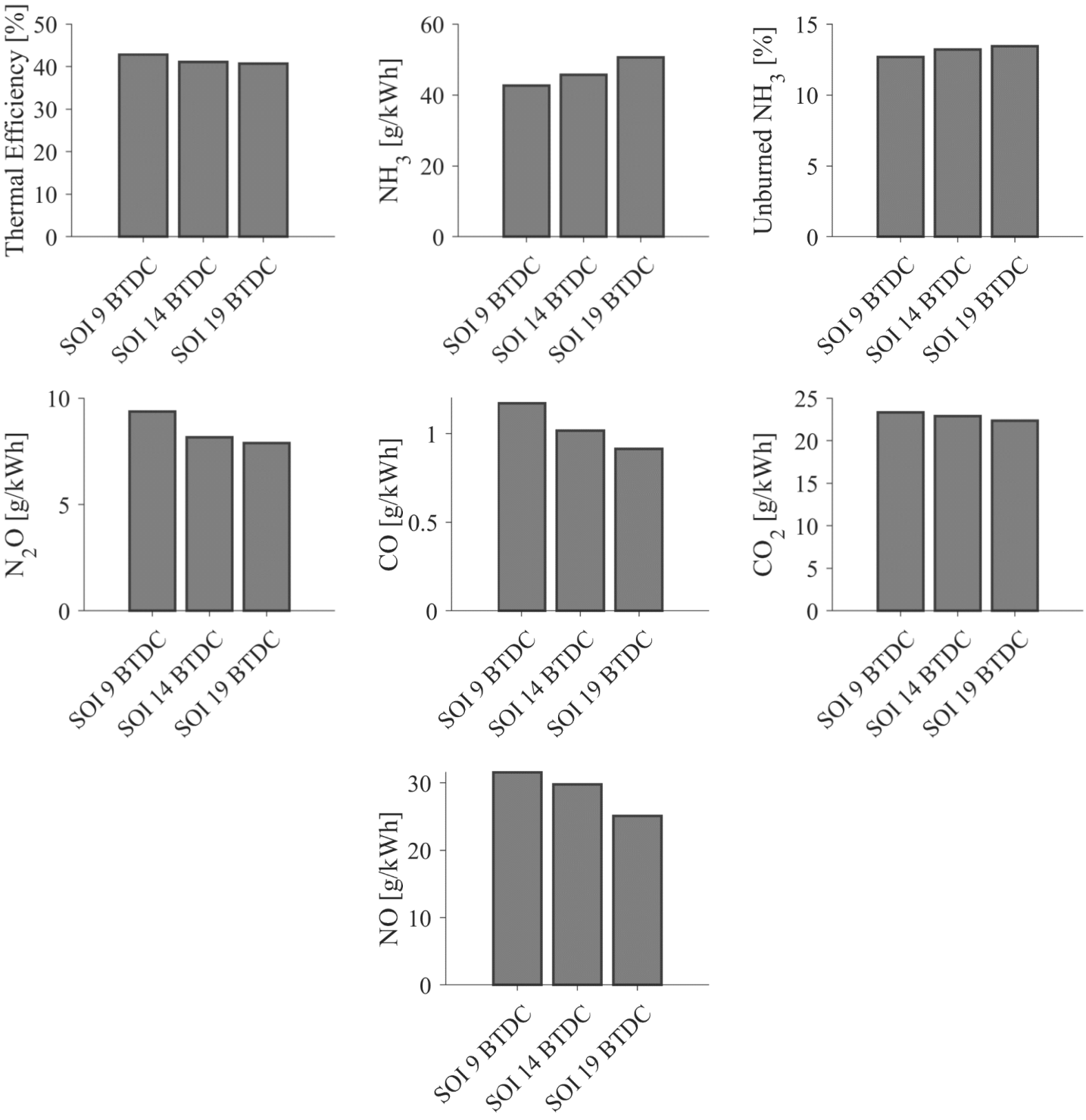

Figure 65: Comparison of brake thermal efficiency, NH_3, N_2O, CO, CO_2, NO_x emissions and unburned ratio of NH_3 between different SOIs at 9 deg, 14 deg and 19 deg BTDC.

6.3.5 Alternative green diesel fuel

In this section, the alternative diesel counterpart fuel (HVO) is utilised as a pilot fuel to investigate the effects on the performance, combustion, and emission characteristics. To demonstrate the maximum effects of HVO, the investigation is carried out with Case 3, as it contains the highest pilot fuel energy content (25%) between among the cases with the hydrogen–ammonia gaseous mixture.

6.3.5.1 Premixed and diffusion FGM manifolds

Figure 66 shows the distribution of H_2, NH_3, and temperature obtained from diffusion flamelets with the incorporation of preferential diffusion effects as a function of the mixture fraction and progress variable for Cases 3 and 5. As mentioned earlier, the mixture fraction is incorporated as a control variable to describe the mixing process. Therefore, the use of HVO results in an increase in temperature with respect to the mixture fraction, indicating that the mixing rate is higher with HVO owing to the HVO's high cetane number. In contrast to diesel, the distribution of high hydrogen concentration in the diffusion manifold is clearly very low, as shown in Figure 66; however, this does not mean that the chemical reaction rate is lower with HVO. For example, in Chapter 5, a comparison of hydrogen variations in non-premixed manifold between that with and without the incorporation of preferential diffusion effects is plotted in Figure 42. The use of the unity Lewis number results in a much higher peak of hydrogen throughout the manifold but yields a lower high-temperature spot. Thus, a similar argument can be applied to the temperature and hydrogen behaviours with HVO in the FGM diffusion manifold. For ammonia, the regions of mixture fraction between 0.2 and 0.4 and progress variable between 0 and 0.4, respectively, show a slightly earlier reduction, which could point to a prior oxidisation of ammonia with HVO compared to diesel. Figure 67 compares the premixed manifolds for H_2, NH_3, and temperature with the incorporation of preferential diffusion effects as a function of the mixture fraction and progress variable for Cases 3 and 5. The premixed flame of HVO is distributed in a very narrow range, indicating the possible lower ignitability of HVO at extremely lean conditions compared to diesel.

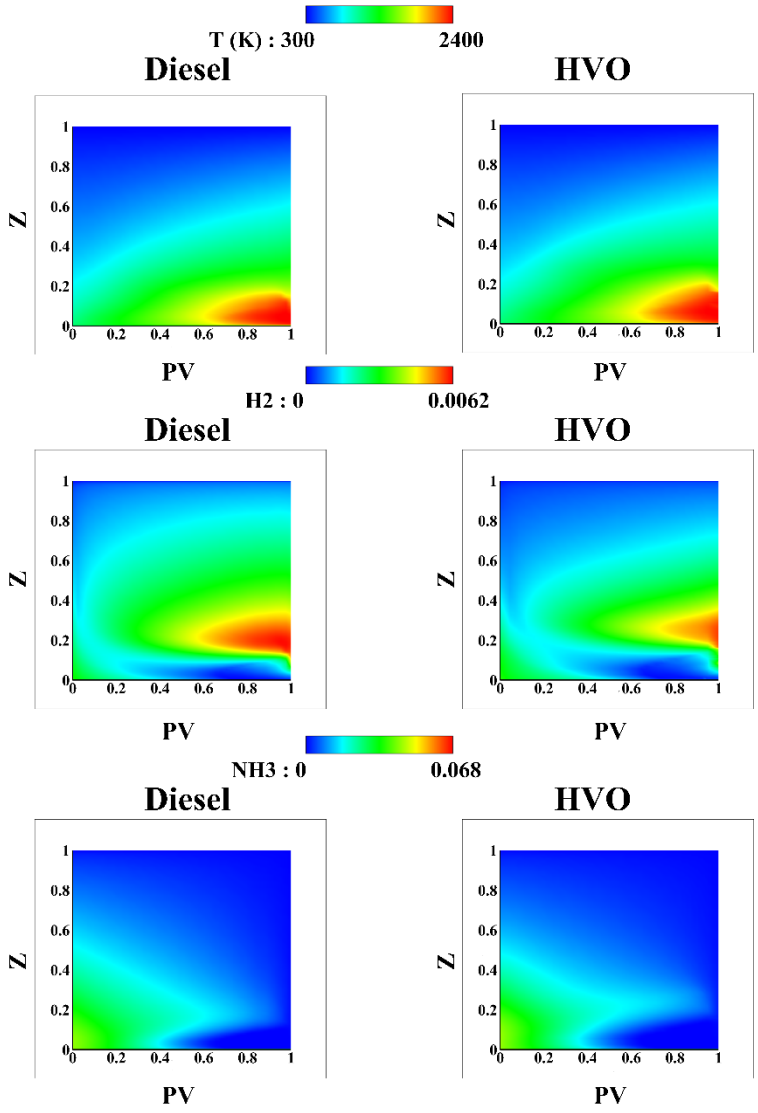

Figure 66: Non-premixed manifolds for H_2, NH_3 and temperature with the incorporation of preferential diffusion effects as a function of the mixture fraction and progress variable for case 3 and 5.

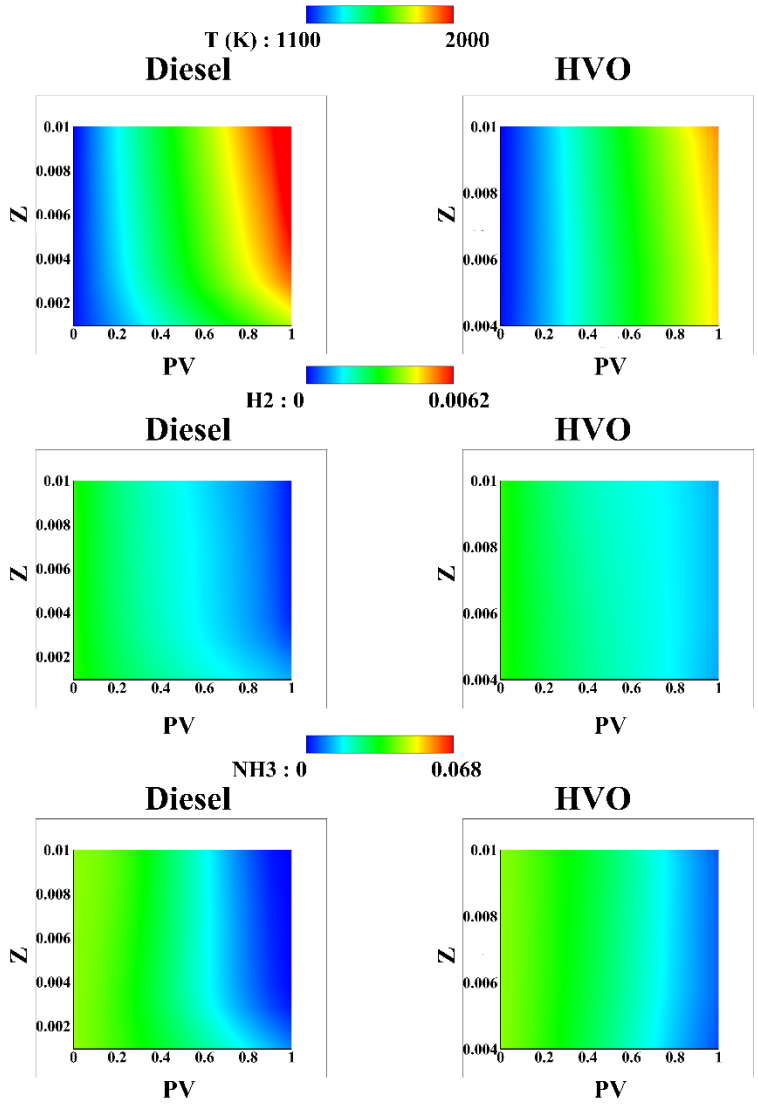

Figure 67: Premixed manifolds for H_2, NH_3 and temperature with the incorporation of preferential diffusion effects as a function of the mixture fraction and progress variable for case 3 and 5.

6.3.5.2 In-cylinder pressure and heat released rate

Figure 68 compares the predicted in-cylinder pressure and heat released rate between diesel and HVO. In general, both trends of in-cylinder pressure and heat released rate are significantly similar for diesel and HVO due to the low contribution of the pilot fuel in the fuel blends (25%). However, the high cetane number of HVO—defined as a measure of fuel ignitibility—results in a shorter

ignition delay, as shown in Figure 68. Aside from the HVO cetane number, HVO fuel droplets penetrate through the air stream easier than diesel, leading to a more homogenous combustible mixture. Therefore, good mixing results in lower physical ignition delay [185, 186]. The shorter ignition delay with HVO shifts the peak of in-cylinder pressure compared to diesel by 1.1 CA deg. Apart from the earlier increase in heat released rate caused by the shorter ignition delay with HVO, as shown in Figure 68, the heat released rate is comparable between diesel and HVO due to the domination of gaseous fuel energy contents in the blended fuel. However, the higher and narrower peak of HVO (indicated by the greater drop rate) suggests a shorter combustion duration.

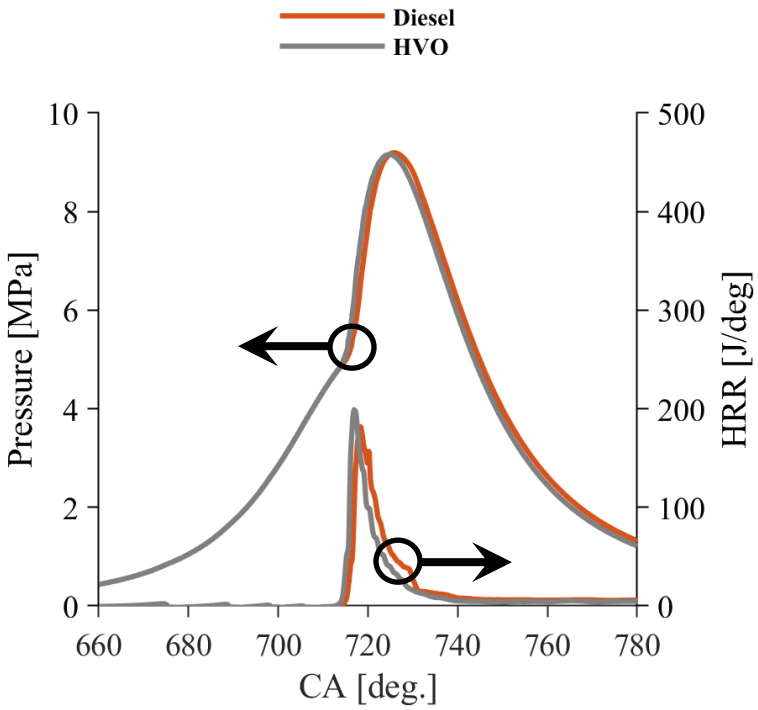

Figure 68: A comparison of predicted in-cylinder pressure and heat released rate between diesel and HVO.

6.3.5.3 In-cylinder temperature

The variations in average in-cylinder temperatures for diesel and HVO are plotted in Figure 69. The high cetane number of HVO results in an earlier increase in temperature compared to diesel. However, the diesel in-cylinder temperature trend shows a greater peak value, and its increase during the first premixed combustion phase lasts for a longer duration. These observations are caused by the shorter ignition delay with HVO, which reduces the energy released during the

premixed combustion and therefore the maximum combustion temperature, as highlighted by Huang et al. [187]. Moreover, the good mixing resulting from the utilisation of HVO provides better variations of the reacting mixture throughout the combustion chamber, translating into lower local temperatures [185, 186]. The obvious differences in the in-cylinder temperatures for HVO and diesel suggests that the HVO exhaust gas temperature is lower, indicating reductions in carbon-based emissions [188].

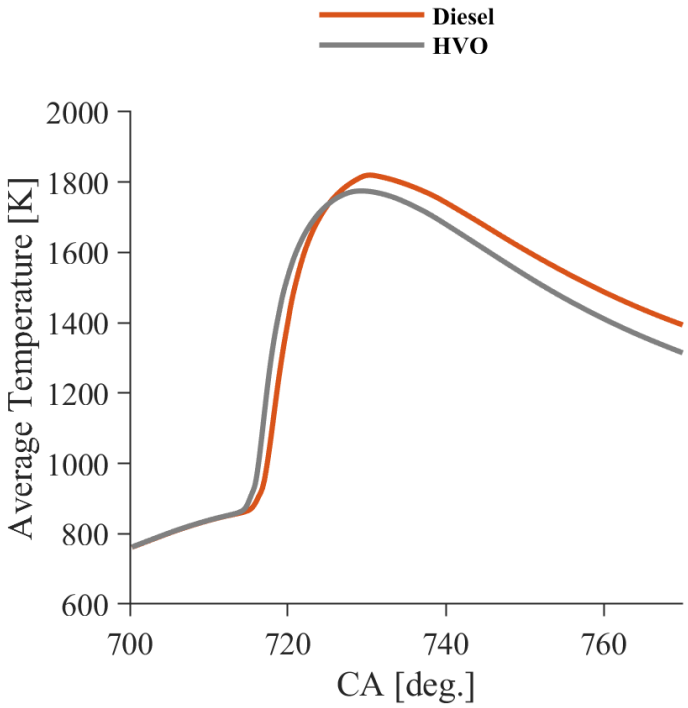

Figure 69: Comparison of average in-cylinder temperature between diesel and HVO.

6.3.5.4 Contour plots of temperature and species concentrations

Figure 70 shows the variations of temperature and H_2 throughout the combustion chamber at 730 CA deg and 750 CA deg for diesel and HVO, respectively. The contours of the liquid fuel demonstrates the disparities noted in the average in-cylinder temperatures. As seen in the temperature contours, the combustion progresses with diesel at higher intensity and burning rates

due to the faster propagation of the flame front. Therefore, the relative changes in temperature distribution between 730 CA deg and 750 CA deg—during the late phase of premixed combustion—are higher for diesel. This leads to the oxidisation of more gaseous fuels—ammonia and hydrogen—with diesel, as displayed in Figure 70. While the distribution of hydrogen with HVO is in a narrower range at 750 CA deg, the consumption rate of hydrogen with diesel is higher. This is because (i) the high hydrogen concentration near the cylinder wall at 750 CA deg is lower with diesel, indicating that the flame front propagates towards the regions with higher hydrogen enrichment and (ii) the difference in the hydrogen mass fraction between 730 CA deg and 750 CA deg is higher with diesel.

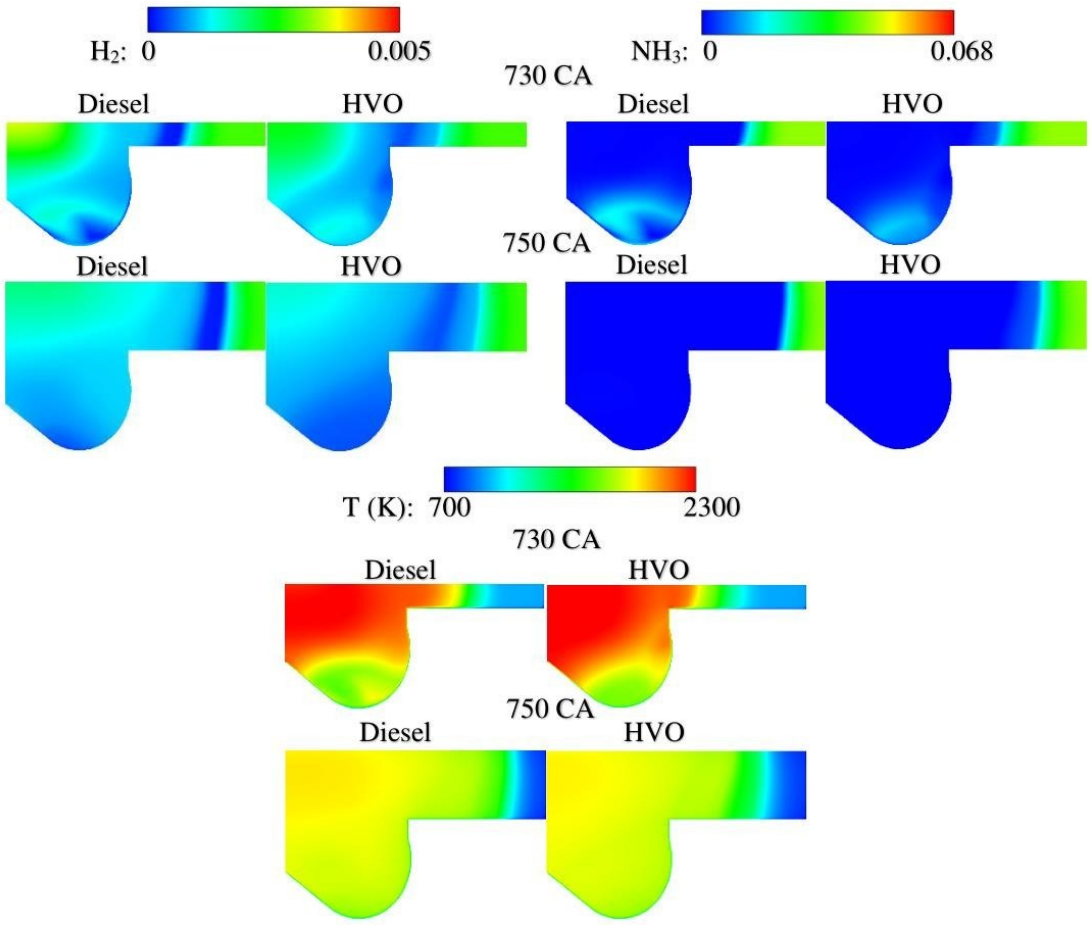

Figure 70: Contour plots of temperature and H2 distributions at 730 CA deg and 750 CA deg for diesel and HVO.

This confirms that the better mixing ratio between the liquid and gaseous mixture with HVO leads to better distribution of premixed mixture, resulting in a lower local temperature as highlighted in Section (6.3.5.3).

As the high-temperature combustion is favoured for NO_x formations, the faster flame propagation with diesel increases its formation, as shown in Figure 71. Surprisingly, the N_2O emission is much higher with HVO, even with the lower consumption rate of ammonia and slower flame propagation during the expansion stroke. This observation needs special treatment in terms of carrying out a sensitive analysis of the chemical reactions in the three-dimensional simulation as N_2O is found to be similar between diesel and HVO, as presented in Chapter 4.

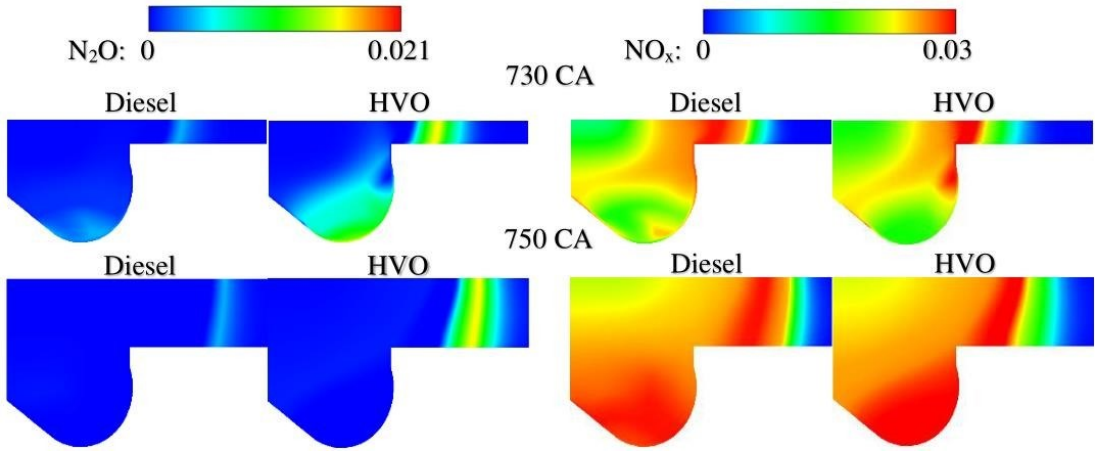

Figure 71: Contour plots of NO_x and N_2O distributions at 730 CA deg and 750 CA deg for diesel and HVO.

6.3.5.5 Indicated thermal efficiency and emissions

Figure 72 shows a comparison of indicated thermal efficiency, NH_3, N_2O, CO, CO_2, NO_x emissions, and the unburnt ratio of NH_3 between diesel and HVO. The differences between HVO and diesel in terms of the performance and harmful emissions are not expected to be large, as the energy contents of hydrogen and ammonia in the presented test case are 25% and 50%—higher than the pilot fuel contribution (25%). The utilisation of HVO slightly reduces the thermal efficiency due to the lower intensity and low burning rate of the late phase of premixed combustion and, as a result, increases indicated specific ammonia emissions.

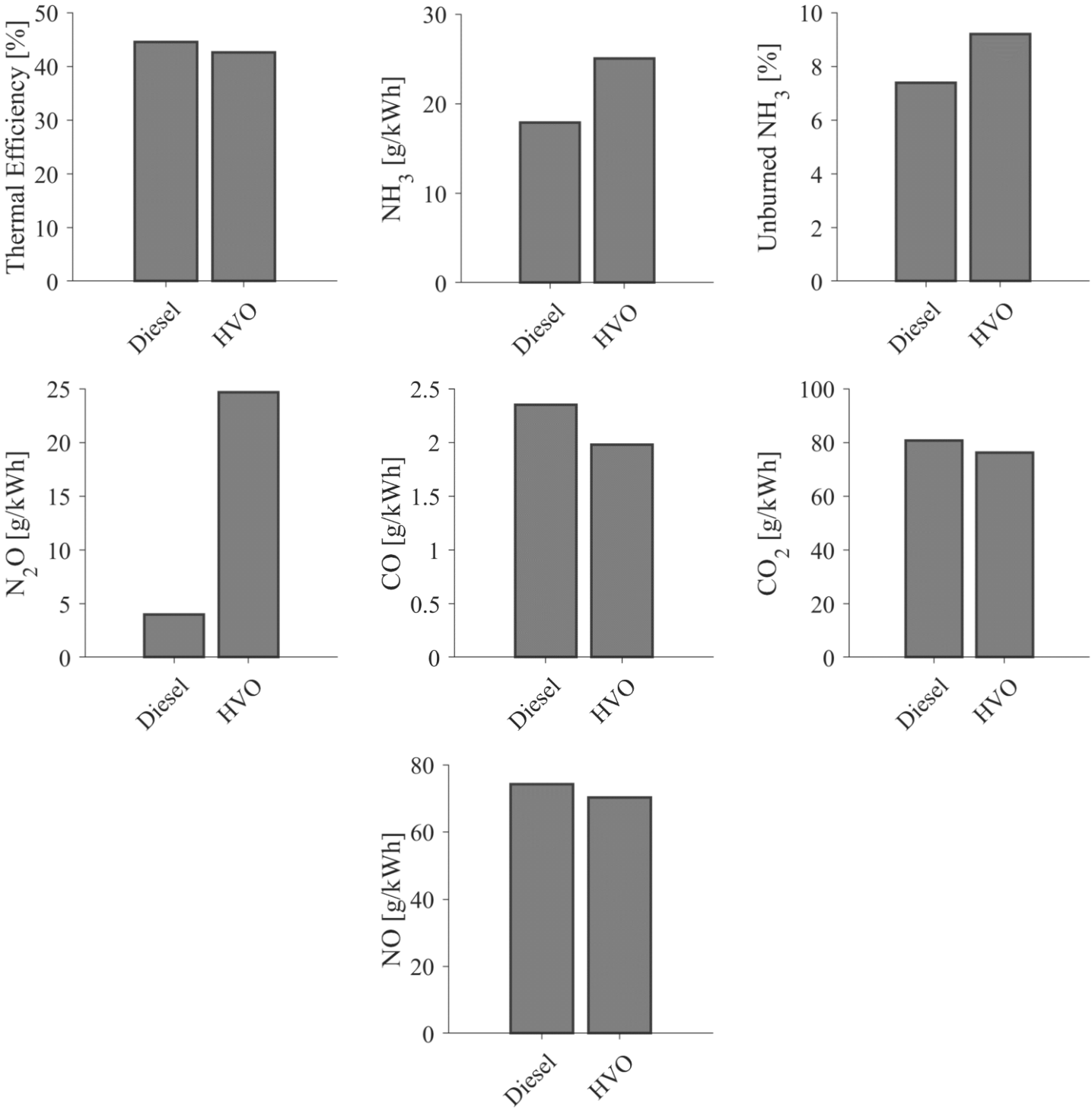

Figure 72: Comparison of brake thermal efficiency, NH_3, N_2O, CO, CO_2, NO_x emissions and unburned ratio of NH_3 between diesel and HVO.

As previously mentioned, the energy released during the premixed combustion is reduced with HVO, leading to lower average in- cylinder temperature. Consequently, the formations of CO, CO_2, and NO_x are suppressed, as can be seen in Figure 72. Interestingly, HVO results in much higher N_2O emissions than diesel, which requires a detailed investigation into the chemical reaction path associated with N_2O to find a solid explanation.

6.3.6 Reactivity controlled compression ignition (RCCI) combustion

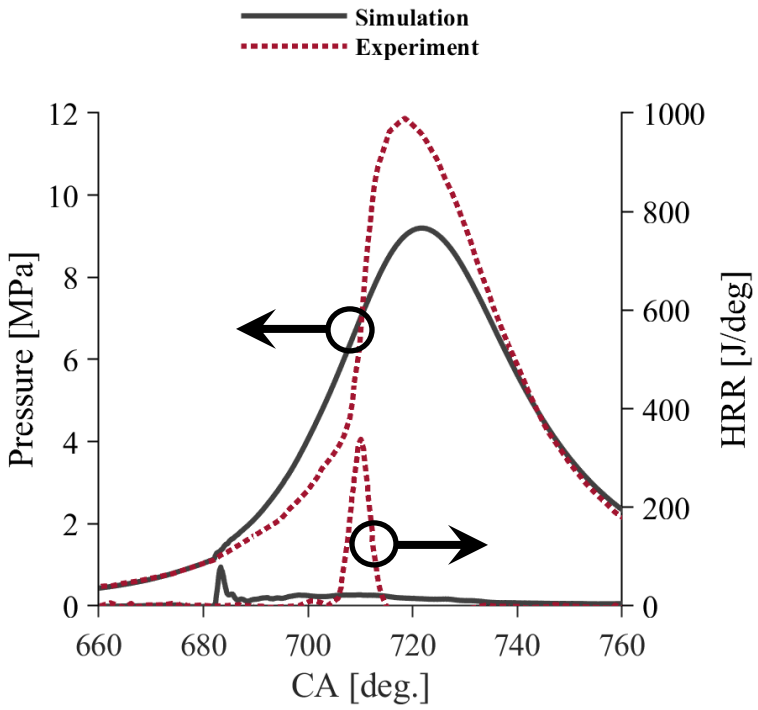

Figure 73: Comparison of predicted and measured in-cylinder pressure and heat released in RCCI combustion mode for case 1.

Figure 73 compares the in-cylinder pressure and heat released rate obtained by the numerical simulation means against the experimental data carried out by Niki el al. [83]. In the presented case, the injection timing of diesel was set at 45 BTDC, aiming to increase the homogeneity between the liquid and gaseous fuels to mitigate emissions. From Figure 73, it is seen that the newly extended FGM hybrid combustion model failed to capture the ignition delay. As mentioned

in Section (3.4.4), the choice of the control variables are key in establishing a successful FGM combustion model to accurately predict any application. As the control variables should describe the major physical and chemical phenomena expected to occur in the application, the ignition delay is an essential difference between the conventional CI combustion and low-temperature combustion concepts, such as the RCCI combustion mode. Therefore, the ignition delay should be described by an extra control variable, which is pressure.

The ignition phasing largely depends on the source term of the progress variable. The source of progress variable, in turn, depends on the production and consumption rates of species throughout the domain. The pressure and temperature are important variables, significantly affecting the progress variable source term. Since the ignition delay is long for low-temperature combustion modes, the production of a large number of flamelets at different pressure levels is required. As the one-dimensional simulations are performed at constant pressure, a new set of simulations is necessary for each different pressure level during tabulation. Ideally, a very high resolution in the pressure levels is needed to predict ignition during CFD simulations. Generally speaking, conventional CI combustion does not require the construction of the look-up table at different pressure levels, as the ignition delay is extremely short compared to RCCI combustion.

6.4 Conclusion

This chapter presented parametric studies aiming to keep up with the vision of independence from fossil fuels combined with the decarbonisation of internal combustion engines. Due to the issues associated with the storage and transportation of hydrogen, ammonia is a highly promising alternative fuel ,as it contains 17.6% hydrogen by weight (hydrogen carrier), is carbon-free, and is easier to store and transport than hydrogen. Therefore, the developed FGM hybrid combustion model implemented in Chapter 5 was applied to simulate an ammonia–diesel CI DF combustion engine and then validate the numerical results against those obtained by an experimental single-cylinder diesel–ammonia CI DF engine carried out by Niki et al. [83]. Then, parametric studies were carried out to clarify the role of the addition of hydrogen to highly ammonia-enriched gaseous mixtures in promoting the mixing, reaction, and burning rates. In addition, the fuel blends were varied, aiming to reduce the pollutant engine-out emissions by reducing the diesel energy content

up to 5%. For the same purpose, diesel was replaced with an alternative diesel fuel (HVO). Furthermore, pilot fuel-injection timings were retarded to provide more homogenous mixture between diesel and gaseous fuel (ammonia and hydrogen).

The main findings of the present study are listed below.

1. The hydrogen addition in highly ammonia-enriched gaseous mixtures causes the in-cylinder parameters to increase consistent with the increase of hydrogen energy content regardless of the ammonia substitution. This is because the high diffusion coefficient and burning rate of hydrogen increase the overall combustion rate and peak heat release rate and, correspondingly, the pressure rise rate, maximum in-cylinder pressure, and average in-cylinder temperature.
2. For all test cases, the increase in hydrogen results in greater thermal efficiency, which is credited to enhanced combustion due to superior combustion given the high hydrogen burning rate. However, the NO_x was the penalty for the increased addition of hydrogen. The increase in alternative carbon-free fuels—ammonia and hydrogen—results in a reduction of carbon-containing emissions.
3. The retarding SOI of diesel increases the physical ignition delay. As a result, the homogeneity between the diesel and premixed mixture is enhanced. Therefore, the first phase of premixed combustion occurs at higher rates, causing the predicted peaks of in-cylinder pressure to increase due to the higher amounts of fuels consumed during the compression stroke. This shortens the combustion duration and leads to lower propagation of the flame front towards the leftover gaseous mixing in the late phase of premixed combustion during the expansion stroke, resulting in a lower exhaust gas temperature.
4. The increase in thermal efficiency is proportional to advancing SOI due to the greater consumption rate of the remaining fuel during the expansion stroke. Consequently, SOI retarding reduces the indicated specific CO, CO_2, NO_x, and N_2O.
5. HVO reduces the physical ignition delay and energy released during the premixed combustion due to its high cetane number and mixing property, respectively, resulting in a lower average in-cylinder temperature. Therefore, the thermal efficiency, NO_x, CO, and CO_2 are decreased. Interestingly, HVO results in much higher N_2O even though the unburnt ammonia is higher.

6. The heat loss to walls is under-predicted, and the under-prediction, in turn, increases for the combustion with higher temperature. This could be caused by the use of Delta function for enthalpy, which assumes that the enthalpy fluctuation is negligible.
7. The control variables incorporated during the FGM tabulation are not sufficient to accurately predict the notably long ignition delay of low-temperature combustion concepts, such as the RCCI combustion mode. Therefore, pressure should be added to the mixture fraction, progress variable, and enthalpy.

Chapter 7: Conclusion and future work

Fossil fuel depletion and the need to enact steep carbon emission cuts have prompted research into the implementation of environmentally benign alternative fuels, such as hydrogen and ammonia. The diesel CI engine produces unsatisfactory carbon-containing emissions in comparison with the gasoline spark ignition (SI) engine. This project employed numerical modelling and simulations methods to conduct a comprehensive investigation of hydrogen and ammonia fuel utilisation in compression ignition DF engine combustion. The project also investigated how diesel pilot fuel in DF engine can be replaced with alternative fuel such as hydro-treated-vegetable oil to make the DF engine even more environmentally friendly. The project developed a flamelet generated manifold hybrid combustion model to accurately predict the multi-stage combustion process of hydrogen and ammonia fuel blends under DF combustion. The project investigated the role of preferential diffusion effects on predicting combustion and emission characteristics of hydrogen blended DF combustion.

The newly developed FGM hybrid combustion model demonstrated its capability of capturing the mixing process, diffusion combustion, premixed combustion and the transition between these two combustion modes for hydrogen-blended DF applications such as diesel-hydrogen and diesel-ammonia-hydrogen fuel blends. In addition, the improved model predicted the ignition process, flame propagation and heat released rate reasonably well for hydrogen-blended DF via preferential diffusion effects. The accurate predictions of such a complex application were accompanied with relatively low computational cost due to the working procedure of the FGM combustion model. Nevertheless, results showed that the heat loss was under-estimated by the improved version of FGM hybrid combustion model, which might be caused by convolving Delta function rather than Beta function for enthalpy during the construction of PDF tables when coupling tabulated data with the CFD solver.

Many combustion modelling approaches have been implemented to simulate the multi-phase combustion mode of DF combustion engine. For example, SAGE combustion model suffers from highly computational costs along with large gradient predictions due to the absence of turbulence-chemistry interaction. In addition, the ECFM combustion model was developed to simulate the DF combustion by incorporating the mixing state, which increased its working procedure and accordingly the computational time. Moreover, the multi-zone combustion model under-predicted

the peak values of in-cylinder pressure and heat release rate in diesel-hydrogen DF combustion process [161]. In contrast to the aforementioned combustion modelling approaches, the newly developed FGM hybrid combustion model demonstrates accurate predictions of the hybrid DF combustion modes using different alternative gaseous (main) and liquid (pilot) fuels with reasonably good computational cost.

The newly developed FGM hybrid combustion models was thoroughly validated against the experimental data of high hydrogen content DF engine combustion carried out by Tsujimura et al. [52], as discussed in Chapter 5, and against the experimental results of ammonia-enriched mixture DF engine combustion carried out by Niki et al. [83], as discussed in Chapter 6. The validation studies show good agreement between predictions and experimental data during the compression, combustion and expansion stages. Chapter 5 presented the potential of the developed FGM combustion model in capturing the high hydrogen content DF multi-stage combustion and, in addition, the potential of high diffusivity of alternative green fuel like hydrogen. Chapter 6 provided a parametric study aiming at reducing the key emissions of hydrogen and ammonia. The proposition of the best test case is based on the performance and emissions characteristics. The highest indicated thermal efficiency and lowest N_2O emissions were recorded to Case 2 and, however, its carbon-based (NO_x) emissions were the highest due to the greatest energy contents of diesel (hydrogen) between the other test cases. In comparison with Case 2 and Case 3, Case 4 achieved the lowest carbon-based emissions, NO_x emissions and indicated thermal efficiency, whereas the N_2O emissions, which is about 300 times more potent than CO_2, were the highest. The HVO-case (Case 5) displayed a comparable indicated thermal efficiency and lower carbon-based and NOx emissions in comparison with that of diesel-case (Case 2); however, its N_2O emissions were significantly higher. Thus, Case 3 is considered as the best test case.

7.1 Summary of outcomes

This PhD generates following four key research outcomes by providing solutions to the Thesis objectives listed in the introduction chapter.

Research outcome 1 – Fundamental study of laminar premixed and non-premixed flames relevant to hydrogen blended DF combustion under engine relevant conditions.

A detailed parametric study was carried out to elucidate fundamental understanding of laminar premixed and non-premixed flames under engine relevant conditions. The study investigated flame structure and propagation of hydrogen-air and hydrogen-ammonia-air gaseous mixtures with two pilot fuels, diesel and HVO, over a wide range of engine relevant conditions. These assessments of the premixed and non-premixed flames were made by varying the initial pressure conditions. The effects of molecular transport properties of species were studied using simulations with a unity Lewis number (constant transport model) or a non-unity Lewis number (mixture-averaged transport model). An instability threshold for both the initial conditions of preheating temperature and pressure was set for the premixed flame because of the obvious instabilities caused by the correlated effects between the high initial pressure and oxidiser temperature. The effects of flow velocity gradients on mixing and reaction rates in diffusion flames by varying the initial strain rates were discussed.

Research outcome 2 – Development of a physics-based FGM hybrid combustion model to predict multistage combustion process of DF combustion

The research developed a FGM hybrid combustion model coupling laminar premixed and laminar non-premixed flamelet databases incorporating preferential diffusion effects. The modelling strategy employed a two-step correction to incorporate preferential diffusion effects: (i) in the one-dimensional laminar flamelet calculations by using the mixture-averaged transport model to include both the non-unity and inconstant species Lewis numbers and (ii) in the three-dimensional simulations by including additional diffusion coefficient terms in the transport equations of the control variables to account for such effects in the turbulence environment. The incorporation of such effects was achieved using two C programming codes to (i) calculate the additional terms of diffusion coefficients and (ii) modify the default diffusion terms, based on the unity Lewis number assumption, aiming to demonstrate the effects of the molecular transport properties on the performance, combustion and emissions characteristics during the one- and three-dimensional simulations run-time. The consequences of incorporating preferential diffusion effects were assessed using simulations carried out with unity- and non-unity Lewis number approaches. In addition, the importance of the two-step correction was clarified by considering the non-unity

Lewis number effects in both one- and three-dimensional simulations and in one-dimensional simulations only.

Research outcome 3 – Development a CFD-based engine combustion modelling framework coupling FGM hybrid combustion model to simulate hydrogen blended DF engine combustion

The research developed a CFD based engine combustion modelling framework incorporating the newly developed FGM hybrid combustion model in the CFD solver. The dual-fuel combustion consists of three distinct phases: first, the diffusion combustion of the pilot fuel with some portion of gaseous mixture drawn to the pilot fuel spray plume; second, the transition between the diffusion combustion and premixed combustion; and third, premixed combustion of gaseous mixture combined with the unburnt pilot fuel. Therefore, the model was developed by first generating a diffusion flamelet database using the counterflow canonical configuration to represent the diffusion combustion; second, generating a premixed flamelet database using the freely propagating canonical configuration to represent the premixed combustion; and third, combining both premixed and non-premixed databases by replacing the mixture fraction values of less than 0.01 part in the non-premixed flamelets with the premixed flamelets to represent the transition between the diffusion combustion and premixed combustion. The last step was based on the assumption that the flamelets with a mixture fraction value of 0.01 or greater lie inside the spray of the pilot fuel (i.e., high gradient of mixture fraction indicating non-premixed combustion), whereas flamelets with mixture fraction values below 0.01 lie outside the spray plume (i.e., low gradient of mixture fraction indicating premixed combustion). The threshold mixture fraction value was used because it represents the quantity of fuel in the mixture. To capture the physical and chemical phenomena expected to occur in the CI DF combustion engine, three control variables were employed: mixture fraction (to describe the mixing process), reaction progress variable (to represent the transition from mixing to ignition) and enthalpy (to represent the heat loss).

Research outcome 4 – Perform a parametric study to analyse hydrogen blended ammonia combustion in a DF engine

The research investigated utilisation of alternative fuels such as ammonia in a compression ignition DF engine using the newly developed FGM hybrid combustion model. A parametric study was conducted to evaluate how hydrogen can be blended with ammonia in a DF engine to improve the performance of a diesel-ammonia DF engine. As ammonia is a hydrogen carrier and is easier to store and transport than hydrogen, the fuel mixtures of the parametric studies were based on increasing and decreasing the ammonia and pilot fuel energy content, respectively, with some addition of hydrogen. Thus, the effects of increasing the energy contribution of environmentally clean alternative fuels – hydrogen and ammonia – on the emissions characteristics were demonstrated. The effects of high hydrogen diffusivity and burning rate in enhancing the poor combustible properties of a highly enriched ammonia mixture on the performance and combustion characteristics were investigated. In addition to the utilisation of alternative fuels in the gaseous mixture, the liquid fuel (diesel) was replaced by its counterpart alternative fuel (HVO) to study the potential additional mitigating effects of HVO on carbon-based emissions.

7.2 Summary of novel fundamental scientific contributions

The key original findings of the thesis are outlined below.

- The preferential diffusion effects were incorporated by means of two-step correction in the one- and three-dimensional simulations to describe the molecular transport properties of a highly hydrogen- and ammonia-enriched gaseous mixture in a CI DF combustion engine.
- A novel FGM hybrid combustion model was developed to predict the five-stage combustion process of a CI DF combustion engine, namely the pilot fuel ignition delay, diffusion combustion, main fuel ignition delay, first premixed combustion and late premixed combustion.
- One of the first investigations of the ammonia-hydrogen gaseous mixture with two pilot fuels – diesel and HVO – in a conventional CI DF combustion engine to achieve clear combustion was conducted.

- Intensive investigations were performed to establish databases of the important key parameters characterising premixed and non-premixed DF flames in a wide range of relevant engine conditions.
- Reduction and optimisation of HVO surrogate fuel – hexadecane – chemistry mechanisms using the Directed Relation Graph with Error Propagation (DRGEP) technique with highly accurate validation against both kinetic modelling and experimental data were carried out.

7.3 Future work

- Further extension of the newly developed FGM combustion model incorporating preferential diffusion effects is required for successful predictions of a multiphase low-temperature combustion concept by adding pressure as an additional control variable to capture the long ignition delay period of the pilot fuel.
- Further optimisation of the extended FGM combustion model is needed to accurately predict heat loss during the last phase of premixed combustion by implementing the Beta function rather than the Delta function for enthalpy.
- Investigations of the accuracy of different transport models – namely, multicomponent, constant Lewis number transport models – are important from a numerical standpoint to address their impacts on predicting preferential diffusion effects.
- Analysis of the N_2O emission chemical reaction paths is needed to provide a solid justification for their significant formation with HVO in comparison with diesel.
- Further development of the FGM combustion model is needed to simulate a dual direct hydrogen-diesel CI DF combustion engine.
- Development and optimisation of a pilot fuel injector is important to control the NO_x engine-out emissions by adjusting the amount of the liquid fuel mass flow rate to a certain level of NO_x emissions.
- The two phase or even multiple phase injections of the pilot fuel are needed to increase the indicated thermal efficiency and decrease the engine-out emissions.

7.4 Technical challenges

In this project, numerical simulations were carried out using ANSYS Fluent. Such commercial CFD software is commonly used and consists of a user-friendly interface that facilitates CFD work. ANSYS Fluent is a closed and robust source; thus, utilisation of the default settings (i.e. the systematic working procedure of the turbulence and/or combustion models) provides accurate predictions. In addition, ANSYS Fluent enhances its standard features with the aid of a user-defined function (UDF), allowing the variables and equations to be customised. For example, a UDF can be used to change the calculations of variables (e.g. density) or to add additional equations through the user-defined scalar. However, the effects of solution convergence are consistent with the level of modifications performed using a UDF, even if it is minor. Furthermore, segmentation faults arose during the simulation run-time when many changes were made. For instance, the transport equation of un-normalised progress variable variance, Equation (3.67), comprises a chemical source term that is not included in the default equation written by the Fluent establisher. This source term can be added through the text user interface (TUI), and it works without including the additional terms of preferential diffusion effects. However, a segmentation fault was obtained when the preferential diffusion coefficients were incorporated into the transport equations of the control variables; thus, the source term was neglected. Further to this, not all solution variables can be accessed using UDF as explicitly stated in the Fluent UDF manual.

The aforementioned technical challenges pose significant limitations in further developments of a combustion model as powerful as the FGM (i.e. incorporating the pressure as an additional term to predict the RCCI combustion mode). Therefore, I firmly and highly recommend using open-source software, such as OpenFOAM, which is more flexible, for further development and optimisation.

Appendices

A Chemistry mechanisms HVO-like (Hexadecane) fuel.

The HVO results were produced using the following reduced chemistry mechanisms of hexadecane, $NC_{16}H_{34}$, (HVO-like fuel). These mechanisms were reduced by the author from 155 species and 645 chemical reactions [107] to 53 species and 288 reactions using the Directed Relation Graph with Error Propagation (DRGEP) technique. The final chemistry mechanisms consist of 71 species and 394 reactions after adding ammonia and NOx sub-mechanisms [106].

	SPECIES CONSIDERED	PHASE	CHARGE	MOLECULAR WEIGHT	TEMPERATURE LOW	TEMPERATURE HIGH	ELEMENT COUNT H	C	O	N	AR	HE
1.	O2	G	0	3.1999E+01	300	5000	0	0	2	0	0	0
2.	N2	G	0	2.8013E+01	300	5000	0	0	0	2	0	0
3.	CO2	G	0	4.4010E+01	300	5000	0	1	2	0	0	0
4.	H2O	G	0	1.8015E+01	300	5000	2	0	1	0	0	0
5.	CO	G	0	2.8011E+01	300	5000	0	1	1	0	0	0
6.	H2	G	0	2.0159E+00	300	5000	2	0	0	0	0	0
7.	OH	G	0	1.7007E+01	300	5000	1	0	1	0	0	0
8.	H2O2	G	0	3.4015E+01	300	5000	2	0	2	0	0	0
9.	HO2	G	0	3.3007E+01	200	3500	1	0	2	0	0	0
10.	H	G	0	1.0080E+00	300	5000	1	0	0	0	0	0
11.	O	G	0	1.5999E+01	300	5000	0	0	1	0	0	0
12.	CH3O	G	0	3.1034E+01	300	5000	3	1	1	0	0	0
13.	CH2O	G	0	3.0026E+01	300	5000	2	1	1	0	0	0
14.	HCO	G	0	2.9019E+01	300	5000	1	1	1	0	0	0
15.	CH2	G	0	1.4027E+01	250	4000	2	1	0	0	0	0
16.	CH3	G	0	1.5035E+01	300	5000	3	1	0	0	0	0
17.	CH4	G	0	1.6043E+01	300	5000	4	1	0	0	0	0
18.	C2H2	G	0	2.6038E+01	300	5000	2	2	0	0	0	0
19.	C2H3	G	0	2.7046E+01	300	5000	3	2	0	0	0	0
20.	C2H4	G	0	2.8054E+01	300	5000	4	2	0	0	0	0
21.	C2H5	G	0	2.9062E+01	300	5000	5	2	0	0	0	0
22.	HCCO	G	0	4.1030E+01	300	4000	1	2	1	0	0	0
23.	CH3CHO	G	0	4.4054E+01	300	5000	4	2	1	0	0	0
24.	CH2CHO	G	0	4.3046E+01	300	5000	3	2	1	0	0	0
25.	C2H6	G	0	3.0070E+01	300	5000	6	2	0	0	0	0
26.	C3H3	G	0	3.9057E+01	300	4000	3	3	0	0	0	0
27.	C3H5	G	0	4.1073E+01	300	5000	5	3	0	0	0	0
28.	C3H6	G	0	4.2081E+01	300	5000	6	3	0	0	0	0
29.	NC3H7	G	0	4.3089E+01	300	5000	7	3	0	0	0	0
30.	N	G	0	1.4007E+01	200	6000	0	0	0	1	0	0
31.	C3H2	G	0	3.8049E+01	150	4000	2	3	0	0	0	0

32. NC3H7O2	G	0	7.5088E+01	300	5000	7	3	2	0	0	0
33. HOCHO	G	0	4.6026E+01	300	5000	2	1	2	0	0	0
34. CH2(S)	G	0	1.4027E+01	300	4000	2	1	0	0	0	0
35. C3H8	G	0	4.4097E+01	300	5000	8	3	0	0	0	0
36. C9H19-1	G	0	1.2725E+02	300	5000	19	9	0	0	0	0
37. C3H4-A	G	0	4.0065E+01	300	4000	4	3	0	0	0	0
38. CH2CO	G	0	4.2038E+01	300	5000	2	2	1	0	0	0
39. PC4H9	G	0	5.7116E+01	300	5000	9	4	0	0	0	0
40. C5H11-1	G	0	7.1143E+01	300	5000	11	5	0	0	0	0
41. C3H5O	G	0	5.7073E+01	300	5000	5	3	1	0	0	0
42. C6H13-1	G	0	8.5171E+01	300	5000	13	6	0	0	0	0
43. C7H15-1	G	0	9.9198E+01	300	5000	15	7	0	0	0	0
44. C7H14-1	G	0	9.8190E+01	300	5000	14	7	0	0	0	0
45. NC16H34	G	0	2.2645E+02	300	5000	34	16	0	0	0	0
46. C16H33	G	0	2.2544E+02	300	5000	33	16	0	0	0	0
47. NC14H30	G	0	1.9840E+02	300	5000	30	14	0	0	0	0
48. C13H27-1	G	0	1.8336E+02	300	5000	27	13	0	0	0	0
49. C12H25-1	G	0	1.6933E+02	300	5000	25	12	0	0	0	0
50. C10H21-1	G	0	1.4128E+02	300	5000	21	10	0	0	0	0
51. C8H17-1	G	0	1.1322E+02	300	5000	17	8	0	0	0	0
52. C13H26-1	G	0	1.8235E+02	300	5000	26	13	0	0	0	0
53. C10H20-1	G	0	1.4027E+02	300	5000	20	10	0	0	0	0
54. N2O	G	0	4.4013E+01	200	6000	0	0	1	2	0	0
55. NH	G	0	1.5015E+01	200	6000	1	0	0	1	0	0
56. NH2	G	0	1.6023E+01	200	6000	2	0	0	1	0	0
57. NH3	G	0	1.7031E+01	200	6000	3	0	0	1	0	0
58. NO2	G	0	4.6005E+01	200	6000	0	0	2	1	0	0
59. HCNO	G	0	4.3025E+01	300	5000	1	1	1	1	0	0
60. HOCN	G	0	4.3025E+01	300	5000	1	1	1	1	0	0
61. HNCO	G	0	4.3025E+01	300	5000	1	1	1	1	0	0
62. NCO	G	0	4.2017E+01	200	6000	0	1	1	1	0	0
63. CN	G	0	2.6018E+01	200	6000	0	1	0	1	0	0
64. HCNN	G	0	4.1033E+01	300	5000	1	1	0	2	0	0
65. HNO	G	0	3.1014E+01	200	6000	1	0	1	1	0	0
66. HCN	G	0	2.7026E+01	200	6000	1	1	0	1	0	0
67. H2CN	G	0	2.8034E+01	300	4000	2	1	0	1	0	0
68. C	G	0	1.2011E+01	200	3500	0	1	0	0	0	0
69. CH	G	0	1.3019E+01	200	3500	1	1	0	0	0	0
70. NNH	G	0	2.9021E+01	200	6000	1	0	0	2	0	0
71. NO	G	0	3.0006E+01	200	6000	0	0	1	1	0	0

REACTIONS CONSIDERED	(k = A T**b exp(-E/RT)) A	b	E
1. H2O2+OH=H2O+HO2	1.00E+12	0.0	0.0
Reverse Arrhenius coefficients:	1.68E+11	0.3	31460.0
Declared duplicate reaction...			
2. H2O2+O2=2HO2	5.94E+17	-0.7	53150.0
Reverse Arrhenius coefficients:	4.20E+14	0.0	11980.0
Declared duplicate reaction...			
3. CH2+O2=CO+H2O	7.28E+19	-2.5	1809.0
Reverse Arrhenius coefficients:	8.51E+20	-2.5	179800.0
4. HCCO+OH=2HCO	1.00E+13	0.0	0.0
Reverse Arrhenius coefficients:	2.41E+14	0.0	40360.0
5. CH2+O2=CO2+H2	1.01E+21	-3.3	1508.0
Reverse Arrhenius coefficients:	3.05E+23	-3.3	186700.0

6.	C3H6=C2H3+CH3	2.73E+62	-13.3	123200.0
	Reverse Arrhenius coefficients:	4.71E+59	-13.2	29540.0
7.	PC4H9=C2H5+C2H4	7.50E+17	-1.4	29580.0
	Reverse Arrhenius coefficients:	3.30E+11	0.0	7200.0
8.	CH3+H=CH2+H2	9.00E+13	0.0	15100.0
	Reverse Arrhenius coefficients:	1.82E+13	0.0	10400.0
9.	C5H11-1=C2H4+NC3H7	7.97E+17	-1.4	29790.0
	Reverse Arrhenius coefficients:	3.30E+11	0.0	7200.0
10.	H2O2+O2=2HO2	1.84E+14	-0.7	39540.0
	Reverse Arrhenius coefficients:	1.30E+11	0.0	-1629.0
	Declared duplicate reaction...			
11.	H2O2+OH=H2O+HO2	5.80E+14	0.0	9560.0
	Reverse Arrhenius coefficients:	9.77E+13	0.3	41020.0
	Declared duplicate reaction...			
12.	C3H5O=C2H3+CH2O	2.03E+12	0.1	23560.0
	Reverse Arrhenius coefficients:	1.50E+11	0.0	10600.0
13.	C3H5+HO2=C3H5O+OH	7.00E+12	0.0	-1000.0
	Reverse Arrhenius coefficients:	2.04E+13	-0.2	12260.0
14.	C3H5+HO2=C2H3+CH2O+OH	1.00E-18	0.0	0.0
	Reverse Arrhenius coefficients:	1.00E-30	0.0	0.0
	Declared duplicate reaction...			
15.	HCCO+O2=CO2+HCO	2.40E+11	0.0	-854.0
	Reverse Arrhenius coefficients:	1.47E+14	0.0	133600.0
16.	C2H4+H2=2CH3	3.77E+12	0.8	84710.0
	Reverse Arrhenius coefficients:	1.00E+14	0.0	32000.0
17.	CH2(S)+M=CH2+M	1.00E+13	0.0	0.0
	Reverse Arrhenius coefficients:	7.16E+15	-0.9	11430.0
18.	C6H13-1=C2H4+PC4H9	5.45E+17	-1.3	29580.0
	Reverse Arrhenius coefficients:	3.30E+11	0.0	7200.0
19.	C7H15-1=C5H11-1+C2H4	8.16E+17	-1.4	30840.0
	Reverse Arrhenius coefficients:	1.00E+11	0.0	8200.0
20.	C7H15-1=C7H14-1+H	4.20E+16	-0.9	37940.0
	Reverse Arrhenius coefficients:	1.00E+13	0.0	2900.0
21.	C7H15-1+O2=C7H14-1+HO2	3.00E-09	0.0	3000.0
	Reverse Arrhenius coefficients:	2.44E-10	0.3	17920.0
22.	C7H14-1+OH=>CH2O+C6H13-1	1.00E+11	0.0	-4000.0
23.	C7H14-1+O=>CH2CHO+C5H11-1	1.00E+11	0.0	-1050.0
24.	C7H14-1=PC4H9+C3H5	1.00E+16	0.0	71000.0
	Reverse Arrhenius coefficients:	1.00E+13	0.0	0.0
25.	C16H33+H=NC16H34	1.00E+14	0.0	0.0
26.	C13H27-1+NC3H7=NC16H34	8.00E+12	0.0	0.0
27.	C12H25-1+PC4H9=NC16H34	8.00E+12	0.0	0.0
28.	C10H21-1+C6H13-1=NC16H34	8.00E+12	0.0	0.0
29.	C9H19-1+C7H15-1=NC16H34	8.00E+12	0.0	0.0
30.	2C8H17-1=NC16H34	8.00E+12	0.0	0.0
31.	C13H27-1+CH3=NC14H30	1.00E+13	0.0	0.0
32.	C12H25-1+C2H5=NC14H30	8.00E+12	0.0	0.0
33.	C10H21-1+PC4H9=NC14H30	8.00E+12	0.0	0.0
34.	C9H19-1+C5H11-1=NC14H30	8.00E+12	0.0	0.0
35.	C8H17-1+C6H13-1=NC14H30	8.00E+12	0.0	0.0
36.	2C7H15-1=NC14H30	8.00E+12	0.0	0.0
37.	NC16H34+H=C16H33+H2	1.88E+05	2.8	6280.0
	Reverse Arrhenius coefficients:	8.93E+03	2.7	10550.0
38.	NC16H34+OH=C16H33+H2O	7.00E+08	1.6	-35.0
	Reverse Arrhenius coefficients:	3.69E+06	1.9	21910.0
39.	NC16H34+O=C16H33+OH	5.72E+05	2.7	2106.0
	Reverse Arrhenius coefficients:	3.80E+02	3.0	6798.0
40.	NC16H34+HO2=C16H33+H2O2	1.68E+13	0.0	20440.0
	Reverse Arrhenius coefficients:	2.05E+13	-0.4	8399.0
41.	NC16H34+O2=C16H33+HO2	2.40E+14	0.0	50150.0
	Reverse Arrhenius coefficients:	6.59E+09	0.7	-541.0
42.	NC16H34+C2H3=C16H33+C2H4	1.00E+12	0.0	18000.0
	Reverse Arrhenius coefficients:	2.57E+12	0.0	25400.0

```
43. C3H6+C13H27-1=C16H33                          1.00E+11    0.0      8200.0
44. NC3H7+C13H26-1=C16H33                         1.00E+11    0.0      8200.0
45. C7H14-1+C9H19-1=C16H33                        1.00E+11    0.0      8200.0
46. C6H13-1+C10H20-1=C16H33                       1.00E+11    0.0      8200.0
47. H+C13H26-1=C13H27-1                           1.00E+13    0.0      2900.0
48. C2H4+C10H21-1=C12H25-1                        1.00E+11    0.0      8200.0
49. C2H4+C8H17-1=C10H21-1                         1.00E+11    0.0      8200.0
50. H+C10H20-1=C10H21-1                           1.00E+13    0.0      2900.0
51. C2H4+C7H15-1=C9H19-1                          1.00E+11    0.0      8200.0
52. C2H4+C6H13-1=C8H17-1                          1.00E+11    0.0      8200.0
53. C3H6+C5H11-1=C8H17-1                          1.00E+11    0.0      8200.0
54. C13H27-1+O2=C13H26-1+HO2                      3.00E-09    0.0      3000.0
55. C10H21-1+O2=C10H20-1+HO2                      3.00E-09    0.0      3000.0
56. C8H17-1=C8H17-1                               5.48E+08    1.6     38760.0
    Reverse Arrhenius coefficients:               1.74E+07    2.0     41280.0
57. C13H26-1+OH=>CH2O+C12H25-1                    1.00E+11    0.0     -4000.0
58. C10H20-1+OH=>CH2O+C9H19-1                     1.00E+11    0.0     -4000.0
59. C10H20-1+O=>CH2CHO+C8H17-1                    1.00E+11    0.0     -1050.0
60. C13H26-1=C10H21-1+C3H5                        1.00E+16    0.0     71000.0
    Reverse Arrhenius coefficients:               1.00E+13    0.0         0.0
61. C10H20-1=C7H15-1+C3H5                         1.00E+16    0.0     71000.0
    Reverse Arrhenius coefficients:               1.00E+13    0.0         0.0
62. H+O2=O+OH                                     1.04E+14    0.0     15310.0
63. O+H2=H+OH                                     5.08E+04    2.7      6292.0
    Reverse Arrhenius coefficients:               2.64E+04    2.7      4880.0
64. OH+H2=H+H2O                                   2.16E+08    1.5      3430.0
    Reverse Arrhenius coefficients:               2.29E+09    1.4     18320.0
65. O+H2O=2OH                                     2.97E+06    2.0     13400.0
    Reverse Arrhenius coefficients:               1.45E+05    2.1     -2904.0
66. H2+M=2H+M                                     4.58E+19   -1.4    104400.0
    H2              Enhanced by    2.500E+00
    H2O             Enhanced by    1.200E+01
    CO              Enhanced by    1.900E+00
    CO2             Enhanced by    3.800E+00
    Reverse Arrhenius coefficients:               1.14E+20   -1.7       820.0
67. O2+M=2O+M                                     4.42E+17   -0.6    118900.0
    H2              Enhanced by    2.500E+00
    H2O             Enhanced by    1.200E+01
    CO              Enhanced by    1.900E+00
    CO2             Enhanced by    3.800E+00
    CH4             Enhanced by    2.000E+00
    C2H6            Enhanced by    3.000E+00
    Reverse Arrhenius coefficients:               6.16E+15   -0.5         0.0
68. OH+M=O+H+M                                    9.78E+17   -0.7    102100.0
    H2              Enhanced by    2.500E+00
    H2O             Enhanced by    1.200E+01
    CO              Enhanced by    1.500E+00
    CO2             Enhanced by    2.000E+00
    CH4             Enhanced by    2.000E+00
    C2H6            Enhanced by    3.000E+00
    Reverse Arrhenius coefficients:               4.71E+18   -1.0         0.0
69. H2O+M=H+OH+M                                  1.91E+23   -1.8    118500.0
    H2              Enhanced by    7.300E-01
    H2O             Enhanced by    1.200E+01
    CH4             Enhanced by    2.000E+00
    C2H6            Enhanced by    3.000E+00
    Reverse Arrhenius coefficients:               4.50E+22   -2.0         0.0
70. H+O2(+M)=HO2(+M)                              4.65E+12    0.4         0.0
    H2              Enhanced by    2.000E+00
    H2O             Enhanced by    1.400E+01
    CO              Enhanced by    1.900E+00
    CO2             Enhanced by    3.800E+00
    O2              Enhanced by    7.800E-01
```

```
    Low pressure limit:  0.90400E+20 -0.15000E+01  0.49200E+03
    TROE centering:      0.50000E+00  0.10000E-29  0.10000E+31  0.10000E+11
71. HO2+H=H2+O2                                    1.66E+13    0.0      823.0
    Reverse Arrhenius coefficients:                3.17E+12    0.3    55510.0
72. HO2+H=2OH                                      7.08E+13    0.0      295.0
    Reverse Arrhenius coefficients:                2.03E+10    0.7    36840.0
73. HO2+O=OH+O2                                    2.85E+10    1.0     -723.9
74. HO2+OH=H2O+O2                                  2.89E+13    0.0     -497.0
    Reverse Arrhenius coefficients:                5.84E+13    0.2    69080.0
75. H2O2+O2=2HO2                                   1.14E+16   -0.3    49730.0
    Reverse Arrhenius coefficients:                1.03E+14    0.0    11040.0
    Declared duplicate reaction...
76. H2O2+O2=2HO2                                   2.14E+13   -0.3    37280.0
    Reverse Arrhenius coefficients:                1.94E+11    0.0    -1409.0
    Declared duplicate reaction...
77. H2O2(+M)=2OH(+M)                               2.00E+12    0.9    48750.0
    H2              Enhanced by    3.700E+00
    H2O             Enhanced by    7.500E+00
    N2              Enhanced by    1.500E+00
    CO              Enhanced by    2.800E+00
    CO2             Enhanced by    1.600E+00
    O2              Enhanced by    1.200E+00
    H2O2            Enhanced by    7.700E+00
    Low pressure limit:  0.24900E+25 -0.23000E+01  0.48750E+05
    TROE centering:      0.43000E+00  0.10000E-29  0.10000E+31
78. H2O2+H=H2O+OH                                  2.41E+13    0.0     3970.0
    Reverse Arrhenius coefficients:                1.26E+08    1.3    71410.0
79. H2O2+H=H2+HO2                                  2.15E+10    1.0     6000.0
    Reverse Arrhenius coefficients:                3.72E+07    1.7    22000.0
80. H2O2+O=OH+HO2                                  9.55E+06    2.0     3970.0
    Reverse Arrhenius coefficients:                8.57E+03    2.7    18560.0
81. H2O2+OH=HO2+H2O                                1.74E+12    0.0      318.0
    Declared duplicate reaction...
82. H2O2+OH=HO2+H2O                                7.59E+13    0.0     7270.0
    Declared duplicate reaction...
83. CO+O(+M)=CO2(+M)                               1.80E+10    0.0     2384.0
    H2              Enhanced by    2.000E+00
    O2              Enhanced by    6.000E+00
    H2O             Enhanced by    6.000E+00
    CO              Enhanced by    1.500E+00
    CO2             Enhanced by    3.500E+00
    CH4             Enhanced by    2.000E+00
    C2H6            Enhanced by    3.000E+00
    Low pressure limit:  0.13500E+25 -0.27880E+01  0.41910E+04
84. CO+O2=CO2+O                                    1.05E+12    0.0    42540.0
    Reverse Arrhenius coefficients:                8.04E+15   -0.8    51230.0
85. CO+OH=CO2+H                                    1.78E+05    1.9    -1158.0
    Reverse Arrhenius coefficients:                4.72E+11    0.7    24260.0
86. CO+HO2=CO2+OH                                  1.57E+05    2.2    17940.0
    Reverse Arrhenius coefficients:                1.19E+08    1.7    79910.0
87. HCO+M=H+CO+M                                   4.75E+11    0.7    14870.0
    H2              Enhanced by    2.000E+00
    H2O             Enhanced by    1.200E+01
    CO              Enhanced by    1.500E+00
    CO2             Enhanced by    2.000E+00
    CH4             Enhanced by    2.000E+00
    C2H6            Enhanced by    3.000E+00
    Reverse Arrhenius coefficients:                3.58E+10    1.0     -457.3
88. HCO+O2=CO+HO2                                  7.58E+12    0.0      410.0
    Reverse Arrhenius coefficients:                1.20E+12    0.3    33950.0
89. HCO+H=CO+H2                                    7.34E+13    0.0        0.0
    Reverse Arrhenius coefficients:                2.21E+12    0.7    88230.0
90. HCO+O=CO+OH                                    3.02E+13    0.0        0.0
```

```
     Reverse Arrhenius coefficients:                4.72E+11    0.6    86820.0
 91. HCO+O=CO2+H                                    3.00E+13    0.0        0.0
     Reverse Arrhenius coefficients:                1.24E+18   -0.6   112200.0
 92. HCO+OH=CO+H2O                                  1.02E+14    0.0        0.0
     Reverse Arrhenius coefficients:                3.26E+13    0.6   103100.0
 93. HCO+CH3=CH4+CO                                 2.65E+13    0.0        0.0
     Reverse Arrhenius coefficients:                7.29E+14    0.2    89770.0
 94. HCO+HO2=CH2O+O2                                2.50E+14   -0.1    13920.0
     Reverse Arrhenius coefficients:                8.07E+15    0.0    53420.0
 95. HCO+HO2=>CO2+H+OH                              3.00E+13    0.0        0.0
 96. CH2O+CO=2HCO                                   9.19E+13    0.4    73040.0
     Reverse Arrhenius coefficients:                1.80E+13    0.0        0.0
 97. 2HCO=>H2+2CO                                   3.00E+12    0.0        0.0
 98. HCO+H(+M)=CH2O(+M)                             1.09E+12    0.5     -260.0
     H2              Enhanced by    2.000E+00
     H2O             Enhanced by    6.000E+00
     CO              Enhanced by    1.500E+00
     CO2             Enhanced by    2.000E+00
     CH4             Enhanced by    2.000E+00
     C2H6            Enhanced by    3.000E+00
     Low pressure limit:  0.13500E+25 -0.25700E+01  0.14250E+04
     TROE centering:      0.78240E+00  0.27100E+03  0.27550E+04  0.65700E+04
 99. CO+H2(+M)=CH2O(+M)                             4.30E+07    1.5    79600.0
     H2              Enhanced by    2.000E+00
     H2O             Enhanced by    6.000E+00
     CO              Enhanced by    1.500E+00
     CO2             Enhanced by    2.000E+00
     CH4             Enhanced by    2.000E+00
     C2H6            Enhanced by    3.000E+00
     Low pressure limit:  0.50700E+28 -0.34200E+01  0.84348E+05
     TROE centering:      0.93200E+00  0.19700E+03  0.15400E+04  0.10300E+05
100. CH2O+OH=HCO+H2O                                7.82E+07    1.6    -1055.0
     Reverse Arrhenius coefficients:                4.90E+06    1.8    29030.0
101. CH2O+H=HCO+H2                                  5.74E+07    1.9     2740.0
     Reverse Arrhenius coefficients:                3.39E+05    2.2    17930.0
102. CH2O+O=HCO+OH                                  6.26E+09    1.1     2260.0
     Reverse Arrhenius coefficients:                1.92E+07    1.4    16040.0
103. CH2O+CH3=HCO+CH4                               3.83E+01    3.4     4312.0
     Reverse Arrhenius coefficients:                2.06E+02    3.2    21040.0
104. CH2O+HO2=HCO+H2O2                              7.10E-03    4.5     6580.0
     Reverse Arrhenius coefficients:                2.43E-02    4.1     5769.0
105. HOCHO=CO+H2O                                   2.45E+12    0.0    60470.0
     Reverse Arrhenius coefficients:                2.26E+03    2.1    52890.0
106. HOCHO=CO2+H2                                   2.95E+09    0.0    48520.0
     Reverse Arrhenius coefficients:                6.77E+05    1.0    51470.0
107. HOCHO=HCO+OH                                   3.47E+22   -1.5   110700.0
     Reverse Arrhenius coefficients:                1.00E+14    0.0        0.0
108. HOCHO+OH=>H2O+CO2+H                            2.62E+06    2.1      916.0
109. HOCHO+OH=>H2O+CO+OH                            1.85E+07    1.5     -962.0
110. HOCHO+H=>H2+CO2+H                              4.24E+06    2.1     4868.0
111. HOCHO+H=>H2+CO+OH                              6.03E+13   -0.3     2988.0
112. HOCHO+CH3=>CH4+CO+OH                           3.90E-07    5.8     2200.0
113. HOCHO+HO2=>H2O2+CO+OH                          1.00E+12    0.0    11920.0
114. HOCHO+O=>CO+2OH                                1.77E+18   -1.9     2975.0
115. CH3O(+M)=CH2O+H(+M)                            6.80E+13    0.0    26170.0
     H2              Enhanced by    2.000E+00
     H2O             Enhanced by    6.000E+00
     CO              Enhanced by    1.500E+00
     CO2             Enhanced by    2.000E+00
     CH4             Enhanced by    2.000E+00
     C2H6            Enhanced by    3.000E+00
     Low pressure limit:  0.18670E+26 -0.30000E+01  0.24307E+05
     TROE centering:      0.90000E+00  0.25000E+04  0.13000E+04  0.10000+100
```

```
116. CH3O+O2=CH2O+HO2                                  4.38E-19    9.5    -5501.0
     Reverse Arrhenius coefficients:                   1.42E-20    9.8    21080.0
117. CH3O+CH3=CH2O+CH4                                 1.20E+13    0.0        0.0
     Reverse Arrhenius coefficients:                   6.75E+13    0.2    82810.0
118. CH3O+H=CH2O+H2                                    2.00E+13    0.0        0.0
     Reverse Arrhenius coefficients:                   1.23E+11    0.7    81270.0
119. CH3O+HO2=CH2O+H2O2                                3.01E+11    0.0        0.0
     Reverse Arrhenius coefficients:                   1.07E+12   -0.0    65270.0
120. CH3+H(+M)=CH4(+M)                                 1.27E+16   -0.6      383.0
     H2              Enhanced by    2.000E+00
     H2O             Enhanced by    6.000E+00
     CO              Enhanced by    1.500E+00
     CO2             Enhanced by    2.000E+00
     CH4             Enhanced by    2.000E+00
     C2H6            Enhanced by    3.000E+00
     Low pressure limit:  0.19816E+34 -0.47600E+01  0.24440E+04
     TROE centering:      0.78300E+00  0.74000E+02  0.29400E+04  0.69600E+04
121. CH4+H=CH3+H2                                      6.14E+05    2.5     9587.0
     Reverse Arrhenius coefficients:                   6.73E+02    2.9     8047.0
122. CH4+OH=CH3+H2O                                    6.12E+04    2.6     2190.0
     Reverse Arrhenius coefficients:                   6.78E+02    2.9    15540.0
123. CH4+O=CH3+OH                                      1.02E+09    1.5     8600.0
     Reverse Arrhenius coefficients:                   5.80E+05    1.9     5648.0
124. CH4+HO2=CH3+H2O2                                  1.13E+01    3.7    21010.0
     Reverse Arrhenius coefficients:                   7.17E+00    3.5     3468.0
125. CH4+CH2=2CH3                                      2.46E+06    2.0     8270.0
     Reverse Arrhenius coefficients:                   1.74E+06    1.9    12980.0
126. CH3+OH=CH2O+H2                                    8.00E+09    0.5    -1755.0
     Reverse Arrhenius coefficients:                   1.07E+12    0.3    68210.0
127. CH3+OH=CH2(S)+H2O                                 4.51E+17   -1.3     1417.0
     Reverse Arrhenius coefficients:                   1.65E+16   -0.9     1039.0
128. CH3+OH=CH3O+H                                     6.94E+07    1.3    11200.0
     Reverse Arrhenius coefficients:                   1.50E+12    0.5     -110.0
129. CH3+OH=CH2+H2O                                    5.60E+07    1.6     5420.0
     Reverse Arrhenius coefficients:                   9.22E+05    2.1    14060.0
130. CH3+HO2=CH3O+OH                                   1.00E+12    0.3     -687.5
     Reverse Arrhenius coefficients:                   6.19E+12    0.1    24550.0
131. CH3+HO2=CH4+O2                                    1.16E+05    2.2    -3022.0
     Reverse Arrhenius coefficients:                   2.02E+07    2.1    53210.0
132. CH3+O=CH2O+H                                      5.54E+13    0.1     -136.0
     Reverse Arrhenius coefficients:                   3.83E+15   -0.1    68410.0
133. CH3+O2=CH3O+O                                     7.55E+12    0.0    28320.0
     Reverse Arrhenius coefficients:                   4.72E+14   -0.5      288.0
134. CH3+O2=CH2O+OH                                    2.64E+00    3.3     8105.0
     Reverse Arrhenius coefficients:                   5.28E-01    3.5    59920.0
135. CH2(S)=CH2                                        1.00E+13    0.0        0.0
     Reverse Arrhenius coefficients:                   4.49E+12   -0.0     9020.0
136. CH2(S)+CH4=2CH3                                   1.60E+13    0.0     -570.0
     Reverse Arrhenius coefficients:                   5.07E+12   -0.1    13160.0
137. CH2(S)+O2=>CO+OH+H                                7.00E+13    0.0        0.0
138. CH2(S)+H2=CH3+H                                   7.00E+13    0.0        0.0
     Reverse Arrhenius coefficients:                   2.02E+16   -0.6    15270.0
139. CH2(S)+H=CH2+H                                    3.00E+13    0.0        0.0
     Reverse Arrhenius coefficients:                   1.35E+13   -0.0     9020.0
140. CH2(S)+O=>CO+2H                                   3.00E+13    0.0        0.0
141. CH2(S)+OH=CH2O+H                                  3.00E+13    0.0        0.0
     Reverse Arrhenius coefficients:                   1.15E+18   -0.8    85230.0
142. CH2(S)+CO2=CH2O+CO                                3.00E+12    0.0        0.0
     Reverse Arrhenius coefficients:                   4.37E+10    0.4    59810.0
143. CH2+H(+M)=CH3(+M)                                 2.50E+16   -0.8        0.0
     H2              Enhanced by    2.000E+00
     H2O             Enhanced by    6.000E+00
     CO              Enhanced by    1.500E+00
```

```
     CO2             Enhanced by    2.000E+00
     CH4             Enhanced by    2.000E+00
     C2H6            Enhanced by    3.000E+00
     Low pressure limit:  0.32000E+28 -0.31400E+01  0.12300E+04
     TROE centering:      0.68000E+00  0.78000E+02  0.19950E+04  0.55900E+04
144. CH2+O2=CH2O+O                                   2.40E+12    0.0     1500.0
     Reverse Arrhenius coefficients:                 5.96E+14   -0.4    60980.0
145. CH2+O2=>CO2+2H                                  5.80E+12    0.0     1500.0
146. CH2+O2=>CO+OH+H                                 5.00E+12    0.0     1500.0
147. CH2+O=>CO+2H                                    5.00E+13    0.0        0.0
148. 2CH3(+M)=C2H6(+M)                               9.21E+16   -1.2      635.8
     H2              Enhanced by    2.000E+00
     H2O             Enhanced by    6.000E+00
     CO              Enhanced by    1.500E+00
     CO2             Enhanced by    2.000E+00
     CH4             Enhanced by    2.000E+00
     C2H6            Enhanced by    3.000E+00
     Low pressure limit:  0.11350E+37 -0.52460E+01  0.17050E+04
     TROE centering:      0.40500E+00  0.11200E+04  0.69600E+02  0.10000E+11
149. C2H5+H(+M)=C2H6(+M)                             5.21E+17   -1.0     1580.0
     H2              Enhanced by    2.000E+00
     H2O             Enhanced by    6.000E+00
     CO              Enhanced by    1.500E+00
     CO2             Enhanced by    2.000E+00
     CH4             Enhanced by    2.000E+00
     C2H6            Enhanced by    3.000E+00
     Low pressure limit:  0.19900E+42 -0.70800E+01  0.66850E+04
     TROE centering:      0.84200E+00  0.12500E+03  0.22190E+04  0.68820E+04
150. C2H6+H=C2H5+H2                                  1.15E+08    1.9     7530.0
     Reverse Arrhenius coefficients:                 1.06E+04    2.6     9760.0
151. C2H6+O=C2H5+OH                                  3.55E+06    2.4     5830.0
     Reverse Arrhenius coefficients:                 1.70E+02    3.1     6648.0
152. C2H6+OH=C2H5+H2O                                1.48E+07    1.9      950.0
     Reverse Arrhenius coefficients:                 1.45E+04    2.5    18070.0
153. C2H6+O2=C2H5+HO2                                6.03E+13    0.0    51870.0
     Reverse Arrhenius coefficients:                 2.92E+10    0.3     -593.0
154. C2H6+CH3=C2H5+CH4                               5.48E-01    4.0     8280.0
     Reverse Arrhenius coefficients:                 4.62E-02    4.2    12050.0
155. C2H6+HO2=C2H5+H2O2                              6.92E+01    3.6    16920.0
     Reverse Arrhenius coefficients:                 3.70E+00    3.6     3151.0
156. CH2(S)+C2H6=CH3+C2H5                            1.20E+14    0.0        0.0
     Reverse Arrhenius coefficients:                 3.20E+12    0.1    17500.0
157. C2H4+H(+M)=C2H5(+M)                             1.08E+12    0.5     1822.0
     H2              Enhanced by    2.000E+00
     H2O             Enhanced by    6.000E+00
     CO              Enhanced by    1.500E+00
     CO2             Enhanced by    2.000E+00
     CH4             Enhanced by    2.000E+00
     C2H6            Enhanced by    3.000E+00
     Low pressure limit:  0.12000E+43 -0.76200E+01  0.69700E+04
     TROE centering:      0.97500E+00  0.21000E+03  0.98400E+03  0.43740E+04
158. C2H5+C2H3=2C2H4                                 6.86E+11    0.1    -4300.0
     Reverse Arrhenius coefficients:                 4.82E+14    0.0    71530.0
159. CH3+C2H5=CH4+C2H4                               1.18E+04    2.5    -2921.0
     Reverse Arrhenius coefficients:                 2.39E+06    2.4    66690.0
160. C2H5+H=2CH3                                     9.69E+13    0.0      220.0
     Reverse Arrhenius coefficients:                 2.03E+09    1.0    10510.0
161. C2H5+H=C2H4+H2                                  2.00E+12    0.0        0.0
     Reverse Arrhenius coefficients:                 4.44E+11    0.4    68070.0
162. C2H5+O=CH3CHO+H                                 1.10E+14    0.0        0.0
     Reverse Arrhenius coefficients:                 1.03E+17   -0.5    77420.0
163. C2H5+O2=C2H4+HO2                                3.78E+14   -1.0     4749.0
     Reverse Arrhenius coefficients:                 4.40E+14   -1.0    18130.0
```

```
     Declared duplicate reaction...
164. C2H5+O2=C2H4+HO2                                  4.00E-01    3.9    13620.0
     Reverse Arrhenius coefficients:                   4.66E-01    3.9    27000.0
     Declared duplicate reaction...
165. C2H5+O2=CH3CHO+OH                                 1.63E+11   -0.3     6150.0
     Reverse Arrhenius coefficients:                   3.63E+13   -0.6    39840.0
     Declared duplicate reaction...
166. C2H5+O2=CH3CHO+OH                                 8.26E+02    2.4     5285.0
     Reverse Arrhenius coefficients:                   2.25E+03    2.3    65970.0
     Declared duplicate reaction...
167. CH3CHO=CH3+HCO                                    3.63E+13    0.0    57200.0
     Reverse Arrhenius coefficients:                   1.01E+04    1.5    -2750.0
     Declared duplicate reaction...
168. CH3CHO=CH3CHO                                     7.41E+12    0.0    53800.0
     Reverse Arrhenius coefficients:                   9.01E+10    0.2    80800.0
169. CH3CHO=CH3+HCO                                    7.69E+20   -1.3    86950.0
     Reverse Arrhenius coefficients:                   1.75E+13    0.0        0.0
     Declared duplicate reaction...
170. CH3CHO+OH=CH3+HOCHO                               3.00E+15   -1.1        0.0
     Reverse Arrhenius coefficients:                   2.37E+16   -1.3    23750.0
171. CH3CHO+OH=CH2CHO+H2O                              1.72E+05    2.4      815.0
     Reverse Arrhenius coefficients:                   1.33E+05    2.5    24950.0
172. CH2CHO=CH2CO+H                                    4.07E+15   -0.3    50600.0
     Reverse Arrhenius coefficients:                   5.00E+13    0.0    12300.0
173. CH2CHO+O2=>CH2O+CO+OH                             8.95E+13   -0.6    10120.0
174. CH2+CO(+M)=CH2CO(+M)                              8.10E+11    0.0        0.0
     H2              Enhanced by    2.000E+00
     H2O             Enhanced by    6.000E+00
     CO              Enhanced by    1.500E+00
     CO2             Enhanced by    2.000E+00
     CH4             Enhanced by    2.000E+00
     C2H6            Enhanced by    3.000E+00
     Low pressure limit:  0.26900E+34 -0.51100E+01  0.70950E+04
     TROE centering:      0.59070E+00  0.27500E+03  0.12260E+04  0.51850E+04
175. CH2CO+H=CH3+CO                                    1.10E+13    0.0     3400.0
     Reverse Arrhenius coefficients:                   2.40E+12    0.0    40200.0
176. CH2CO+H=HCCO+H2                                   2.00E+14    0.0     8000.0
     Reverse Arrhenius coefficients:                   1.43E+11    0.5     4520.0
177. CH2CO+O=CH2+CO2                                   1.75E+12    0.0     1350.0
     Reverse Arrhenius coefficients:                   2.85E+09    0.8    49440.0
178. CH2CO+O=HCCO+OH                                   1.00E+13    0.0     8000.0
     Reverse Arrhenius coefficients:                   3.72E+09    0.5     3108.0
179. CH2CO+OH=HCCO+H2O                                 1.00E+13    0.0     2000.0
     Reverse Arrhenius coefficients:                   7.60E+10    0.4    13410.0
180. CH2(S)+CH2CO=C2H4+CO                              1.60E+14    0.0        0.0
     Reverse Arrhenius coefficients:                   3.75E+14    0.2   103400.0
181. HCCO+OH=>H2+2CO                                   1.00E+14    0.0        0.0
182. H+HCCO=CH2(S)+CO                                  1.10E+13    0.0        0.0
     Reverse Arrhenius coefficients:                   4.06E+07    1.6    18540.0
183. HCCO+O=>H+2CO                                     8.00E+13    0.0        0.0
184. HCCO+O2=>OH+2CO                                   4.20E+10    0.0      850.0
185. C2H3+H(+M)=C2H4(+M)                               6.08E+12    0.3      280.0
     H2              Enhanced by    2.000E+00
     H2O             Enhanced by    6.000E+00
     CO              Enhanced by    1.500E+00
     CO2             Enhanced by    2.000E+00
     CH4             Enhanced by    2.000E+00
     C2H6            Enhanced by    3.000E+00
     Low pressure limit:  0.14000E+31 -0.38600E+01  0.33200E+04
     TROE centering:      0.78200E+00  0.20750E+03  0.26630E+04  0.60950E+04
186. C2H4(+M)=C2H2+H2(+M)                              8.00E+12    0.4    88770.0
     H2              Enhanced by    2.000E+00
     H2O             Enhanced by    6.000E+00
```

```
     CO              Enhanced by    1.500E+00
     CO2             Enhanced by    2.000E+00
     CH4             Enhanced by    2.000E+00
     C2H6            Enhanced by    3.000E+00
     Low pressure limit:  0.70000E+51 -0.93100E+01  0.99860E+05
     TROE centering:      0.73450E+00  0.18000E+03  0.10350E+04  0.54170E+04
187. C2H4+H=C2H3+H2                                 5.07E+07    1.9    12950.0
     Reverse Arrhenius coefficients:                1.60E+04    2.4     5190.0
188. C2H4+O=CH3+HCO                                 8.56E+06    1.9      183.0
     Reverse Arrhenius coefficients:                3.30E+02    2.6    26140.0
189. C2H4+O=CH2CHO+H                                4.99E+06    1.9      183.0
     Reverse Arrhenius coefficients:                1.54E+09    1.2    18780.0
190. C2H4+OH=C2H3+H2O                               1.80E+06    2.0     2500.0
     Reverse Arrhenius coefficients:                6.03E+03    2.4     9632.0
191. C2H4+CH3=C2H3+CH4                              6.62E+00    3.7     9500.0
     Reverse Arrhenius coefficients:                1.91E+00    3.8     3280.0
192. C2H4+O2=C2H3+HO2                               4.00E+13    0.0    58200.0
     Reverse Arrhenius coefficients:                6.63E+10    0.2    -4249.0
193. C2H4+HO2=CH3CHO+OH                             2.23E+12    0.0    17190.0
     Reverse Arrhenius coefficients:                4.28E+14   -0.4    37500.0
194. CH2(S)+CH3=C2H4+H                              2.00E+13    0.0        0.0
     Reverse Arrhenius coefficients:                6.13E+19   -1.2    73050.0
195. C2H3(+M)=C2H2+H(+M)                            3.86E+08    1.6    37050.0
     H2              Enhanced by    2.000E+00
     H2O             Enhanced by    6.000E+00
     CO              Enhanced by    1.500E+00
     CO2             Enhanced by    2.000E+00
     CH4             Enhanced by    2.000E+00
     C2H6            Enhanced by    3.000E+00
     Low pressure limit:  0.25650E+28 -0.34000E+01  0.35799E+05
     TROE centering:      0.19816E+01  0.53837E+04  0.42932E+01 -0.79500E-01
196. C2H3+O2=C2H2+HO2                               5.19E+15   -1.2     3310.0
     Reverse Arrhenius coefficients:                2.66E+16   -1.3    17860.0
197. C2H3+O2=CH2O+HCO                               8.50E+28   -5.3     6500.0
     Reverse Arrhenius coefficients:                3.99E+27   -4.9    93450.0
198. C2H3+O2=CH2CHO+O                               5.50E+14   -0.6     5260.0
     Reverse Arrhenius coefficients:                3.00E+18   -1.4    16300.0
199. CH3+C2H3=CH4+C2H2                              3.92E+11    0.0        0.0
     Reverse Arrhenius coefficients:                3.50E+14   -0.2    70780.0
200. C2H3+H=C2H2+H2                                 9.64E+13    0.0        0.0
     Reverse Arrhenius coefficients:                9.43E+13    0.3    69240.0
201. C2H3+OH=C2H2+H2O                               3.01E+13    0.0        0.0
     Reverse Arrhenius coefficients:                3.12E+14    0.1    84130.0
202. C2H2+O2=HCCO+OH                                2.00E+08    1.5    30100.0
     Reverse Arrhenius coefficients:                2.04E+06    1.5    32270.0
203. C2H2+O=CH2+CO                                  8.20E+09    1.1     2370.0
     Reverse Arrhenius coefficients:                4.79E+04    2.3    48830.0
204. C2H2+O=HCCO+H                                  5.30E+04    2.7     2360.0
     Reverse Arrhenius coefficients:                1.87E+05    2.3    21260.0
205. C2H2+OH=CH2CO+H                                3.24E+13    0.0    12000.0
     Reverse Arrhenius coefficients:                3.06E+17   -0.8    35790.0
206. C2H2+OH=CH3+CO                                 4.83E-04    4.0    -2000.0
     Reverse Arrhenius coefficients:                3.49E-06    4.6    52120.0
207. C3H8(+M)=CH3+C2H5(+M)                          1.29E+37   -5.8    97380.0
     H2              Enhanced by    2.000E+00
     H2O             Enhanced by    6.000E+00
     CO              Enhanced by    1.500E+00
     CO2             Enhanced by    2.000E+00
     CH4             Enhanced by    2.000E+00
     C2H6            Enhanced by    3.000E+00
     Low pressure limit:  0.56400E+75 -0.15740E+02  0.98714E+05
     TROE centering:      0.31000E+00  0.50000E+02  0.30000E+04  0.90000E+04
208. C3H8=NC3H7+H                                   3.75E+17   -0.4   101200.0
```

```
     Reverse Arrhenius coefficients:                  1.00E+14    0.0        0.0
209. C3H8+O2=NC3H7+HO2                                6.00E+13    0.0    52290.0
     Reverse Arrhenius coefficients:                  3.35E+10    0.3      -59.0
210. H+C3H8=H2+NC3H7                                  3.49E+05    2.7     6450.0
     Reverse Arrhenius coefficients:                  3.72E+01    3.3     8790.0
211. C3H8+O=NC3H7+OH                                  3.71E+06    2.4     5505.0
     Reverse Arrhenius coefficients:                  2.05E+02    3.0     6433.0
212. C3H8+OH=NC3H7+H2O                                1.05E+10    1.0     1586.0
     Reverse Arrhenius coefficients:                  1.19E+07    1.5    18820.0
213. C3H8+HO2=NC3H7+H2O2                              4.08E+01    3.6    17160.0
     Reverse Arrhenius coefficients:                  2.52E+00    3.5     3500.0
214. CH3+C3H8=CH4+NC3H7                               9.04E-01    3.6     7154.0
     Reverse Arrhenius coefficients:                  8.79E-02    3.8    11030.0
215. C2H3+C3H8=C2H4+NC3H7                             1.00E+11    0.0    10400.0
     Reverse Arrhenius coefficients:                  1.31E+11    0.0    17800.0
216. C2H5+C3H8=C2H6+NC3H7                             1.00E+11    0.0    10400.0
     Reverse Arrhenius coefficients:                  3.63E+10    0.0     9934.0
217. C3H8+C3H5=NC3H7+C3H6                             7.94E+11    0.0    20500.0
     Reverse Arrhenius coefficients:                  5.37E+16   -1.3    13400.0
218. NC3H7=CH3+C2H4                                   9.97E+40   -8.6    41430.0
     Reverse Arrhenius coefficients:                  1.90E+34   -7.0    17100.0
219. NC3H7=H+C3H6                                     8.78E+39   -8.1    46580.0
     Reverse Arrhenius coefficients:                  2.07E+37   -7.4    12020.0
220. NC3H7+O2=C3H6+HO2                                3.00E-19    0.0     3000.0
     Reverse Arrhenius coefficients:                  2.00E-19    0.0    17500.0
221. C2H3+CH3(+M)=C3H6(+M)                            2.50E+13    0.0        0.0
     Low pressure limit:  0.42700E+59 -0.11940E+02  0.97698E+04
     TROE centering:      0.17500E+00  0.13406E+04  0.60000E+05  0.10140E+05
222. C3H6=C3H5+H                                      2.01E+61  -13.3   118500.0
     Reverse Arrhenius coefficients:                  2.04E+61  -13.5    30610.0
223. C3H6+O=C2H5+HCO                                  1.58E+07    1.8    -1216.0
     Reverse Arrhenius coefficients:                  9.19E+01    2.7    23110.0
224. C3H6+O=>CH2CO+CH3+H                              2.50E+07    1.8       76.0
225. C3H6+O=C3H5+OH                                   5.24E+11    0.7     5884.0
     Reverse Arrhenius coefficients:                  1.10E+11    0.7    20150.0
226. C3H6+OH=C3H5+H2O                                 3.12E+06    2.0     -298.0
     Reverse Arrhenius coefficients:                  1.34E+07    1.9    30270.0
     Declared duplicate reaction...
227. C3H6+HO2=C3H5+H2O2                               2.70E+04    2.5    12340.0
     Reverse Arrhenius coefficients:                  6.34E+06    1.8    12010.0
228. C3H6+H=C3H5+H2                                   1.73E+05    2.5     2492.0
     Reverse Arrhenius coefficients:                  7.02E+04    2.5    18170.0
     Declared duplicate reaction...
229. C3H6+H=C2H4+CH3                                  2.30E+13    0.0     2547.0
     Reverse Arrhenius coefficients:                  7.27E+07    1.3    11200.0
230. C3H6+O2=C3H5+HO2                                 4.00E+12    0.0    39900.0
     Reverse Arrhenius coefficients:                  8.51E+12   -0.3      887.0
     Declared duplicate reaction...
231. C3H6+CH3=C3H5+CH4                                2.21E+00    3.5     5675.0
     Reverse Arrhenius coefficients:                  8.18E+02    3.1    22890.0
232. C3H6+C2H5=C3H5+C2H6                              1.00E+11    0.0     9800.0
     Reverse Arrhenius coefficients:                  5.37E+05    1.3    16440.0
233. C3H5=C2H2+CH3                                    2.40E+48   -9.9    82080.0
     Reverse Arrhenius coefficients:                  2.61E+46   -9.8    36950.0
234. C3H5=C3H4-A+H                                    4.19E+13    0.2    61930.0
     Reverse Arrhenius coefficients:                  2.40E+11    0.7     3007.0
235. C3H5+H=C3H4-A+H2                                 1.23E+03    3.0     2582.0
     Reverse Arrhenius coefficients:                  2.82E+00    3.8    47220.0
236. C3H5+CH3=C3H4-A+CH4                              1.00E+11    0.0        0.0
     Reverse Arrhenius coefficients:                  4.92E+12    0.1    47780.0
237. C3H5+C2H5=C2H6+C3H4-A                            4.00E+11    0.0        0.0
     Reverse Arrhenius coefficients:                  1.80E+12    0.1    40330.0
238. C3H5+C2H5=C2H4+C3H6                              4.00E+11    0.0        0.0
```

```
     Reverse Arrhenius coefficients:                6.94E+16   -1.3    52800.0
239. C3H5+C2H3=C2H4+C3H4-A                          1.00E+12    0.0        0.0
     Reverse Arrhenius coefficients:                1.62E+13    0.1    48190.0
240. C3H4-A+C3H6=2C3H5                              4.75E+08    0.7    28700.0
     Reverse Arrhenius coefficients:                8.43E+10    0.0     -262.0
241. C3H5+O2=C3H4-A+HO2                             2.18E+21   -2.9    30760.0
     Reverse Arrhenius coefficients:                2.61E+19   -2.4    20710.0
242. C3H5+O2=CH2CHO+CH2O                            7.14E+15   -1.2    21050.0
     Reverse Arrhenius coefficients:                4.94E+16   -1.4    88620.0
243. C3H5+O2=>C2H2+CH2O+OH                          9.72E+29   -5.7    21450.0
244. C3H4-A+M=C3H3+H+M                              1.14E+17    0.0    70000.0
     Reverse Arrhenius coefficients:                1.80E+15   -0.4    10610.0
245. C3H4-A+O2=C3H3+HO2                             4.00E+13    0.0    39160.0
     Reverse Arrhenius coefficients:                3.17E+11   -0.1      311.0
246. C3H4-A+HO2=CH2CO+CH2+OH                        4.00E+12    0.0    19000.0
     Reverse Arrhenius coefficients:                1.00E+00    0.0        0.0
247. C3H4-A+OH=CH2CO+CH3                            3.12E+12    0.0     -397.0
     Reverse Arrhenius coefficients:                1.81E+17   -1.4    36070.0
248. C3H4-A+OH=C3H3+H2O                             1.00E+07    2.0     1000.0
     Reverse Arrhenius coefficients:                1.60E+05    2.2    31730.0
249. C3H4-A+O=C2H4+CO                               7.80E+12    0.0     1600.0
     Reverse Arrhenius coefficients:                3.27E+08    1.3   121900.0
250. C3H4-A+O=C2H2+CH2O                             3.00E-03    4.6    -4243.0
     Reverse Arrhenius coefficients:                2.32E+02    3.2    81190.0
251. C3H4-A+H=C3H3+H2                               2.00E+07    2.0     5000.0
     Reverse Arrhenius coefficients:                3.02E+04    2.3    20840.0
252. C3H4-A+CH3=C3H3+CH4                            3.67E-02    4.0     6830.0
     Reverse Arrhenius coefficients:                5.06E-02    3.8    24210.0
253. C3H4-A+C3H5=C3H3+C3H6                          2.00E+11    0.0     7700.0
     Reverse Arrhenius coefficients:                2.64E+19   -2.7    42140.0
254. C3H3+OH=C3H2+H2O                               1.00E+13    0.0        0.0
     Reverse Arrhenius coefficients:                1.34E+15    0.0    15680.0
255. C3H3+O2=CH2CO+HCO                              3.01E+10    0.0     2870.0
     Reverse Arrhenius coefficients:                4.88E+11    0.0    59470.0
256. C3H2+O2=HCO+HCCO                               5.00E+13    0.0        0.0
     Reverse Arrhenius coefficients:                2.33E+14   -0.2    77190.0
257. C3H4-A+HO2=C2H4+CO+OH                          1.00E+12    0.0    14000.0
     Reverse Arrhenius coefficients:                1.00E+00    0.0        0.0
258. C3H4-A+HO2=C3H3+H2O2                           3.00E+13    0.0    14000.0
     Reverse Arrhenius coefficients:                1.55E+16   -1.4    44000.0
259. C2H2+CH3=C3H4-A+H                              6.74E+19   -2.1    31590.0
     Reverse Arrhenius coefficients:                6.41E+25   -3.3    21770.0
260. C3H3+H=C3H2+H2                                 5.00E+13    0.0        0.0
     Reverse Arrhenius coefficients:                6.00E+07    1.4     4110.0
261. C3H2+OH=C2H2+HCO                               5.00E+13    0.0        0.0
     Reverse Arrhenius coefficients:                2.28E+16   -0.3    75020.0
262. C3H2+O2=>HCCO+CO+H                             5.00E+13    0.0        0.0
263. NC3H7O2=NC3H7+O2                               2.40E+20   -1.6    35960.0
     Reverse Arrhenius coefficients:                4.52E+12    0.0        0.0
264. NC3H7O2=C3H6+HO2                               4.31E+36   -7.5    39510.0
     Reverse Arrhenius coefficients:                1.02E+28   -5.6    19440.0
265. NC3H7+H=C2H5+CH3                               3.70E+24   -2.9    12500.0
266. NC3H7+OH=C3H6+H2O                              2.40E+13    0.0        0.0
267. C3H6+OH=C3H5+H2O                               3.10E+06    2.0     -298.3
     Declared duplicate reaction...
268. C3H6+H=C3H5+H2                                 1.70E+05    2.5     2492.8
     Declared duplicate reaction...
269. C2H2+CH3(+M)=C3H5(+M)                          6.00E+08    0.0        0.0
     Low pressure limit:  0.20000E+10  0.10000E+01  0.00000E+00
     TROE centering:      0.50000E+00  0.10000E+31  0.00000E+00
270. C3H5+H(+M)=C3H6(+M)                            2.00E+14    0.0        0.0
     CH4             Enhanced by    2.000E+00
     CO              Enhanced by    1.500E+00
```

```
     CO2             Enhanced by    2.000E+00
     C2H6            Enhanced by    3.000E+00
     H2O             Enhanced by    6.000E+00
     H2              Enhanced by    2.000E+00
     Low pressure limit:  0.13300E+61 -0.12000E+02  0.59680E+04
     TROE centering:      0.20000E-01  0.10970E+04  0.10970E+04  0.68600E+04
271. C3H5+HO2=C3H6+O2                                 2.66E+12    0.0        0.0
     Declared duplicate reaction...
272. C3H5+HO2=OH+C2H3+CH2O                            3.00E+12    0.0        0.0
     Declared duplicate reaction...
273. CH3+C2H3=C3H5+H                                  1.50E+24   -2.8    18618.5
274. C3H3+HO2=OH+CO+C2H3                              8.00E+11    0.0        0.0
275. C2H5+O2=C2H4+HO2                                 2.09E+09    0.5     -391.4
     Declared duplicate reaction...
     Rate coefficients at P=4.00E-02(atm)             2.094E+09    0.5     -391.4
     Rate coefficients at P=1.00E+00(atm)             1.843E+07    1.1     -720.6
     Rate coefficients at P=1.00E+01(atm)             7.561E+14   -1.0     4749.0
276. C2H5+O2=C2H4+HO2                                 6.61E+00    3.5    14160.0
     Declared duplicate reaction...
277. CH2CO+CH3=C2H5+CO                                4.77E+04    2.3     9468.0
278. 2C2H3=C2H2+C2H4                                  9.60E+11    0.0        0.0
279. C2H4+OH=CH3CHO+H                                 2.94E+09    0.9    12530.0
280. C2H3+O2=>H+CO+CH2O                               5.19E+15   -1.3     3313.0
281. C2H2+HCO=C2H3+CO                                 1.00E+07    2.0     6000.0
282. CH3CHO(+M)=CH3+HCO(+M)                           2.45E+22   -1.7    86360.0
     Low pressure limit:  0.10300E+60 -0.11300E+02  0.95910E+05
     TROE centering:      0.24900E-02  0.71810E+03  0.60890E+01  0.37800E+04
283. CH3CHO+H=CH2CHO+H2                               2.72E+03    3.1     5210.0
284. CH2CHO(+M)=CH2CO+H(+M)                           1.43E+15   -0.1    45600.0
     Low pressure limit:  0.60000E+30 -0.38000E+01  0.43420E+05
     TROE centering:      0.98500E+00  0.39300E+03  0.98000E+10  0.50000E+10
285. CH2CHO(+M)=CH3+CO(+M)                            2.93E+12    0.3    40300.0
     Low pressure limit:  0.95200E+34 -0.50700E+01  0.41300E+05
     TROE centering:      0.71300E-16  0.11500E+04  0.49900E+10  0.17900E+10
286. CH2CHO+O2=CH2CO+HO2                              1.88E+05    2.4    23730.0
     Rate coefficients at P=1.00E-02(atm)             1.880E+05    2.4    23730.0
     Rate coefficients at P=1.00E-01(atm)             1.880E+05    2.4    27370.0
     Rate coefficients at P=1.00E+00(atm)             2.510E+05    2.3    23800.0
     Rate coefficients at P=1.00E+01(atm)             7.050E+07    1.6    25290.0
287. CH3CHO(+M)=CH4+CO(+M)                            2.72E+21   -1.7    86360.0
     Low pressure limit:  0.11440E+59 -0.11300E+02  0.95910E+05
     TROE centering:      0.24900E-02  0.71810E+03  0.60890E+01  0.37800E+04
288. CH2+O2=HCO+OH                                    1.06E+13    0.0     1500.0
289. N+NO<=>N2+O                                      2.70E+13    0.0      355.0
290. N+O2<=>NO+O                                      9.00E+09    1.0     6500.0
291. N+OH<=>NO+H                                      3.36E+13    0.0      385.0
292. N2O+O<=>N2+O2                                    1.40E+12    0.0    10810.0
293. N2O+O<=>2NO                                      2.90E+13    0.0    23150.0
294. N2O+H<=>N2+OH                                    3.87E+14    0.0    18880.0
295. N2O+OH<=>N2+HO2                                  2.00E+12    0.0    21060.0
296. N2O(+M)<=>N2+O(+M)                               7.91E+10    0.0    56020.0
     Low pressure limit:  0.63700E+15  0.00000E+00  0.56640E+05
     H2              Enhanced by    2.000E+00
     H2O             Enhanced by    6.000E+00
     CH4             Enhanced by    2.000E+00
     CO              Enhanced by    1.500E+00
     CO2             Enhanced by    2.000E+00
     C2H6            Enhanced by    3.000E+00
297. HO2+NO<=>NO2+OH                                  2.11E+12    0.0     -480.0
298. NO+O+M<=>NO2+M                                   1.06E+20   -1.4        0.0
     H2              Enhanced by    2.000E+00
     H2O             Enhanced by    6.000E+00
     CH4             Enhanced by    2.000E+00
```

```
     CO              Enhanced by    1.500E+00
     CO2             Enhanced by    2.000E+00
     C2H6            Enhanced by    3.000E+00
299. NO2+O<=>NO+O2                                 3.90E+12    0.0     -240.0
300. NO2+H<=>NO+OH                                 1.32E+14    0.0      360.0
301. NH+O<=>NO+H                                   4.00E+13    0.0        0.0
302. NH+H<=>N+H2                                   3.20E+13    0.0      330.0
303. NH+OH<=>HNO+H                                 2.00E+13    0.0        0.0
304. NH+OH<=>N+H2O                                 2.00E+09    1.2        0.0
305. NH+O2<=>HNO+O                                 4.61E+05    2.0     6500.0
306. NH+O2<=>NO+OH                                 1.28E+06    1.5      100.0
307. NH+N<=>N2+H                                   1.50E+13    0.0        0.0
308. NH+H2O<=>HNO+H2                               2.00E+13    0.0    13850.0
309. NH+NO<=>N2+OH                                 2.16E+13   -0.2        0.0
310. NH+NO<=>N2O+H                                 3.65E+14   -0.5        0.0
311. NH2+O<=>OH+NH                                 3.00E+12    0.0        0.0
312. NH2+O<=>H+HNO                                 3.90E+13    0.0        0.0
313. NH2+H<=>NH+H2                                 4.00E+13    0.0     3650.0
314. NH2+OH<=>NH+H2O                               9.00E+07    1.5     -460.0
315. NNH<=>N2+H                                    3.30E+08    0.0        0.0
316. NNH+M<=>N2+H+M                                1.30E+14   -0.1     4980.0
     H2              Enhanced by    2.000E+00
     H2O             Enhanced by    6.000E+00
     CH4             Enhanced by    2.000E+00
     CO              Enhanced by    1.500E+00
     CO2             Enhanced by    2.000E+00
     C2H6            Enhanced by    3.000E+00
317. NNH+O2<=>HO2+N2                               5.00E+12    0.0        0.0
318. NNH+O<=>OH+N2                                 2.50E+13    0.0        0.0
319. NNH+O<=>NH+NO                                 7.00E+13    0.0        0.0
320. NNH+H<=>H2+N2                                 5.00E+13    0.0        0.0
321. NNH+OH<=>H2O+N2                               2.00E+13    0.0        0.0
322. NNH+CH3<=>CH4+N2                              2.50E+13    0.0        0.0
323. H+NO+M<=>HNO+M                                4.48E+19   -1.3      740.0
     H2              Enhanced by    2.000E+00
     H2O             Enhanced by    6.000E+00
     CH4             Enhanced by    2.000E+00
     CO              Enhanced by    1.500E+00
     CO2             Enhanced by    2.000E+00
     C2H6            Enhanced by    3.000E+00
324. HNO+O<=>NO+OH                                 2.50E+13    0.0        0.0
325. HNO+H<=>H2+NO                                 9.00E+11    0.7      660.0
326. HNO+OH<=>NO+H2O                               1.30E+07    1.9     -950.0
327. HNO+O2<=>HO2+NO                               1.00E+13    0.0    13000.0
328. CN+O<=>CO+N                                   7.70E+13    0.0        0.0
329. CN+OH<=>NCO+H                                 4.00E+13    0.0        0.0
330. CN+H2O<=>HCN+OH                               8.00E+12    0.0     7460.0
331. CN+O2<=>NCO+O                                 6.14E+12    0.0     -440.0
332. CN+H2<=>HCN+H                                 2.95E+05    2.5     2240.0
333. NCO+O<=>NO+CO                                 2.35E+13    0.0        0.0
334. NCO+H<=>NH+CO                                 5.40E+13    0.0        0.0
335. NCO+OH<=>NO+H+CO                              2.50E+12    0.0        0.0
336. NCO+N<=>N2+CO                                 2.00E+13    0.0        0.0
337. NCO+O2<=>NO+CO2                               2.00E+12    0.0    20000.0
338. NCO+M<=>N+CO+M                                3.10E+14    0.0    54050.0
     H2              Enhanced by    2.000E+00
     H2O             Enhanced by    6.000E+00
     CH4             Enhanced by    2.000E+00
     CO              Enhanced by    1.500E+00
     CO2             Enhanced by    2.000E+00
     C2H6            Enhanced by    3.000E+00
339. NCO+NO<=>N2O+CO                               1.90E+17   -1.5      740.0
340. NCO+NO<=>N2+CO2                               3.80E+18   -2.0      800.0
```

```
341. HCN+M<=>H+CN+M                                   1.04E+29   -3.3   126600.0
     H2              Enhanced by    2.000E+00
     H2O             Enhanced by    6.000E+00
     CH4             Enhanced by    2.000E+00
     CO              Enhanced by    1.500E+00
     CO2             Enhanced by    2.000E+00
     C2H6            Enhanced by    3.000E+00
 342. HCN+O<=>NCO+H                                   2.03E+04    2.6     4980.0
 343. HCN+O<=>NH+CO                                   5.07E+03    2.6     4980.0
 344. HCN+O<=>CN+OH                                   3.91E+09    1.6    26600.0
 345. HCN+OH<=>HOCN+H                                 1.10E+06    2.0    13370.0
 346. HCN+OH<=>HNCO+H                                 4.40E+03    2.3     6400.0
 347. HCN+OH<=>NH2+CO                                 1.60E+02    2.6     9000.0
 348. H+HCN(+M)<=>H2CN(+M)                            3.30E+13    0.0        0.0
     Low pressure limit:  0.14000E+27 -0.34000E+01  0.19000E+04
     H2              Enhanced by    2.000E+00
     H2O             Enhanced by    6.000E+00
     CH4             Enhanced by    2.000E+00
     CO              Enhanced by    1.500E+00
     CO2             Enhanced by    2.000E+00
     C2H6            Enhanced by    3.000E+00
 349. H2CN+N<=>N2+CH2                                 6.00E+13    0.0      400.0
 350. C+N2<=>CN+N                                     6.30E+13    0.0    46020.0
 351. CH+N2<=>HCN+N                                   3.12E+09    0.9    20130.0
 352. CH+N2(+M)<=>HCNN(+M)                            3.10E+12    0.1        0.0
     Low pressure limit:  0.13000E+26 -0.31600E+01  0.74000E+03
     TROE centering:      0.66700E+00  0.23500E+03  0.21170E+04  0.45360E+04
     H2              Enhanced by    2.000E+00
     H2O             Enhanced by    6.000E+00
     CH4             Enhanced by    2.000E+00
     CO              Enhanced by    1.500E+00
     CO2             Enhanced by    2.000E+00
     C2H6            Enhanced by    3.000E+00
 353. CH2+N2<=>HCN+NH                                 1.00E+13    0.0    74000.0
 354. CH2(S)+N2<=>NH+HCN                              1.00E+11    0.0    65000.0
 355. C+NO<=>CN+O                                     1.90E+13    0.0        0.0
 356. C+NO<=>CO+N                                     2.90E+13    0.0        0.0
 357. CH+NO<=>HCN+O                                   4.10E+13    0.0        0.0
 358. CH+NO<=>H+NCO                                   1.62E+13    0.0        0.0
 359. CH+NO<=>N+HCO                                   2.46E+13    0.0        0.0
 360. CH2+NO<=>H+HNCO                                 3.10E+17   -1.4     1270.0
 361. CH2+NO<=>OH+HCN                                 2.90E+14   -0.7      760.0
 362. CH2+NO<=>H+HCNO                                 3.80E+13   -0.4      580.0
 363. CH2(S)+NO<=>H+HNCO                              3.10E+17   -1.4     1270.0
 364. CH2(S)+NO<=>OH+HCN                              2.90E+14   -0.7      760.0
 365. CH2(S)+NO<=>H+HCNO                              3.80E+13   -0.4      580.0
 366. CH3+NO<=>HCN+H2O                                9.60E+13    0.0    28800.0
 367. CH3+NO<=>H2CN+OH                                1.00E+12    0.0    21750.0
 368. HCNN+O<=>CO+H+N2                                2.20E+13    0.0        0.0
 369. HCNN+O<=>HCN+NO                                 2.00E+12    0.0        0.0
 370. HCNN+O2<=>O+HCO+N2                              1.20E+13    0.0        0.0
 371. HCNN+OH<=>H+HCO+N2                              1.20E+13    0.0        0.0
 372. HCNN+H<=>CH2+N2                                 1.00E+14    0.0        0.0
 373. HNCO+O<=>NH+CO2                                 9.80E+07    1.4     8500.0
 374. HNCO+O<=>HNO+CO                                 1.50E+08    1.6    44000.0
 375. HNCO+O<=>NCO+OH                                 2.20E+06    2.1    11400.0
 376. HNCO+H<=>NH2+CO                                 2.25E+07    1.7     3800.0
 377. HNCO+H<=>H2+NCO                                 1.05E+05    2.5    13300.0
 378. HNCO+OH<=>NCO+H2O                               3.30E+07    1.5     3600.0
 379. HNCO+OH<=>NH2+CO2                               3.30E+06    1.5     3600.0
 380. HNCO+M<=>NH+CO+M                                1.18E+16    0.0    84720.0
     H2              Enhanced by    2.000E+00
     H2O             Enhanced by    6.000E+00
```

```
     CH4             Enhanced by    2.000E+00
     CO              Enhanced by    1.500E+00
     CO2             Enhanced by    2.000E+00
     C2H6            Enhanced by    3.000E+00
381. HCNO+H<=>H+HNCO                                  2.10E+15   -0.7     2850.0
382. HCNO+H<=>OH+HCN                                  2.70E+11    0.2     2120.0
383. HCNO+H<=>NH2+CO                                  1.70E+14   -0.8     2890.0
384. HOCN+H<=>H+HNCO                                  2.00E+07    2.0     2000.0
385. HCCO+NO<=>HCNO+CO                                9.00E+12    0.0        0.0
386. CH3+N<=>H2CN+H                                   6.10E+14   -0.3      290.0
387. CH3+N<=>HCN+H2                                   3.70E+12    0.1      -90.0
388. NH3+H<=>NH2+H2                                   5.40E+05    2.4     9915.0
389. NH3+OH<=>NH2+H2O                                 5.00E+07    1.6      955.0
390. NH3+O<=>NH2+OH                                   9.40E+06    1.9     6460.0
391. NH+CO2<=>HNO+CO                                  1.00E+13    0.0    14350.0
392. CN+NO2<=>NCO+NO                                  6.16E+15   -0.8      345.0
393. NCO+NO2<=>N2O+CO2                                3.25E+12    0.0     -705.0
394. N+CO2<=>NO+CO                                    3.00E+12    0.0    11300.0

UNITS for the preceding reactions (unless otherwise noted):
      A units mole-cm-sec-K, E units cal/mole
```

B The code of FGM tabulation constructions.

The diffusion FGM manifolds were constructed using the following MATLAB code, which is written in C++ programming language. The premixed FGM manifold can be constructed using the below code from line 230 and below with very slight modifications as explained from line 190 to 228.

```
%%%%%%%%%%%%%%%%%%%%%%%%%%%%%%%%%%%%%%%%%%%%%%%%%%%%%%%%%%%%%%%%%%%%%%%%
%%%         This code constructs the FGM manifolds                     %%%
%%%     By transforming the coordinate of diffusion                    %%%
%%%    flamelets from time and distance to mixture                     %%%
%%%           fraction and progress variable                           %%%
%%%                                                                    %%%
%%%                                                                    %%%
%%%    Two files needed to construct the FGM manifold:                 %%%
%%%     1. yi files contain the all required data.                     %%%
%%%     2. si files contain the source term of species.                %%%
%%%                                                                    %%%
%%%                                                                    %%%
%%%     It is important to mention that the (##) sign                  %%%
%%%   represents a certain number due to the variation                 %%%
%%%         of some inputs from a case to another.                     %%%
%%%%%%%%%%%%%%%%%%%%%%%%%%%%%%%%%%%%%%%%%%%%%%%%%%%%%%%%%%%%%%%%%%%%%%%%

% Assign the number of Yi files, which is equal to Si files
NumOfFiles = ##;

% In both Yi and Si files, the data starts from the 22nd line.
NumOfEmptyLines = 22;

% Column number of mixture fraction in Yi input files.
ColNumOfMixFra = ##;

%%%%%%%%%%%%%%%%%%%%%%%%%%%%%%%%%%%%%%%%%%%%%%%%%%%%%%%%%%%%%%%%%%%%%%%%
%%%            This part of the code unites                            %%%
%%%    the mixture fraction values in the input files                  %%%
%%%               by means of interpolation                            %%%
%%%      as it varies in the consecutive input files                   %%%
%%%    due to the inclusion of igniting and stationary                 %%%
%%%                        flamelets.                                  %%%
%%%%%%%%%%%%%%%%%%%%%%%%%%%%%%%%%%%%%%%%%%%%%%%%%%%%%%%%%%%%%%%%%%%%%%%%

% Beginning of a loop by reading the yi and si consecutive files
for IndexOfFile =  NumOfFiles:-1:0
    InputYiFile = strcat('yi' , num2str(IndexOfFile) , '.dat');
    NumOfYiFiles = fopen(InputYiFile,'r');
    if NumOfYiFiles == -1
        return ;
    end
    InputSiFile = strcat('si' , num2str(IndexOfFile) , '.dat');
    NumOfSiFiles = fopen(InputSiFile,'r');
    if NumOfSiFiles == -1
```

```
46          return ;
47      end
48
49      % Same procedure implemented above is used to create the new output files
50      % to write new Yi and Si files after uniting the mixture fraction
51      % by interpolation.
52      OutYiFile = strcat('yi' , num2str(IndexOfFile) , '00_out.dat');
53      OpenOutYiFiles = fopen(OutYiFile,'wt+');
54      if OpenOutYiFiles == -1
55          return ;
56      end
57      OutSiFile = strcat('si' , num2str(IndexOfFile) , '00_out.dat');
58      OpenOutSiFiles = fopen(OutSiFile,'wt+');
59      if OpenOutSiFiles == -1
60          return ;
61      end
62
63      % initializing a variable to get the data line by line.
64      NumOfLine = 0;
65      % initializing arrays to store the data of Yi and Si files.
66      ArrayForYi = [];
67      ArrayForSi = [];
68      while (~feof(NumOfYiFiles) && ~feof(NumOfSiFiles) )
69          % Read one line from NumOfYi(Si)Files and store it in LineOfYi(Si)File
70          LineOfYiFile = fgetl(NumOfYiFiles);
71          LineOfSiFile = fgetl(NumOfSiFiles);
72          NumOfLine = NumOfLine + 1;
73
74          % copying the headers from the yi(si)##.dat files to yi(si)##00_out.dat.
75          if NumOfLine <= NumOfEmptyLines
76              fprintf(OpenOutYiFiles, char(LineOfYiFile));
77              fprintf(OpenOutYiFiles, '\n');
78              fprintf(OpenOutSiFiles, char(LineOfYiFile));
79              fprintf(OpenOutSiFiles, '\n');
80              continue;
81          end
82
83          % copying data (Numbers).
84          if IndexOfFile == NumOfFiles
85              fprintf(OpenOutYiFiles, char(LineOfYiFile));
86              fprintf(OpenOutYiFiles, '\n');
87              fprintf(OpenOutSiFiles, char(LineOfYiFile));
88              fprintf(OpenOutSiFiles, '\n');
89
90          end
91
92          % Splitting the string with ' ' delimiter.
93          SplitStringofYi = strsplit(LineOfYiFile,' ');
94          SplitStringofSi = strsplit(LineOfSiFile,' ');
95
96          % Storing the data arrays.
97          ArrayForYi = [ArrayForYi; SplitStringofYi];
98          ArrayForSi = [ArrayForSi; SplitStringofSi];
99
100     end
101
102
103     fclose(NumOfYiFiles);
104     fclose(NumOfSiFiles);
105
106     % As the set of mixture fraction differs from a file to another, it was
107     % decided to use the set of mixture fraction values in the last input file
108     % (stationary flamelet) to describe the reaction zone properly due to the
```

```
109     % adaptive gridding technique utilised by CHEM1D.
110
111     if IndexOfFile == NumOfFiles
112        NewOfMixFra = str2double(ArrayForYi(:,ColNumOfMixFra));
113     else
114
115         % Getting the data of Yi file and assign a variable for default
116         % mixture fraction (OldMixFra) for interpolation.
117         [row, col] = size(ArrayForYi);
118         DataOfYiFile = zeros(row,col-1);
119         DataOfYiFile(:,1) = str2double(ArrayForYi(:,2));
120         OldMixFra = str2double(ArrayForYi(:,ColNumOfMixFra));
121
122      % Distinguishing the indices of duplicated values of mixture fraction to
123      % skip them during the interpolation process to avoid errors.
124         [~,index] = unique(OldMixFra);
125
126         % Starting the interpolation loop.
127         for ii = 3:col
128             if ii == ColNumOfMixFra
129                 DataOfYiFile(:, ii-1) = NewOfMixFra;
130                 continue
131             end
132
133             % Interpolation.
134             DataOfYiFile(index, ii-1) =
interp1(OldMixFra(index),str2double(ArrayForYi(index,ii)),NewOfMixFra(index));
135
136         end
137
138         % Writing the interpolated data in the output Yi files.
139         for ii = 1:row
140             % Dilimiter at the beginning (from left).
141             wrString = "    ";
142             for jj = 1: (col-1)
143              % Writing the space ("    ") at the beginning of the string.
144                 if jj == 1
145                    wrString =  strcat(wrString,  sprintf("%d", jj));
146                 else
147                    % Writing the interpolated data in the string.
148                    wrString =  strcat(wrString, " ");   % Dilimiter between data.
149                    wrString =  strcat(wrString, sprintf("%.9E",
DataOfYiFile(ii,jj)));
150                 end
151             end
152             % writing the data in the output file.
153          fprintf(OpenOutYiFiles, wrString);
154             fprintf(OpenOutYiFiles, '\n');
155         end
156
157
158         % Same porcess is implemented for si###.dat files.
159         [row, col] = size(ArrayForSi);
160         DataOfSiFile = zeros(row,col-1);
161         DataOfSiFile(:,1) = str2double(ArrayForSi(:,2));
162
163         [~,index] = unique(OldMixFra);
164
165         for ii = 3:col
166             DataOfSiFile(index, ii-1) =
interp1(OldMixFra(index),str2double(ArrayForSi(index,ii)),NewOfMixFra(index));
167         end
```

```

       for ii = 1:row
           wrString = "   ";
           for jj = 1: (col-1)
               if jj == 1

                  wrString =  strcat(wrString,  sprintf("%d", jj));
               else
                  wrString =  strcat(wrString, " ");
                  wrString =  strcat(wrString, sprintf("%.9E",
DataOfSiFile(ii,jj)));
               end
           end
           fprintf(OpenOutSiFiles, wrString);
           fprintf(OpenOutSiFiles, '\n');
       end
   end
   fclose(OpenOutYiFiles);
   fclose(OpenOutSiFiles);

end


%%%%%%%%%%%%%%%%%%%%%%%%%%%%%%%%%%%%%%%%%%%%%%%%%%%%%%%%%%%%%%%%%%%%%%%%%
%%%      The following loop re-arranges the data in new output       %%%
%%%      files named collection##.scv files. The new arrangement      %%%
%%%      aims to gather the data, which has the same value of         %%%
%%%      mixture fraction, in one output file. At this stage, the     %%%
%%%      values of mixture fraction (Z) is united in the input files  %%%
%%%      by interpolation.                                            %%%
%%%                                                                   %%%
%%%      Thus, the following part of the code:                        %%%
%%%                                                                   %%%
%%%      1) reads yi100_out.dat and si100.dat.                        %%%
%%%      2) extract the first row, which has Z of 1                   %%%
%%%      3) write it as the first row in collection1.scv.             %%%
%%%      4) extract the second row, which has Z of                    %%%
%%%         (i.e. 0.99)                                               %%%
%%%      5) write it as the first row in collection2.scv and so on    %%%
%%%         until the last column (i.e. 200) which has                %%%
%%%         Z of 0, and write in collection200.scv.                   %%%
%%%      6) the same procedure is repeated for                        %%%
%%%         yi200_out.dat and si200.dat (with writing the             %%%
%%%         data in the second row in collection#.scv)                %%%
%%%         until the last input files (yi###_out.dat and si###.dat). %%%
%%%                                                                   %%%
%%%      This procedure ensures that every collection#.scv file has   %%%
%%%      a set of data with one mixture fraction value.               %%%
%%%      Doing this makes sure that the final flamelet output file    %%%
%%%      matches the flamelet format accepted by Fluent as each       %%%
%%%      flamelet should consist of one mixture fraction value.       %%%
%%%                                                                   %%%
%%%      The premixed flamelets are generated with one mixture        %%%
%%%      value by default. Thus, the above explained procedure        %%%
%%%      differs. To demonstrate the difference in constructing       %%%
%%%      the premixed and diffusion manifolds:                        %%%
%%%                                                                   %%%
%%%      1) The light blue lines are only for premixed flamelets      %%%
%%%      2) the red lines are only for diffusion flamelets            %%%
%%%      3) The normal colored lines for both flamelets               %%%
%%%                                                                   %%%
%%%%%%%%%%%%%%%%%%%%%%%%%%%%%%%%%%%%%%%%%%%%%%%%%%%%%%%%%%%%%%%%%%%%%%%%%

```

```
230
231MaxNumOfLine = 0;
232for IndexOfFile =  1:NumOfFiles;
233    InputYiFile = strcat('yi' , num2str(IndexOfFile) , '00_out.dat');
234    NumOfYiFiles = fopen(InputYiFile,'r');
235    if NumOfYiFiles == -1
236        return ;
237    end
238    InputSiFile = strcat('si' , num2str(IndexOfFile) , '00_out.dat');
239    NumOfSiFiles = fopen(InputSiFile,'r');
240    if NumOfSiFiles == -1
241        return ;
242    end
243
244 % Creating collection##.csv files. (For premixed manifold constructions)
245    ConcatOutputFile = strcat( 'collection' , (IndexOfFile) , '.csv');
246
247    OutputFile = fopen(ConcatOutputFile, 'wt');
248
249    NumOfLine = 0;
250
251    %(For premixed manifold constructions)
252    ArrayForYi = [];
253    ArrayForSi = [];
254    while (~feof(NumOfYiFiles) && ~feof(NumOfSiFiles) )
255        LineOfYiFile = fgetl(NumOfYiFiles);
256        LineOfSiFile = fgetl(NumOfSiFiles);
257        NumOfLine = NumOfLine + 1;
258
259        % This if statement reads the headers and remove
260        % them from the new outputs (collection #) files as they are not needed.
261        if NumOfLine <= NumOfEmptyLines
262            continue;
263        end
264
265        % Converting numbers (i.e. from -.89 to -0.89) to avoid
266        % errors.
267        LineOfYiFile = strrep(LineOfYiFile, '-.', '-0.');
268        LineOfSiFile = strrep(LineOfSiFile, '-.', '-0.');
269
270        % Removing leading spaces to avoid errors.
271        LineOfYiFile = strtrim(LineOfYiFile);
272        LineOfSiFile = strtrim(LineOfSiFile);
273
274        % Skipping empty spaces to avoid errors.
275        if isempty(LineOfYiFile) || isempty(LineOfSiFile)
276            break
277        end
278
279        % Creating collection##.csv files.
280        ConcatOutputFile = strcat( 'collection' , num2str(NumOfLine -
NumOfEmptyLines) , '.csv');
281        if IndexOfFile ==  1
282            % writing data.
283            OutputFile = fopen(ConcatOutputFile, 'wt');
284        else
285            % Appending data to exist files.
286            OutputFile = fopen(ConcatOutputFile, 'a+');
287        end
288
289        SplitStringofSi2 = strsplit(LineOfSiFile, ' ');
290
291        % Getting the source terms of species chosen to represent PV
```

```
        % getting the source term of species chosen to represent PV.
        LineOfFile = strcat(LineOfYiFile, {' '}, SplitStringofSi2(##), {' '});

%%%%%%%%%%%%%%%%%%%%%%%%%%%%%%%%%%%%%%%%%%%%%%%%%%%%%%%%%%%%%%%%%%%%%%%%%
%%%                                                                   %%%
%%%       For example, if the species chosen to represent PV are      %%%
%%%       hydrogen and water and their column numbers are 5 and 6     %%%
%%%       , respectively. The above command should be:                %%%
%%%                                                                   %%%
%%%       LineOfFile = strcat(LineOfYiFile, {' '},                    %%%
%%%       SplitStringofSi2(5), {' '}, SplitStringofSi2(6), {' '});    %%%
%%%                                                                   %%%
%%%%%%%%%%%%%%%%%%%%%%%%%%%%%%%%%%%%%%%%%%%%%%%%%%%%%%%%%%%%%%%%%%%%%%%%%

        LineOfFile = strtrim(LineOfFile);

        fprintf(OutputFile, char(LineOfFile));
        fprintf(OutputFile, '\n');

        % For Premixed manifolds.
        SplitStringofYi = strsplit(LineOfYiFile,' ');
        SplitStringofSi = strsplit(LineOfSiFile,' ');

        ArrayForYi = [ArrayForYi; SplitStringofYi];
        ArrayForSi = [ArrayForSi; SplitStringofSi];

        fclose(OutputFile);
    end

 % For premixed manifolds
 fclose(OutputFile);

 % For only diffusion manifolds.
    if MaxNumOfLine < NumOfLine;
       MaxNumOfLine = NumOfLine;
    end
    fclose(NumOfYiFiles);
    fclose(NumOfSiFiles);

 end

% creating and then opening the flamelet file, respectively.
outputfilename = 'flamelet.fla'
OutputFile = fopen(outputfilename,'w');


%%%%%%%%%%%%%%%%%%%%%%%%%%%%%%%%%%%%%%%%%%%%%%%%%%%%%%%%%%%%%%%%%%%%%%%%%
%%%                                                                   %%%
%%%       The following loop is written to:-                          %%%
%%%                                                                   %%%
%%%       1. Open the new input files named collection##.scv and,     %%%
%%%          then, stored the data in an array.                       %%%
%%%       2. Write the headers for each flamelet. Each flamelet in    %%%
%%%          the 'flamelet.dat' has the same mixture fraction value.  %%%
%%%       3. Calculate the progress variable 'PV'.                    %%%
%%%       4. Arrange the PV to be monotonically increased from 0 to 1 %%%
%%%          and, accordingly, the rest of data.                      %%%
%%%       5. Unite the PV values for all flamelets by interpolation.  %%%
%%%       6. Interpolate the data with respect to PV.                 %%%
%%%       7. Writing the data in the same format accepted by Fluent.  %%%
%%%                                                                   %%%
%%%%%%%%%%%%%%%%%%%%%%%%%%%%%%%%%%%%%%%%%%%%%%%%%%%%%%%%%%%%%%%%%%%%%%%%%

```

```
MaxNumOfLine = MaxNumOfLine - NumOfEmptyLines;
 for IndexOfFile =  (MaxNumOfLine) : -1  : 1
    ConcatInputFile = strcat('collection' , num2str(IndexOfFile) , '.csv');
    InputFile = fopen(ConcatInputFile,'r');

    if InputFile == -1
       continue;
    end
    Array = [];
    while (~feof(InputFile))

  % getting the data stored in the collection.scv file line by line.
       LineOfFile = fgetl(InputFile);
       SplitString = strsplit(LineOfFile, ' ');
       Array = [Array ; SplitString];

    end
    fclose(InputFile) ;

    % Writing the headers for each flamelet.
    fprintf(OutputFile, 'HEADER\r');
    fprintf(OutputFile, 'PREMIX_STOICH_SCADIS\t0.000000E+00\r');
    fprintf(OutputFile,  'Z         \t%s\r', char(Array(1,##)));
    fprintf(OutputFile, 'NUMOFSPECIES\t##\r');
    fprintf(OutputFile, 'GRIDPOINTS\t%d\r', ##);
    fprintf(OutputFile, 'STOICH_Z\t##\r');
    fprintf(OutputFile, 'PRESSURE\t%s\r', char(Array(1,##)));
    fprintf(OutputFile, 'BODY\r');

    Array = str2double(Array);


    % Calculating the un-normalised PV.
    PV = (Array(:,##)/###) + (Array(:,##)/###) + (Array(:,##)/###);

%%%%%%%%%%%%%%%%%%%%%%%%%%%%%%%%%%%%%%%%%%%%%%%%%%%%%%%%%%%%%%%%%%%%%%%%%
%%%                                                                   %%%
%%%       For example, if the species chosen to represent PV are      %%%
%%%       hydrogen and water and their column numbers are 5 and 6     %%%
%%%       , respectively. The above command should be:                %%%
%%%                                                                   %%%
%%%       PV = (Array(:,5)/2.02) + (2* Array(:,6)/18.02);             %%%
%%%                                                                   %%%
%%%       2.02 and 18.02 are the molecular weight of hydrogen         %%%
%%%       and water, respectively.                                    %%%
%%%                                                                   %%%
%%%%%%%%%%%%%%%%%%%%%%%%%%%%%%%%%%%%%%%%%%%%%%%%%%%%%%%%%%%%%%%%%%%%%%%%%

    % Getting the maximum and minimum values of PV for normalisation.
    Unpvmax = max(PV);
    Unpvmin = min(PV);

    % Calculating the PV Numerator.
    Numerator = PV - Unpvmin;

    [row,col] = size(Array);
    if Unpvmax ~= Unpvmin
        % Normalising PV.
        PV = Numerator /(Unpvmax - Unpvmin);

      % Arrange the PV to be monotonically increased from 0 to 1
      % and, accordingly, the rest of data.
        for i = 1 : (length(PV) - 1)
```

```
            for j = (i + 1): length(PV)

                % order PV from 0 to 1.
                if (PV(i) > PV(j))
                   temp = PV(i);
                   PV(i) = PV(j);
                   PV(j) = temp;

                % order the rest of data based on the new PV arrangement.
                   for  k = 1: col
                    temp = Array(i,k);
                    Array(i,k) = Array(j,k);
                    Array(j,k) = temp;
                   end

                end
            end
        end
    end


    % It important to mention that the PV values can be obtained in
    % a similar way used to obtain the mixture fraction as earlier
    % done. However, it was decided to assign the PV values to have
    % the same PV values for diffusion and premixed flamelets.

    newPV(1,1:##) = 0:(1/##):(1/##)*(##);

%%%%%%%%%%%%%%%%%%%%%%%%%%%%%%%%%%%%%%%%%%%%%%%%%%%%%%%%%%%%%%%%%%%%%%%%%
%%%                                                                   %%%
%%%       For example, if the grid points are 100. The above          %%%
%%%       command should be:                                          %%%
%%%                                                                   %%%
%%%       newPV(1,1:100) = 0:(1/99):(1/99)*(99);                      %%%
%%%                                                                   %%%
%%%      Using this command results in 100 values ranging            %%%
%%%      from 0 to 1 with 0.0101010101010101 difference              %%%
%%%      between a value to another                                   %%%
%%%                                                                   %%%
%%%%%%%%%%%%%%%%%%%%%%%%%%%%%%%%%%%%%%%%%%%%%%%%%%%%%%%%%%%%%%%%%%%%%%%%%

    [~,Index] = unique(PV);

    % Interpolating the other variables.
    if (IndexOfFile <= (MaxNumOfLine - 1))
        if norm(PV) ~= 0
            for ii = 1: col
                Array(Index, ii) = interp1(PV(Index),Array(Index,
ii),newPV(Index));
            end

            PV = newPV;
        end
    end

    % Writing the flamelets data in the same formatted accepted by Fluent.
    fprintf(OutputFile, 'REACTION_PROGRESS\r');
    for i = 1: length(PV)
        r = rem( i , 5 );
        if r == 0
            fprintf(OutputFile, '%.9E\r', PV(i));
        elseif i ~= length(PV)
            fprintf(OutputFile, '%.9E\t', PV(i));
```

```
        else
            fprintf(OutputFile, '%.9E\r', PV(i));
        end
    end

    % The ## sign in the following lines represents the column number of
    % temperature in the array.
    fprintf(OutputFile, 'TEMPERATURE\r');
    for i = 1: length(Array(:,##))
        r = rem( i , 5 );
        if r == 0
            fprintf(OutputFile, '%.9E\r', Array(i,##));
        elseif i ~= length(Array(:,##))
            fprintf(OutputFile, '%.9E\t', Array(i,##));
        else
            fprintf(OutputFile, '%.9E\r', Array(i,##));
        end
    end

    % The ## sign in the following lines represents the column number
    % of O2 mass fraction in the array.
    fprintf(OutputFile, 'massfraction-o2\r');
    for i = 1: length(Array(:,##))
        r = rem( i , 5 );
        if r == 0
            fprintf(OutputFile, '%.9E\r', Array(i,##));
        elseif i ~= length(Array(:,##))
            fprintf(OutputFile, '%.9E\t', Array(i,##));
        else
            fprintf(OutputFile, '%.9E\r', Array(i,##));
        end
    end

    % The ## sign in the following lines represents the column number
    % of N2 mass fraction in the array.
    fprintf(OutputFile, 'massfraction-n2\r');
    for i = 1: length(Array(:,##))
        r = rem( i , 5 );
        if r == 0
            fprintf(OutputFile, '%.9E\r', Array(i,##));
        elseif i ~= length(Array(:,##))
            fprintf(OutputFile, '%.9E\t', Array(i,##));
        else
            fprintf(OutputFile, '%.9E\r', Array(i,##));
        end
    end

    % .
    % .
    % .
    % .



    % Similar procedure should be written for the rest of data and
    % the differences lie in the name and column number of the variable
    % as demonstrated for temperature, O2 and N2.


end

fclose(OutputFile);
```

C Source code of computing the preferential diffusion coefficients.

The additional terms incorporated in the transport equations of control variables were calculated using the following code written in C programming language. It was coded using Code::Blocks 20.03 software with GUN GCC compiler to calculate the preferential diffusion coefficients from the PDF table, which contains an extremely huge number of data. Thus, the locally allocated memory should be increased to avoid the errors during the code run-time. This can be done by the following steps:

1. Open Code::Blocks 20.03.
2. Go to settings > compiler.
3. Go to the linker settings option.
4. Write ‘’ -Wl,--stack,50000000000 ‘’ in the link libraries.
5. Click on ‘’ Add ‘’ and then ‘’ OK ‘’.

```
#include <stdio.h>
#include <string.h>
#include <math.h>
//------------------------------------------------------------------------//
//                                                                        //
//    Due to the variations of some inputs from a case to another,        //
//    the ## sign represents a certain number which fits the case.        //
//                                                                        //
//------------------------------------------------------------------------//

// Gridpoints of control variables.
#define Z_GP     ##
#define ZVar_GP  ##
#define PV_GP    ##
#define PvVar_GP ##
#define H_GP     ##
#define NumOfSpec    ##

//------------------------------------------------------------------------//
//                                                                        //
// The following lines are the functions used to construct                //
// the additional terms of preferential diffusion effects.                //
//                                                                        //
//------------------------------------------------------------------------//

```

```
// The following function exports the output files
void Export4D(const char* Filename, double  Input[Z_GP][ZVar_GP][H_GP][PV_GP])
{
 if (Filename == NULL) return;

 FILE *file = fopen(Filename, "wb");
 if (file == NULL) return;
 for (int ii = 0; ii < Z_GP * ZVar_GP * H_GP * PV_GP; ii++)
 {
     char aaa[30];
     int i,j,k,m;
     memset(aaa, 0x0, sizeof(aaa));


        i = ii % Z_GP;
        j = (ii / Z_GP) % ZVar_GP;

        k = (ii / ZVar_GP / Z_GP) % H_GP;
        m = (ii / ZVar_GP / Z_GP / H_GP) % PV_GP;
     sprintf(aaa, "%lf\n", Input[i][j][k][m]);

     fwrite(aaa, strlen(aaa), 1, file);
 }
 fclose(file);
}

// The following function calculates the 1D gradient.
// It is written to be used in the 4D gradient function
// (GradOf4D) as shown below
int GradOf1D(double* Input, double* Output, int length)
{
 if (Input == NULL || Output == NULL || length <= 0)
     return 0;
 int i;
 for (i = 0; i < length; i++)
     Output[i] = 0;

 if (length > 1)
 {
     Output[0] = Input[1] - Input[0];
     Output[length - 1] = Input[length - 1] - Input[length - 2];
 }
 if (length > 2)
 {
     for (i = 1; i < (length-1); i++)
     {
         Output[i] = (Input[i+1] - Input[i - 1])/2;
     }
 }
 return 1;
}

// The following function calculates the gradient of 4D matrix
int GradOf4D(double  Input[Z_GP][ZVar_GP][H_GP][PV_GP], double
Output[Z_GP][ZVar_GP][H_GP][PV_GP])
{
 if (Input == NULL || Output == NULL)
     return 0;

 for (int i = 0; i < PV_GP; i++)
 {
     double tt_3d[Z_GP][ZVar_GP][H_GP];
     for (int ii = 0; ii < H_GP; ii++)
```

```
88      {
89          double tt_2d[Z_GP][ZVar_GP];
90          for (int iii = 0; iii < ZVar_GP; iii++)
91          {
92              double temp[Z_GP];
93              double temp_Grad[Z_GP];
94              for (int m = 0; m < Z_GP; m++)
95                  temp[m] = Input[m][iii][ii][i];
96
97              GradOf1D(temp, temp_Grad, PV_GP);
98
99              for (int m = 0; m < Z_GP; m++)
100                 tt_2d[m][iii] = temp_Grad[m];
101         }
102
103         for (int m = 0; m < Z_GP; m++)
104             for (int n = 0; n < ZVar_GP; n++)
105                 tt_3d[m][n][ii] = tt_2d[m][n];
106
107
108     }
109     for (int m = 0; m < Z_GP; m++)
110         for (int n = 0; n < ZVar_GP; n++)
111             for (int nn = 0; nn < H_GP; nn++)
112                 Output[m][n][nn][i] = tt_3d[m][n][nn];
113 }
114 return 1;
115}
116
117// The following function initialises 4D matrix with zeros
118 void InitialOf4dWithZeros(double Input[Z_GP][ZVar_GP][H_GP][PV_GP])
119{
120 for (int i = 0; i < Z_GP; i++)
121     for (int ii = 0; ii < ZVar_GP; ii++)
122         for (int iii = 0; iii < H_GP; iii++)
123             for (int iiii = 0; iiii < PV_GP; iiii++)
124                 Input[i][ii][iii][iiii] = 0;
125
126}
127
128// The following function performs a division operation between two 4D matrices
129 void DivOf4D(double Input1[Z_GP][ZVar_GP][H_GP][PV_GP], double
Input2[Z_GP][ZVar_GP][H_GP][PV_GP], double Output[Z_GP][ZVar_GP][H_GP][PV_GP])
130{
131 for (int i = 0; i < Z_GP; i++)
132     for (int ii = 0; ii < ZVar_GP; ii++)
133         for (int iii = 0; iii < H_GP; iii++)
134             for (int iiii = 0; iiii < PV_GP; iiii++)
135             {
136                 if (Input2[i][ii][iii][iiii] == 0)
137                     Output[i][ii][iii][iiii] = 0;
138                 else
139                     Output[i][ii][iii][iiii] = Input1[i][ii][iii][iiii] /
Input2[i][ii][iii][iiii];
140             }
141}
142
143// The following function performs a multiplication
144// operation between two 4D matrices.
145 void MultiOf4D(double Input1[Z_GP][ZVar_GP][H_GP][PV_GP], double
Input2[Z_GP][ZVar_GP][H_GP][PV_GP], double Output[Z_GP][ZVar_GP][H_GP][PV_GP])
146{
147 for (int i = 0; i < Z_GP; i++)
```

```
148     for (int ii = 0; ii < ZVar_GP; ii++)
149         for (int iii = 0; iii < H_GP; iii++)
150             for (int iiii = 0; iiii < PV_GP; iiii++)
151             {
152                 Output[i][ii][iii][iiii] = Input1[i][ii][iii][iiii] *
Input2[i][ii][iii][iiii];
153             }
154}
155
156// The following function performs an addition operation
157// between two 4D matrices.
158 void AddOf4D(double Input1[Z_GP][ZVar_GP][H_GP][PV_GP], double
Input2[Z_GP][ZVar_GP][H_GP][PV_GP], double Output[Z_GP][ZVar_GP][H_GP][PV_GP])
159{
160 for (int i = 0; i < Z_GP; i++)
161     for (int ii = 0; ii < ZVar_GP; ii++)
162         for (int iii = 0; iii < H_GP; iii++)
163             for (int iiii = 0; iiii < PV_GP; iiii++)
164             {
165                 Output[i][ii][iii][iiii] = Input1[i][ii][iii][iiii] +
Input2[i][ii][iii][iiii];
166             }
167}
168
169// The following function performs a multiplication
170// operation between a 4D matrix and number.
171 void MultiOf4dByNmub(double Input1[Z_GP][ZVar_GP][H_GP][PV_GP], double Input2,
double Output[Z_GP][ZVar_GP][H_GP][PV_GP])
172{
173 for (int i = 0; i < Z_GP; i++)
174     for (int ii = 0; ii < ZVar_GP; ii++)
175         for (int iii = 0; iii < H_GP; iii++)
176             for (int iiii = 0; iiii < PV_GP; iiii++)
177             {
178                 Output[i][ii][iii][iiii] = Input1[i][ii][iii][iiii] * Input2;
179             }
180}
181
182// The following function performs an addition
183// operation between a 4D matrix and number.
184 void AddOf4dByNmub(double Input1[Z_GP][ZVar_GP][H_GP][PV_GP], double Input2,
double Output[Z_GP][ZVar_GP][H_GP][PV_GP])
185{
186 for (int i = 0; i < Z_GP; i++)
187     for (int ii = 0; ii < ZVar_GP; ii++)
188         for (int iii = 0; iii < H_GP; iii++)
189             for (int iiii = 0; iiii < PV_GP; iiii++)
190             {
191                 Output[i][ii][iii][iiii] = Input1[i][ii][iii][iiii] + Input2;
192             }
193}
194
195// The following function performs a division
196// operation between a 4D matrix and number.
197 void DivOf4dByNmub(double Input1[Z_GP][ZVar_GP][H_GP][PV_GP], double Input2,
double Output[Z_GP][ZVar_GP][H_GP][PV_GP])
198{
199 for (int i = 0; i < Z_GP; i++)
200     for (int ii = 0; ii < ZVar_GP; ii++)
201         for (int iii = 0; iii < H_GP; iii++)
202             for (int iiii = 0; iiii < PV_GP; iiii++)
203             {
204                  if (Input2 == 0)
```

```
205                     Output[i][ii][iii][iiii] = 0;
206                 else
207                 Output[i][ii][iii][iiii] = Input1[i][ii][iii][iiii] / Input2;
208             }
209}
210
211// The following function performs a power operation of 4D matrix
212 void PowerOf4D(double Input1[Z_GP][ZVar_GP][H_GP][PV_GP], double Input2, double
Output[Z_GP][ZVar_GP][H_GP][PV_GP])
213{
214 for (int i = 0; i < Z_GP; i++)
215     for (int ii = 0; ii < ZVar_GP; ii++)
216         for (int iii = 0; iii < H_GP; iii++)
217             for (int iiii = 0; iiii < PV_GP; iiii++)
218             {
219                 Output[i][ii][iii][iiii] = pow(Input1[i][ii][iii][iiii], Input2);
220             }
221}
222
223// Initialising variables for reading purposes
224int NumOfVar = 0;
225int NumOfIndex = 0;
226
227int main()
228{
229 // Declaration of variables
230 double UnPV_CH2O[Z_GP][ZVar_GP][H_GP][PV_GP];
231 double UnPV_H2O[Z_GP][ZVar_GP][H_GP][PV_GP];
232 double UnPV_CO[Z_GP][ZVar_GP][H_GP][PV_GP];
233 double UnPV_CO2[Z_GP][ZVar_GP][H_GP][PV_GP];
234 double UnPV_HO2[Z_GP][ZVar_GP][H_GP][PV_GP];
235 double UnPV_Temp1[Z_GP][ZVar_GP][H_GP][PV_GP];
236 double UnPV_Temp2[Z_GP][ZVar_GP][H_GP][PV_GP];
237 double UnPV_Temp3[Z_GP][ZVar_GP][H_GP][PV_GP];
238 double UnPV[Z_GP][ZVar_GP][H_GP][PV_GP];
239 double C_Atom[NumOfSpec];
240 double O_Atom[NumOfSpec];
241 double H_Atom[NumOfSpec];
242 double MixOfOx = ##;
243 double DenaOfMix = ##; // Mixture fraction (MF) at fuel inlet - MF at oxidiser inlet
244 double Yc[NumOfSpec][Z_GP][ZVar_GP][H_GP][PV_GP];
245 double Yh[NumOfSpec][Z_GP][ZVar_GP][H_GP][PV_GP];
246 double Yo[NumOfSpec][Z_GP][ZVar_GP][H_GP][PV_GP];
247 double SumOfYc[Z_GP][ZVar_GP][H_GP][PV_GP];
248 double SumOfYh[Z_GP][ZVar_GP][H_GP][PV_GP];
249 double SumOfYo[Z_GP][ZVar_GP][H_GP][PV_GP];
250 double MaxFra[Z_GP][ZVar_GP][H_GP][PV_GP];
251 double Temp_Z1[NumOfSpec][Z_GP][ZVar_GP][H_GP][PV_GP];
252 double Temp_Z2[NumOfSpec][Z_GP][ZVar_GP][H_GP][PV_GP];
253 double Temp_Z3[NumOfSpec][Z_GP][ZVar_GP][H_GP][PV_GP];
254 double Cp[NumOfSpec];
255 double hf[NumOfSpec];
256 double MM[NumOfSpec];
257 double Tempp1[Z_GP][ZVar_GP][H_GP][PV_GP];
258 double Tempp2[Z_GP][ZVar_GP][H_GP][PV_GP];
259 double Temp1[Z_GP][ZVar_GP][H_GP][PV_GP];
260 double Temp2[Z_GP][ZVar_GP][H_GP][PV_GP];
261 double Temp3[Z_GP][ZVar_GP][H_GP][PV_GP];
262 double Temp4[Z_GP][ZVar_GP][H_GP][PV_GP];
263 double Temp5[Z_GP][ZVar_GP][H_GP][PV_GP];
264 double Enth[NumOfSpec][Z_GP][ZVar_GP][H_GP][PV_GP];
265 double TotEnth[Z_GP][ZVar_GP][H_GP][PV_GP];
266 double Tref = 298.15;
```

```
267 double GradOfUnPV[Z_GP][ZVar_GP][H_GP][PV_GP];
268 double GradOfMaxFra[Z_GP][ZVar_GP][H_GP][PV_GP];
269 double GradOfTotEnth[Z_GP][ZVar_GP][H_GP][PV_GP];
270 double NumOfGrid;
271 double Species[NumOfSpec][Z_GP][ZVar_GP][H_GP][PV_GP];
272 double GradOfSpecies[NumOfSpec][Z_GP][ZVar_GP][H_GP][PV_GP];
273 double LL[NumOfSpec];
274 double WeiCoe[NumOfSpec];
275 double ZOfSpecies[NumOfSpec];
276 double MultiOfSpeciGrad[NumOfSpec][Z_GP][ZVar_GP][H_GP][PV_GP];
277 double MultiOfPvSpeciGrad[NumOfSpec][Z_GP][ZVar_GP][H_GP][PV_GP];
278 double MultiOfZSpeciGrad[NumOfSpec][Z_GP][ZVar_GP][H_GP][PV_GP];
279 double EnthOfSpecies[NumOfSpec][Z_GP][ZVar_GP][H_GP][PV_GP];
280 double MultiOfEnthSpeciGrad[NumOfSpec][Z_GP][ZVar_GP][H_GP][PV_GP];
281 double TermOfPV[Z_GP][ZVar_GP][H_GP][PV_GP];
282 double TermOfZ[Z_GP][ZVar_GP][H_GP][PV_GP];
283 double TermOfH[Z_GP][ZVar_GP][H_GP][PV_GP];
284 double CpDivLamd[Z_GP][ZVar_GP][H_GP][PV_GP];
285 double Temperature[Z_GP][ZVar_GP][H_GP][PV_GP];
286 FILE* file;
287
288 file = fopen("AtomOfC.txt", "rb");
289 if (file == NULL)
290 {
291     printf("failed to open the file of species C atom\n");
292     return 0;
293 }
294
295 for(int n = 0; n < NumOfSpec; n++)
296    {
297        fscanf(file, "%lf\n", &C_Atom[n]);
298    }
299
300 fclose(file);
301
302    file = fopen("AtomOfO.txt", "rb");
303 if (file == NULL)
304 {
305     printf("failed to open the file of species O atom\n");
306     return 0;
307 }
308
309 for(int n = 0; n < NumOfSpec; n++)
310    {
311        fscanf(file, "%lf\n", &O_Atom[n]);
312    }
313
314 fclose(file);
315
316    file = fopen("AtomOfH.txt", "rb");
317 if (file == NULL)
318 {
319     printf("failed to open the file of species H atom\n");
320     return 0;
321 }
322
323 for(int n = 0; n < NumOfSpec; n++)
324    {
325        fscanf(file, "%lf\n", &H_Atom[n]);
326    }
327
328 fclose(file);
329
```

```
330 file = fopen("EnthOfForm.txt", "rb");
331 if (file == NULL)
332 {
333     printf("failed to open the file of species enthalpy of formation\n");
334     return 0;
335 }
336
337 for(int n = 0; n < NumOfSpec; n++)
338    {
339        fscanf(file, "%lf\n", &hf[n]);
340    }
341
342 fclose(file);
343
344    file = fopen("SpecHeat.txt", "rb");
345 if (file == NULL)
346 {
347     printf("failed to open the file of species specific heat\n");
348     return 0;
349 }
350
351 for(int n = 0; n < NumOfSpec; n++)
352    {
353        fscanf(file, "%lf\n", &Cp[n]);
354    }
355
356 fclose(file);
357
358    file = fopen("MoleWei.txt", "rb");
359 if (file == NULL)
360 {
361     printf("failed to open the file of species Molecular weight\n");
362     return 0;
363 }
364
365 for(int n = 0; n < NumOfSpec; n++)
366    {
367        fscanf(file, "%lf\n", &MM[n]);
368    }
369
370 fclose(file);
371
372    file = fopen("LewisNumber.txt", "rb");
373 if (file == NULL)
374 {
375     printf("failed to open the file of species Lewis number\n");
376     return 0;
377 }
378
379 for(int n = 0; n < NumOfSpec; n++)
380    {
381        fscanf(file, "%lf\n", &LL[n]);
382    }
383
384 fclose(file);
385
386    file = fopen("SpeMixFra.txt", "rb");
387 if (file == NULL)
388 {
389     printf("failed to open the file of species mixture fraction\n");
390     return 0;
391 }
392
```

```
393 for(int n = 0; n < NumOfSpec; n++)
394    {
395        fscanf(file, "%lf\n", &ZOfSpecies[n]);
396    }
397
398 fclose(file);
399
400 file = fopen("Filename", "rb");
401 if (file == NULL)
402 {
403     printf("file open failed\n");
404     return 0;
405 }
406
407 char buffer[100];
408 memset(buffer, 0x0, sizeof(buffer));
409 char TEMP_HEARDER[50]; sprintf(TEMP_HEARDER, "293 %d %d %d %d)(", Z_GP,
ZVar_GP,H_GP,PV_GP);
410 char SPECIES_HEARDER[50]; sprintf(SPECIES_HEARDER, "299 %d %d %d %d %d)(", Z_GP,
ZVar_GP,PvVar_GP,PV_GP, NumOfSpec+1 );
411
412 //--------------------------------------------------------------------------//
413 //                                                                          //
414 //  In the input file, each variable has a unique header. For example,      //
415 //  the temperature header is as follows:                                   //
416 //                                  /*******************************/       //
417 //  (200 (293 ## ## ## ##)(         /* ## represents the grid       */      //
418 //  1st value                       /* points of mixture fraction,  */      //
419 //  2nd value                       /* it variance, enthalpy and    */      //
420 //  .                               /* PV, respectively.            */      //
421 //  .                               /*******************************/       //
422 //  .                                                                       //
423 //  last value                                                              //
424 //  ))                                   /* means end of data */            //
425 //                                                                          //
426 //  Thus, the following while loop reads the input file line by line,       //
427 //  searching for the header of temperature. Once the header is matched     //
428 //  the definition in line 409, the code will read the data line by         //
429 //  line and stored in Temperature[Z_GP][ZVar_GP][H_GP][PV_GP].             //
430 //  If the code reaches the ''))'' sign, it will stop reading the           //
431 //  the temperature and then do the same for species data.                  //
432 //                                                                          //
433 //--------------------------------------------------------------------------//
434
435 while (fgets(buffer, sizeof(buffer), file))
436 {
437        //  strchr function is for searching character in array. Thus, this
438        //  line checks if 0x0a (=\n = newline character) exists
439     char *temp = strchr(buffer, 0x0a);
440        //  if 0x0a exists, remove it.
441     if (temp != 0) temp[0] = 0x0;
442        //  strchr function is for searching character in array. Thus, this
443        //  line checks if 0x0d (=\r = line terminator) exists
444     temp = strchr(buffer, 0x0d);
445     //  if 0x0d exists, remove it.
446     if (temp != 0) temp[0] = 0x0;
447        //  Search in the input file for the headers of the required
448        //  variables. strlen function calculates the length of a given
449        //  string.
450        if(strchr(buffer, '(') != NULL && strlen(buffer) >= 10)
451        {
452            //  strcmp function compares the string. Thus, if the string
453            //  matches the string of temperature header
```

```
454             //  the variable will be initialised and then the data will read
455             //  line by line.
456             if (strcmp(&buffer[6], TEMP_HEARDER) == 0)
457             {
458                 NumOfVar = 1;
459                 NumOfIndex = 0;
460                 continue;
461             }
462             else if (strcmp(&buffer[6], SPECIES_HEARDER) == 0)
463             {
464                 NumOfVar = 2;
465                 NumOfIndex = 0;
466                 continue;
467             }
468         }
469     // means end of variable.
470         else if (strcmp(buffer, "))") == 0)
471         {
472                 NumOfVar = 0;
473                 NumOfIndex = 0;
474                 continue;
475         }
476 
477     if (NumOfVar == 0) continue;
478 
479     double x = 0;
480     sscanf(buffer, "%lf", &x);
481 
482         if (NumOfVar == 1)
483     {
484         // Converting the Temperature from a column to 4D matrix
485         int i, j, k, m;
486 
487         i = NumOfIndex % Z_GP;
488         j = (NumOfIndex / Z_GP) % ZVar_GP;
489 
490         k = (NumOfIndex / ZVar_GP / Z_GP) % H_GP;
491         m = (NumOfIndex / ZVar_GP / Z_GP / H_GP) % PV_GP;
492 
493         Temperature[i][j][k][m] = x;
494     }
495     else if (NumOfVar == 2)
496     {
497         // Converting the species from a column to 4D matrix for each specie.
498         int i, j, k, m;
499 
500         i = NumOfIndex % Z_GP;
501         j = (NumOfIndex / Z_GP) % ZVar_GP;
502 
503         k = (NumOfIndex / ZVar_GP / Z_GP) % PvVar_GP;
504         m = (NumOfIndex / ZVar_GP / Z_GP / PvVar_GP) % PV_GP;
505 
506         NumOfGrid = Z_GP *  ZVar_GP * PV_GP * PvVar_GP;
507         int n = NumOfIndex / NumOfGrid;
508             if (NumOfIndex < (NumOfGrid * NumOfSpec))
509             {
510                 Species[n][i][j][k][m] = x;
511             }
512     }
513     NumOfIndex++;
514 
515     memset(buffer, 0x0, sizeof(buffer));
516     }
```

```
517 fclose(file);
518
519    printf("Finishing reading the data file\n");
520
521 //  Removing the PV variance by taking the values at PV variance of 0.
522 //  Then, duplicating it to the number of H, since the species mole
523 //  fractions are maintained constant with enthalpy variations
524 //  during the PDF integration.
525 for (int n = 0; n < NumOfSpec; n++)
526 {
527     for (int k = 1; k < H_GP; k++)
528     {
529         for (int i = 0; i < Z_GP; i++)
530         {
531             for (int j = 0; j < ZVar_GP; j++)
532             {
533                 for (int m = 0; m < PV_GP; m++)
534                 {
535                     Species[n][i][j][k][m] = Species[n][i][j][0][m];
536
537                 }
538             }
539         }
540     }
541 }
542
543 printf("Conversion of Species dimensions is done\n");
544
545    //  In the following part, the species mole fractions are converted
546    //  to species mass fractions
547    double MM1[Z_GP][ZVar_GP][H_GP][PV_GP];
548    double NewSpecie[NumOfSpec][Z_GP][ZVar_GP][H_GP][PV_GP];
549
550    NumOfGrid = Z_GP*ZVar_GP*H_GP*PV_GP;
551
552    for (int n = 0 ; n < NumOfSpec; n++)
553    {
554
555        for (int nn = 0; nn < NumOfGrid; nn++)
556        {
557            int i = nn % Z_GP;
558         int j = (nn / Z_GP) % ZVar_GP;
559         int k = (nn / ZVar_GP / Z_GP) % H_GP;
560         int m = (nn / ZVar_GP / Z_GP / H_GP) % PV_GP;
561         NewSpecie[n][i][j][k][m] = Species[n][i][j][k][m] * MM[n];
562        }
563    }
564    for (int nn = 0; nn < NumOfGrid; nn++)
565    {
566        int i = nn % Z_GP;
567        int j = (nn / Z_GP) % ZVar_GP;
568
569        int k = (nn / ZVar_GP / Z_GP) % H_GP;
570        int m = (nn / ZVar_GP / Z_GP / H_GP) % PV_GP;
571        double temp_sum = 0;
572        for (int n = 0 ; n < NumOfSpec; n++)
573        {
574            temp_sum += NewSpecie[n][i][j][k][m];
575        }
576        MM1[i][j][k][m] = temp_sum;
577    }
578
579    for (int n = 0 ; n < NumOfSpec; n++)
```

```
580     {
581         for (int nn = 0; nn < NumOfGrid; nn++)
582         {
583          int i = nn % Z_GP;
584          int j = (nn / Z_GP) % ZVar_GP;
585          int k = (nn / ZVar_GP / Z_GP) % H_GP;
586          int m = (nn / ZVar_GP / Z_GP / H_GP) % PV_GP;
587          NewSpecie[n][i][j][k][m] = NewSpecie[n][i][j][k][m] / MM1[i][j][k][m];
588         }
589     }
590
591     printf("Conversion of Species from mole to mass fraction is done\n");
592
593     // Calculating the un-normalised PV. ## represents the number of species
594     // in the species list and the number of its molecular weight in the MM
595     // array
596     DivOf4dByNmub(NewSpecie[##], MM[##], UnPV_CH2O);
597     DivOf4dByNmub(NewSpecie[##], MM[##], UnPV_H2O);
598     DivOf4dByNmub(NewSpecie[##], MM[##], UnPV_CO);
599     DivOf4dByNmub(NewSpecie[##], MM[##], UnPV_CO2);
600     DivOf4dByNmub(NewSpecie[##], MM[##], UnPV_HO2);
601
602     AddOf4D(UnPV_CH2O, UnPV_H2O, UnPV_Temp1);
603     AddOf4D(UnPV_Temp1, UnPV_CO, UnPV_Temp2);
604     AddOf4D(UnPV_Temp2, UnPV_CO2, UnPV_Temp3);
605     AddOf4D(UnPV_Temp3, UnPV_HO2, UnPV);
606
607     // Calculating the mixture fraction
608     InitialOf4dWithZeros(SumOfYc);
609     InitialOf4dWithZeros(SumOfYh);
610     InitialOf4dWithZeros(SumOfYo);
611
612     for (int n = 0 ; n < NumOfSpec; n++)
613     {
614         MultiOf4dByNmub(NewSpecie[n], C_Atom[n], Yc[n]);
615         MultiOf4dByNmub(NewSpecie[n], H_Atom[n], Yh[n]);
616         MultiOf4dByNmub(NewSpecie[n], O_Atom[n], Yo[n]);
617
618         // Division of Yc, Yh and Yo by the molecular weights of C, H and O
619         // Atoms. MM is the molecular weight and ## is the number of  C, H
620         // and O atoms in MM array
621         DivOf4dByNmub(Yc[n], MM[##], Temp_Z1[n]);
622         DivOf4dByNmub(Yh[n], MM[##], Temp_Z2[n]);
623         DivOf4dByNmub(Yo[n], MM[##], Temp_Z3[n]);
624
625         // Multiplication of Yc, Yh and Yo by the constants in Bilger's formula.
626         MultiOf4dByNmub(Temp_Z1[n], 2, Temp_Z1[n]);
627         MultiOf4dByNmub(Temp_Z2[n], 0.5, Temp_Z2[n]);
628         MultiOf4dByNmub(Temp_Z3[n], -1, Temp_Z3[n]);
629
630         AddOf4D(SumOfYc, Temp_Z1[n], SumOfYc);
631         AddOf4D(SumOfYh, Temp_Z2[n], SumOfYh);
632         AddOf4D(SumOfYo, Temp_Z3[n], SumOfYo);
633     }
634
635     AddOf4D(SumOfYc, SumOfYh, MaxFra);
636     AddOf4D(MaxFra, SumOfYo, MaxFra);
637
638     AddOf4dByNmub(MaxFra, -1*MixOfOx, MaxFra);
639     DivOf4dByNmub(MaxFra, DenaOfMix, MaxFra);
640
641     // Calculating the enthalpy.
642     AddOf4dByNmub(Temperature, -1*Tref, Tempp1);
```

```
643
644     InitialOf4dWithZeros(TotEnth);
645 for (int n = 0; n < NumOfSpec; n++)
646 {
647     MultiOf4dByNmub(Tempp1, Cp[n], Tempp2) ;
648     AddOf4dByNmub(Tempp2, hf[n], EnthOfSpecies[n]);
649     MultiOf4D(NewSpecie[n], EnthOfSpecies[n], Enth[n]);
650     AddOf4D(TotEnth, Enth[n], TotEnth);
651 }
652
653    printf("Calculation of CVs is done\n");
654
655 // Getting the gradients of species
656 for (int n = 0; n < NumOfSpec; n++)
657 {
658     GradOf4D(NewSpecie[n], GradOfSpecies[n]);
659 }
660
661    printf("Calculation of species gradients is done\n");
662
663 // getting the gradients of the control variables
664    GradOf4D(UnPV, GradOfUnPV);
665    GradOf4D(MaxFra, GradOfMaxFra);
666    GradOf4D(TotEnth, GradOfTotEnth);
667
668    printf("Calculation of CVs Gradients is done\n");
669
670 // Calculating the gradient part in the additional terms
671 // Temp1, Temp2, Temp3, Temp4 and Temp5 are temporary variables
672 for (int n = 0; n < NumOfSpec; n++)
673 {
674     DivOf4D(GradOfSpecies[n], GradOfUnPV, Temp1);
675
676     DivOf4D(GradOfSpecies[n], GradOfTotEnth, Temp2);
677     DivOf4D(GradOfTotEnth, GradOfUnPV, Temp3);
678     MultiOf4D(Temp2, Temp3, Temp3);
679
680     DivOf4D(GradOfSpecies[n], GradOfMaxFra, Temp4);
681     DivOf4D(GradOfMaxFra, GradOfUnPV, Temp5);
682     MultiOf4D(Temp4, Temp5, Temp5);
683
684     AddOf4D(Temp1, Temp3, Temp3);
685     AddOf4D(Temp3, Temp5, MultiOfSpeciGrad[n]);
686
687 }
688
689 printf("Calculation of gradient parts is done\n");
690
691 for (int n = 0; n < NumOfSpec; n++)
692 {
693     LL[n] = ((1 / LL[n] ) - 1);
694 }
695
696 printf("Calculation of Le number term is done\n");
697
698 for (int n = 0; n < NumOfSpec; n++)
699 {
700     MultiOf4dByNmub(MultiOfSpeciGrad[n], LL[n], MultiOfSpeciGrad[n]);
701 }
702
703    printf("Multiplication of gradient parts and species Le number is done\n");
704
705 // Calculating the  Cp and Lamda part
```

```
706
707 MultiOf4dByNmub(Temperature, 1.0f / 298.0f, CpDivLamd);
708 PowerOf4D(CpDivLamd, 0.69, CpDivLamd);
709 MultiOf4dByNmub(CpDivLamd, 2.58e-5, CpDivLamd);
710
711 printf("Calculation of Cp and Lamda part is done\n");
712
713 // Calculating the weighting coefficient of pv
714
715 for (int n = 0; n < NumOfSpec; n++)
716 {
717     WeiCoe[n] = 1 / MM[n];
718 }
719
720 printf("Calculation of species PV is done\n");
721
722 // Species weighting coefficient of pv are multiplied with Le and Grad.
723 // part
724 for (int n = 0; n < NumOfSpec; n++)
725 {
726     MultiOf4dByNmub(MultiOfSpeciGrad[n], WeiCoe[n], MultiOfPvSpeciGrad[n]);
727 }
728
729 printf("Multiplication of species PVs by Le and Grad. part is done \n");
730
731 // Summation of PV term
732 InitialOf4dWithZeros(TermOfPV);
733 for (int n = 0; n < NumOfSpec; n++)
734 {
735     AddOf4D(TermOfPV, MultiOfPvSpeciGrad[n], TermOfPV);
736 }
737
738 // Summation of PV term is multiplied by the Cp and Lamda part.
739 MultiOf4D(CpDivLamd, TermOfPV, TermOfPV);
740
741 // Same process implemented with PV is implemented with mixture fraction.
742 for (int n = 0; n < NumOfSpec; n++)
743 {
744     MultiOf4dByNmub(MultiOfSpeciGrad[n], ZOfSpecies[n], MultiOfZSpeciGrad[n]);
745 }
746
747 InitialOf4dWithZeros(TermOfZ);
748 for (int n = 0; n < NumOfSpec; n++)
749 {
750     AddOf4D(TermOfZ, MultiOfZSpeciGrad[n], TermOfZ);
751 }
752
753 MultiOf4D(CpDivLamd, TermOfZ, TermOfZ);
754
755 // Same process is implemented with enthalpy
756 for (int n = 0; n < NumOfSpec; n++)
757 {
758     MultiOf4D(EnthOfSpecies[n], MultiOfSpeciGrad[n], MultiOfEnthSpeciGrad[n]);
759
760 }
761
762 InitialOf4dWithZeros(TermOfH);
763 for (int n = 0; n < NumOfSpec; n++)
764 {
765     AddOf4D(TermOfH, MultiOfEnthSpeciGrad[n], TermOfH);
766 }
767
768 MultiOf4D(CpDivLamd, TermOfH, TermOfH);
```

```
769
770 // Exporting the additional terms.
771 Export4D("Temperature.txt", Temperature);
772 Export4D("TermOfH.txt", TermOfH);
773 Export4D("TermOfZ.txt", TermOfZ);
774 Export4D("TermOfPV.txt", TermOfPV);
775}
```

D Source code of incorporating the preferential diffusion coefficients in the transport equations of control variables.

The preferential diffusion coefficients were incorporated in the transport equations of the control variables by means of the user-defined functions (UDF) file coded in C programming language. The code does not modify the PDF table and is programmed to retrieve the values of mean temperature and then to find their indices. Hence, the values of the additional terms are obtained based on the indices and values of the mean temperature. The source code is as follows:

```
#include "udf.h"
#include "pdf_props.h"
#include "pdf_table.h"

// declaring the grid points of control variables.
#define Z_GP ##
#define ZVar_GP ##
#define PV_GP ##
#define H_GP ##

// GP = (Z_GP*ZVar_GP*PV_GP*H_GP)
#define GP ##

real PV_Term[GP];
real Z_Term[GP];
real H_Term[GP];
real MeanOfTemp[GP];



// The following function reads the input files.
 DEFINE_EXECUTE_ON_LOADING(FileReading, FileReading)
{
 int i, ii, j, jj, n;
 FILE *file;

```

```
// Reading the PV additional term
file = fopen("TermOfPV.txt", "r");

n=0;
for (i = 0; i < PV_GP; i++)
{
    for (ii = 0; ii < H_GP; ii++)
    {
        for (j = 0; j < ZVar_GP; j++)
        {
            for (jj = 0; jj < Z_GP; jj++)
            {
                fscanf(file, "%le\n", &PV_Term[n]);
                n += 1;
            }
        }
    }
}

 fclose(file);

// Reading the Mixture fraction additional term
file = fopen("TermOfZ.txt", "r");

n=0;
for (i = 0; i < PV_GP; i++)
{
    for (ii = 0; ii < H_GP; ii++)
    {
        for (j = 0; j < ZVar_GP; j++)
        {
            for (jj = 0; jj < Z_GP; jj++)
            {
                fscanf(file, "%le\n", &Z_Term[n]);
                n += 1;
            }
        }
    }
}

fclose(file);

// Reading the enthalpy additional term
file = fopen("TermOfH.txt", "r");

n=0;
for (i = 0; i < PV_GP; i++)
{
    for (ii = 0; ii < H_GP; ii++)
    {
        for (j = 0; j < ZVar_GP; j++)
        {
            for (jj = 0; jj < Z_GP; jj++)
            {
                fscanf(file, "%le\n", &H_Term[n]);
                n += 1;
            }
        }
    }
}

    fclose(file);

```

```
90  // Reading the mean temperature
91  file = fopen("Temperature.txt", "r");
92
93  n = 0;
94  for (i = 0; i < PV_GP; i++)
95  {
96      for (ii = 0; ii < H_GP; ii++)
97      {
98          for (j = 0; j < ZVar_GP; j++)
99          {
100             for (jj = 0; jj < Z_GP; jj++)
101             {
102                 fscanf(file, "%le\n", &MeanOfTemp[n]);
103                 n += 1;
104             }
105         }
106     }
107 }
108
109     fclose(file);
110}
111
112// The following function finds the indices of a variable
113// based on its retrieved values.
114 void IndexFinder(int IndexOfVar[2], real *Varr, real *Var, int VarGP)
115{
116    int i;
117    int ii;
118    int iii;
119
120    if (*Varr < Var[0])
121    {
122        printf("Lower than the range.\n");
123        *Varr=Var[0];
124        IndexOfVar[0] = 0;
125        IndexOfVar[1] = 1;
126        return;
127    }
128    if (*Varr > Var[VarGP - 1])
129    {
130        printf("Higher than the range.\n");
131        *Varr=Var[VarGP-1];
132        IndexOfVar[0] = VarGP - 2;
133        IndexOfVar[1] = VarGP - 1;
134        return;
135    }
136    i = 0;
137    ii = VarGP;
138
139    while (ii > i + 1)
140    {
141        iii = (i + ii) / 2;
142        if (*Varr < Var[iii])
143        ii = iii;
144        else
145        i = iii;
146    }
147    IndexOfVar[0] = i;
148    IndexOfVar[1] = i + 1;
149    return;
150}
151
152// The following function performs a linear
```

```
153// interpolation (required in LinearInter function)
154 real LinearInterpolation(real PreX, real CurrX, real NextX, real CurrY, real
NextY)
155{
156    real Result;
157    Result =  (NextY - CurrY) / (NextX - CurrX) * (PreX - CurrX) + CurrY;
158    return Result;
159}
160
161
162// The following function interpolates a 4D matrix
163 real LinearInter(int *Var_Index1, real *Varr1, real Var1 , real *VarTerm)
164{
165 real Result;
166 Result = LinearInterpolation(Var1, Varr1[Var_Index1[0]], Varr1[Var_Index1[1]],
VarTerm[Var_Index1[0]], VarTerm[Var_Index1[1]]);
167 return Result;
168}
169
170
171//-------------------------------------------------------------------------//
172//                                                                         //
173// The following function is used to                                       //
174// 1. find the indices of the retrieved mean temperatures.                 //
175// 2. retrieve the right values of the additional terms based on           //
176//    the indices of the mean temperature.                                 //
177// 3. multiply the PV gradient by the retrieved values of preferential     //
178//    diffusion  coefficients.                                             //
179//                                                                         //
180// To the best of the author's knowledge, the only way to add              //
181// any additional term to any default transport equation incorporated      //
182// by ANSYS Fluent establisher is to use the source term function.         //
183//                                                                         //
184// Using the source function to add a extra term does not mean             //
185// that this term is a source term as Fluent will deal with it             //
186// as a number.                                                            //
187//                                                                         //
188//-------------------------------------------------------------------------//
189 DEFINE_SOURCE(MixFra,c,t,dS,eqn)
190{
191 // Declaration
192 real MeanOfTempp;
193 real InterpZTerm;
194 real ZTerm;
195 int Tempp_Index[2];
196 real DV[ND_ND], GradOfPV;
197
198 // Retrieving the mean temperature.
199 MeanOfTempp = C_T(c,t);
200
201 // find the indices of mean temperature based on its retrieved values.
202 IndexFinder(Tempp_Index, &MeanOfTempp, MeanOfTemp, GP);
203
204 // Performing linear interpolation to obtained the
205 // additional terms values of mixture fraction.
206 InterpZTerm = LinearInter(Tempp_Index, MeanOfTemp, MeanOfTempp, Z_Term);
207
208 // checking whether storage has been allocated for the variable or
209 // not --- SV_ contains the time-integral of PV ---
210 if(NNULLP(THREAD_STORAGE(t,SV_PREMIXC_G)))
211 {
212     // Assigning the PV values to DV array
213     NV_V(DV, =, C_STORAGE_R_NV(c,t,SV_PREMIXC_G));
```

```
214     //NV performs the dot product of DV and DV
215     GradOfPV = sqrt(NV_DOT(DV,DV));
216 }
217
218 // multiply the Z term by the PV graident.
219 ZTerm = GradOfPV * InterpZTerm;
220
221 return ZTerm;
222}
223
224// Same process is repeated for PV.
225 DEFINE_SOURCE(PV,c,t,dS,eqn)
226{
227
228 real MeanOfTempp;
229 real InterpPVTerm;
230 real PVTerm;
231 int Tempp_Index[2];
232 real DV[ND_ND], GradOfPV;
233
234 MeanOfTempp = C_T(c,t);
235
236 IndexFinder(Tempp_Index, &MeanOfTempp, MeanOfTemp, GP);
237
238 InterpPVTerm = LinearInter(Tempp_Index, MeanOfTemp, MeanOfTempp, PV_Term);
239
240 if(NNULLP(THREAD_STORAGE(t,SV_PREMIXC_G)))
241 {
242     NV_V(DV, =, C_STORAGE_R_NV(c,t,SV_PREMIXC_G));
243     GradOfPV = sqrt(NV_DOT(DV,DV));
244 }
245
246 PVTerm = GradOfPV * InterpPVTerm;
247
248 return PVTerm;
249}
250// Same process is repeated for enthalpy.
251 DEFINE_SOURCE(Enth,c,t,dS,eqn)
252{
253
254 real MeanOfTempp;
255 real InterpHTerm;
256 real HTerm;
257 int Tempp_Index[2];
258 real DV[ND_ND], GradOfPV;
259
260 MeanOfTempp = C_T(c,t);
261
262 IndexFinder(Tempp_Index, &MeanOfTempp, MeanOfTemp, GP);
263
264 InterpHTerm = LinearInter(Tempp_Index, MeanOfTemp, MeanOfTempp, H_Term);
265
266
267 if(NNULLP(THREAD_STORAGE(t,SV_PREMIXC_G)))
268 {
269     NV_V(DV, =, C_STORAGE_R_NV(c,t,SV_PREMIXC_G));
270     GradOfPV = sqrt(NV_DOT(DV,DV));
271 }
272
273 HTerm = GradOfPV * InterpHTerm;
274
275 return HTerm;
276}
```

E Additional figures of elevated pressure effects on the laminar premixed and non-premixed flames.

E1. Premixed Flame.

- Case 2.

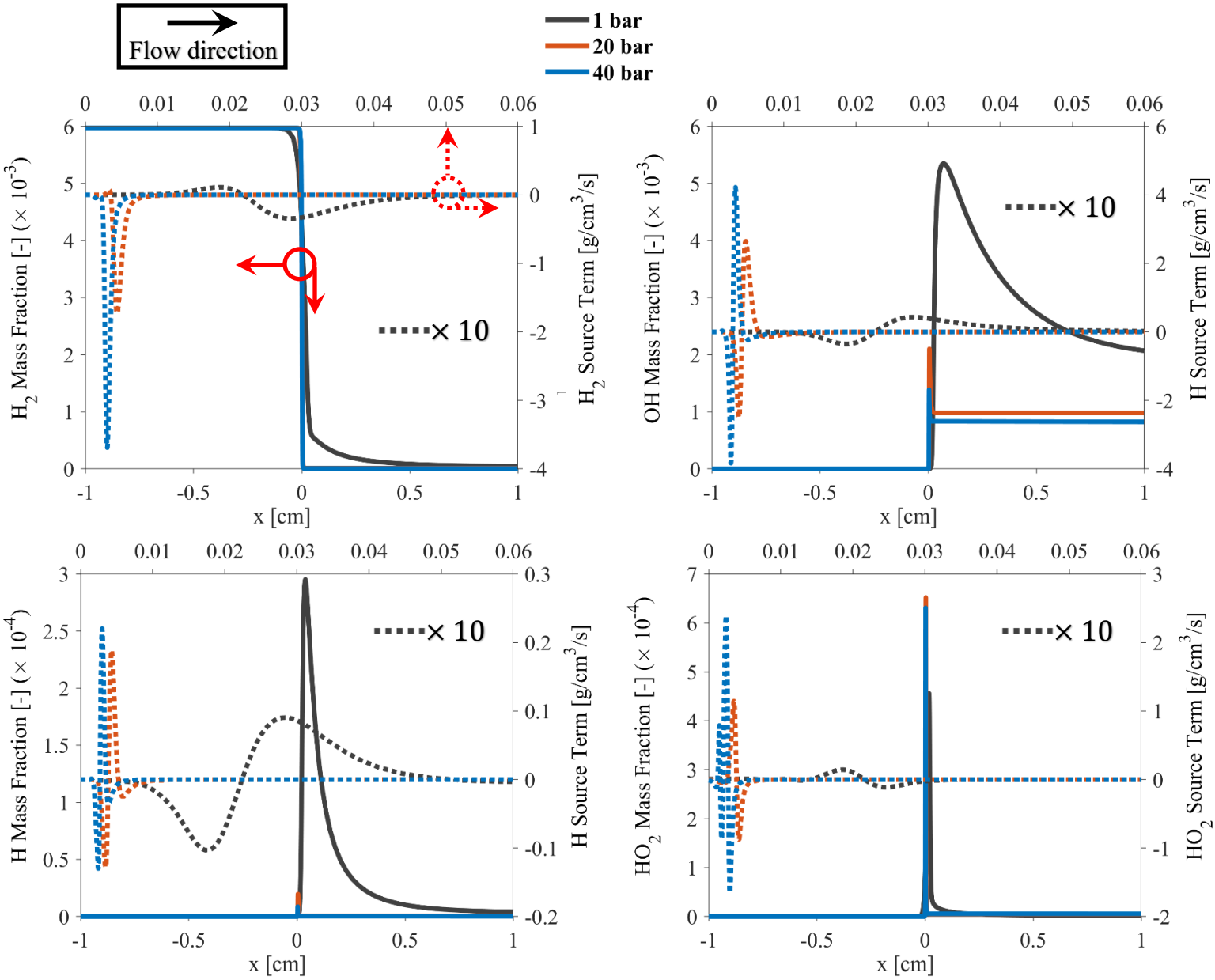

Figure E 1: A comparison of H_2, H, OH and HO_2 mass fraction and source terms at various pressure levels of case 2.

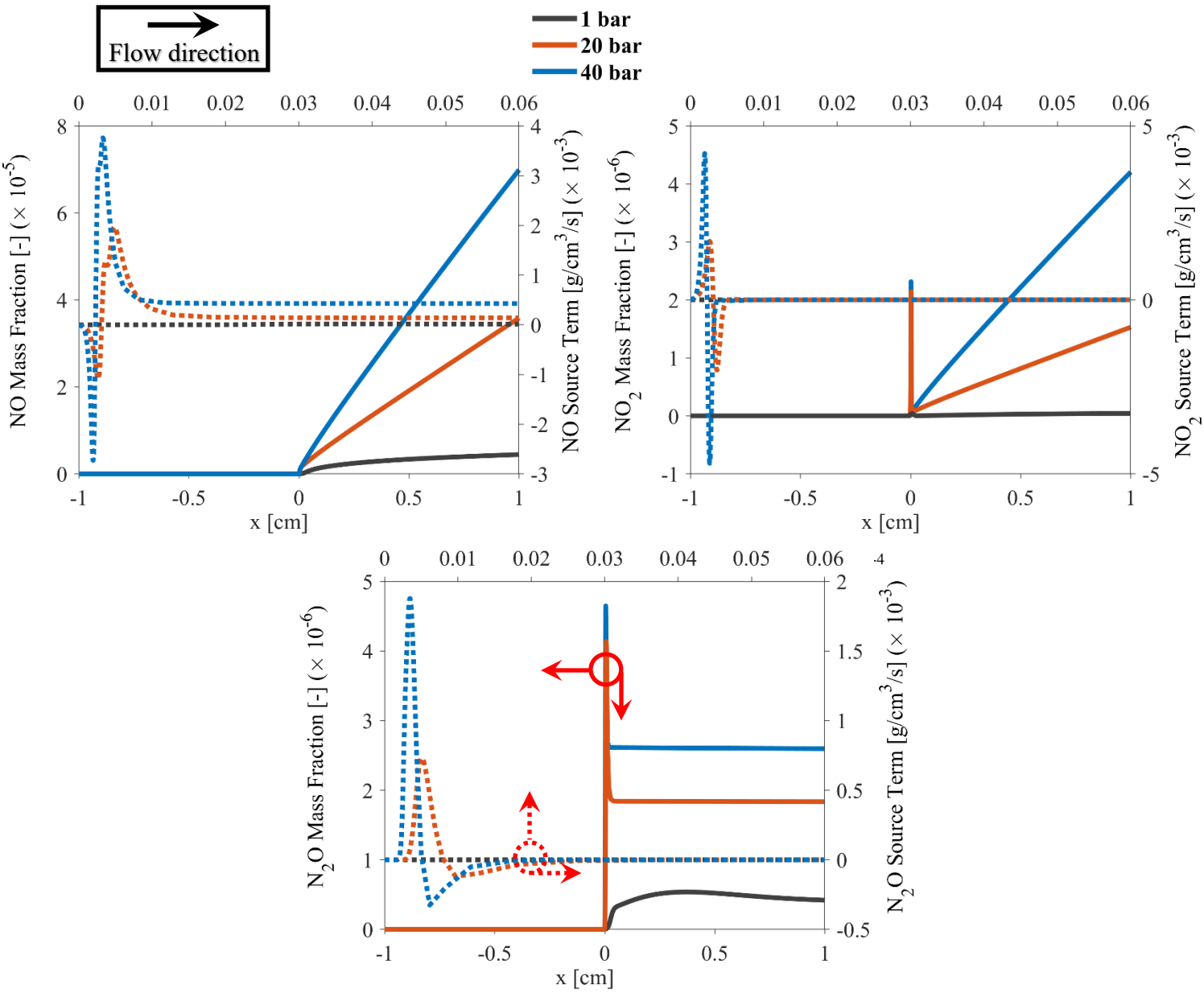

Figure E 2: A comparison of NO, NO_2 and N_2O mass fraction and source terms at various pressure levels for case 2.

- Case 3.

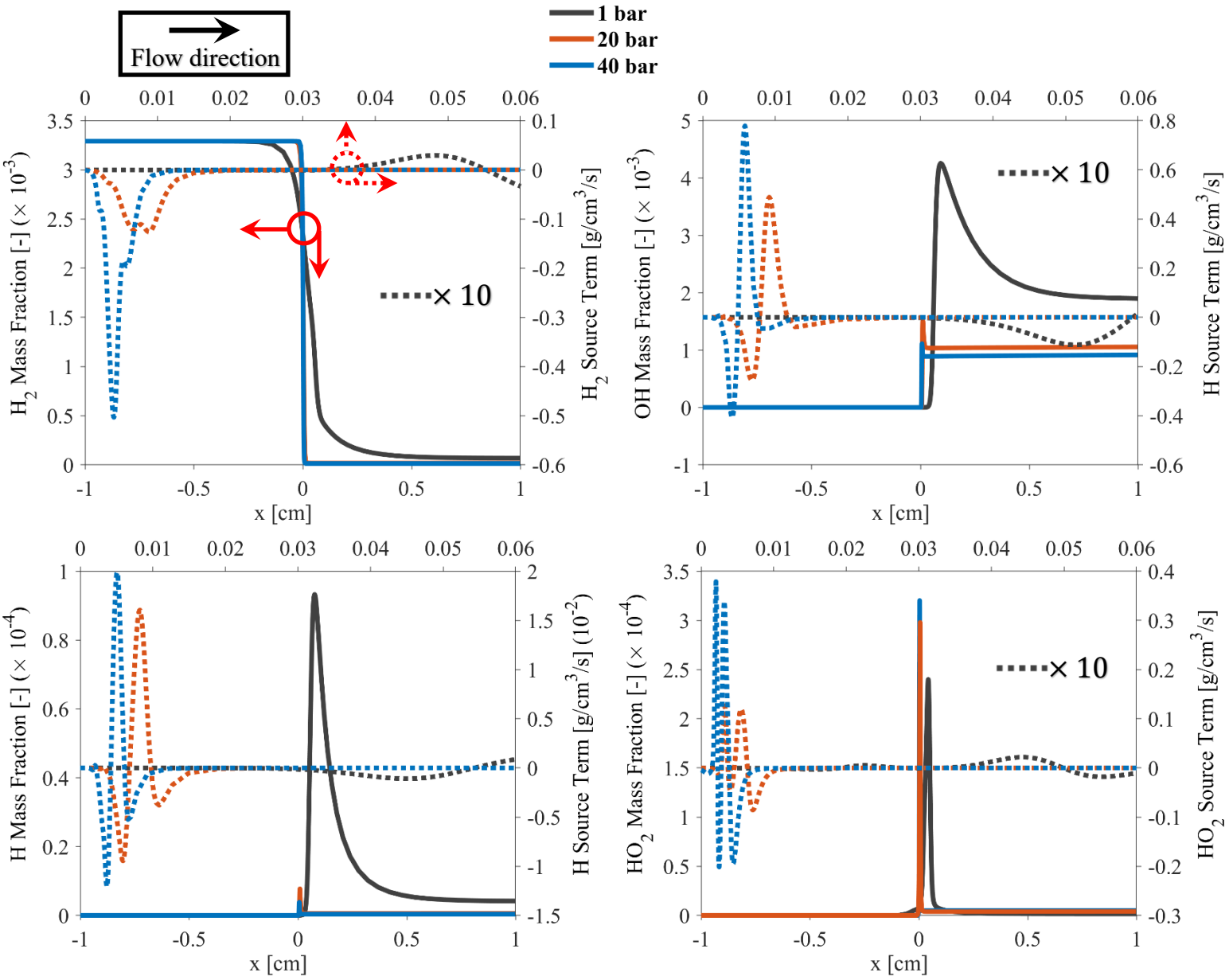

Figure E 3: A comparison of H_2, H, OH and HO_2 mass fraction and source terms at various pressure levels of case 3.

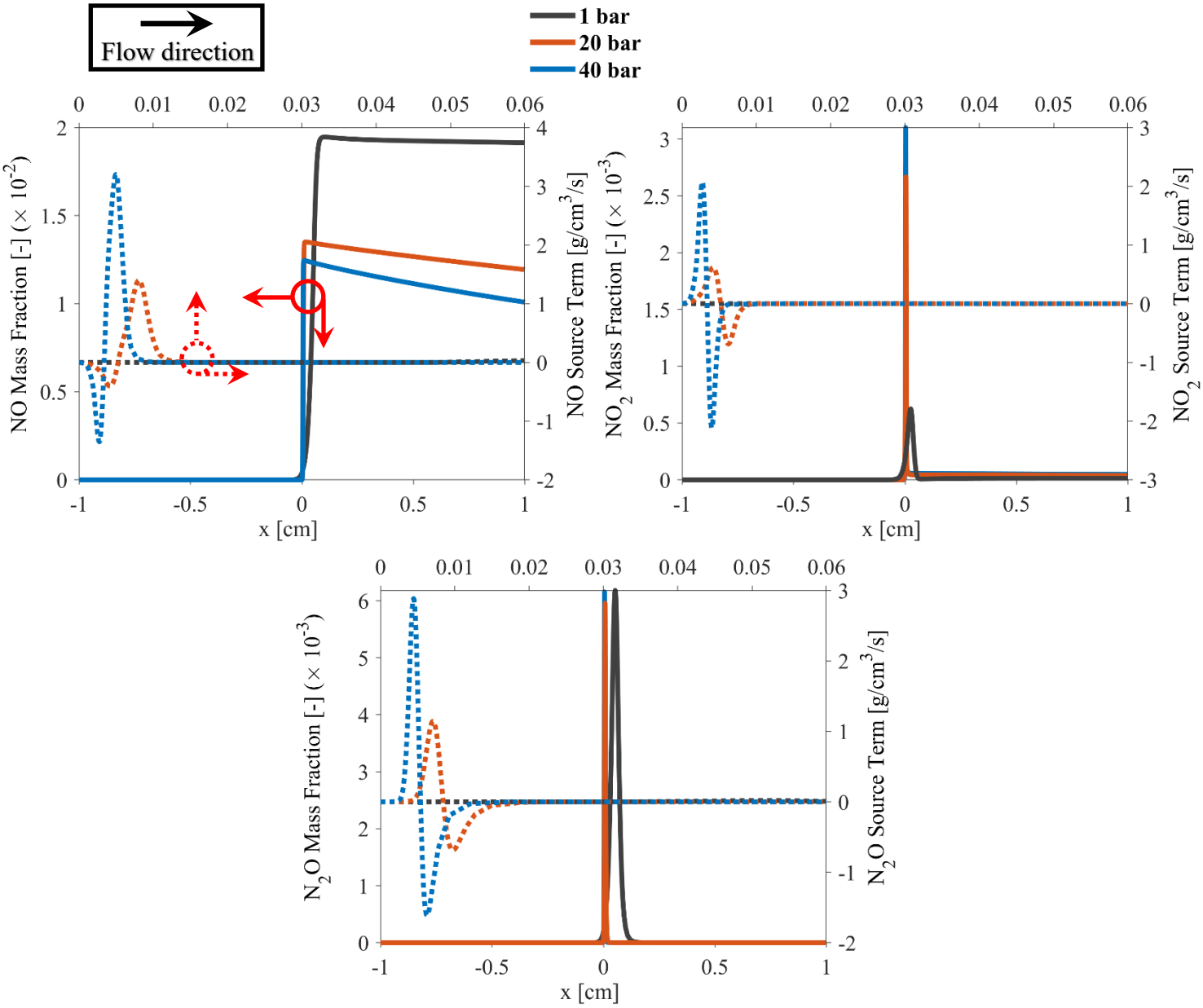

Figure E 4: A comparison of NO, NO_2 and N_2O mass fraction and source terms at various pressure levels for case 3.

- Case 4.

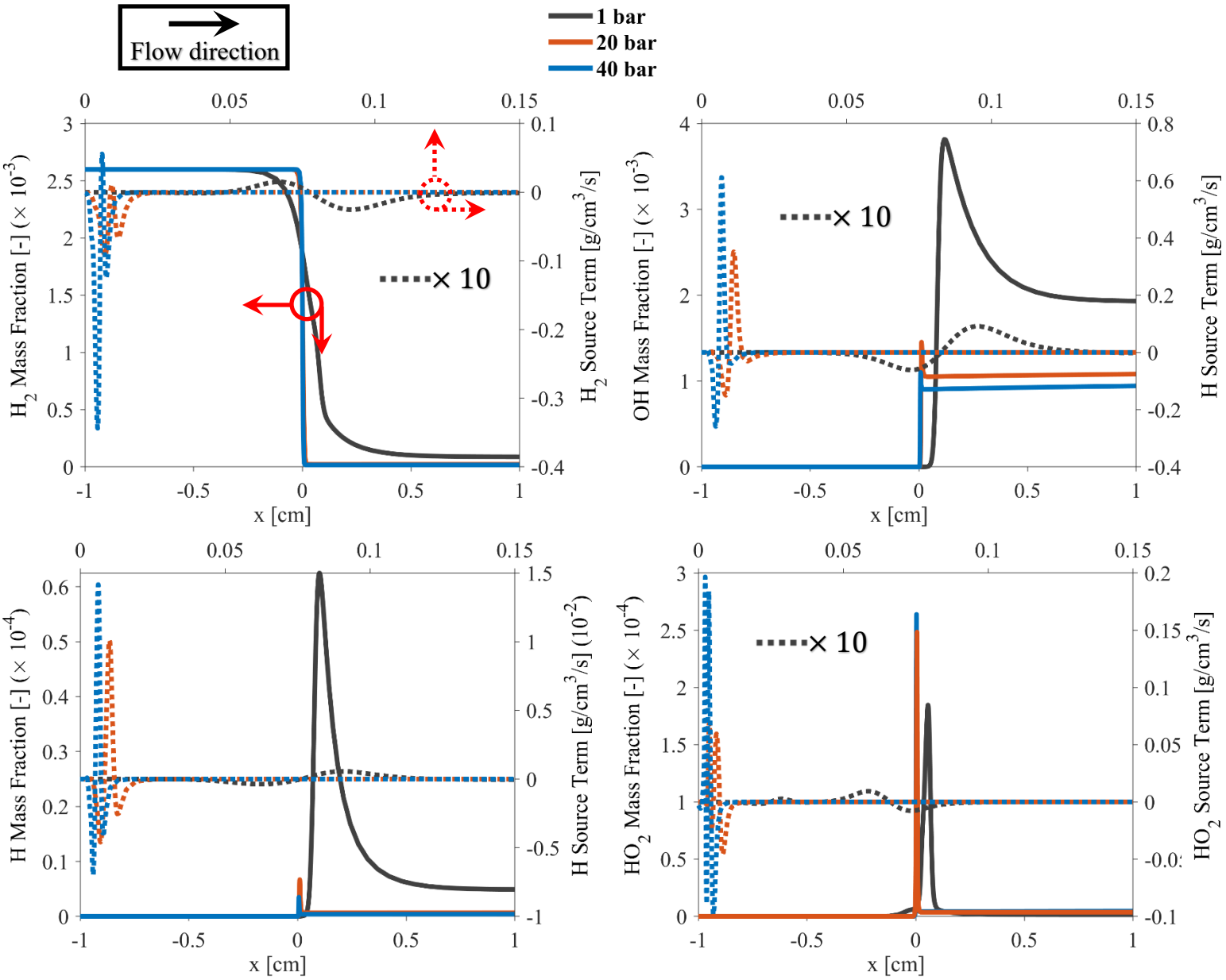

Figure E 5: A comparison of H_2, H, OH and HO_2 mass fraction and source terms at various pressure levels of case 4.

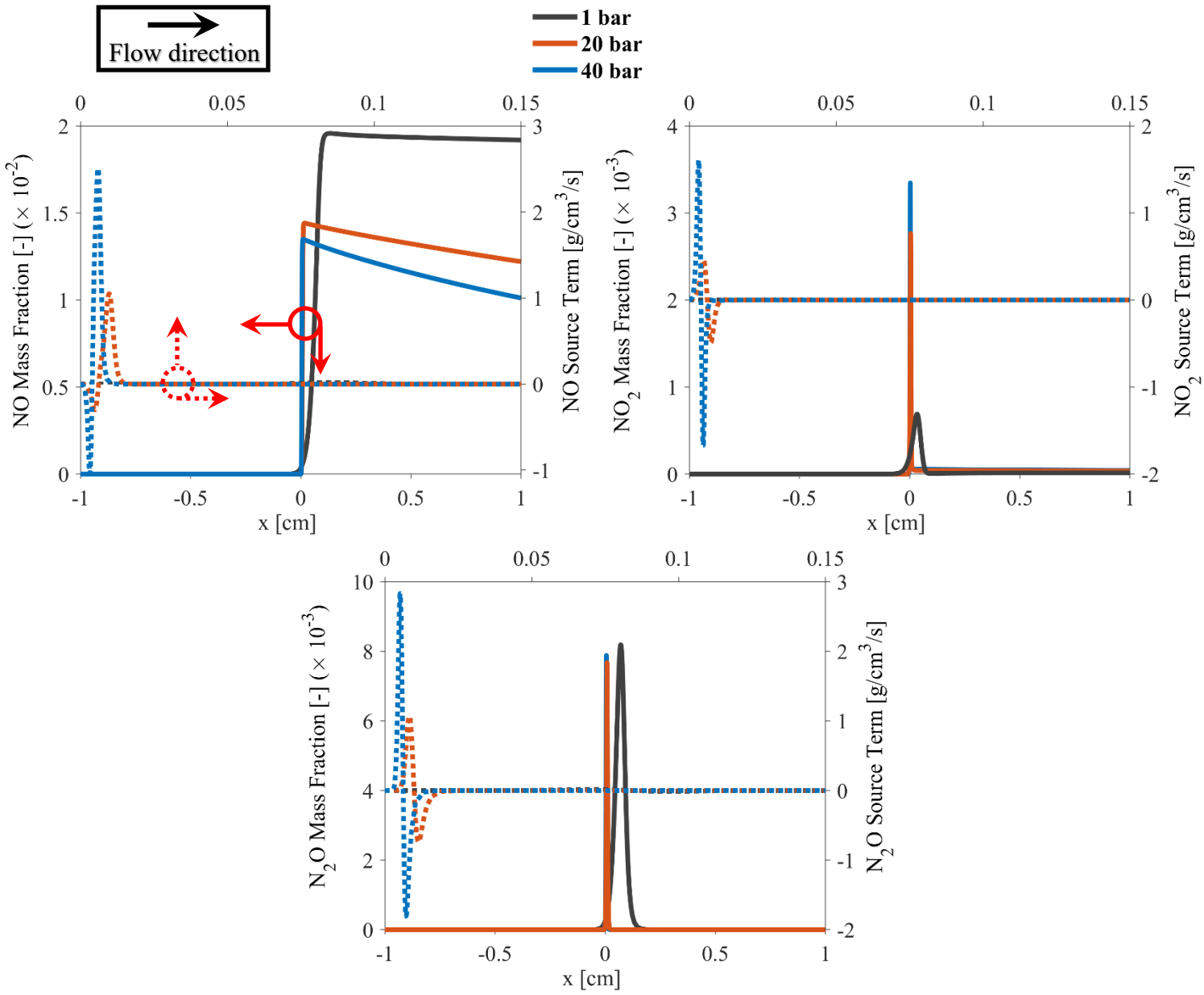

Figure E 6: A comparison of NO, NO_2 and N_2O mass fraction and source terms at various pressure levels for case 4.

- Case 5.

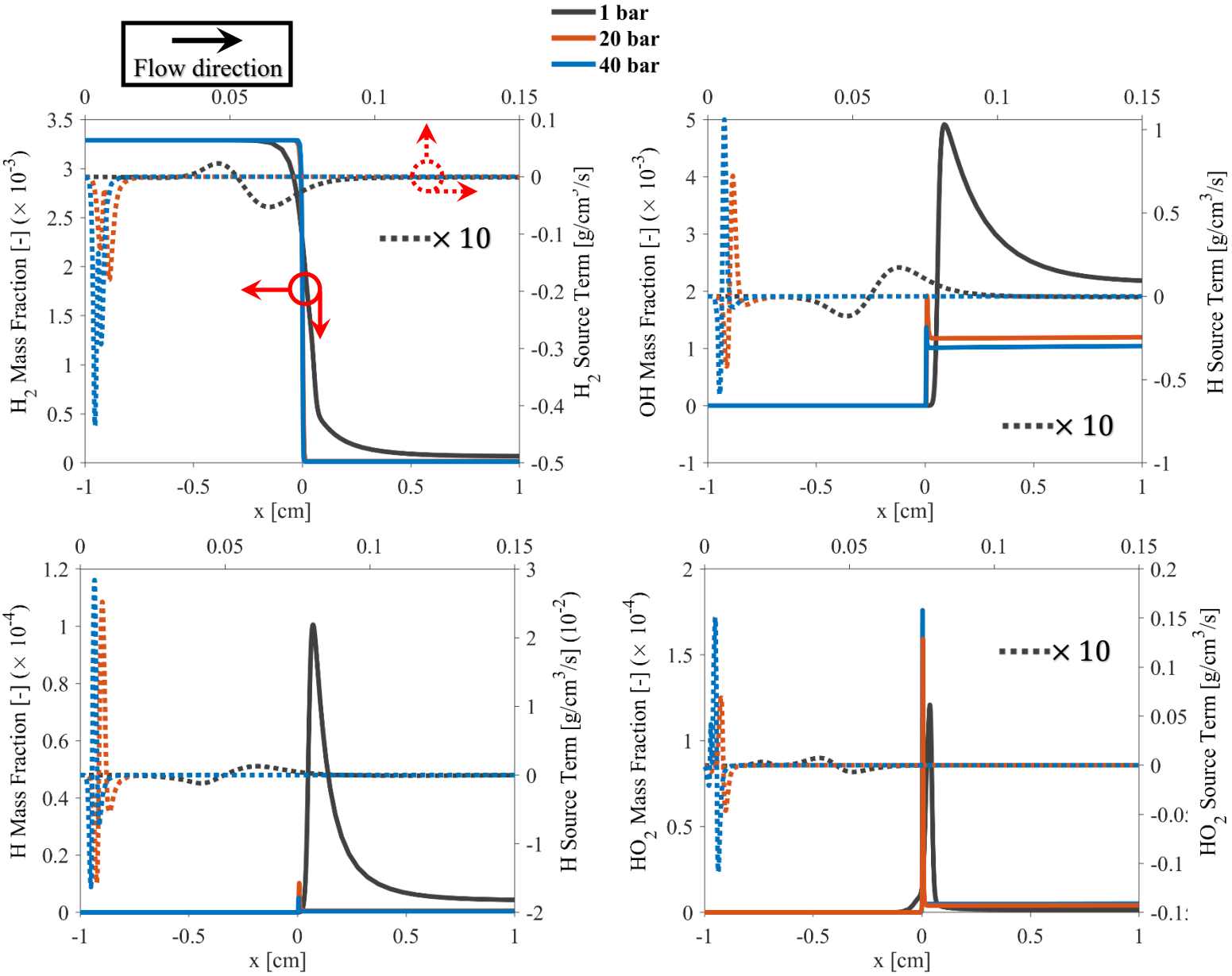

Figure E 7: A comparison of H_2, H, OH and HO_2 mass fraction and source terms at various pressure levels of case 5.

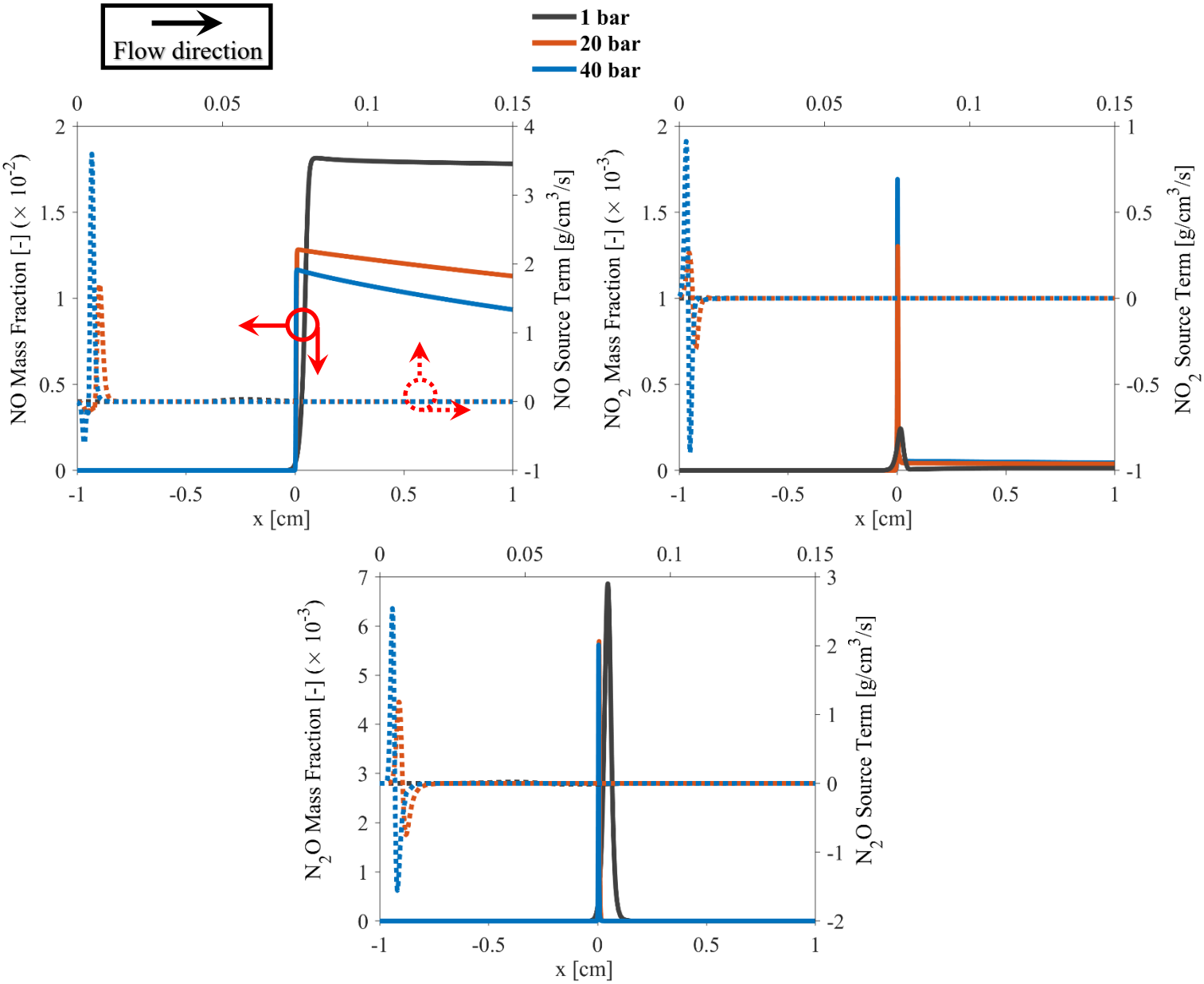

Figure E 8: A comparison of NO, NO_2 and N_2O mass fraction and source terms at various pressure levels for case 5.

E2. Non-Premixed Flame.

- Case 2.

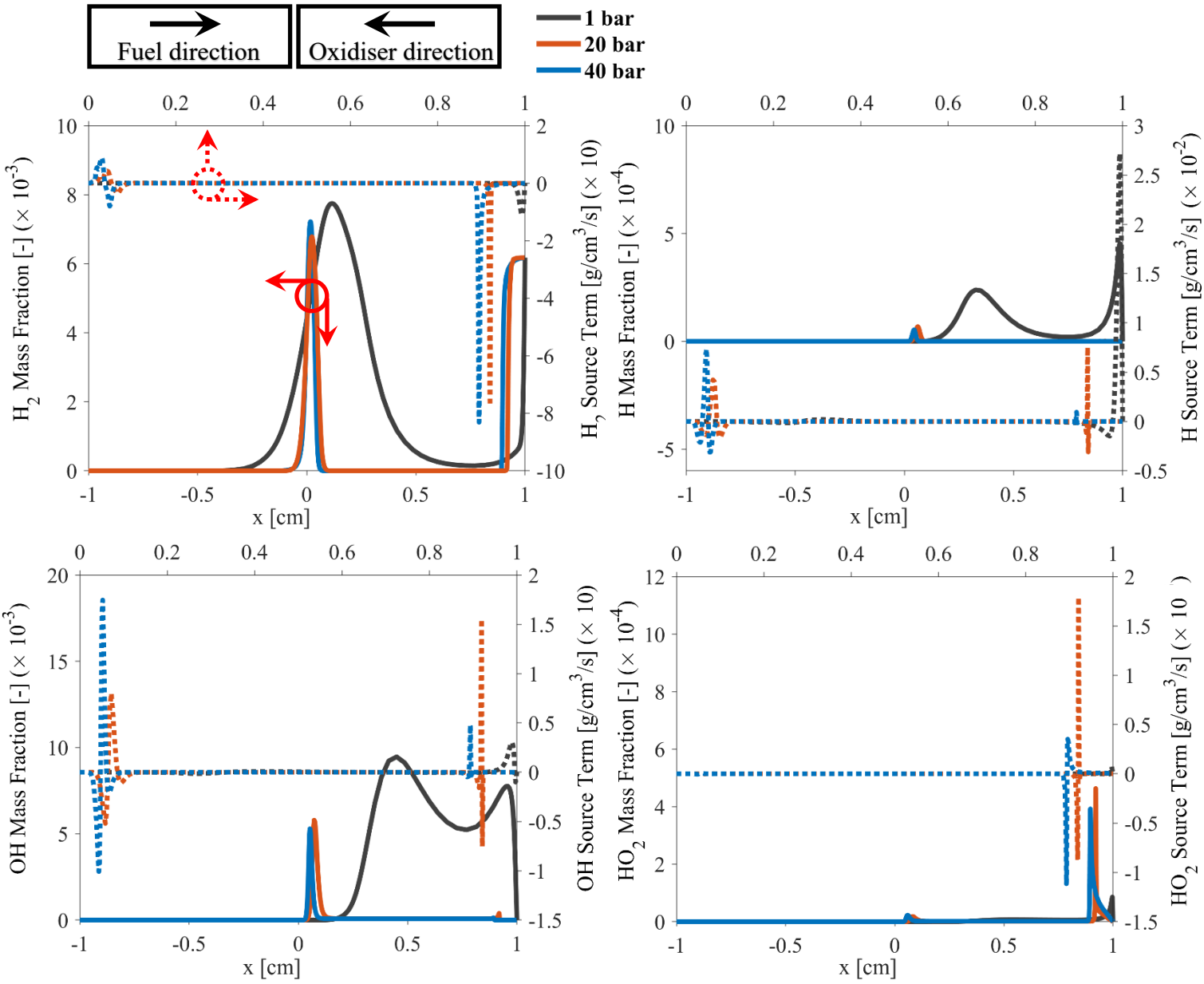

Figure E 9: A comparison of H_2, H, OH and HO_2 mass fraction and source terms at various pressure levels of case 2.

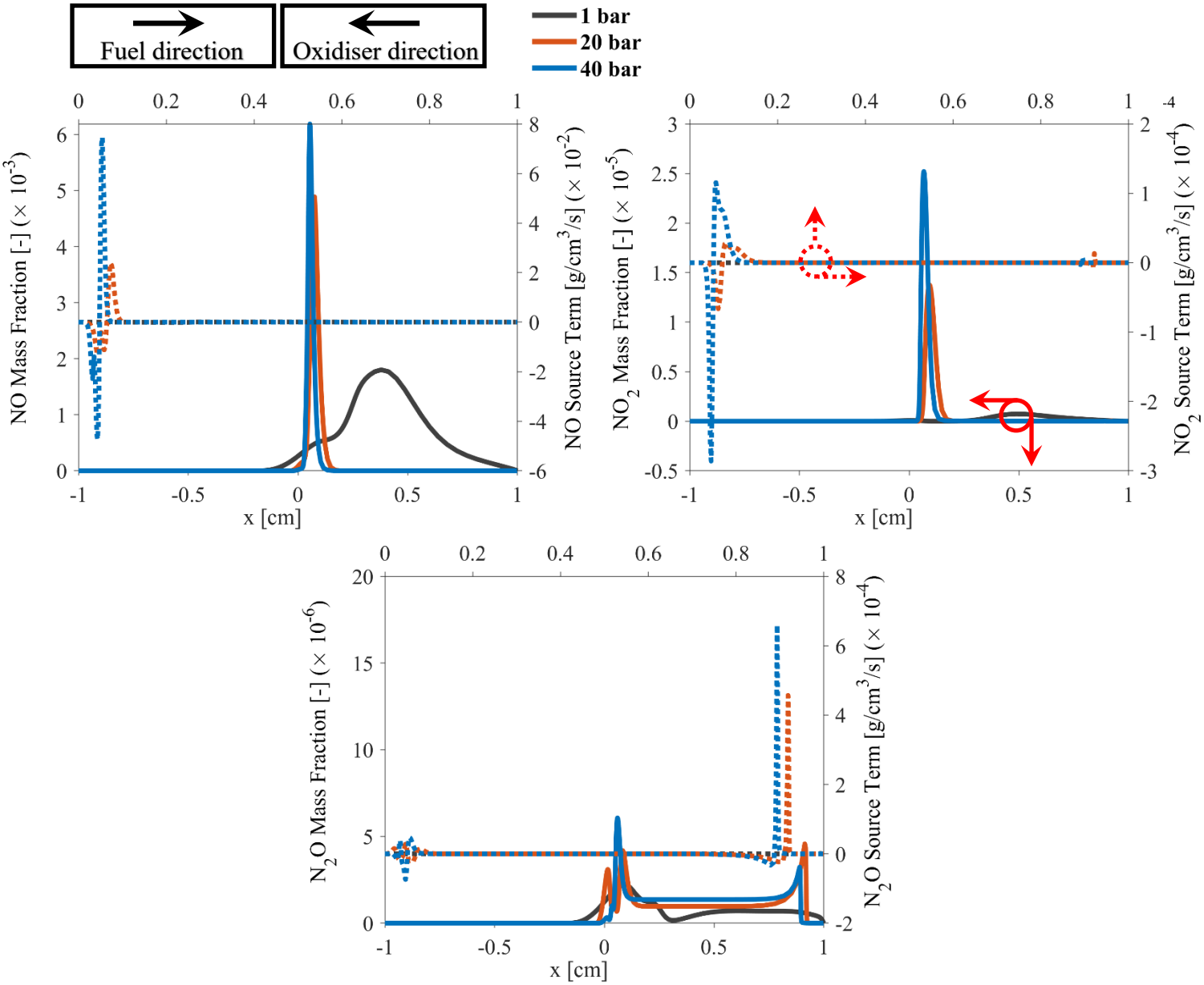

Figure E 10: A comparison of NO, NO_2 and N_2O mass fraction and source terms at various pressure levels for case 2.

- Case 3.

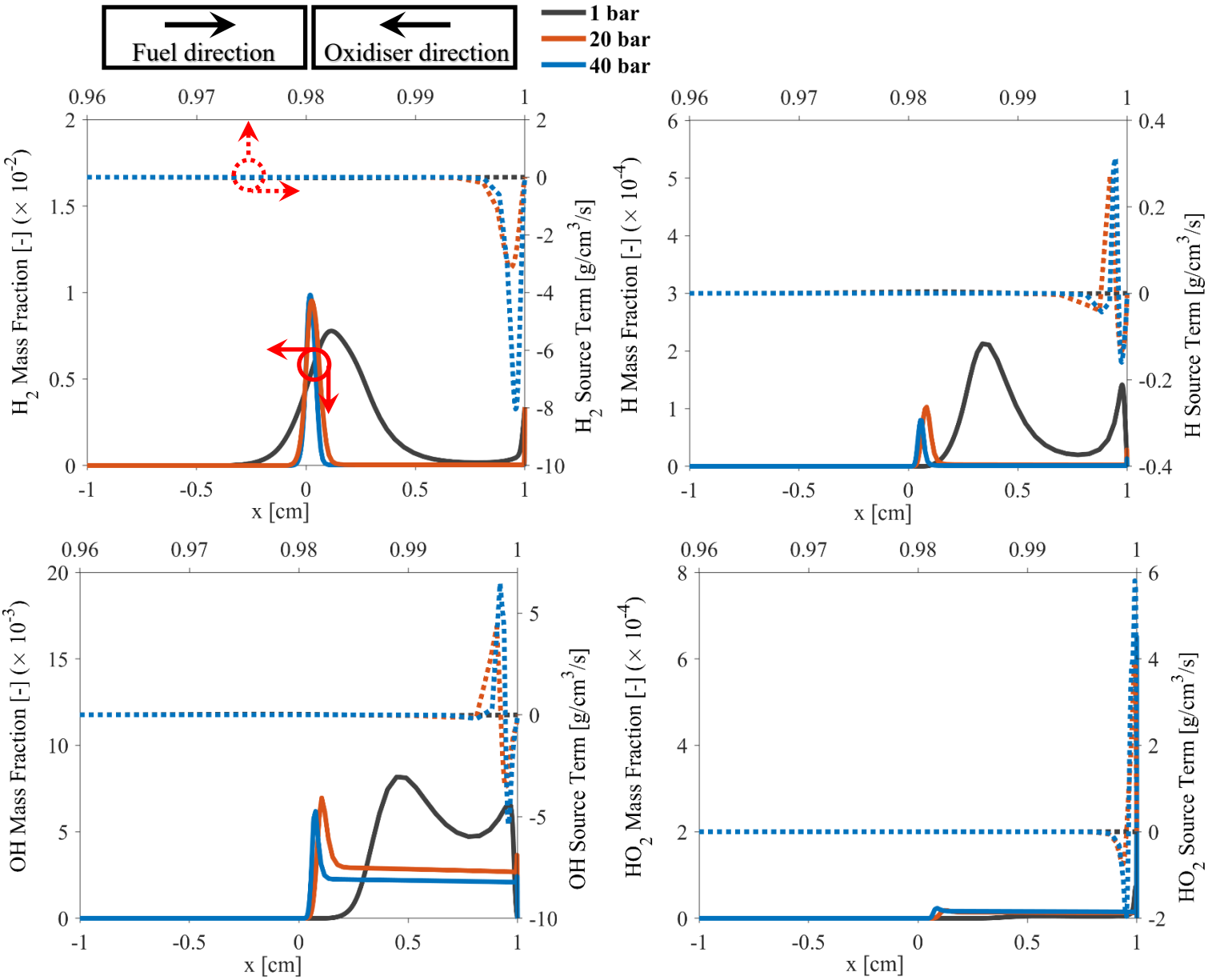

Figure E 11: A comparison of H_2, H, OH and HO_2 mass fraction and source terms at various pressure levels of case 3.

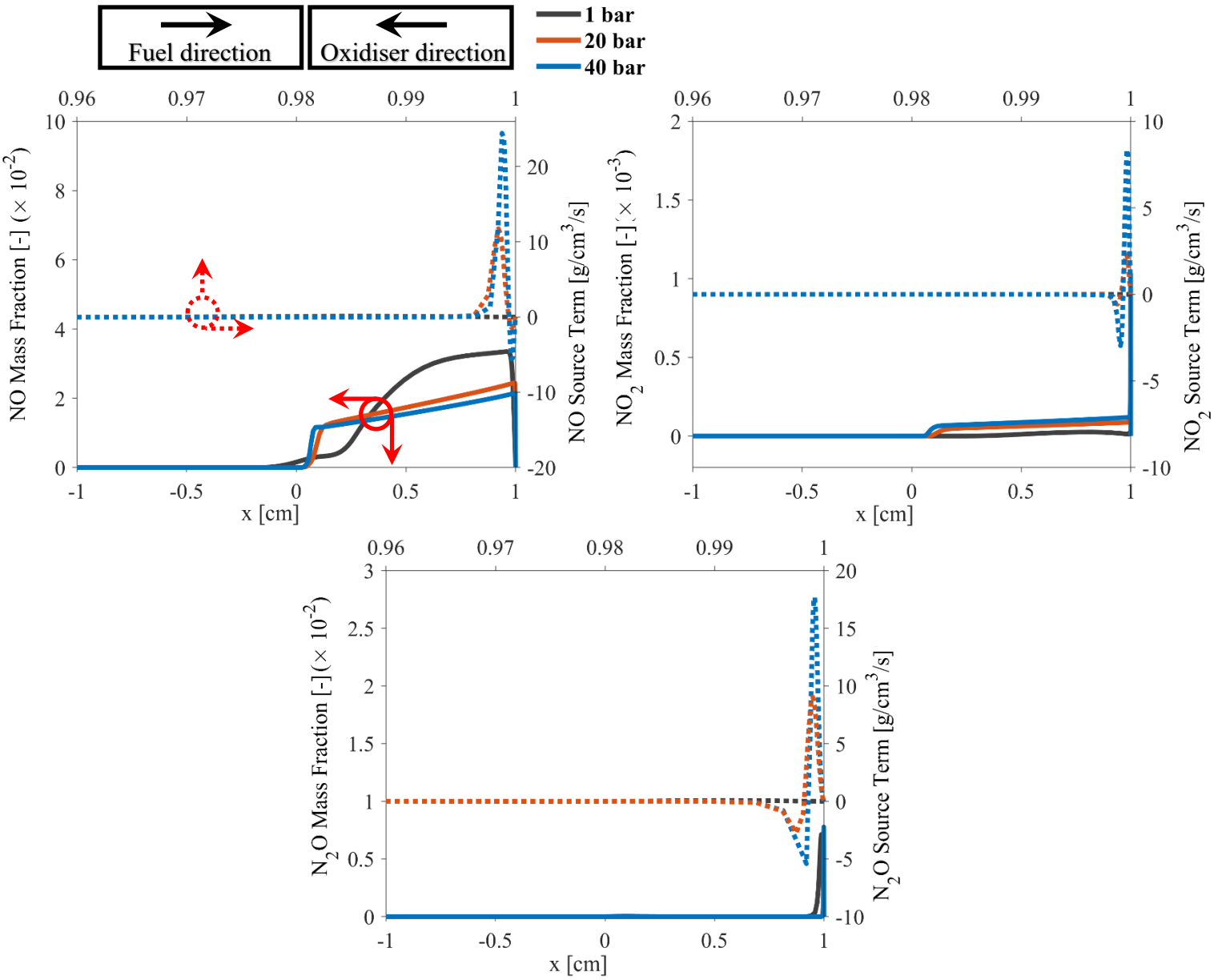

Figure E 12: A comparison of NO, NO_2 and N_2O mass fraction and source terms at various pressure levels for case 3.

- Case 4.

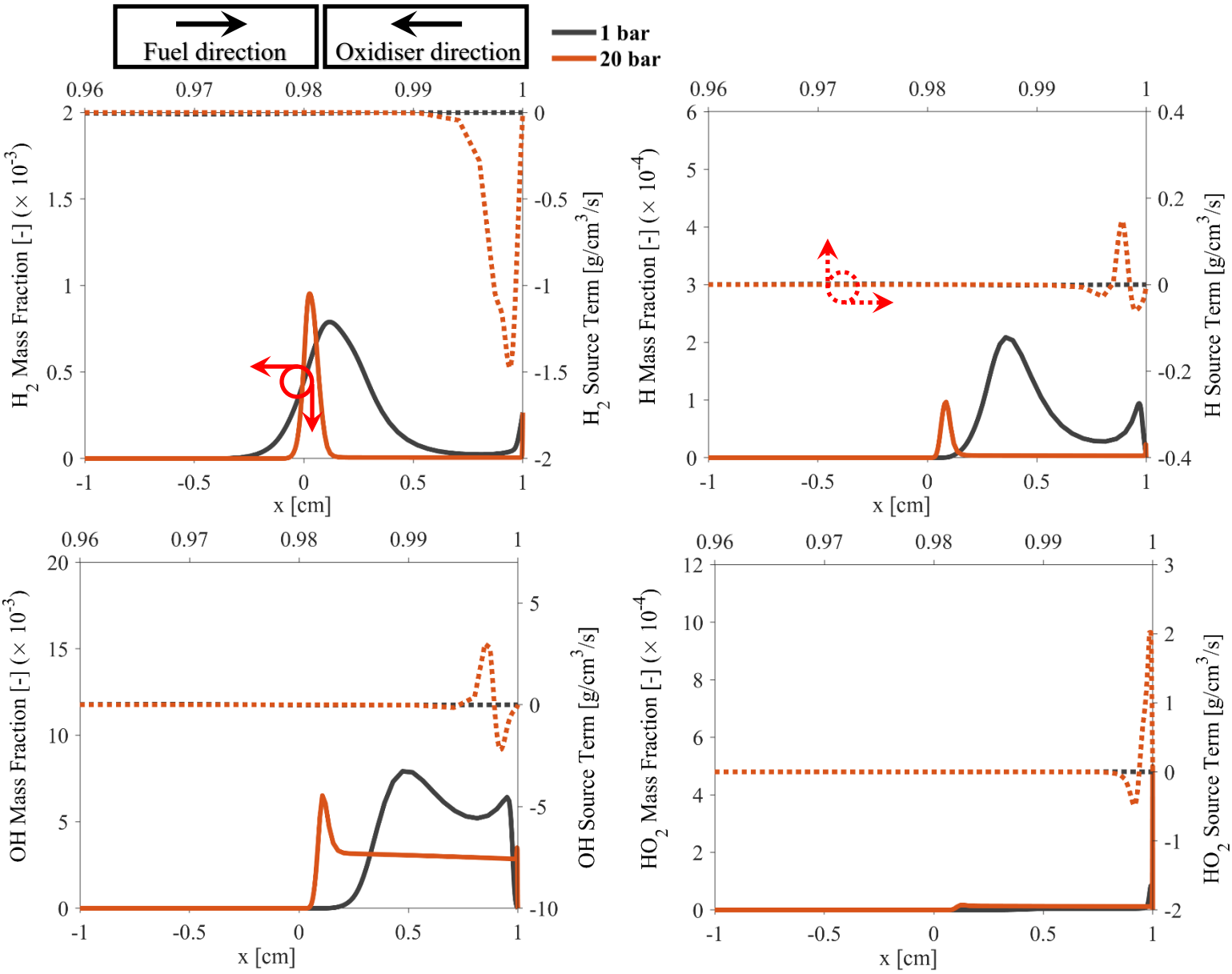

Figure E 13: A comparison of H_2, H, OH and HO_2 mass fraction and source terms at various pressure levels of case 4.

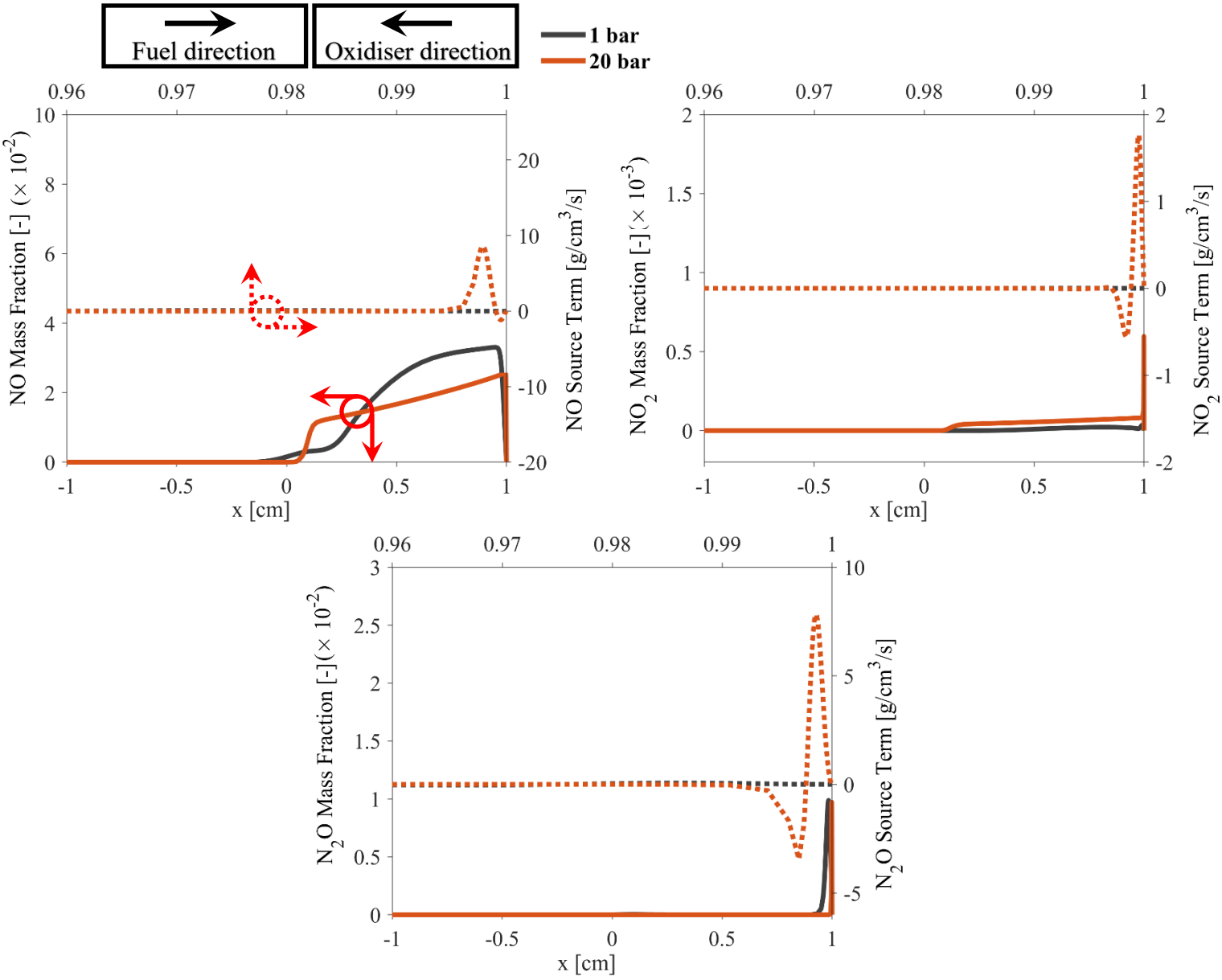

Figure E 14: A comparison of NO, NO_2 and N_2O mass fraction and source terms at various pressure levels for case 4.

- Case 5.

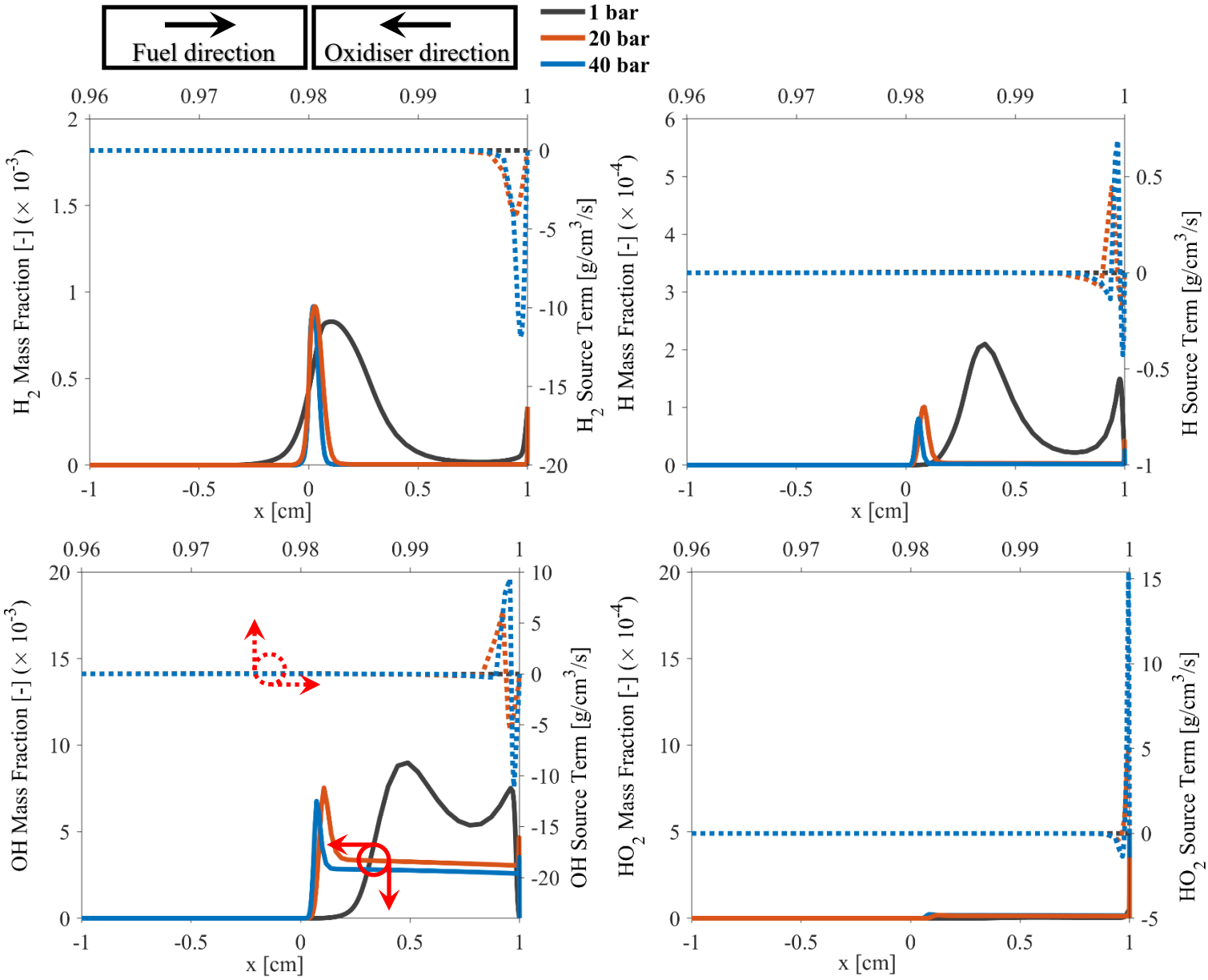

Figure E 15: A comparison of H_2, H, OH and HO_2 mass fraction and source terms at various pressure levels of case 5.

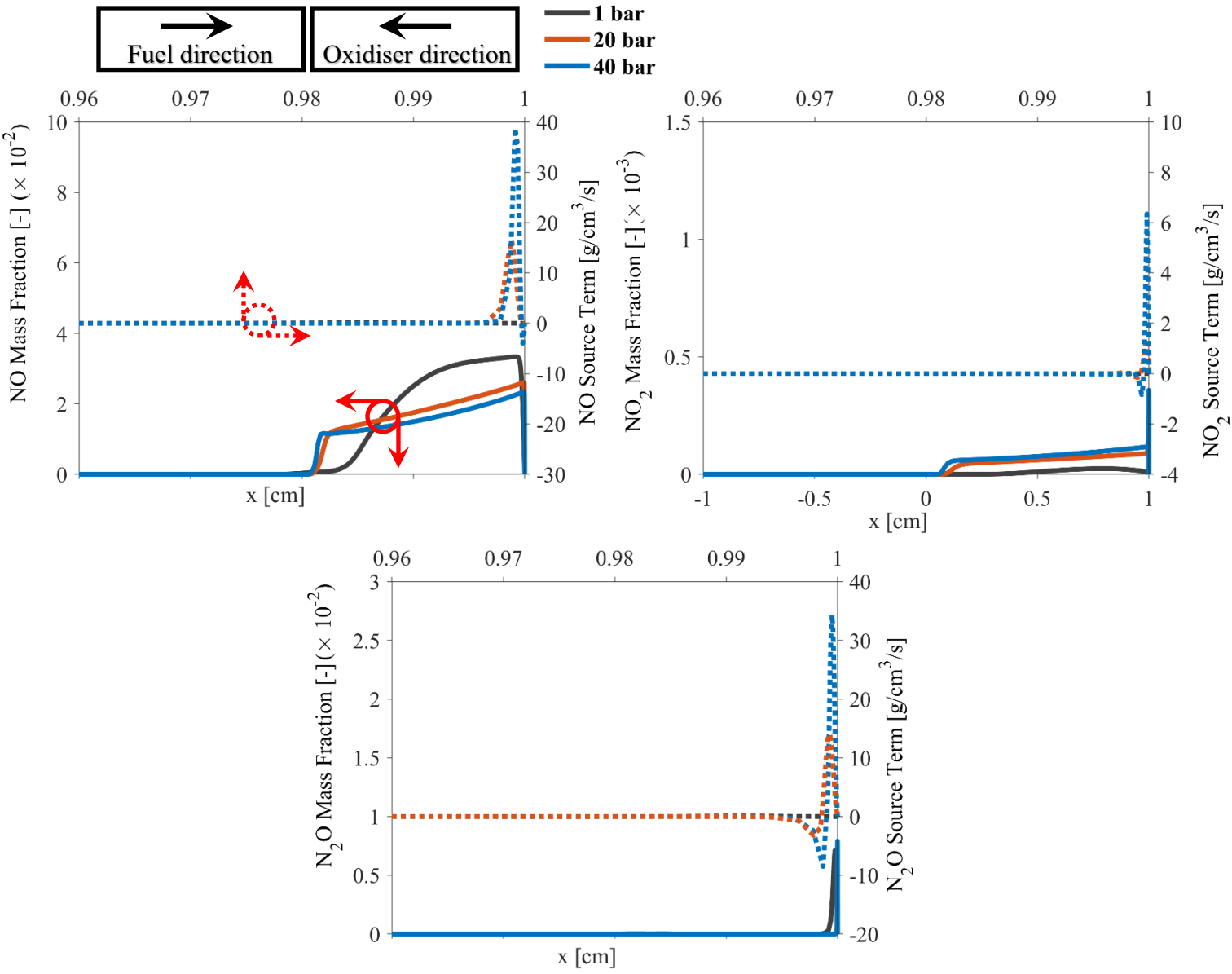

Figure E 16: A comparison of NO, NO_2 and N_2O mass fraction and source terms at various pressure levels for case 5.

References

[1] P. de Almeida and P. D. Silva. "The peak of oil production—Timings and market recognition". *Energy Policy,* Vol. 37, No. 4, pp. 1267-1276, 2009, DOI: https://doi.org/10.1016/j.enpol.2008.11.016.

[2] N. Saravanan, G. Nagarajan, G. Sanjay, C. Dhanasekaran, and K. M. Kalaiselvan. "Combustion analysis on a DI diesel engine with hydrogen in dual fuel mode". *Fuel,* Vol. 87, No. 17-18, pp. 3591-3599, 2008, DOI: https://doi.org/10.1016/j.fuel.2008.07.011.

[3] T. Shudo, S. Nabetani, and Y. Nakajima. "Analysis of the degree of constant volume and cooling loss in a spark ignition engine fuelled with hydrogen". *International Journal of Engine Research,* Vol. 2, No. 1, pp. 81-92, 2001, DOI: https://doi.org/10.1243/1468087011545361.

[4] V. Chintala and K. A. Subramanian. "A comprehensive review on utilization of hydrogen in a compression ignition engine under dual fuel mode". *Renewable and Sustainable Energy Reviews,* Vol. 70, pp. 472-491, 2017, DOI: https://doi.org/10.1016/j.rser.2016.11.247.

[5] H. Köse and M. Ciniviz. "An experimental investigation of effect on diesel engine performance and exhaust emissions of addition at dual fuel mode of hydrogen". *Fuel Processing Technology,* Vol. 114, pp. 26-34, 2013, DOI: https://doi.org/10.1016/j.fuproc.2013.03.023.

[6] W. W. Pulkrabek. *Engineering Fundamentals of the Internal Combustion Engine*. Upper Saddle River, New Jersay: Prentice Hall, 2004.

[7] T. Azuma. "Representation of abonormal combustion". https://carfromjapan.com/article/car-maintenance/common-engine-knocking-causes/ (Accessed on 1/11/2019).

[8] X. Han, Z. Wang, Y. He, Y. Zhu, and K. Cen. "Experimental and kinetic modeling study of laminar burning velocities of NH3/syngas/air premixed flames". *Combustion and Flame,* Vol. 213, pp. 1-13, 2020, DOI: https://doi.org/10.1016/j.combustflame.2019.11.032.

[9] O. Kurata *et al.* "Performances and emission characteristics of NH3–air and NH3CH4–air combustion gas-turbine power generations". *Proceedings of the Combustion Institute,* Vol. 36, No. 3, pp. 3351-3359, 2017, DOI: https://doi.org/10.1016/j.proci.2016.07.088.

[10] K. Ryu, G. E. Zacharakis-Jutz, and S.-C. Kong. "Performance enhancement of ammonia-fueled engine by using dissociation catalyst for hydrogen generation". *International Journal of Hydrogen Energy,* Vol. 39, No. 5, pp. 2390-2398, 2014, DOI: https://doi.org/10.1016/j.ijhydene.2013.11.098.

[11] A. Afif, N. Radenahmad, Q. Cheok, S. Shams, J. H. Kim, and A. K. Azad. "Ammonia-fed fuel cells: a comprehensive review". *Renewable and Sustainable Energy Reviews,* Vol. 60, pp. 822-835, 2016, DOI: https://doi.org/10.1016/j.rser.2016.01.120.

[12] A. Hayakawa, T. Goto, R. Mimoto, Y. Arakawa, T. Kudo, and H. Kobayashi. "Laminar burning velocity and Markstein length of ammonia/air premixed flames at various pressures". *Fuel,* Vol. 159, pp. 98-106, 2015, DOI: https://doi.org/10.1016/j.fuel.2015.06.070.

[13] A. E. Dahoe. "Laminar burning velocities of hydrogen–air mixtures from closed vessel gas explosions". *Journal of Loss Prevention in the Process Industries,* Vol. 18, No. 3, pp. 152-166, 2005, DOI: https://doi.org/10.1016/j.jlp.2005.03.007.

[14] A. A. Khateeb, T. F. Guiberti, X. Zhu, M. Younes, A. Jamal, and W. L. Roberts. "Stability limits and NO emissions of technically-premixed ammonia-hydrogen-nitrogen-air swirl flames". *International Journal of Hydrogen Energy,* Vol. 45, No. 41, pp. 22008-22018, 2020, DOI: https://doi.org/10.1016/j.ijhydene.2020.05.236.

[15] C. Lhuillier, P. Brequigny, N. Lamoureux, F. Contino, and C. Mounaïm-Rousselle. "Experimental investigation on laminar burning velocities of ammonia/hydrogen/air mixtures at elevated temperatures". *Fuel,* Vol. 263, p. 116653, 2020, DOI: https://doi.org/10.1016/j.fuel.2019.116653.

[16] J. Chen, X. Jiang, X. Qin, and Z. Huang. "Effect of hydrogen blending on the high temperature auto-ignition of ammonia at elevated pressure". *Fuel,* Vol. 287, p. 119563, 2021, DOI: https://doi.org/10.1016/j.fuel.2020.119563.

[17] A. Ichikawa, A. Hayakawa, Y. Kitagawa, K. D. Kunkuma Amila Somarathne, T. Kudo, and H. Kobayashi. "Laminar burning velocity and Markstein length of ammonia/hydrogen/air premixed flames at elevated pressures". *International Journal of*

Hydrogen Energy, Vol. 40, No. 30, pp. 9570-9578, 2015, DOI: https://doi.org/10.1016/j.ijhydene.2015.04.024.

[18] B. Mei, J. Zhang, X. Shi, Z. Xi, and Y. Li. "Enhancement of ammonia combustion with partial fuel cracking strategy: Laminar flame propagation and kinetic modeling investigation of NH3/H2/N2/air mixtures up to 10 atm". *Combustion and Flame,* Vol. 231, p. 111472, 2021, DOI: https://doi.org/10.1016/j.combustflame.2021.111472.

[19] J. Otomo, M. Koshi, T. Mitsumori, H. Iwasaki, and K. Yamada. "Chemical kinetic modeling of ammonia oxidation with improved reaction mechanism for ammonia/air and ammonia/hydrogen/air combustion". *International Journal of Hydrogen Energy,* Vol. 43, No. 5, pp. 3004-3014, 2018, DOI: https://doi.org/10.1016/j.ijhydene.2017.12.066.

[20] E. I. Nouvelles. https://www.ifpenergiesnouvelles.com/article/biofuels-dashboard-2019 (Accessed on 01/05/2022).

[21] A. M. Liaquat, H. H. Masjuki, M. A. Kalam, and I. M. Rizwanul Fattah. "Impact of biodiesel blend on injector deposit formation". *Energy,* Vol. 72, pp. 813-823, 2014, DOI: https://doi.org/10.1016/j.energy.2014.06.006.

[22] K. Velmurugan and A. P. Sathiyagnanam. "Effect of biodiesel fuel properties and formation of NOx emissions: a review". *International Journal of Ambient Energy,* Vol. 38, No. 6, pp. 644-651, 2017, DOI: https://doi.org/10.1080/01430750.2016.1155486.

[23] C. Vo, C. Charoenphonphanich, P. Karin, S. Susumu, and K. Hidenori. "Effects of variable O2 concentrations and injection pressures on the combustion and emissions characteristics of the petro-diesel and hydrotreated vegetable oil-based fuels under the simulated diesel engine condition". *Journal of the Energy Institute,* Vol. 91, No. 6, pp. 1071-1084, 2018, DOI: https://doi.org/10.1016/j.joei.2017.07.002.

[24] E. International. https://www.ukimediaevents.com/publication/c141a6ab/1 (Accessed on 01/05/2022).

[25] J. A. van Oijen, A. Donini, R. J. M. Bastiaans, J. H. M. ten Thije Boonkkamp, and L. P. H. de Goey. "State-of-the-art in premixed combustion modeling using flamelet generated manifolds". *Progress in Energy and Combustion Science,* Vol. 57, pp. 30-74, 2016, DOI: https://doi.org/10.1016/j.pecs.2016.07.001.

[26] P. K. Bose and D. Maji. "An experimental investigation on engine performance and emissions of a single cylinder diesel engine using hydrogen as inducted fuel and diesel as

injected fuel with exhaust gas recirculation". *International Journal of Hydrogen Energy,* Vol. 34, No. 11, pp. 4847-4854, 2009, DOI: https://doi.org/10.1016/j.ijhydene.2008.10.077.

[27] E. L. Miller *et al.* "U.S. Department of Energy Hydrogen and Fuel Cells Program: Progress, Challenges and Future Directions". *MRS Advances,* Vol. 1, No. 42, pp. 2839-2855, 2016, DOI: https://doi.org/10.1557/adv.2016.495.

[28] H. Koten. "Hydrogen effects on the diesel engine performance and emissions". *International Journal of Hydrogen Energy,* Vol. 43, No. 22, pp. 10511-10519, 2018, DOI: https://doi.org/10.1016/j.ijhydene.2018.04.146.

[29] M. Ji and J. Wang. "Review and comparison of various hydrogen production methods based on costs and life cycle impact assessment indicators". *International Journal of Hydrogen Energy,* Vol. 46, No. 78, pp. 38612-38635, 2021, DOI: https://doi.org/10.1016/j.ijhydene.2021.09.142.

[30] P. Nikolaidis and A. Poullikkas. "A comparative overview of hydrogen production processes". *Renewable and Sustainable Energy Reviews,* Vol. 67, pp. 597-611, 2017, DOI: https://doi.org/10.1016/j.rser.2016.09.044.

[31] N. Z. Muradov. "How to produce hydrogen from fossil fuels without CO2 emission". *International Journal of Hydrogen Energy,* Vol. 18, No. 3, pp. 211-215, 1993, DOI: https://doi.org/10.1016/0360-3199(93)90021-2.

[32] A. Iulianelli, S. Liguori, J. Wilcox, and A. Basile. "Advances on methane steam reforming to produce hydrogen through membrane reactors technology: A review". *Catalysis Reviews,* Vol. 58, No. 1, pp. 1-35, 2016, DOI: https://doi.org/10.1080/01614940.2015.1099882.

[33] T. Y. Amiri, K. Ghasemzageh, and A. Iulianelli. "Membrane reactors for sustainable hydrogen production through steam reforming of hydrocarbons: A review". *Chemical Engineering and Processing - Process Intensification,* Vol. 157, p. 108148, 2020, DOI: https://doi.org/10.1016/j.cep.2020.108148.

[34] N. L. Garland. "US Department of Energy Fuel Cell Technologies Program". in *18th World Hydrogen Energy Conference 2010–WHEC 2010 Proceedings Speeches and Plenary Talks*, 2010.

[35] S. Arvelakis and E. G. Koukios. "Physicochemical upgrading of agroresidues as feedstocks for energy production via thermochemical conversion methods". *Biomass and Bioenergy,* Vol. 22, No. 5, pp. 331-348, 2002, DOI: https://doi.org/10.1016/S0961-9534(01)00056-3.

[36] T. Kato. "Present status of hydrogen production by electrolysis". *Nihon Enerugi Gakkaishi/Journal of the Japan Institute of Energy,* Vol. 88, pp. 371-377, 2009.

[37] J. Andersson and S. Grönkvist. "Large-scale storage of hydrogen". *International Journal of Hydrogen Energy,* Vol. 44, No. 23, pp. 11901-11919, 2019, DOI: https://doi.org/10.1016/j.ijhydene.2019.03.063.

[38] P. Adelhelm and P. E. de Jongh. "The impact of carbon materials on the hydrogen storage properties of light metal hydrides". *Journal of Materials Chemistry,* Vol. 21, No. 8, pp. 2417-2427, 2011, DOI: https://doi.org/10.1039/C0JM02593C.

[39] T. Zhang, H. Miyaoka, H. Miyaoka, T. Ichikawa, and Y. Kojima. "Review on Ammonia Absorption Materials: Metal Hydrides, Halides, and Borohydrides". *ACS Applied Energy Materials,* Vol. 1, No. 2, pp. 232-242, 2018, DOI: https://doi.org/10.1016/S0360-3199(01)00026-X.

[40] K. Reddi, M. Mintz, A. Elgowainy, and E. Sutherland. "13 - Building a hydrogen infrastructure in the United States". in *Compendium of Hydrogen Energy*, M. Ball, A. Basile, and T. N. Veziroğlu Eds. Oxford. Woodhead Publishing, 2016, pp. 293-319.

[41] M. E. Demir and I. Dincer. "Cost assessment and evaluation of various hydrogen delivery scenarios". *International Journal of Hydrogen Energy,* Vol. 43, No. 22, pp. 10420-10430, 2018, DOI: https://doi.org/10.1016/j.ijhydene.2017.08.002.

[42] A. Witkowski, A. Rusin, M. Majkut, and K. Stolecka. "Analysis of compression and transport of the methane/hydrogen mixture in existing natural gas pipelines". *International Journal of Pressure Vessels and Piping,* Vol. 166, pp. 24-34, 2018, DOI: https://doi.org/10.1016/j.ijpvp.2018.08.002.

[43] S. Verhelst and R. Sierens. "Hydrogen engine-specific properties". *International Journal of Hydrogen Energy,* Vol. 26, No. 9, pp. 987-990, 2001, DOI: https://doi.org/10.1016/S0360-3199(01)00026-X.

[44] A. Mohammadi, M. Shioji, Y. Nakai, W. Ishikura, and E. Tabo. "Performance and combustion characteristics of a direct injection SI hydrogen engine". *International Journal*

of Hydrogen Energy, Vol. 32, No. 2, pp. 296-304, 2007, DOI: https://doi.org/10.1016/j.ijhydene.2006.06.005.

[45] C. Liew *et al.* "An experimental investigation of the combustion process of a heavy-duty diesel engine enriched with H2". *International Journal of Hydrogen Energy,* Vol. 35, No. 20, pp. 11357-11365, 2010, DOI: https://doi.org/10.1016/j.ijhydene.2010.06.023.

[46] P. Dimitriou and T. Tsujimura. "A review of hydrogen as a compression ignition engine fuel". *International Journal of Hydrogen Energy,* Vol. 42, No. 38, pp. 24470-24486, 2017, DOI: https://doi.org/10.1016/j.ijhydene.2017.07.232.

[47] A. Yapicioglu and I. Dincer. "Performance assesment of hydrogen and ammonia combustion with various fuels for power generators". *International Journal of Hydrogen Energy,* Vol. 43, No. 45, pp. 21037-21048, 2018, DOI: https://doi.org/10.1016/j.ijhydene.2018.08.198.

[48] H. Eichlseder, T. Wallner, R. Freymann, and J. Ringler. *The Potential of Hydrogen Internal Combustion Engines in a Future Mobility Scenario*. 2003.

[49] C. White, R. Steeper, and A. Lutz. "The hydrogen-fueled internal combustion engine: a technical review". *International Journal of Hydrogen Energy,* Vol. 31, No. 10, pp. 1292-1305, 2006, DOI: https://doi.org/10.1016/j.ijhydene.2005.12.001.

[50] W. F. Stockhausen *et al.* "Ford P2000 Hydrogen Engine Design and Vehicle Development Program". *SAE Technical Papers* 2002, DOI: https://doi.org/10.4271/2002-01-0240.

[51] Y. Karagöz, İ. Güler, T. Sandalcı, L. Yüksek, and A. S. Dalkılıç. "Effect of hydrogen enrichment on combustion characteristics, emissions and performance of a diesel engine". *International Journal of Hydrogen Energy,* Vol. 41, No. 1, pp. 656-665, 2016, DOI: https://doi.org/10.1016/j.ijhydene.2015.09.064.

[52] T. Tsujimura and Y. Suzuki. "The utilization of hydrogen in hydrogen/diesel dual fuel engine". *International Journal of Hydrogen Energy,* Vol. 42, No. 19, pp. 14019-14029, 2017, DOI: https://doi.org/10.1016/j.ijhydene.2017.01.152.

[53] I. T. Yilmaz, A. Demir, and M. Gumus. "Effects of hydrogen enrichment on combustion characteristics of a CI engine". *International Journal of Hydrogen Energy,* Vol. 42, No. 15, pp. 10536-10546, 2017, DOI: https://doi.org/10.1016/j.ijhydene.2017.01.214.

[54] C. Mansour, A. Bounif, A. Aris, and F. Gaillard. "Gas–Diesel (dual-fuel) modeling in diesel engine environment". *International Journal of Thermal Sciences,* Vol. 40, No. 4, pp. 409-424, 2001, DOI: https://doi.org/10.1016/S1290-0729(01)01223-6.

[55] B. B. Sahoo, N. Sahoo, and U. K. Saha. "Effect of engine parameters and type of gaseous fuel on the performance of dual-fuel gas diesel engines—A critical review". *Renewable and Sustainable Energy Reviews,* Vol. 13, No. 6-7, pp. 1151-1184, 2009, DOI: https://doi.org/10.1016/j.rser.2008.08.003.

[56] N. Saravanan and G. Nagarajan. "An experimental investigation of hydrogen-enriched air induction in a diesel engine system". *International Journal of Hydrogen Energy,* Vol. 33, No. 6, pp. 1769-1775, 2008, DOI: https://doi.org/10.1016/j.ijhydene.2007.12.065.

[57] G. A. Karim. *DUAL FUEL ENGINE*. 1st Edition. CRC Press 2015.

[58] J. Stewart. "Combustion Diagnostic of a dual fuel CI engine: an experimental and theoretical study". Doctor of Philosophy, Loughborough University, 2006.

[59] M. Y. E. Selim. "Sensitivity of dual fuel engine combustion and knocking limits to gaseous fuel composition". *Energy Conversion and Management,* Vol. 45, No. 3, pp. 411-425, 2004, DOI: https://doi.org/10.1016/S0196-8904(03)00150-X.

[60] P. Sharma and A. Dhar. "Effect of hydrogen supplementation on engine performance and emissions". *International Journal of Hydrogen Energy,* Vol. 43, No. 15, pp. 7570-7580, 2018, DOI: https://doi.org/10.1016/j.ijhydene.2018.02.181.

[61] D. B. Lata and A. Misra. "Theoretical and experimental investigations on the performance of dual fuel diesel engine with hydrogen and LPG as secondary fuels". *International Journal of Hydrogen Energy,* Vol. 35, No. 21, pp. 11918-11931, 2010, DOI: https://doi.org/10.1016/j.ijhydene.2010.08.039.

[62] H. Li *et al.* "An investigation of the combustion process of a heavy-duty dual fuel engine supplemented with natural gas or hydrogen". *International Journal of Hydrogen Energy,* Vol. 42, No. 5, pp. 3352-3362, 2017, DOI: https://doi.org/10.1016/j.ijhydene.2016.12.115.

[63] V. Chintala and K. A. Subramanian. "Experimental investigation on effect of enhanced premixed charge on combustion characteristics of a direct injection diesel engine". *International Journal of Advances in Engineering Sciences and Applied Mathematics,* journal article Vol. 6, No. 1, pp. 3-16, 2014, DOI: https://doi.org/10.1007/s12572-014-0109-7.

[64] V. Gnanamoorthi and V. T. Vimalananth. "Effect of hydrogen fuel at higher flow rate under dual fuel mode in CRDI diesel engine". *International Journal of Hydrogen Energy,* Vol. 45, No. 33, pp. 16874-16889, 2020, DOI: https://doi.org/10.1016/j.ijhydene.2020.04.145.

[65] V. S. Yadav, D. Sharma, and S. L. Soni. "Performance and combustion analysis of hydrogen-fuelled C.I. engine with EGR". *International Journal of Hydrogen Energy,* Vol. 40, No. 12, pp. 4382-4391, 2015, DOI: https://doi.org/10.1016/j.ijhydene.2015.01.162.

[66] Y. Niki, Y. Nitta, H. Sekiguchi, and K. Hirata. "Diesel fuel multiple injection effects on emission characteristics of diesel engine mixed ammonia gas into intake air". *Journal of Engineering for Gas Turbines and Power,* Vol. 141, No. 6, 2019, DOI: https://doi.org/10.1115/1.4042507.

[67] A. Dimitriadis *et al.* "Improving PM-NOx trade-off with paraffinic fuels: A study towards diesel engine optimization with HVO". *Fuel,* Vol. 265, p. 116921, 2020, DOI: https://doi.org/10.1016/j.fuel.2019.116921.

[68] K. S. Varde and G. A. Frame. "Hydrogen aspiration in a direct injection type diesel engine-its effects on smoke and other engine performance parameters". *International Journal of Hydrogen Energy,* Vol. 8, No. 7, pp. 549-555, 1983, DOI: https://doi.org/10.1016/0360-3199(83)90007-1.

[69] V. Chintala and K. A. Subramanian. "Assessment of maximum available work of a hydrogen fueled compression ignition engine using exergy analysis". *Energy,* Vol. 67, pp. 162-175, 2014, DOI: https://doi.org/10.1016/j.energy.2014.01.094.

[70] A. M. L. M. Wagemakers and C. A. J. Leermakers. "Review on the Effects of Dual-Fuel Operation, Using Diesel and Gaseous Fuels, on Emissions and Performance". *SAE Technical Paper Series,* 2012, DOI: https://doi.org/10.4271/2012-01-0869.

[71] M. Masood, S. Mehdi, and P. Ram Reddy. *Experimental Investigations on a Hydrogen-Diesel Dual Fuel Engine at Different Compression Ratios*. 2007.

[72] S. Jafarmadar. "Exergy analysis of hydrogen/diesel combustion in a dual fuel engine using three-dimensional model". *International Journal of Hydrogen Energy,* Vol. 39, No. 17, pp. 9505-9514, 2014, DOI: https://doi.org/10.1016/j.ijhydene.2014.03.152.

[73] M. S. Kumar, A. Kerihuel, J. Bellettre, and M. Tazerout. "A comparative study of different methods of using animal fat as a fuel in a compression ignition engine". *Journal of*

Engineering for Gas Turbines and Power, Vol. 128, No. 4, pp. 907-914, 2006, DOI: https://doi.org/10.1115/1.2180278.

[74] S. M. Lambe and H. C. Watson. "Low polluting, energy efficient C.I. hydrogen engine". *International Journal of Hydrogen Energy,* Vol. 17, No. 7, pp. 513-525, 1992, DOI: https://doi.org/10.1016/0360-3199(92)90151-L.

[75] G. Tripathi, P. Sharma, A. Dhar, and A. Sadiki. "Computational investigation of diesel injection strategies in hydrogen-diesel dual fuel engine". *Sustainable Energy Technologies and Assessments,* Vol. 36, p. 100543, 2019, DOI: https://doi.org/10.1016/j.seta.2019.100543.

[76] J. H. Zhou, C. S. Cheung, W. Z. Zhao, and C. W. Leung. "Diesel–hydrogen dual-fuel combustion and its impact on unregulated gaseous emissions and particulate emissions under different engine loads and engine speeds". *Energy,* Vol. 94, pp. 110-123, 2016, DOI: https://doi.org/10.1016/j.energy.2015.10.105.

[77] A. J. Reiter and S.-C. Kong. "Combustion and emissions characteristics of compression-ignition engine using dual ammonia-diesel fuel". *Fuel,* Vol. 90, No. 1, pp. 87-97, 2011, DOI: https://doi.org/10.1016/j.fuel.2010.07.055.

[78] K. O. P. Bjørgen, D. R. Emberson, and T. Løvås. "Combustion and soot characteristics of hydrotreated vegetable oil compression-ignited spray flames". *Fuel,* Vol. 266, p. 116942, 2020, DOI: https://doi.org/10.1016/j.fuel.2019.116942.

[79] V. Chintala and K. A. Subramanian. "Experimental investigations on effect of different compression ratios on enhancement of maximum hydrogen energy share in a compression ignition engine under dual-fuel mode". *Energy,* Vol. 87, pp. 448-462, 2015, DOI: https://doi.org/10.1016/j.energy.2015.05.014.

[80] Y. Karagöz, T. Sandalcı, L. Yüksek, and A. S. Dalkılıç. "Engine performance and emission effects of diesel burns enriched by hydrogen on different engine loads". *International Journal of Hydrogen Energy,* Vol. 40, No. 20, pp. 6702-6713, 2015, DOI: https://doi.org/10.1016/j.ijhydene.2015.03.141.

[81] H. Aatola, Larmi, M., Sarjovaara, T., and Mikkonen, S. "Hydrotreated Vegetable Oil (HVO) as a Renewable Diesel Fuel: Trade-off between NOx, Particulate Emission, and Fuel Consumption of a Heavy Duty Engine". *SAE Int. J. Engines,* Vol. 1, No. 1, pp. 1251-1262, 2009, DOI: https://doi.org/10.4271/2008-01-2500.

[82] T. Sandalcı and Y. Karagöz. "Experimental investigation of the combustion characteristics, emissions and performance of hydrogen port fuel injection in a diesel engine". *International Journal of Hydrogen Energy,* Vol. 39, No. 32, pp. 18480-18489, 2014, DOI: https://doi.org/10.1016/j.ijhydene.2014.09.044.

[83] Y. Niki. "Experimental Investigation of Effects of Split Diesel-Pilot Injection on Emissions From Ammonia-Diesel Dual Fuel Engine". in *ASME 2021 Internal Combustion Engine Division Fall Technical Conference*, 2021, vol. ASME 2021 Internal Combustion Engine Division Fall Technical Conference, doi: https://doi.org/10.1115/ICEF2021-66341.

[84] J. Hunicz, M. Mikulski, P. C. Shukla, and M. S. Gęca. "Partially premixed combustion of hydrotreated vegetable oil in a diesel engine: Sensitivity to boost and exhaust gas recirculation". *Fuel,* Vol. 307, p. 121910, 2022, DOI: https://doi.org/10.1016/j.fuel.2021.121910.

[85] H. Li, S. Liu, C. Liew, Y. Li, S. Wayne, and N. Clark. "An investigation on the mechanism of the increased NO 2 emissions from H 2 -diesel dual fuel engine". *International Journal of Hydrogen Energy,* Vol. 43, No. 7, pp. 3837-3844, 2018, DOI: https://doi.org/10.1016/j.ijhydene.2018.01.001.

[86] G. K. Lilik, H. Zhang, J. M. Herreros, D. C. Haworth, and A. L. Boehman. "Hydrogen assisted diesel combustion". *International Journal of Hydrogen Energy,* Vol. 35, No. 9, pp. 4382-4398, 2010, DOI: https://doi.org/10.1016/j.ijhydene.2010.01.105.

[87] V. Chintala and K. A. Subramanian. "Experimental investigation of hydrogen energy share improvement in a compression ignition engine using water injection and compression ratio reduction". *Energy Conversion and Management,* Vol. 108, pp. 106-119, 2016, DOI: https://doi.org/10.1016/j.enconman.2015.10.069.

[88] G. P. Prabhukumar, S. Swaminathan, B. Nagalingam, and K. V. Gopalakrishnan. "Water induction studies in a hydrogen-diesel dual-fuel engine". *International Journal of Hydrogen Energy,* Vol. 12, No. 3, pp. 177-186, 1987, DOI: https://doi.org/10.1016/0360-3199(87)90151-0.

[89] X. Zhen *et al.* "The engine knock analysis – An overview". *Applied Energy,* Vol. 92, pp. 628-636, 2012, DOI: https://doi.org/10.1016/j.apenergy.2011.11.079.

[90] T. Miyamoto, H. Hasegawa, M. Mikami, N. Kojima, H. Kabashima, and Y. Urata. "Effect of hydrogen addition to intake gas on combustion and exhaust emission characteristics of

a diesel engine". *International Journal of Hydrogen Energy,* Vol. 36, No. 20, pp. 13138-13149, 2011, DOI: https://doi.org/10.1016/j.ijhydene.2011.06.144.

[91] X. Liu, H. Wang, Z. Zheng, and M. Yao. "Numerical investigation on the combustion and emission characteristics of a heavy-duty natural gas-diesel dual-fuel engine". *Fuel,* Vol. 300, p. 120998, 2021, DOI: https://doi.org/10.1016/j.fuel.2021.120998.

[92] S. Frankl and S. Gleis. "Development of a 3D-Computational Fluid Dynamics Model for a Full Optical High-Pressure Dual-Fuel Engine". *SAE International Journal of Engines,* Vol. 13, No. 2, pp. 241-252, 2020, DOI: https://doi.org/10.4271/03-13-02-0017.

[93] P. Senecal *et al. Multi-Dimensional Modeling of Direct-Injection Diesel Spray Liquid Length and Flame Lift-off Length using CFD and Parallel Detailed Chemistry*. 2003.

[94] B. Tekgül, H. Kahila, O. Kaario, and V. Vuorinen. "Large-eddy simulation of dual-fuel spray ignition at different ambient temperatures". *Combustion and Flame,* Vol. 215, pp. 51-65, 2020, DOI: https://doi.org/10.1016/j.combustflame.2020.01.017.

[95] S. M. Hosseini and R. Ahmadi. "Performance and emissions characteristics in the combustion of co-fuel diesel-hydrogen in a heavy duty engine". *Applied Energy,* Vol. 205, pp. 911-925, 2017, DOI: https://doi.org/10.1016/j.apenergy.2017.08.044.

[96] C. J. Ramsay, K. K. J. R. Dinesh, W. Fairney, and N. Vaughan. "A numerical study on the effects of constant volume combustion phase on performance and emissions characteristics of a diesel-hydrogen dual-fuel engine". *International Journal of Hydrogen Energy,* Vol. 45, No. 56, pp. 32598-32618, 2020, DOI: https://doi.org/10.1016/j.ijhydene.2020.09.021.

[97] Z. Wang, F. Zhang, Y. Xia, D. Wang, Y. Xu, and G. Du. "Combustion phase of a diesel/natural gas dual fuel engine under various pilot diesel injection timings". *Fuel,* Vol. 289, p. 119869, 2021, DOI: https://doi.org/10.1016/j.fuel.2020.119869.

[98] O. Colin, A. Benkenida, and C. Angelberger. "3d Modeling of Mixing, Ignition and Combustion Phenomena in Highly Stratified Gasoline Engines". *Oil & Gas Science and Technology-revue De L Institut Francais Du Petrole - OIL GAS SCI TECHNOL,* Vol. 58, No. 1, pp. 47-62, 2003, DOI: https://doi.org/10.2516/ogst:2003004.

[99] O. Colin and A. Benkenida. "The 3-Zones Extended Coherent Flame Model (Ecfm3z) for Computing Premixed/Diffusion Combustion". *Oil & Gas Science and Technology-revue De L Institut Francais Du Petrole - OIL GAS SCI TECHNOL,* Vol. 59, pp. 593-609, 2004, DOI: https://doi.org/10.2516/ogst:2004043.

[100] K. K. J. Ranga Dinesh, H. Shalaby, K. H. Luo, J. A. van Oijen, and D. Thévenin. "High hydrogen content syngas fuel burning in lean premixed spherical flames at elevated pressures: Effects of preferential diffusion". *International Journal of Hydrogen Energy,* Vol. 41, No. 40, pp. 18231-18249, 2016, DOI: https://doi.org/10.1016/j.ijhydene.2016.07.086.

[101] K. K. J. Ranga Dinesh, H. Shalaby, K. H. Luo, J. A. van Oijen, and D. Thévenin. "Heat release rate variations in high hydrogen content premixed syngas flames at elevated pressures: Effect of equivalence ratio". *International Journal of Hydrogen Energy,* Vol. 42, No. 10, pp. 7029-7044, 2017, DOI: https://doi.org/10.1016/j.ijhydene.2016.11.205.

[102] F. A. Williams. R. Hanson, D. T. Pratt, and D. J. Seery. Eds. *combustion theory*. 2nd Edition. The Benjamin/Cummings Publishing Company, 1994.

[103] C. K. Law. *Combustion Physics*. Cambridge: Cambridge University Press, 2006.

[104] W. P. Jones and R. P. Lindstedt. "Global reaction schemes for hydrocarbon combustion". *Combustion and Flame,* Vol. 73, No. 3, pp. 233-249, 1988, DOI: https://doi.org/10.1016/0010-2180(88)90021-1.

[105] A. Kéromnès *et al.* "An experimental and detailed chemical kinetic modeling study of hydrogen and syngas mixture oxidation at elevated pressures". *Combustion and Flame,* Vol. 160, No. 6, pp. 995-1011, 2013, DOI: https://doi.org/10.1016/j.combustflame.2013.01.001.

[106] Gregory P. Smith *et al.* "GRI-Mech 3.0". http://combustion.berkeley.edu/gri-mech/version30/text30.html (Accessed on 12/2/2022).

[107] X. Guo *et al.* "Development of a Diesel/Natural Gas Mechanism Model for the CFD Simulation of Dual-Fuel Engine". *ACS Omega,* Vol. 6, No. 33, pp. 21543-21555, 2021, DOI: https://doi.org/10.1021/acsomega.1c02514.

[108] S. Park, Y. Ra, R. D. Reitz, W. J. Pitz, and E. Kurtz. "Development of a reduced tri-propylene glycol monomethyl ether–n-hexadecane–poly-aromatic hydrocarbon mechanism and its application for soot prediction". *International Journal of Engine Research,* Vol. 17, No. 9, pp. 969-982, 2016, DOI: https://doi.org/10.1177/1468087416632367.

[109] F. Chiñas-Castillo and H. A. Spikes. "Behaviour of colloidally-dispersed solid particles in very thin film lubricated contacts". in *Tribology Series*. vol. 38, D. Dowson *et al.* Eds. Elsevier, 2000, pp. 719-731.

[110] Z. Zhang *et al.* "Experimental and Numerical Investigation on the Macroscopic Characteristics of Hydrotreated Vegetable Oil (HVO) Spray". *Energy Procedia,* Vol. 142, pp. 474-480, 2017, DOI: https://doi.org/10.1016/j.egypro.2017.12.074.

[111] T. Poinsot and D. Veynante. *Theoretical and Numerical Combustion*. 2nd Edition. Edwards, 2005.

[112] H. K. Versteeg and W. Malalasekera. *An Introduction to Computational Fluid Dynamics*. Second Edition. Pearson Education Limited, 2007.

[113] P. K. G. Pantangi. "Large Eddy Simulation of Mixing and Combustion in Combustion Systems under Non-adiabatic Conditions". Dissertation, Mechanical engineering, Darmstadt zur, 2016.

[114] N. Peter. Combustion Theory. [Online] Available: Available Online: https://www.itv.rwth-aachen.de/fileadmin/Downloads/Summerschools/Peters_Summerschool_reference.pdf : Last Accessed: August 26, 2018.

[115] H. Bongers. "Analysis of flamelet-based methods to reduce chemical kinetics in flame computations". PhD, Department of Mechanical Engineering, Eindhoven University of Technology, 2005.

[116] N. Peters. "Laminar flamelet concepts in turbulent combustion". *Symposium (International) on Combustion,* Vol. 21, No. 1, pp. 1231-1250, 1988, DOI: https://doi.org/10.1016/S0082-0784(88)80355-2.

[117] A. Donini, R. J. M. Bastiaans, J. A. van Oijen, and L. P. H. de Goey. "A five dimensional implementation of the flamelet generated manifolds technique for gas turbine application". 2015.

[118] J. van Oijen. "Flamelet-generated manifolds : development and application to premixed laminar flames". Doctor of Philosophy, Department of Mechanical Engineering, Eindhoven University of Technology, 2002.

[119] J. A. van Oijen, F. A. Lammers, and L. P. H. de Goey. "Modeling of complex premixed burner systems by using flamelet-generated manifolds". *Combustion and Flame,* Vol. 127, No. 3, pp. 2124-2134, 2001, DOI: https://doi.org/10.1016/S0010-2180(01)00316-9.

[120] A. W. Vreman, B. A. Albrecht, J. A. van Oijen, L. P. H. de Goey, and R. J. M. Bastiaans. "Premixed and nonpremixed generated manifolds in large-eddy simulation of Sandia flame D and F". *Combustion and Flame,* Vol. 153, No. 3, pp. 394-416, 2008, DOI: https://doi.org/10.1016/j.combustflame.2008.01.009.

[121] W. J. S. Ramaekers, J. A. van Oijen, and L. P. H. de Goey. "A Priori Testing of Flamelet Generated Manifolds for Turbulent Partially Premixed Methane/Air Flames". *Flow, Turbulence and Combustion,* Vol. 84, No. 3, pp. 439-458, 2010, DOI: https://doi.org/10.1007/s10494-009-9223-1.

[122] U. Maas and S. B. Pope. "Simplifying chemical kinetics: Intrinsic low-dimensional manifolds in composition space". *Combustion and Flame,* Vol. 88, No. 3, pp. 239-264, 1992, DOI: https://doi.org/10.1016/0010-2180(92)90034-M.

[123] S. H. Lam and D. A. Goussis. "Understanding complex chemical kinetics with computational singular perturbation". *Symposium (International) on Combustion,* Vol. 22, No. 1, pp. 931-941, 1989, DOI: https://doi.org/10.1016/S0082-0784(89)80102-X.

[124] J. A. V. Oijen and L. P. H. D. Goey. "Modelling of Premixed Laminar Flames using Flamelet-Generated Manifolds". *Combustion Science and Technology,* Vol. 161, No. 1, pp. 113-137, 2000, DOI: https://doi.org/10.1080/00102200008935814.

[125] L. M. T. Somers. "The simulation of flat flames with detailed and reduced chemical models". PhD, Mechanical Engineering, Eindhoven University of Technology, 1994.

[126] J. O. Hirschfelder, C. F. Curtiss, R. B. Bird, W. University of, and L. Naval Research. *Molecular theory of gases and liquids*. New York: Wiley (in English), 1954.

[127] R. W. Bilger. "The structure of turbulent nonpremixed flames". *Symposium (International) on Combustion,* Vol. 22, No. 1, pp. 475-488, 1989, DOI: https://doi.org/10.1016/S0082-0784(89)80054-2.

[128] J. A. M. de Swart, R. J. M. Bastiaans, J. A. van Oijen, L. P. H. de Goey, and R. S. Cant. "Inclusion of Preferential Diffusion in Simulations of Premixed Combustion of Hydrogen/Methane Mixtures with Flamelet Generated Manifolds". *Flow, Turbulence and Combustion,* Vol. 85, No. 3, pp. 473-511, 2010, DOI: https://doi.org/10.1007/s10494-010-9279-y.

[129] K. Bray, P. Domingo, and L. Vervisch. "Role of the progress variable in models for partially premixed turbulent combustion". *Combustion and Flame,* Vol. 141, No. 4, pp. 431-437, 2005, DOI: https://doi.org/10.1016/j.combustflame.2005.01.017.

[130] D. W. Stanton and C. J. Rutland. "Modeling Fuel Film Formation and Wall Interaction in Diesel Engines". 1996. [Online]. Available: https://doi.org/10.4271/960628.

[131] R. Reitz. "Modeling atomization processes in high-pressure vaporizing sprays". *Atomisation Spray Technology,* Vol. 3, pp. 309-337, 1987.

[132] R. D. Reitz and J. C. Beale. "MODELING SPRAY ATOMIZATION WITH THE KELVIN-HELMHOLTZ/RAYLEIGH-TAYLOR HYBRID MODEL". Vol. 9, No. 6, pp. 623-650, 1999, DOI: https://doi.org/10.1615/AtomizSpr.v9.i6.40.

[133] D. G. Holmes and S. D. Connell. "Solution of the 2D Navier-Stokes equations on unstructured adaptive grids". 1989.

[134] R. Rausch, J. Batina, and H. Yang. "Spatial adaption procedures on unstructured meshes for accurate unsteady aerodynamic flow computation". Vol. 91, 1991, DOI: https://doi.org/10.2514/6.1991-1106.

[135] T. Barth and D. Jespersen. "The design and application of upwind schemes on unstructured meshes". in *27th Aerospace Sciences Meeting*. American Institute of Aeronautics and Astronautics, 1989.

[136] R. I. Issa. "Solution of the implicitly discretised fluid flow equations by operator-splitting". *Journal of Computational Physics,* Vol. 62, No. 1, pp. 40-65, 1986, DOI: https://doi.org/10.1016/0021-9991(86)90099-9.

[137] G. H. Markstein. *Nonsteady flame propagation*. Oxford; New York: Published for and on behalf of Advisory Group for Aeronautical Research and Development, North Atlantic Treaty Organization by Pergamon Press; , 1964.

[138] G. I. Sivashinsky. "Diffusional-Thermal Theory of Cellular Flames". *Combustion Science and Technology,* Vol. 15, No. 3-4, pp. 137-145, 1977, DOI: https://doi.org/10.1080/00102207708946779.

[139] G. Darrieus. "Propagation d'un front de flamme". *La Technique Moderne,* Vol. 30, p. 18, 1938.

[140] L. Landau. "On the theory of slow combustion". in *Dynamics of curved fronts*. Elsevier, 1988, pp. 403-411.

[141] F. H. Vance, Y. Shoshin, J. A. van Oijen, and L. P. H. de Goey. "Effect of Lewis number on premixed laminar lean-limit flames stabilized on a bluff body". *Proceedings of the Combustion Institute,* Vol. 37, No. 2, pp. 1663-1672, 2019, DOI: https://doi.org/10.1016/j.proci.2018.07.072.

[142] Q. Liu, X. Chen, J. Huang, Y. Shen, Y. Zhang, and Z. Liu. "The characteristics of flame propagation in ammonia/oxygen mixtures". *Journal of Hazardous Materials,* Vol. 363, pp. 187-196, 2019, DOI: https://doi.org/10.1016/j.jhazmat.2018.09.073.

[143] S. Xie, Z. Lu, and Z. Chen. "Effects of strain rate and Lewis number on forced ignition of laminar counterflow diffusion flames". *Combustion and Flame,* Vol. 226, pp. 302-314, 2021, DOI: https://doi.org/10.1016/j.combustflame.2020.12.027.

[144] E. C. Okafor *et al.* "Experimental and numerical study of the laminar burning velocity of CH4–NH3–air premixed flames". *Combustion and Flame,* Vol. 187, pp. 185-198, 2018, DOI: https://doi.org/10.1016/j.combustflame.2017.09.002.

[145] O. C. Kwon and G. M. Faeth. "Flame/stretch interactions of premixed hydrogen-fueled flames: measurements and predictions". *Combustion and Flame,* Vol. 124, No. 4, pp. 590-610, 2001, DOI: https://doi.org/10.1016/S0010-2180(00)00229-7.

[146] Y. Li, M. Bi, B. Li, and W. Gao. "Explosion behaviors of ammonia–air mixtures". *Combustion Science and Technology,* Vol. 190, No. 10, pp. 1804-1816, 2018, DOI: https://doi.org/10.1080/00102202.2018.1473859.

[147] B. Li, N. Liu, R. Zhao, H. Zhang, and F. N. Egolfopoulos. "Flame propagation of mixtures of air with high molecular weight neat hydrocarbons and practical jet and diesel fuels". *Proceedings of the Combustion Institute,* Vol. 34, No. 1, pp. 727-733, 2013, DOI: https://doi.org/10.1016/j.proci.2012.05.063.

[148] C. J. Sun, C. J. Sung, L. He, and C. K. Law. "Dynamics of weakly stretched flames: quantitative description and extraction of global flame parameters". *Combustion and Flame,* Vol. 118, No. 1, pp. 108-128, 1999, DOI: https://doi.org/10.1016/S0010-2180(98)00137-0.

[149] E. C. Okafor *et al.* "Measurement and modelling of the laminar burning velocity of methane-ammonia-air flames at high pressures using a reduced reaction mechanism". *Combustion and Flame,* Vol. 204, pp. 162-175, 2019, DOI: https://doi.org/10.1016/j.combustflame.2019.03.008.

[150] R. J. Blint. "The Relationship of the Laminar Flame Width to Flame Speed". *Combustion Science and Technology,* Vol. 49, No. 1-2, pp. 79-92, 1986, DOI: https://doi.org/10.1080/00102208608923903.

[151] S. Bougrine, S. Richard, and D. Veynante. "On the combination of complex chemistry with a 0-D coherent flame model to account for the fuel properties in spark ignition engines simulations: Application to methane-air-diluents mixtures". *Proceedings of the Combustion Institute,* Vol. 33, No. 2, pp. 3123-3130, 2011, DOI: https://doi.org/10.1016/j.proci.2010.06.017.

[152] J. Vancoillie, J. Demuynck, J. Galle, S. Verhelst, and J. A. van Oijen. "A laminar burning velocity and flame thickness correlation for ethanol–air mixtures valid at spark-ignition engine conditions". *Fuel,* Vol. 102, pp. 460-469, 2012, DOI: https://doi.org/10.1016/j.fuel.2012.05.022.

[153] R. J. Varghese, H. Kolekar, V. R. Kishore, and S. Kumar. "Measurement of laminar burning velocities of methane-air mixtures simultaneously at elevated pressures and elevated temperatures". *Fuel,* Vol. 257, p. 116120, 2019, DOI: https://doi.org/10.1016/j.fuel.2019.116120.

[154] Z. Liu, S. Yang, C. K. Law, and A. Saha. "Cellular instability in Le < 1 turbulent expanding flames". *Proceedings of the Combustion Institute,* Vol. 37, No. 2, pp. 2611-2618, 2019, DOI: https://doi.org/10.1016/j.proci.2018.07.056.

[155] Z. Liu, V. R. Unni, S. Chaudhuri, R. Sui, C. K. Law, and A. Saha. "Self-turbulization in cellularly unstable laminar flames". *Journal of Fluid Mechanics,* Vol. 917, p. A53, 2021, Art no. A53, DOI: https://doi.org/10.1017/jfm.2021.330.

[156] M. Mitu, D. Razus, V. Giurcan, and D. Oancea. "Experimental and Numerical Study of Laminar Burning Velocity of Ethane–Air Mixtures of Variable Initial Composition, Temperature and Pressure". *Energy & Fuels,* Vol. 28, No. 3, pp. 2179-2188, 2014, DOI: https://doi.org/10.1021/ef402197y.

[157] M. Mitu, D. Razus, V. Giurcan, and D. Oancea. "Normal burning velocity and propagation speed of ethane–air: Pressure and temperature dependence". *Fuel,* Vol. 147, pp. 27-34, 2015, DOI: https://doi.org/10.1016/j.fuel.2015.01.026.

[158] J. Liu, Q. Guo, J. Guo, and F. Wang. "Optimization of a diesel/natural gas dual fuel engine under different diesel substitution ratios". *Fuel,* Vol. 305, p. 121522, 2021, DOI: https://doi.org/10.1016/j.fuel.2021.121522.

[159] H. An, W. M. Yang, A. Maghbouli, J. Li, S. K. Chou, and K. J. Chua. "A numerical study on a hydrogen assisted diesel engine". *International Journal of Hydrogen Energy,* Vol. 38, No. 6, pp. 2919-2928, 2013, DOI: https://doi.org/10.1016/j.ijhydene.2012.12.062.

[160] G. A. Karim. "Combustion in Gas Fueled Compression: Ignition Engines of the Dual Fuel Type". *Journal of Engineering for Gas Turbines and Power,* Vol. 125, No. 3, pp. 827-836, 2003, DOI: https://doi.org/10.1115/1.1581894.

[161] S. Tüchler and P. Dimitriou. "On the capabilities and limitations of predictive, multi-zone combustion models for hydrogen-diesel dual fuel operation". *International Journal of Hydrogen Energy,* Vol. 44, No. 33, pp. 18517-18531, 2019, DOI: https://doi.org/10.1016/j.ijhydene.2019.05.172.

[162] K. K. J. Ranga Dinesh, X. Jiang, J. A. van Oijen, R. J. M. Bastiaans, and L. P. H. de Goey. "Hydrogen-enriched nonpremixed jet flames: Effects of preferential diffusion". *International Journal of Hydrogen Energy,* Vol. 38, No. 11, pp. 4848-4863, 2013, DOI: https://doi.org/10.1016/j.ijhydene.2013.01.171.

[163] A. Maghbouli, R. K. Saray, S. Shafee, and J. Ghafouri. "Numerical study of combustion and emission characteristics of dual-fuel engines using 3D-CFD models coupled with chemical kinetics". *Fuel,* Vol. 106, pp. 98-105, 2013, DOI: https://doi.org/10.1016/j.fuel.2012.10.055.

[164] V. Knop, A. Benkenida, S. Jay, and O. Colin. "Modelling of combustion and nitrogen oxide formation in hydrogen-fuelled internal combustion engines within a 3D CFD code". *International Journal of Hydrogen Energy,* Vol. 33, No. 19, pp. 5083-5097, 2008, DOI: https://doi.org/10.1016/j.ijhydene.2008.06.027.

[165] H. Kahila, A. Wehrfritz, O. Kaario, and V. Vuorinen. "Large-eddy simulation of dual-fuel ignition: Diesel spray injection into a lean methane-air mixture". *Combustion and Flame,* Vol. 199, pp. 131-151, 2019, DOI: https://doi.org/10.1016/j.combustflame.2018.10.014.

[166] E. Abtahizadeh, P. de Goey, and J. van Oijen. "Development of a novel flamelet-based model to include preferential diffusion effects in autoignition of CH4/H2 flames".

Combustion and Flame, Vol. 162, No. 11, pp. 4358-4369, 2015, DOI: https://doi.org/10.1016/j.combustflame.2015.06.015.

[167] G. Merker, S. Christian, and R. Teichmann. *Combustion Engines Development*. Berlin: Heidelberg, 2009.

[168] X. Jiang, Y. Pan, Y. Liu, W. Sun, and Z. Huang. "Experimental and kinetic study on ignition delay times of lean n-butane/hydrogen/argon mixtures at elevated pressures". *International Journal of Hydrogen Energy,* Vol. 42, No. 17, pp. 12645-12656, 2017, DOI: https://doi.org/10.1016/j.ijhydene.2017.03.196.

[169] H. Ritchie and M. Roser. "Fossil Fuels". Our World in Data. https://ourworldindata.org/energy (Accessed on 29-4-2022).

[170] United Nations. The Paris Agreement. https://unfccc.int/process-and-meetings/the-paris-agreement/the-paris-agreement (Accessed on 29-4-2022).

[171] M. Koike, H. Miyagawa, T. Suzuoki, and K. Ogasawara. "Ammonia as a hydrogen energy carrier and its application to internal combustion engines". in *Sustainable Vehicle Technologies*, Gaydon and Warwickshire Eds. Woodhead Publishing, 2012, pp. 61-70.

[172] P. Van Blarigan. "Advanced internal combustion engine research". *DOE Hydrogen Program Review NREL-CP-570-28890,* pp. 1-19, 2000.

[173] J. T. Gray Jr, E. Dimitroff, N. T. Meckel, and R. Quillian Jr. "Ammonia fuel—engine compatibility and combustion". *SAE Transactions,* pp. 785-807, 1967.

[174] United States Environmental Protection Agency. "Overview of greenhouse gases". https://www.epa.gov/ghgemissions/overview-greenhouse-gases (Accessed on 29-4-2022).

[175] A. J. Reiter and S.-C. Kong. "Demonstration of Compression-Ignition Engine Combustion Using Ammonia in Reducing Greenhouse Gas Emissions". *Energy & Fuels,* Vol. 22, No. 5, pp. 2963-2971, 2008, DOI: https://doi.org/10.1021/ef800140f.

[176] S. Kong. "Combustion efficiency and exhaust emissions of ammonia combustion in diesel engines". in *2008 Annual NH3 Fuel Conference. MINNEAPOLIS: NH3 Fuel Association*, 2008, pp. 29-30.

[177] Y. Niki, Y. Nitta, H. Sekiguchi, and K. Hirata. "Emission and combustion characteristics of diesel engine fumigated with ammonia". in *Internal Combustion Engine Division Fall Technical Conference*, 2018, vol. 51982: American Society of Mechanical Engineers.

[178] J. H. Lee, J. H. Kim, J. H. Park, and O. C. Kwon. "Studies on properties of laminar premixed hydrogen-added ammonia/air flames for hydrogen production". *International Journal of Hydrogen Energy,* Vol. 35, No. 3, pp. 1054-1064, 2010, DOI: https://doi.org/10.1016/j.ijhydene.2009.11.071.

[179] F. R. Westlye, A. Ivarsson, and J. Schramm. "Experimental investigation of nitrogen based emissions from an ammonia fueled SI-engine". *Fuel,* Vol. 111, pp. 239-247, 2013, DOI: https://doi.org/10.1016/j.fuel.2013.03.055.

[180] C. S. Mørch, A. Bjerre, M. P. Gøttrup, S. C. Sorenson, and J. Schramm. "Ammonia/hydrogen mixtures in an SI-engine: Engine performance and analysis of a proposed fuel system". *Fuel,* Vol. 90, No. 2, pp. 854-864, 2011, DOI: https://doi.org/10.1016/j.fuel.2010.09.042.

[181] S. Frigo and R. Gentili. "A Hybrid Vehicle Powered by Ammonia and Hydrogen". in *Proceedings of the 10th NH3 Fuel Conference, Sacramento, CA, USA*, 2013, pp. 22-25.

[182] S. Frigo and R. Gentili. "Further evolution of an ammonia fuelled range extender for hybrid vehicles". *Proceedings of the NH3 Fuel Association,* pp. 21-24, 2014.

[183] M. Pochet, I. Truedsson, F. Foucher, H. Jeanmart, and F. Contino. "Ammonia-Hydrogen Blends in Homogeneous-Charge Compression-Ignition Engine". *SAE Technical Papers,* Vol. 2017-24-0087, 2017, DOI: https://doi.org/10.4271/2017-24-0087.

[184] W. Tao, T. Sun, W. Guo, K. Lu, L. Shi, and H. Lin. "The effect of diesel pilot injection strategy on combustion and emission characteristic of diesel/methanol dual fuel engine". *Fuel,* Vol. 324, p. 124653, 2022, DOI: https://doi.org/10.1016/j.fuel.2022.124653.

[185] T. Bohl, A. Smallbone, G. Tian, and A. P. Roskilly. "Particulate number and NOx trade-off comparisons between HVO and mineral diesel in HD applications". *Fuel,* Vol. 215, pp. 90-101, 2018, DOI: https://doi.org/10.1016/j.fuel.2017.11.023.

[186] Q. Cheng, H. Tuomo, O. T. Kaario, and L. Martti. "Spray dynamics of HVO and EN590 diesel fuels". *Fuel,* Vol. 245, pp. 198-211, 2019, DOI: https://doi.org/10.1016/j.fuel.2019.01.123.

[187] Y. Huang, S. Wang, and L. Zhou. "Effects of Fischer-Tropsch diesel fuel on combustion and emissions of direct injection diesel engine". *Frontiers of Energy and Power Engineering in China,* Vol. 2, No. 3, pp. 261-267, 2008, DOI: https://doi.org/10.1007/s11708-008-0062-x.

[188] M. Ghazikhani, M. Hatami, B. Safari, and D. Domiri Ganji. "Experimental investigation of exhaust temperature and delivery ratio effect on emissions and performance of a gasoline–ethanol two-stroke engine". *Case Studies in Thermal Engineering,* Vol. 2, pp. 82-90, 2014, DOI: https://doi.org/10.1016/j.csite.2014.01.001.